Control Over Cadmium Chalcogenide Nanocrystal Heterostructures via Precursor Conversion Kinetics

Leslie Sachiyo Hamachi

Submitted in partial fulfillment of the requirements for the degree of Doctor of Philosophy in the Graduate School of Arts and Sciences

COLUMBIA UNIVERSITY

2018

ABSTRACT

Control Over Cadmium Chalcogenide Nanocrystal Heterostructures via Precursor Conversion Kinetics

Leslie Sachiyo Hamachi

Semiconductor nanocrystals have immense potential to make an impact in consumer products due to their narrow, tunable emission linewidths. One factor limiting their use is the ease and reproducibility of core/shell nanocrystal syntheses. This thesis aims to address this issue by providing chemical control over the formation of core/shell nanostructures by replacing engineering controls with kinetic controls.

Chapter 1 contextualizes our study on nanoparticle synthesis with a brief discussion on the physics of quantum confinement and the importance of narrow size dispersities, core/shell band alignments, and low lattice mismatches and strain at core/shell nanocrystal interfaces. Next, the evolution of cadmium chalcogenide nanocrystal reagents is described, ranging from the original organometallic reagents used in the 1980s to modern approaches involving cadmium phosphonates and carboxylates. This is followed by a description of chalcogen precursors, highlighting the recent introduction of molecules whose well-controlled and tunable reaction rates allow for the size tuning of nanocrystals at 100% yield, and accompanying theories on nanocrystal nucleation.

Chapter 2 covers work to expand the library of available sulfur precursors to a wider range of molecules relevant for the synthesis of cadmium sulfide nanocrystals. Using thioureas alone, only very fast or very slow precursor conversion rates can be accessed. This limits the accessible sizes of cadmium sulfide nanocrystals using a single hot injection of precursor at standardized reaction conditions. We observe that thiocarbonate and thiocarbamate precursors with varying electronic substituents allow access to intermediate precursor conversion rates and cadmium sulfide nanocrystal sizes. Interestingly, we note that these new precursor classes nucleate particles with higher monodispersity than ones synthesized from thioureas. These results indicate that in addition to precursor structure controlling precursor conversion rate, precursor structure additionally impacts nanocrystal monodispersity.

Chapter 3 expands the library of sulfur and selenium precursors to include cyclic thiones and selenones which extends chemical control of precursor conversion kinetics to cover five orders of magnitude. This unprecedented breadth of rate control allows for the simultaneous hot injection of multiple precursors to generate core/shell or alloyed nanoparticles using precursor reactivity. Using this new synthetic strategy, we observe that kinetic control runs into several issues which we partially attribute to differences in cadmium sulfide and cadmium selenide critical concentrations and growth rates. Nevertheless, combined with a

syringe pump shelling method, we are able to access core/shell and alloyed nanocrystals with photoluminescence quantum yields of 67-81%.

Chapter 4 applies the concept of nanostructure control via precursor conversion kinetics to a better model system: two-dimensional nanoplatelets. Cadmium chalcogenide nanoplatelets are highly desirable materials due to their exceptionally narrow emission full width half max (FWHM) values which make them pure emitters relative to quantum dots or organic dyes. We synthesize 3 monolayer thick nanoplatelets whose lateral dimensions vary from 10 nm x 10 nm to 186 x 100 nm and demonstrate compositional control on the smallest platelet sizes with STEM EELS.

TABLE OF CONTENTS

List of Charts, Graphs, and Illustrations

Acknowledgments

There are a lot of terrific people I must thank who have been instrumental in developing me into the scientist I am today. First of all, this PhD would not have been possible without the mentorship and guidance of Prof. Jonathan Owen. When I first met Jon during my grad school visit, I was struck by the synthetic rigor he brings to nanoscience and immediately knew I wanted to join his lab. As a scientist interested in using chemistry to tackle materials science problems, I can't think of a better person to have worked with. I am very grateful to have learned so much from Jon and our fantastic group of labmates and collaborators over the past five years. Additional thanks to the current and former members of my committee throughout my PhD: Prof. Xavier Roy, Prof. Jack Norton, Prof. Louis Brus, Prof. Rachel Austin, Prof. Xiaoyang Zhu, and Prof. Wei Min for your support and your constructive criticism that helps drive me to become a better scientist.

Special acknowledgement is due to Dr. Ilan Jen-La Plante, a superstar postdoc that I worked closely with during the first few years of my PhD. I greatly admire her in so many ways from her synthetic prowess, electron microscopy expertise, and capacity to mentor younger students, all while maintaining several hobbies (that I have been inspired to pick up) such as rock climbing and running.

I could not have asked for a better lab mentor and am extremely grateful for her mentorship, training and support.

Additional special thanks to Dr. Jonathan De Roo, another incredibly talented postdoc from whom I have learned a tremendous amount. I am very inspired by the scientist that he is and am grateful for his mentorship both inside and outside the lab. I can't think of a better scientific collaborator, running buddy, or scientific outreach event partner and will fondly remember the time we spent sharing a fume hood.

Another big thank you to former Owen Lab graduate students Prof. Mark Hendricks and Dr. Michael Campos whose pioneering work on thio- and selenoureas laid the groundwork for my project. I have learned so much from both of them regarding to how to think about nanocrystal synthesis, how to mentor undergraduates on the synthesis team, and where to get the best tacos and chicken tortas in NYC. Additional special thanks to Mike for helping me run my first experiments in the Owen Lab.

Thank you to the members of the solid-state lighting team: Dr. Michael Campos, Iva Rreza, Dr. Haoran Yang, Dr. Emory Chan, Dr. Joe Treadway, and Camille Violet. I have really enjoyed getting to work with and learn from all of you on a project that has such potential to do good in the world. The future of solid-state lighting is in your incredibly capable hands.

One of the highlights of graduate school has been working with several hard-working undergraduates (and a high school student!) on the synthesis team. Contributing to the work in Chapter 2, Aidan Coryell synthesized the first thiocarbonate molecule that led us to realize that this was an exciting new precursor class. Victor Gordillo synthesized thiocarbamate molecules to study the effect of electronic substituents on precursor conversion rate. Contributing to the work in Chapter 3, Greg Cleveland and Kevin Qian worked on developing the synthesis of cyclic thiones and selenones used in one-pot core/shell reactions. I take particular pleasure in being the first graduate student to have worked with Kevin and to have seen him grow from learning how to run NMRs to now basically being as effective as a graduate student while only being a college Sophomore. Contributing to the work in Chapter 4, high school student Isabel Billinge, synthesized new trisubstituted thioureas. She possessed an incredible maturity for a high school student and I enjoyed all of her puns.

Special thanks to many of my labmates past and present: the Owen Lab's first graduate student Dr. Nicholas Anderson who carries such a presence, Dr. Peter Chen who is responsible for all the trips to St. Vitus, resident physicist Dr. Octavi Semonin who empowered me to fix and repair lab equipment, Trevor Hull who I'll always think of as that guy who is super into Willy Wonka, Iva Rreza with whom it's fun to fantasize about becoming wine chemists, Matthew Greenberg

who does some really aesthetically pleasing science, Brandon McMurtry who unfailingly orders the strangest thing off any restaurant menu, Ellie Bennett whose elegant elemental maps will help us understand ZnS shelling leading to better LEDs, Natalie Saenz whose can-do attitude and pep I greatly admire, Eric Riesel for the lab fruit and always striving to keep a growth based learning mindset, and Dr. Anindya Swarnakar for the helpful discussions on main group chemistry and garam masalas. A big thank you to all of the other Owen Lab members and visiting researchers I have had the pleasure of working alongside. An additional thank you to collaborators and colleagues Soham Banerjee, Prof. Simon Billinge, Prof. Andrew Crowther, Dr. Archana Raja, Dr. Wieteke de Boer, Dr. Andi Hartel, Dr. Chris Choi, and Prof. John Kymissis.

Thank you to electron microscopists Dr. Willem Walravens and Dr. Amirali Zangiabadi for teaching me the basics of STEM and STEM-EDX imaging, Dr. Chris Goulbourne for teaching me how to prep negative stain samples, and Kelsey Jordan at NYSBC for teaching me how to plunge freeze and perform cryo-EM experiments. Additional thanks to Dr. Peter Ercius at NCEM, and Prof. David Muller, Prof. Lena Kourkoutis, and Dr. Benjamin Savitzky at CCMR for helpful discussions and much appreciated efforts to elementally map three monolayer thick nanoplatelet samples. As a synthetic chemist, I have benefitted immensely from your expertise in learning how to better characterize my samples.

Professionally, I also must thank Prof. Eleanor Johnson for her unwavering support of my career aspirations, Prof. Rachel Austin and Prof. Michael Campbell at Barnard for helpful discussions and insight to teaching chemistry at Primarily Undergraduate Institutions, and Prof. Theanne Schiros and Prof. Karen Pearson at the Fashion Institute of Technology for providing me the opportunity to explore the intersection of my interests in chemistry and fashion design.

My scientific journey started before coming to Columbia. Thank you to Dr. Katie Thornburg, my high school chemistry teacher and Dr. Michael Natan along with the rest of the team at Oxonica Materials, Inc. that inspired my interest in nanotechnology and started my aspirations towards obtaining a chemistry PhD. Thank you to Dr. Jessica Smith, my graduate student mentor in Prof. Paul Alivisatos's lab at UC Berkeley as well as Prof. Delia Milliron and Prof. Rafaella Buonsanti at the Molecular Foundry at LBNL for providing me the opportunity to perform undergraduate research.

Thank you to the countless friends who have grown along with me during my journey through graduate school. You all know who you are and I am forever grateful for our memories. Members of the board games crew, Dessert Club, the Spicy Boyz softball team, IM basketball and volleyball teams, the Starcraft II games group, Columbia University Ballet Ensemble, my co-Friday Synthesis Symposium

organizer Dr. Alex Radtke, and co-Happy Hour Chair Dr. Patrick Quinlivan, this whole experience would not have been the same without all of you.

Lastly, thank you to my family for their support of my scientific aspirations, from my dad's desire to try to understand everything written in each scientific paper I am a part of, to my mom's many letters and care packages from home, and my sister's frequent visits filled with distractions and delicious food I didn't even know existed. Thank you to my grandparents and wonderfully supportive extended family who never cease to tell me how proud they are of me. I love you. None of this would have been possible without your support.

CHAPTER 1. Introduction to Semiconductor Nanocrystals

Table of Contents

1.1. Context and Motivation

Cadmium chalcogenide quantum dot technologies have come a long way since their initial description by Brus et al., in the 1980s.[1] After a series of key synthetic advances such as ZnS overcoating,[2] development of giant multi-shell architectures,[3] and graded architectures,[4] quantum dots are now available commercially in QLED TVs (Nanosys, Samsung) and solid state lighting (OSRAM).[5] Energy savings are a large driver of the incorporation of quantum dots into solid-state lighting; the United States Department of Energy estimates that by 2035, solid-state lighting could potentially reduce national lighting electricity use by 5.1 quads, lowering U.S. electricity bills collectively by $50 billion.[6] The advantage of quantum dots in solid-state lighting is their narrower red emission profiles in comparison to conventionally used rare earth phosphors which emit wasted energy in the form of heat (Figure 1.1.1).

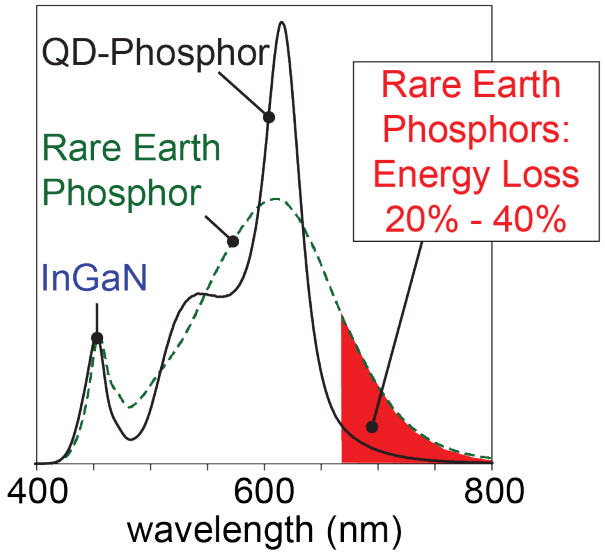

Figure 1.1.1. Replacing rare earth phosphors with quantum dot phosphors in solid state lighting provides 20-40% less energy loss.

In addition to use in solid-state lighting and displays, quantum dots are also useful as fluorescent biological imaging probes because of their high two photon absorbance cross sections[7] and photostability compared to organic dyes or genetically encoded proteins.[8] Other advantages of quantum dots include their high photoluminescence quantum yields (PLQY), narrow emission full width half max (FWHM) values, rapid fluorescence decay kinetics, and ease of color tunability via quantum confinement, especially when compared to organic dyes.[9] The utility of these materials is quite apparent, but what is a quantum dot?

1.2. Emergent Properties at the Nanoscale

1.2.1. Defining the Nanoscale

We live in a world where we interact with objects on the macroscale. Objects are composed of on the order of 10^{23} atoms. As objects shrink in size to the nanoscale, on the order of a few thousand atoms, novel properties arise that are distinct from their bulk, macroscale counterparts (Figure 1.2.1). These are referred to as emergent properties.[10] For example, it is easy to imagine forces such as friction[11] or conductance[12] that we know how to describe at the macroscale breaking down on the level of the interaction of individual molecules or atoms at the nanoscale.

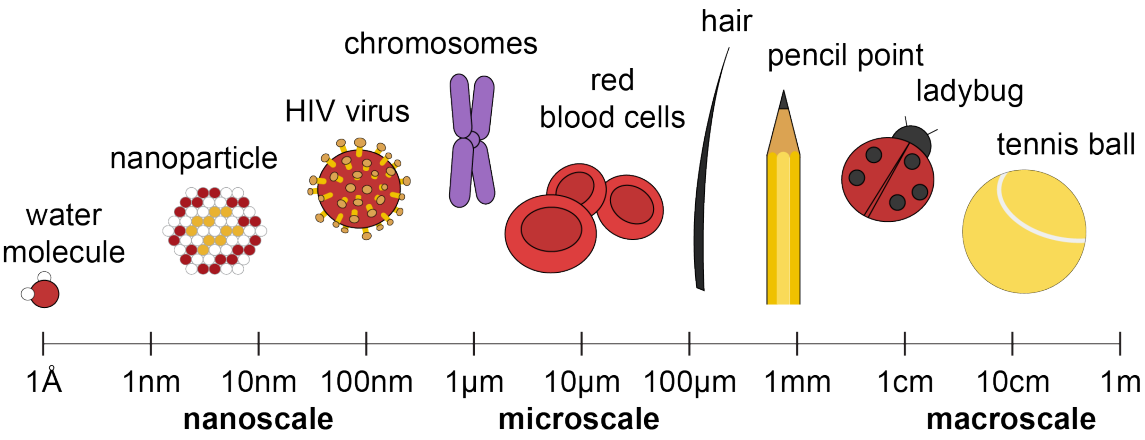

Figure 1.2.1. Visual representation of length scales from macro to micro to nano.

1.2.2. Quantum Confinement and Size Effects

Quantum confinement is another important nanoscale size effect that occurs in semiconductors. Semiconductors are materials that possess narrow band gaps, between metals which possess no band gap and insulators which possess extremely large band gaps (Figure 1.2.2). Specific energies of light can excite a semiconductor to generate an exciton, which is an electron/hole pair.

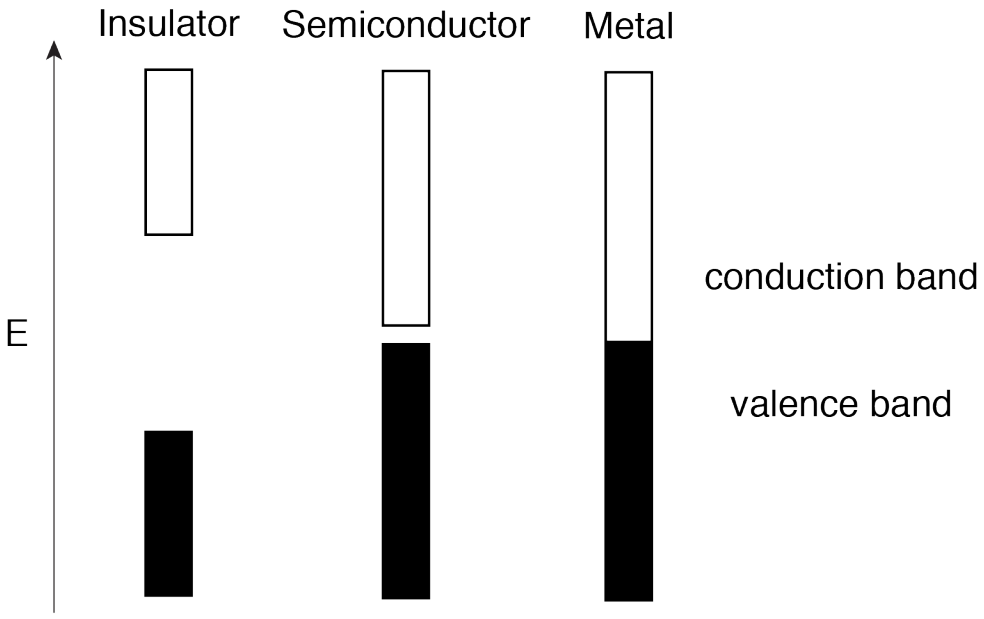

Figure 1.2.2. Relative valence and conduction band gaps for an insulator, semiconductor, and metal.

In semiconductor nanocrystals, excitons can be modeled by the Bohr model of the hydrogen atom. Mathematically, the Bohr radius (r_B) of an exciton can be described by:

$$r_B = \frac{4\pi\varepsilon_0\hbar^2}{e^2 m}$$

Equation 1.2.1.

where ε_0 is the dielectric of the semiconductor, $\hbar$ is the reduced Planck's constant, e is the charge of an electron, and m is the mass of the carrier.[13] Thus, the Bohr radius varies in different materials. For CdS, r_B = 2.8 nm, and for CdSe r_B = 5.6 nm.[14] It is possible to synthesize a semiconductor nanocrystal whose dimensions are smaller than that of the material's exciton Bohr radius which leads to a phenomenon called quantum confinement (Figure 1.2.3). Confinement of the exciton widens the bandgap of the semiconductor, resulting in a blueshift of the material's absorbance and fluorescence spectra. Because of quantum confinement's effect on semiconductor nanocrystals, sometimes these materials are referred to as quantum dots.[15]

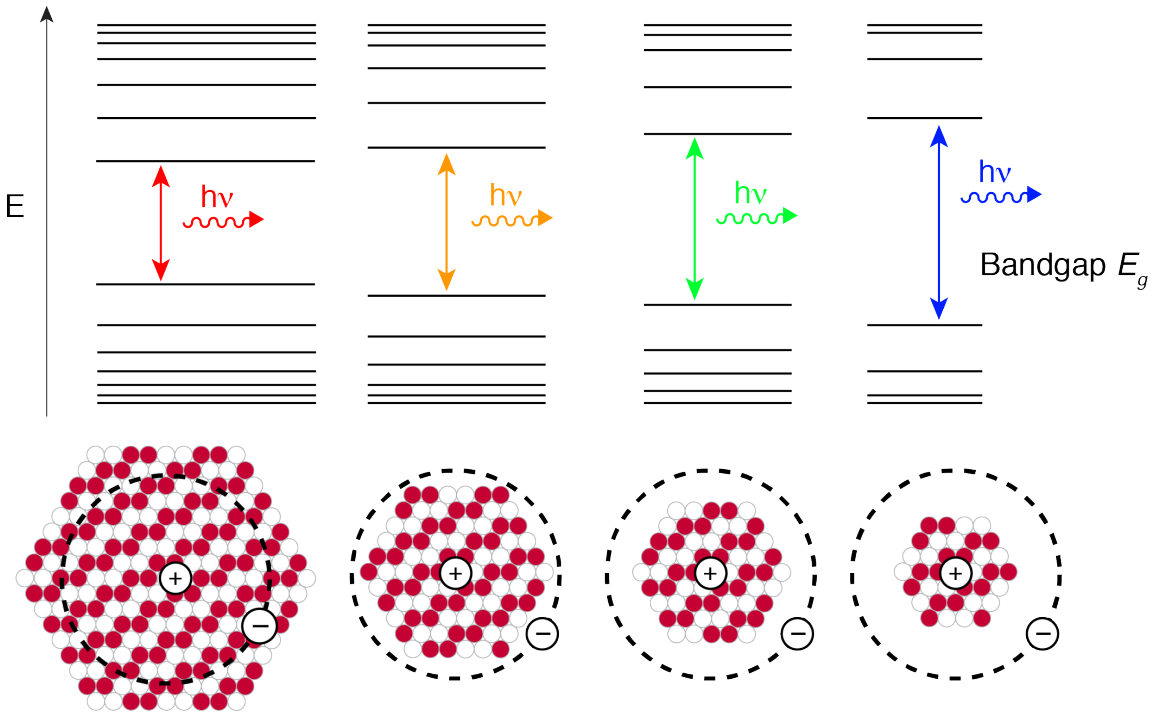

Figure 1.2.3. Quantum confinement effects widen the bandgap of the semiconductor nanocrystal causing a size dependence of fluorescence.

Quantum confinement's effect on the bandgap of a nanocrystal may be described by the Brus equation:

$$E_{bandgap}(r) = E_{bandgap}(bulk) + \frac{\hbar^2\pi^2}{2r^2}\left[\frac{1}{m_e} + \frac{1}{m_h}\right] - \frac{1.8e^2}{\varepsilon r}$$

Equation 1.2.2.

where r is the nanocrystal radius, $\hbar$ is the reduced Planck constant, m_e is the effective mass of the electron, m_h is the effective mass of the hole, e is the charge of an electron, and ε is the dielectric of the semiconductor.[16]

Exploiting the relationship between nanocrystal radius and band gap, empirical sizing formulas have been developed that relate the wavelength of the material's first excitonic transition to nanocrystal size:

CdSe: $$D = (1.6122 \times 10^{-9})\lambda^4 - (2.6575 \times 10^{-6})\lambda^3 + (1.6242 \times 10^{-3})\lambda^2 - (0.4277)\lambda + (41.57)$$

Equation 1.2.3.

CdS: $$D = (-6.6521 \times 10^{-8})\lambda^3 + (1.9557 \times 10^{-4})\lambda^2 - (9.2352 \times 10^{-2})\lambda + (13.29)$$

Equation 1.2.4.

where D (nm) is the diameter of a nanocrystal sample, and λ (nm) is the wavelength of the first excitonic absorption peak.[17] Because bandgap energy depends on size, a nanocrystal sample's size dispersity can have dramatic effects on the sharpness of an ensemble of nanocrystals' absorbance and emission spectra. Therefore, much effort has been invested into controlling particle monodispersity.

Many scientists including physicists, materials scientists, and a wide variety of engineers are involved with the efforts to investigate the photophysical properties of semiconductor nanocrystals. In this thesis, we approach quantum

dots from the synthetic inorganic chemist's approach which can be described as follows.

1.3. The Synthetic Inorganic Chemist's Approach

1.3.1. Band Alignments

Chemists are accustomed to describing bonding based on a molecular orbital picture. When describing a molecule with two interacting atomic orbitals, a molecular orbital picture is relatively straightforward and results in the formation of a bonding and an antibonding orbital. When describing a macroscale solid, involving 10^{23} interacting atoms, one can imagine that the resultant bonding and antibonding orbitals now compose a continuum of energy levels, rather than distinct, bonding and antibonding orbitals (Figure 1.3.1). Electrons associated with the interacting atoms then fill the associated energy levels. Chemists describe the highest occupied molecular orbital (HOMO) and lowest unoccupied molecular orbital (LUMO) of molecular systems, whereas for larger systems, materials scientists describe the valence and conduction bands of semiconductors (Figure 1.2.2).

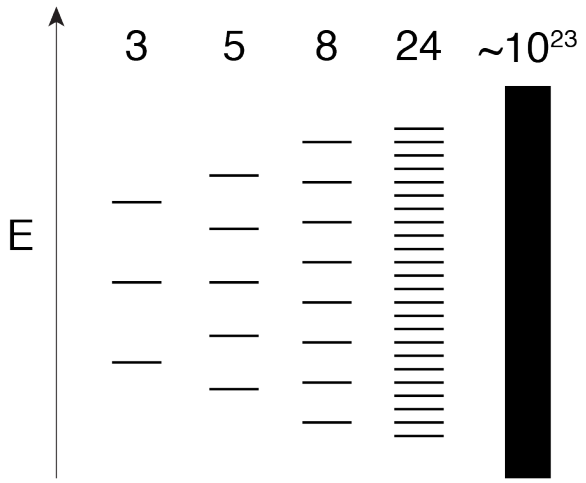

Figure 1.3.1. Representation of the increasing number of molecular orbitals as the number of interacting atomic orbitals increases.

Quantum dots fall in a middle regime not well described by either a bulk continuum of energies nor a molecular orbital picture. However, one of the ways in which the chemist's view of molecular orbitals enhances the materials scientist's view of quantum dots deals with the description of nanocrystal surface chemistry.

1.3.2. Surface Chemistry

Nanocrystals possess high surface to volume ratios due to their small size, rendering the chemistry of their surfaces extremely important. A semiconductor nanocrystal's inorganic surface atoms are typically bound to organic ligands that help keep the nanocrystals colloidally dispersed. In contrast with tetrahedrally coordinated cadmium chalcogenide core atoms that sit in a zincblende or wurtzite lattice, the undercoordinated surface atoms possess energy levels that lie mid-

bandgap and give rise to surface traps (Figure 1.3.2). Careful passivation of these surface states is possible using ligands.

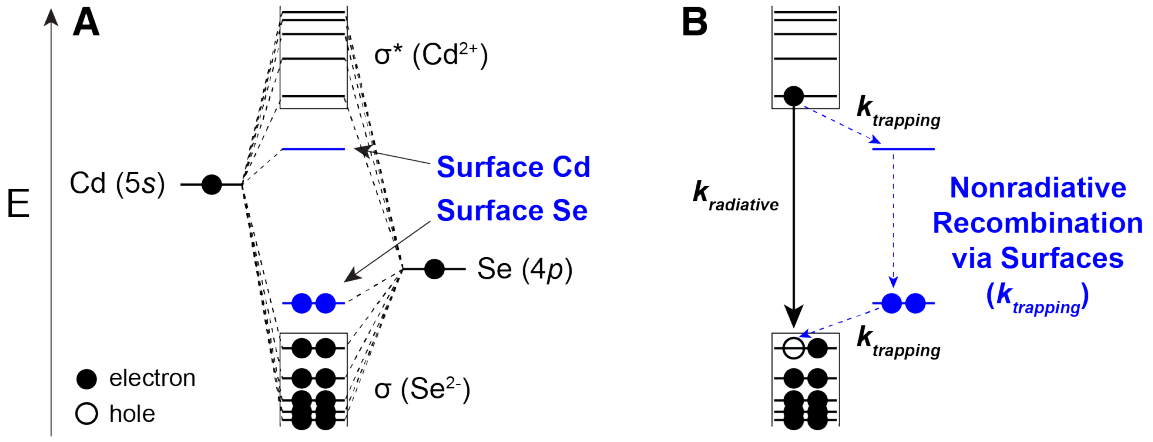

Figure 1.3.2. A) Diagram of undercoordinated Cd and Se atoms that lead to surface traps. B) Surface traps lead to nonradiative recombination.

Synthetic inorganic chemists describe nanocrystal surfaces using Malcom Green's covalent bond classification system,[18] which involves X type ligands as one electron donors, L type ligands as neutral two electron donors, and Z type ligands as neutral acceptors. These are the most common bonding motifs found on cadmium chalcogenide nanocrystal surfaces (Figure 1.3.3),[19] although more complex binding motifs are possible both in this system and on other types of nanocrystals.[20-21] In order to reduce the non-radiative pathways afforded by surface traps, Z-type ligands can be used to passivate surface chalcogens, and L-type ligands can passivate surface cadmium atoms. The surface chemistry of

nanocrystals and passivation of surface traps dramatically impact properties such as photoluminescence quantum yields[19] and fluorescence lifetimes.[22] Additionally, our understanding of nanocrystal surfaces is particularly important in the discussion of surface ligand exchange, a process necessary for applications requiring charge transport or water solubility. Charge transport can be favored by fewer insulating ligands, while water solubility can be imparted by hydrophilic ligands.

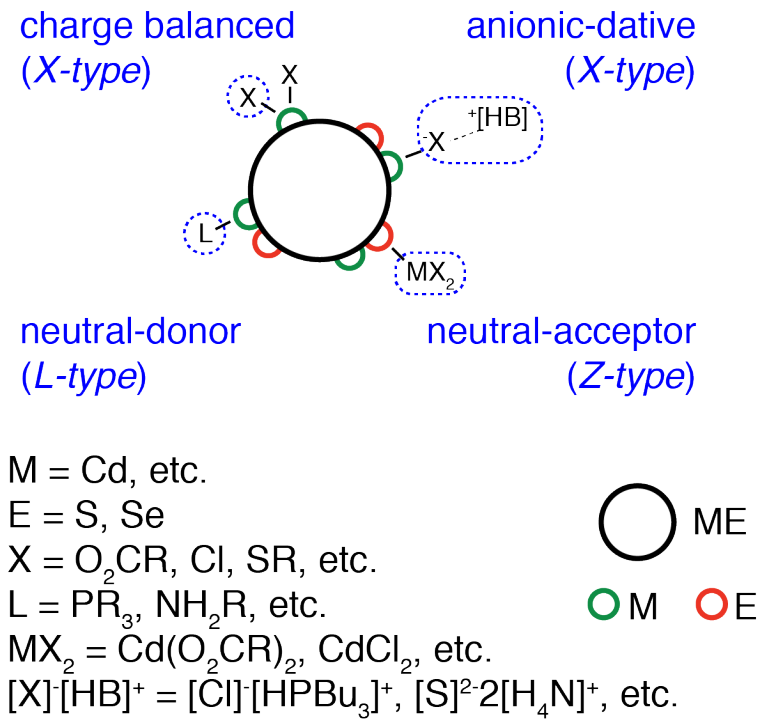

Figure 1.3.3. Covalent bond classification system applied to nanocrystal surfaces.

1.3.3. Core/Shell

An alternative to using organic ligands to passivate mid-gap surface states is shelling the nanoparticle with a semiconductor material that has a wider band gap (Figure 1.3.4). If both the valence and conduction band energies of the shell material are higher in energy than that of the core material, the shell provides a potential barrier that helps prevent both the electron and hole from being able to access surface traps. This is a type I band alignment (Figure 1.3.5A). A second option, called a type II band alignment, occurs if the valence and conduction bands are offset so that the electron and hole localize on different materials (Figure 1.3.5B).[23-24] The third option, the quasi-type II band alignment, occurs in CdSe/CdS core/shell systems where the hole is localized on the core material and the electron localizes across the entire structure (Figure 1.3.5C). This is common in CdSe@CdS seeded nanorod structures.[25] Type I and quasi type II band alignments have been shown to increase the photoluminescence quantum yield of these materials, essential for their utility in the range of applications previously described.[2, 26]

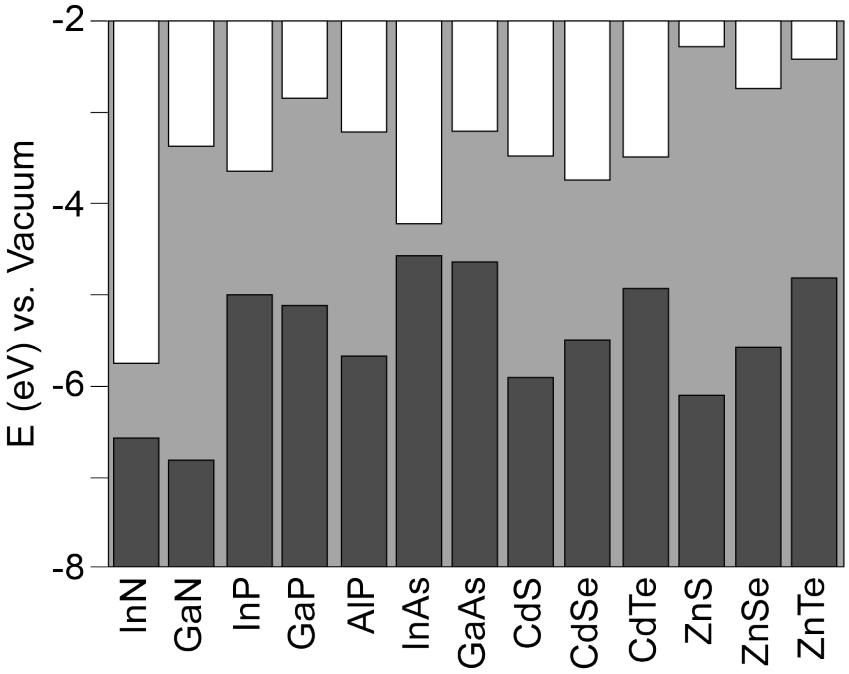

Figure 1.3.4. Valence (dark grey) and conduction band (white) offsets of selected III-V and II-VI semiconductors.[23]

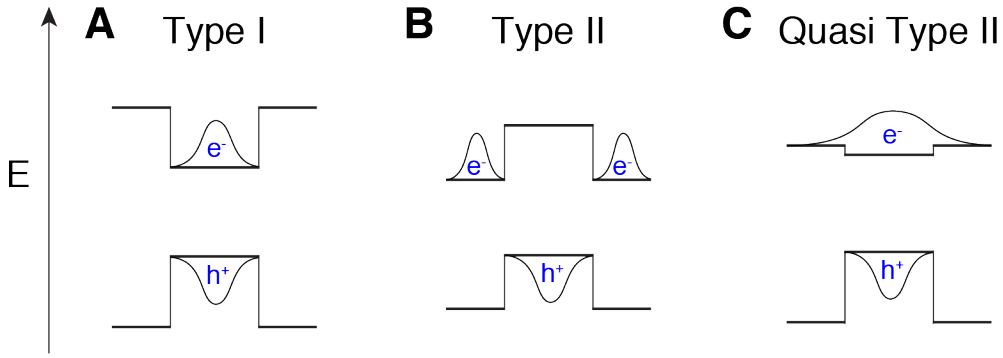

Figure 1.3.5. Energy level diagram of the valence and conduction band offsets for A) type I, B) type II, and C) quasi type II core/shell semiconductor heterostructures.

In addition to relative band alignments, crystal structure and minimizing lattice constant mismatches are important considerations in designing core/shell

heterostructures. Lattice mismatches can cause strain-induced defects at material interfaces that limit the performance of core/shells with favorable band alignments. One example occurs in CdSe/ZnS core/shell nanocrystals with a 12% lattice mismatch that makes it difficult to grow high quality shells thicker than 2-3 monolayers thick (Table 1.3.1).[27] Other strategies to reduce interfacial strain related defects include growing core/multi-shell nanocrystals that gradually transition between materials with less lattice mismatch such as CdSe/ZnSe/ZnS,[28] introducing alloying in between the layers such as CdSe/CdS/$Cd_{1-x}Zn_xS$/ZnS,[29] or growing spherical quantum wells with thin emissive layers such as CdS/CdSe/CdS core/shell/shell nanocrystals.[30]

Table 1.3.1. Common semiconductor zincblende lattice parameters.[31-32]

	Sulfide	**Selenide**	**Telluride**	**Phosphide**	**Arsenide**
Zinc	0.541 nm	0.567 nm	0.610 nm		
Cadmium	0.582 nm	0.608 nm	0.648 nm		
Mercury	0.585 nm	0.609 nm	0.645 nm		
Aluminum				0.546 nm	0.566 nm
Gallium				0.545 nm	0.565 nm
Indium				0.586 nm	0.605 nm

1.4. Nanocrystal Synthesis

1.4.1. Historical Context

Following the work of Steigerwald and Brus in the 1980s,[1] Murray and Bawendi developed a monodisperse cadmium chalcogenide nanocrystal synthesis via the hot injection of dimethyl cadmium and bis(trimethylsilyl)sulfide/selenide or tri-*n*-octylphosphine sulfide/selenide.[33] Due to the extreme reactivity of these precursors at elevated reaction temperatures (300 °C), these reactions proceed via "burst nucleation" and mixing-limited reaction kinetics.[34] In order to obtain the desired nanocrystal sizes, reactions must be stopped before the complete consumption of precursors, relying on engineering controls rather than chemical control.

In subsequent years, the field moved towards "greener" reagents for both the metal and chalcogen precursors. The highly toxic organometallic cadmium precursor was replaced with cadmium phosphonates or cadmium carboxylates synthesized via the reaction of CdO and phosphonic acids or carboxylic acids in situ,[35-36] and the chalcogen precursors expanded to include mixtures of sulfur and selenium in octadecene which generate H_2S and H_2Se in situ.[37-38] Additionally, as an alternative to hot injection syntheses, Hyeon popularized heat-up reactions.[39-40] These reactions rely on carefully controlled heating rates to afford control over the nanocrystal products. To date, some of the most robust zincblende CdSe

nanocrystals in the literature are synthesized via a heat-up reaction using chemicals such as SeO_2.[41]

1.4.2. Precursor Conversion Limited Kinetics

In many nanocrystal reactions, the size of the nanocrystal is controlled via altering reaction temperatures and/or terminating reactions early to achieve desired sizes, which limits yields and increases synthetic variability.[42] More recently, both theory and experiment have demonstrated that tuning the size of nanocrystals can be accomplished by changing precursor conversion rates.[36, 42-44]

These observations build on work performed by LaMer and Dinegar in the 1950s that proposes a three step model for nanocrystal nucleation.[45-46] The first phase describes precursor conversion to soluble solute until a critical concentration C_{crit} is reached that triggers nucleation. The second phase describes a rapid period of nucleation that can be thought to be instantaneous. Nucleation is followed by the third phase of growth whereby additional solute that is produced grows the existing nanocrystal nuclei (Figure 1.4.1).

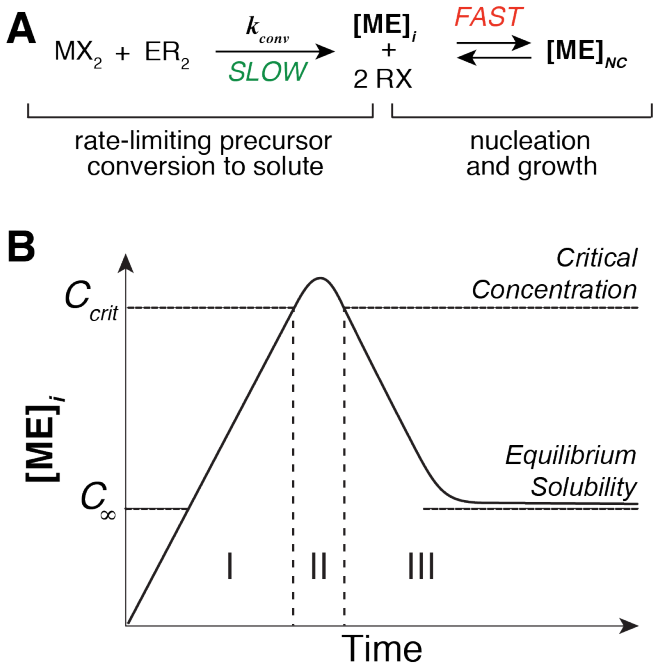

Figure 1.4.1. A) Reaction scheme depicting precursor conversion limited nanocrystal growth and B) LaMer model highlighting the three phases of a nanocrystal reaction.

In the 1990s, Sugimoto enhanced the LaMer model by considering the mass balance of the solute. This model predicts that the number of nuclei generated during nucleation depends only on the solute supply rate and the growth rate of the material, independent of nucleation kinetics.[47-48] This relationship arises from the mass balance equation, which states that all solute produced during nucleation must be consumed by nucleation or growth:

$$Production = Consumption_{nucleation} + Consumption_{growth}$$

Equation 1.4.1.

which can be written as:

$$Q_0 V_m = v_0 \frac{dn}{dt} + \dot{v} n$$

Equation 1.4.2.

where Q_0 is the supply rate of solute during nucleation, V_m is the molar volume of the solid, v_0 is the initial particle volume of the stable nuclei, $\frac{dn}{dt}$ is the rate of stable nuclei production, $\dot{v}$ is the average growth rate of stable nuclei during nucleation, and n is the number of stable particles. We can rewrite Equation 1.4.2 as

$$n = \frac{V_m}{\dot{v}} Q_0$$

Equation 1.4.3.

accounting for the ratio $\frac{dn}{dt}$ decreasing to zero at the end of nucleation and solving for n. Thus, we can see the theoretical basis for the relationship between the number of nanocrystals nucleated in a reaction directly relates to Q_0 which is affected by the rate of precursor conversion. The validity of this model was experimentally supported via studies on the precipitation of AgCl and AgBr crystals.[47-48]

In 2017, Peters further enhanced Sugimoto's model by correcting the equations to account for systems with slow growth kinetics.[49] This model helps to explain some deviations from linearity observed for particle numbers vs. solute

production rates for PbS, PbSe, and CdSe made from thioureas, selenoureas, and phosphine selenides.[42, 44, 50] However, at the limit of fast growth kinetics, the model can be simplified to Sugimoto's equation.[49]

Because of the demonstrated relationship between precursor conversion rate, the number of nanocrystals nucleated, and final nanocrystal size at full reaction yield, recent efforts have gone into developing new chalcogen precursor libraries. Control over precursor conversion rates led to the development of nanocrystal reactions that utilize chemical kinetics to produce desired nanocrystal sizes at full yields, in contrast with previous methods that require stopping reactions early.[51] One such promising class of compounds with tunable reaction rates are thio- and selenoureas which have been mainly used for the synthesis of PbS and PbSe nanocrystals, although their utility towards other metal sulfides and selenides has been demonstrated.[42, 44] Expanding the library of chalcogenourea precursors to ones optimized for the synthesis of CdS and CdSe nanocrystals motivated this thesis.

1.4.3. Nanocrystals as Living Polymers

Nanocrystal nucleation theories have thus far described materials consisting of a single binary semiconductor. This is because core/shell nanocrystal syntheses rely on synthetic methods that are empirically designed to avoid nucleation of shell precursors and do not rely on the kinetics of shell material

solute supply rates.[52] These methods are discussed in further detail in Chapter 3. With the design of new nanocrystal precursors that react to full yield with well-defined conversion rates, we can begin to imagine new chemical methods to access core/shell nanocrystals that draw inspiration from thinking about nanocrystals as living polymers.[53] Much like living polymerization has transformed polymer chemistry,[54-55] we believe that development of these new precursor libraries unlocks the potential to access nanocrystals with a finer level of radial composition control than ever before.

1.5. Conclusion

Precise control over the core/shell structures of colloidal semiconductor nanocrystals enable their use in a myriad of applications that seek to make major impacts on the energy efficiency landscape of solid state lighting and increase the performance of emissive displays. Since their discovery in the 1980s, both the chemistry to make these nanocrystals and the way we think about their synthesis have evolved greatly; from empirically designed reactions to the inorganic chemist's emerging model of precursor conversion limited nanocrystal synthesis and coordination chemistry of nanocrystal surfaces.

It is upon this foundation that we seek to transform the multi-step synthesis of graded alloy core/shell nanocrystals into an elegant single injection process that relies on the reaction chemistry of precursor molecules. Using this as a guiding

principle, the following two chapters explore the development of new classes of chalcogen precursors that react with highly tunable rates, allowing access to fine changes in precursor conversion reactivity. The third and fourth chapters culminate with the application of this precursor library towards the achievement of our goal, gaining new insight into core/shell nanocrystal heterostructures accessible via kinetic control of precursor conversion.

1.6. Plain English Summary

Semiconductor nanocrystals are useful in a variety of commercial applications due to their light emission, the color of which varies based on particle size. These nanoparticles are very tiny objects consisting of thousands of atoms and their small size lead to complex physics that enable the size dependence of the colors they emit. The efforts of synthetic inorganic chemists have led to the development of new syntheses of nanocrystals that rely on the chemical reaction rates of libraries of precursors. This has the potential to reinvent the way that the field synthesizes core/shell nanocrystals.

1.7. References

(1) Steigerwald, M. L.; Alivisatos, A. P.; Gibson, J.; Harris, T.; Kortan, R.; Muller, A.; Thayer, A.; Duncan, T.; Douglass, D.; Brus, L. E., Surface Derivatization and Isolation of Semiconductor Cluster Molecules. *J. Am. Chem. Soc.* **1988,** *110* (10), 3046-3050.

(2) Hines, M. A.; Guyot-Sionnest, P., Synthesis and Characterization of Strongly Luminescing ZnS-Capped CdSe Nanocrystals. *J. Phys. Chem.* **1996,** *100* (2), 468-471.

(3) Chen, Y.; Vela, J.; Htoon, H.; Casson, J. L.; Werder, D. J.; Bussian, D. A.; Klimov, V. I.; Hollingsworth, J. A., "Giant" Multishell CdSe Nanocrystal Quantum Dots with Suppressed Blinking. *J. Am. Chem. Soc.* **2008,** *130* (15), 5026-5027.

(4) Nasilowski, M.; Spinicelli, P.; Patriarche, G.; Dubertret, B., Gradient CdSe/CdS Quantum Dots with Room Temperature Biexciton Unity Quantum Yield. *Nano Lett.* **2015,** *15* (6), 3953-3958.

(5) Palomaki, P. Quantum Dot Downconverters for SSL. https://www.energy.gov/sites/prod/files/2018/02/f48/palomaki_qd-downconverters_nashville18_0.pdf, (2018).

(6) U.S. Department of Energy. LED Efficacy: What America Stands to Gain. https://www.energy.gov/sites/prod/files/2016/10/f33/efficacy-fs_oct2017.pdf, (2018).

(7) Clapp, A. R.; Pons, T.; Medintz, I. L.; Delehanty, J. B.; Melinger, J. S.; Tiefenbrunn, T.; Dawson, P. E.; Fisher, B. R.; O'Rourke, B.; Mattoussi, H., Two‐Photon Excitation of Quantum‐Dot‐Based Fluorescence Resonance Energy Transfer and Its Applications. *Adv. Mater.* **2007,** *19* (15), 1921-1926.

(8) Biju, V.; Itoh, T.; Ishikawa, M., Delivering Quantum Dots to Cells: Bioconjugated Quantum Dots for Targeted and Nonspecific Extracellular and Intracellular Imaging. *Chem. Soc. Rev.* **2010,** *39* (8), 3031-3056.

(9) Wegner, K. D.; Hildebrandt, N., Quantum Dots: Bright and Versatile *In Vitro* and *In Vivo* Fluorescence Imaging Biosensors. *Chem. Soc. Rev.* **2015,** *44* (14), 4792-4834.

(10) Murph, S. E. H.; Coopersmith, K. J.; Larsen, G. K., Nanoscale Materials: Fundamentals and Emergent Properties. In *Anisotropic and Shape-Selective Nanomaterials*, Springer: 2017; pp 7-28.

(11) Mo, Y.; Turner, K. T.; Szlufarska, I., Friction Laws at the Nanoscale. *Nature* **2009,** *457* (7233), 1116.

(12) Aviram, A.; Ratner, M., Molecular Rectifiers. *Chem. Phys. Lett.* **1974,** *29* (2), 277-283.

(13) Ashcroft, N. W.; Mermin, N. D., *Solid State Physics*. Brooks/Cole, Cengage Learning: 1976.
(14) Ekimov, A. I.; Hache, F.; Schanne-Klein, M. C.; Ricard, D.; Flytzanis, C.; Kudryavtsev, I. A.; Yazeva, T. V.; Rodina, A. V.; Efros, A. L., Absorption and Intensity-Dependent Photoluminescence Measurements on CdSe Quantum Dots: Assignment of the First Electronic Transitions. *J. Opt. Soc. Am. B* **1993,** *10* (1), 100-107.
(15) Alivisatos, A. P., Semiconductor Clusters, Nanocrystals, and Quantum Dots. *Science* **1996,** *271* (5251), 933-937.
(16) Brus, L., Electronic Wave Functions in Semiconductor Clusters: Experiment and Theory. *J. Phys. Chem.* **1986,** *90* (12), 2555-2560.
(17) Li, J.; Chen, J.; Shen, Y.; Peng, X., Extinction Coefficient Per CdE (E = Se or S) Unit For Zinc-Blende CdE Nanocrystals. *Nano Res.* **2018**.
(18) Green, M. L. H., A New Approach to the Formal Classification of Covalent Compounds of the Elements. *J. Organomet. Chem.* **1995,** *500* (1-2), 127-148.
(19) Anderson, N. C.; Hendricks, M. P.; Choi, J. J.; Owen, J. S., Ligand Exchange and the Stoichiometry of Metal Chalcogenide Nanocrystals: Spectroscopic Observation of Facile Metal-Carboxylate Displacement and Binding. *J. Am. Chem. Soc.* **2013,** *135* (49), 18536-18548.
(20) De Roo, J.; Ibáñez, M.; Geiregat, P.; Nedelcu, G.; Walravens, W.; Maes, J.; Martins, J. C.; Van Driessche, I.; Kovalenko, M. V.; Hens, Z., Highly Dynamic Ligand Binding and Light Absorption Coefficient of Cesium Lead Bromide Perovskite Nanocrystals. *ACS Nano* **2016,** *10* (2), 2071-2081.
(21) De Roo, J.; Justo, Y.; De Keukeleere, K.; Van den Broeck, F.; Martins, J. C.; Van Driessche, I.; Hens, Z., Carboxylic‐Acid‐Passivated Metal Oxide Nanocrystals: Ligand Exchange Characteristics of a New Binding Motif. *Angew. Chem. Int. Ed.* **2015,** *54* (22), 6488-6491.
(22) Busby, E.; Anderson, N. C.; Owen, J. S.; Sfeir, M. Y., Effect of Surface Stoichiometry on Blinking and Hole Trapping Dynamics in CdSe Nanocrystals. *J. Phys. Chem. C* **2015,** *119* (49), 27797-27803.
(23) Reiss, P.; Protière, M.; Li, L., Core/Shell Semiconductor Nanocrystals. *Small* **2009,** *5* (2), 154-168.
(24) Enright, M. J.; Cossairt, B., Synthesis of Tailor-Made Colloidal Semiconductor Heterostructures. *Chem. Comm.* **2018**.
(25) Allione, M.; Ballester, A.; Li, H.; Comin, A.; Movilla, J. L.; Climente, J. I.; Manna, L.; Moreels, I., Two-Photon-Induced Blue Shift of Core and Shell Optical Transitions in Colloidal CdSe/CdS Quasi-Type II Quantum Rods. *ACS Nano* **2013,** *7* (3), 2443-2452.
(26) Chen, O.; Zhao, J.; Chauhan, V. P.; Cui, J.; Wong, C.; Harris, D. K.; Wei, H.; Han, H.; Fukumura, D.; Jain, R. K.; Bawendi, M. G., Compact High-Quality

CdSe-CdS Core-Shell Nanocrystals with Narrow Emission Linewidths and Suppressed Blinking. *Nat. Mater.* **2013,** *12*, 445-451.

(27) de Mello Donegá, C., Synthesis and Properties of Colloidal Heteronanocrystals. *Chem. Soc. Rev.* **2011,** *40* (3), 1512-1546.

(28) Talapin, D. V.; Mekis, I.; Götzinger, S.; Kornowski, A.; Benson, O.; Weller, H., CdSe/CdS/ZnS and CdSe/ZnSe/ZnS Core−Shell−Shell Nanocrystals. *J. Phys. Chem. B* **2004,** *108* (49), 18826-18831.

(29) Xie, R.; Kolb, U.; Li, J.; Basché, T.; Mews, A., Synthesis and Characterization of Highly Luminescent CdSe−Core CdS/$Zn_{0.5}Cd_{0.5}$S/ZnS Multishell Nanocrystals. *J. Am. Chem. Soc.* **2005,** *127* (20), 7480-7488.

(30) Jeong, B. G.; Park, Y.; Chang, J. H.; Cho, I.; Kim, J. K.; Kim, H.; Char, K.; Cho, J.; Klimov, V. I.; Park, P.; Lee, D. C.; Bae, W. K., Colloidal Spherical Quantum Wells with Near-Unity Photoluminescence Quantum Yield and Suppressed Blinking. *ACS Nano* **2016,** *10* (10), 9297-9305.

(31) West, A. R., *Basic Solid State Chemistry*. John Wiley & Sons Inc: 1999.

(32) Palmer, D. W. Properties of III-V Semiconductors. www.semiconductors.co.uk, 2006.02.

(33) Murray, C. B.; Norris, D. J.; Bawendi, M. G., Synthesis and Characterization of Nearly Monodisperse CdE (E= Sulfur, Selenium, Tellurium) Semiconductor Nanocrystallites. *J. Am. Chem. Soc.* **1993,** *115* (19), 8706-8715.

(34) García-Rodríguez, R. l.; Hendricks, M. P.; Cossairt, B. M.; Liu, H.; Owen, J. S., Conversion Reactions of Cadmium Chalcogenide Nanocrystal Precursors. *Chem. Mater.* **2013,** *25* (8), 1233-1249.

(35) Peng, Z. A.; Peng, X., Formation of High-Quality CdTe, CdSe, and CdS Nanocrystals Using CdO as Precursor. *J. Am. Chem. Soc.* **2001,** *123* (1), 183-184.

(36) Liu, H.; Owen, J. S.; Alivisatos, A. P., Mechanistic Study of Precursor Evolution in Colloidal Group II-VI Semiconductor Nanocrystal Synthesis. *J. Am. Chem. Soc.* **2007,** *129* (2), 305-312.

(37) Yu, W. W.; Peng, X., Formation of High-Quality CdS and Other II-VI Semiconductor Nanocrystals in Noncoordinating Solvents: Tunable Reactivity of Monomers. *Angew. Chem. Int. Ed.* **2002,** *41* (13), 2368-2371.

(38) Jasieniak, J.; Bullen, C.; van Embden, J.; Mulvaney, P., Phosphine-Free Synthesis of CdSe Nanocrystals. *J. Phys. Chem. B* **2005,** *109* (44), 20665-20668.

(39) Park, J.; An, K.; Hwang, Y.; Park, J.-G.; Noh, H.-J.; Kim, J.-Y.; Park, J.-H.; Hwang, N.-M.; Hyeon, T., Ultra-Large-Scale Syntheses of Monodisperse Nanocrystals. *Nat. Mater.* **2004,** *3* (12), 891.

(40) Joo, J.; Na, H. B.; Yu, T.; Yu, J. H.; Kim, Y. W.; Wu, F.; Zhang, J. Z.; Hyeon, T., Generalized and Facile Synthesis of Semiconducting Metal Sulfide Nanocrystals. *J. Am. Chem. Soc.* **2003,** *125* (36), 11100-11105.

(41) Yang, Y. A.; Wu, H.; Williams, K. R.; Cao, Y. C., Synthesis of CdSe and CdTe Nanocrystals Without Precursor Injection. *Angew. Chem. Int. Ed.* **2005,** *117* (41), 6870-6873.
(42) Hendricks, M. P.; Campos, M. P.; Cleveland, G. T.; Jen-La Plante, I.; Owen, J. S., A Tunable Library of Substituted Thiourea Precursors to Metal Sulfide Nanocrystals. *Science* **2015,** *348* (6240), 1226-1230.
(43) Abe, S.; Cabek, R. K.; De Geyter, B.; Hens, Z., Tuning the Postfocused Size of Colloidal Nanocrystals by the Reaction Rate: From Theory to Application. *ACS Nano* **2012,** *6* (1), 42-53.
(44) Campos, M. P.; Hendricks, M. P.; Beecher, A. N.; Walravens, W.; Swain, R. A.; Cleveland, G. T.; Hens, Z.; Sfeir, M. Y.; Owen, J. S., A Library of Selenourea Precursors to PbSe Nanocrystals with Size Distributions Near the Homogenous Limit. *J. Am. Chem. Soc.* **2017,** *139* (6), 2296-2305.
(45) LaMer, V. K.; Dinegar, R. H., Theory, Production and Mechanism of Formation of Monodispersed Hydrosols. *J. Am. Chem. Soc.* **1950,** *72* (11), 4847-4854.
(46) LaMer, V. K., Nucleation in Phase Transitions. *Ind. Eng. Chem.* **1952,** *44* (6), 1270-1277.
(47) Sugimoto, T.; Shiba, F.; Sekiguchi, T.; Itoh, H., Spontaneous Nucleation of Monodisperse Silver Halide Particles from Homogeneous Gelatin Solution I: Silver Chloride. *Colloids Surf. A* **2000,** *164* (2-3), 183-203.
(48) Sugimoto, T.; Shiba, F., Spontaneous Nucleation of Monodisperse Silver Halide Particles from Homogeneous Gelatin Solution II: Silver Bromide. *Colloids Surf. A* **2000,** *164* (2-3), 205-215.
(49) Chu, D. B.; Owen, J. S.; Peters, B., Nucleation and Growth Kinetics from LaMer Burst Data. *J. Phys. Chem. A* **2017,** *121* (40), 7511-7517.
(50) Owen, J. S.; Chan, E. M.; Liu, H.; Alivisatos, A. P., Precursor Conversion Kinetics and the Nucleation of Cadmium Selenide Nanocrystals. *J. Am. Chem. Soc.* **2010,** *132* (51), 18206-18213.
(51) Hens, Z., Economical Routes to Colloidal Nanocrystals. *Science* **2015,** *348* (6240), 1211-1212.
(52) Li, J. J.; Wang, Y. A.; Guo, W.; Keay, J. C.; Mishima, T. D.; Johnson, M. B.; Peng, X., Large-Scale Synthesis of Nearly Monodisperse CdSe/CdS Core/Shell Nanocrystals Using Air-Stable Reagents via Successive Ion Layer Adsorption and Reaction. *J. Am. Chem. Soc.* **2003,** *125* (41), 12567-12575.
(53) Jansons, A. W.; Plummer, L. K.; Hutchison, J. E., Living Nanocrystals. *Chem. Mater.* **2017,** *29* (13), 5415-5425.
(54) Szwarc, M., 'Living' Polymers. *Nature* **1956,** *178* (4543), 1168.

(55) Patterson, G., In Retrospect: Sixty Years of Living Polymers. *Nature* **2016,** *536* (7616), 276.

CHAPTER 2. Kinetic Control Over CdS Nanocrystal Nucleation Using a Library of Thiocarbonates, Thiocarbamates, Thioureas, and Related Precursors

Table of Contents

Reproduced in part from:

Hamachi, L. S.; Jen-La Plante, I.; Coryell, A. C.; De Roo, J.; Owen, J. S. *Chem. Mater.* **2017**, *29* (20), 8711.

2.1. Abstract

2.1.1. Technical Abstract

We report a family of substituted thiocarbonates, thiocarbamates, thioureas and phosphanecarbothioamides and their reaction with cadmium oleate at 180–240 °C to form zincblende CdS nanocrystals (D = 2.2–5.9 nm). To monitor the kinetics of CdS formation with UV–vis spectroscopy, the size dependence of the extinction coefficient for $\lambda_{max}(1S_e–1S_{1/2h})$ is determined. The precursor conversion reactivity spans 5 orders of magnitude depending on the precursor structure (2°-thioureas > 3°-thioureas ≥ 2°-thiocarbamates ≥ 3°-phosphanecarbothioamides > 2°-thiocarbonates > 4°-thioureas ≥ 3°-thiocarbamates). The concentration of nanocrystals formed during nucleation increases when more reactive precursors are used, allowing the final size to be controlled by the precursor structure. ^{1}H NMR spectroscopy is used to monitor the reaction of di-*p*-tolyl thiocarbonate and cadmium oleate where di-*p*-tolyl carbonate and oleic anhydride coproducts can be identified. These coproducts further decompose into *p*-tolyl oleate and *p*-cresol. The spectral features of CdS nanocrystals produced from thiocarbonates are exceptionally narrow (95–161 meV FWHM) as compared to those made from thioureas (137–174 meV FWHM) under otherwise identical conditions, indicating that certain precursors nucleate narrower size distributions than others.

2.1.2. Plain English Abstract

Cadmium chalcogenide nanocrystals are highly desirable materials because they possess the ability to emit colors that span the entire rainbow of the visible spectrum. In this section, we build and leverage a library of sulfur containing compounds as precursors for CdS nanocrystal synthesis. Each sulfur precursor's specific substitution pattern influences the rate of nanocrystal formation, which in turn influences the number and size of the nanocrystals produced. We have utilized our chemical control of nanocrystal formation rates towards 1) developing size tunable CdS nanocrystal syntheses and 2) studying additional effects of precursor molecule structure, such as nanocrystal monodispersity.

2.2. Context

Cadmium sulfide (CdS) semiconductor nanocrystals are studied as a single component material for use in solar cells,[1] photocatalysis,[2] and as stress sensors.[3] Due to quantum confinement effects, the physical and spectroscopic properties of these nanocrystals are strongly dependent on their size and size distributions. For example, a distribution of band gaps stemming from a large size distribution creates energetic disorder that disrupts charge transport through nanocrystalline films.[4] Additionally, a narrow emission linewidth is essential for luminescence applications.[5]

Mechanistic studies have shown that the nucleation and growth of metal chalcogenide nanocrystals are often limited by the kinetics of precursor conversion.[6] The conversion reaction thereby controls the flow of metal chalcogenide monomers into the medium where they supersaturate, nucleate, and grow into nanocrystals.[7] In this mechanistic scenario, the kinetics of precursor conversion allows precise and predictable control over the nanocrystal size while optimizing the size dispersity, yield, and reaction temperature. This has inspired many precursor molecule classes such as substituted thio/selenoureas, silyl/germanyl phosphines and arsines, phosphine chalcogenides, and dichalchogenides that provide control over II–VI,[6, 8-11] IV–VI,[8-9, 12] and III–V[13-15] nanocrystal syntheses.

CdS nanocrystals have classically been synthesized from bis-(trimethylsilyl)sulfide,[16] phosphine sulfides,[17] or sulfur dissolved in octadecene.[18-19] These precursors provide limited tunability and/or produce unwanted side products. In our attempts to synthesize CdS nanocrystals from thioureas, we found that *N,N'*-disubstituted and most *N,N,N'*-trisubstituted thioureas were too reactive toward cadmium oleate to provide tunable control over the nanocrystal size in the range of temperatures needed for optimal crystal growth. On the other hand, the reactivity of most *N,N,N',N'*-tetrasubstituted thioureas is comparatively sluggish at temperatures where cadmium carboxylate is stable. Therefore, we

sought precursors with reactivities between those of *N,N,N'*-trisubstituted and *N,N,N',N'*-tetrasubstituted thioureas that could also be tuned by adjusting the substituents.

In the literature, other precursors such as thioacetamide have been used to prepare PbS nanosheets[20] or nanoparticles,[21] and metal dithiocarbamates have been used to prepare CuInS nanoparticles.[22] Because of this, substituting heteroatoms for the nitrogen atoms present in thioureas seemed promising. Substituted thioacetamides and thioketones could potentially be good sulfur precursors, however they suffer from a lack of easy synthetic tunability afforded by thioureas. Because of the wide availability of phenols, amines, isothiocyanates, phosphines, and chlorothionoformates, we investigated the synthesis of CdS nanocrystals from substituted thiocarbonates, thiocarbamates, and phosphanecarbothioamides. Among these, and suitably reactive thioureas, the thiocarbonate class produces significantly narrower size distributions.

2.3. Sulfur Precursors

2.3.1. Synthesis of a Library

A variety of *O,O'*-disubstituted thiocarbonates are obtained in good yields from *O*-aryl-chlorothionoformates or 1,1-thiocarbonyldiimidazole (Table 2.3.1).[23] While the reaction of phenols and chlorothionoformate proceeds to completion

after 10 min at 80 °C, the analogous reaction with 1,1-thiocarbonyldiimidazole requires 16 h in refluxing acetonitrile and trifluoroacetic acid (10 mol %) to complete the second substitution. Similarly, secondary amines react with 1,1-thiocarbonyldiimidazole to provide *N,N,N',N'*-tetrasubstituted thioureas. Again, the first imidazole substitution proceeds rapidly while the second required stirring overnight, although the reaction could be conducted at room temperature because of the greater nucleophilicity of amines. Following recrystallization from methanol, acetonitrile, or dichloromethane, analytically pure, white, microcrystalline products are obtained in 44–76% isolated yields.

Analogous to the reaction of amines with isothiocyanates to form di- and trisubstituted thioureas, phosphanecarbothioamides could be prepared via the reaction of phosphines and isothiocyanates upon mild heating.[24] These compounds are easily isolated as analytically pure, yellow microcrystalline products.

Table 2.3.1. Synthesis of substituted thiocarbonate, thiocarbamate, phosphanecarbothioamide, and *N,N,N′,N′*-tetrasubstituted thiourea precursors used in this study. Experimental conditions and characterization noted in Experimental Details. [a] Commercially available. [b] Synthesized as published previously.[8] [c] Synthesized as published previously.[24]

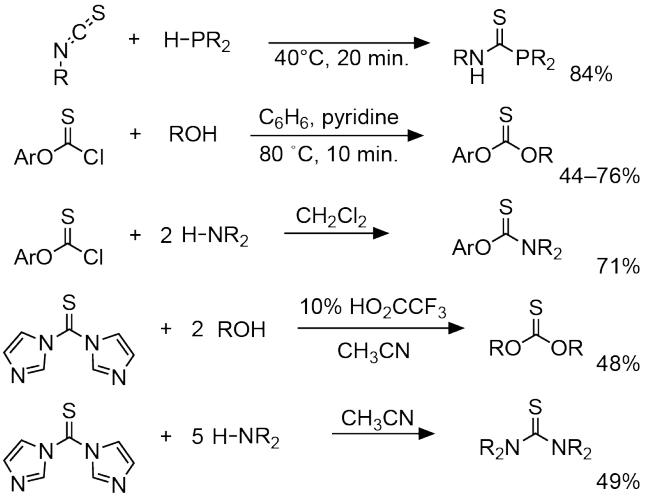

Compound	X_1	X_2	Yield (%)
1a	*O*-4-MeO-Ph	*O*-4-MeO-Ph	48
1b	*O*-4-Me-Ph	*O*-4-MeO-Ph	67
1c	*O*-4-Me-Ph	*O*-4-Me-Ph	76
1d	*O*-4-Me-Ph	*O*-Ph	66
1e	*O*-Ph	*O*-Ph	67
1f	*O*-4-Me-Ph	*O*-4-Cl-Ph	68
1g	*O*-4-Me-Ph	*O*-4-CF_3-Ph	61
1h	*O*-4-Me-Ph	*O*-Cy	62
1i	*O*-Ph	*O*-4-Cl-Ph	60
1j	*O*-4-Me-Ph	*O*-2,6-diMe-Ph	44
2	*O*-4-Me-Ph	*N*-H(4-Me-Ph)	71
3	*O*-4-Me-Ph	*N*-(CH_3)Ph	74
4	*N*-H(4-Me-Ph)	*N*-H(4-Me-Ph)	[a]
5a	*N*-HPh	*N*-(*n*-Bu)$_2$	[b]
5b	*N*-HPh	*N*-(CH_3)Ph	92

6a	*N*-$(CH_3)_2$	*N*-$(CH_3)_2$	[a]
6b	*N*-(pyrr)	*N*-(pyrr)	49
7	*N*-HPh	*P*-Ph_2	[c]

2.4. Synthesis of CdS Nanocrystals

2.4.1. Synthesis and Basic Characterizations

CdS nanocrystals were synthesized by injecting a solution of the precursors shown in Table 2.4.1 (**1a**–**7**) into 1.2–1.5 equiv of cadmium oleate dissolved in octadecene at 180–240 °C (Figure 2.4.1). Reaction temperatures as low as 180 °C could be used without significantly broadening the nanocrystals optical features. Oleic acid (2.4 equiv) is added to improve the thermal stability of the cadmium oleate precursor, which occasionally decomposed to a turbid mixture when stirred in octadecene at 240 °C on its own. Higher temperatures lead to greater problems with the decomposition of cadmium oleate. Zincblende nanocrystals with a wide range of final diameters (D = 2.2–5.9 nm) are obtained depending on the sulfur precursor used (Figure 2.4.1).

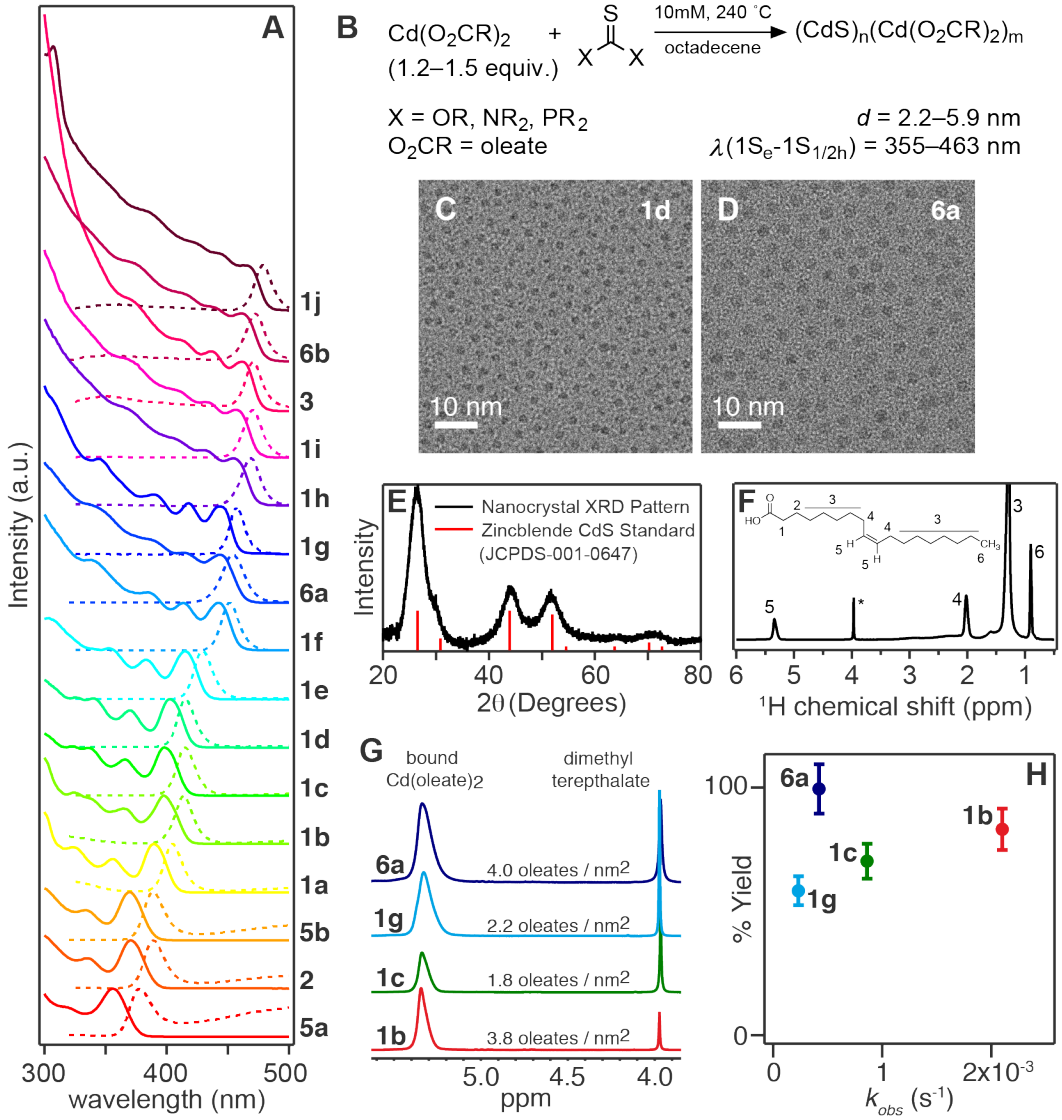

Figure 2.4.1. A) Final absorption and photoluminescence spectra of CdS nanocrystals obtained using the precursor shown. B) Standard reaction conditions for the synthesis of CdS nanocrystals from a sulfur precursor listed in Table 2.3.1. C-D) TEM images of nanocrystals prepared from **1d** and **6a**. E) powder X-ray diffraction (PXRD) of zincblende nanocrystal product. F) Representative ^{1}H NMR of isolated nanocrystal sample. G) Ligand coverages for several thiocarbonate and thiourea reactions. H) % Yields as determined from ligand coverage and mass of isolated product.

Table 2.4.1. Table of all sulfur precursors, k_{obs} values, nanocrystal yields as determined via UV-vis and [a] determined by weighing the isolated product and subtracting the known mass of ligands as determined by ^{1}H NMR, diameter, particle #, 1st excitonic feature, reaction time, and FWHM of product. See Nanocrystal Formation Kinetics and Cadmium Sulfide Reaction Yield Determination sections in the experimental for details. *At 240 °C, this compound reacts with mixing limited kinetics, so a comparison was conducted at 180 °C and a relative value is reported in this table.

Cpd	k_{obs}	CdS yield (%)	Diamter (nm)	Particle # x 10^{16}	λ_{max}	Time (min)	FWHM (eV)
1a	2.2 x 10^{-3}	67	3.13	15.3	392	30	137
1b	2.1 x 10^{-3}	75 (83)[a]	3.26	15.7	396	45	139
1c	8.6 x 10^{-4}	89 (70)[a]	3.32	14.4	398	60	132
1d	8.0 x 10^{-4}	70	3.86	9.78	414	120	127
1e	4.5 x 10^{-4}	62	4.04	7.17	419	120	123
1f	2.9 x 10^{-4}	73	4.93	4.63	442	240	112
1g	2.3 x 10^{-4}	57 (58) [a]	5.02	3.22	444	300	95
1h	2.1 x 10^{-4}	66	5.45	2.77	454	305	114
1i	8.2 x 10^{-5}	56	5.58	2.17	457	720	108
1j	4.8 x 10^{-5}	53	5.85	1.51	463	720	96
2	1.5 x 10^{-2}	103	2.73	39.8	378	3	161
3	8.1 x 10^{-5}	62	5.67	2.37	459	1271	100
4*	2.9 x 10^{-1}	-	-	-	-	-	-
5a	5.3 x 10^{-2}	93	2.18	64.1	355	1.5	175
5b	1.4 x 10^{-2}	110	2.65	40.2	375	4	169
6a	4.2 x 10^{-4}	98 (99) [a]	4.98	5.54	443	180	138
6b	2.9 x 10^{-4}	103	5.63	3.98	458	245	106
7*	3.6 x 10^{-2}	-	-	-	-	-	-

Oleic acid can also be used to adjust the nanocrystal size (Figure 2.4.2), which has previously been linked to changes in monomer solubility in studies of CdSe nanocrystals.[6, 25]

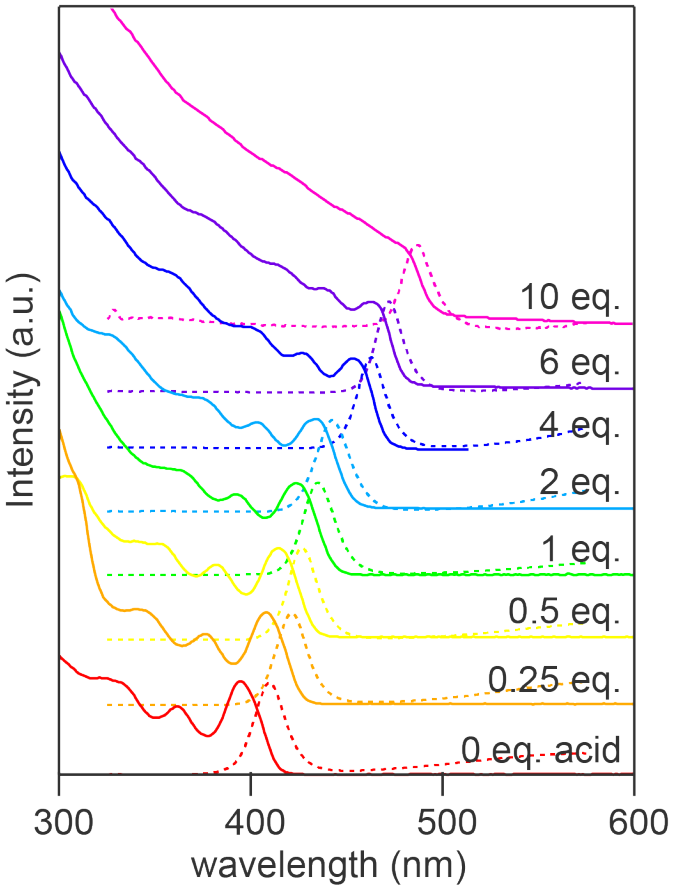

Figure 2.4.2. Final spectra of reactions of **6a** at standard reaction conditions with different equivalences of oleic acid added show size tunability.

A Cd:S stoichiometry greater than 1:1 provides cadmium oleate ligands that passivate the nanocrystal surface and maintain the colloidal stability.[26-30] Reactions that produce smaller final sizes required a greater amount of cadmium oleate (1.5 equivalents) to prevent loss of the narrow optical features toward the end of the

reaction (Figure 2.4.3). Similar broadening is observed in the synthesis of small diameter PbS nanocrystals if lead oleate is not present in sufficient excess.[8] Depletion of metal oleate by the conversion reaction is thought to reduce the ligand coverage and destabilize the colloidal dispersion, particularly at long reaction times. The greater surface area to volume ratio and metal enrichment of small nanocrystals could magnify the effect.[31-36] Following the synthesis, the nanocrystals are carefully purified by precipitation and centrifugation until the ^{1}H NMR spectrum only displays the broad resonances of surface bound cadmium oleate ligands. The oleate coverages obtained this way range from 1.8–4.0 nm^{-2}, which is similar to oleate coverages on CdSe nanocrystals (Figure 2.4.1).[26]

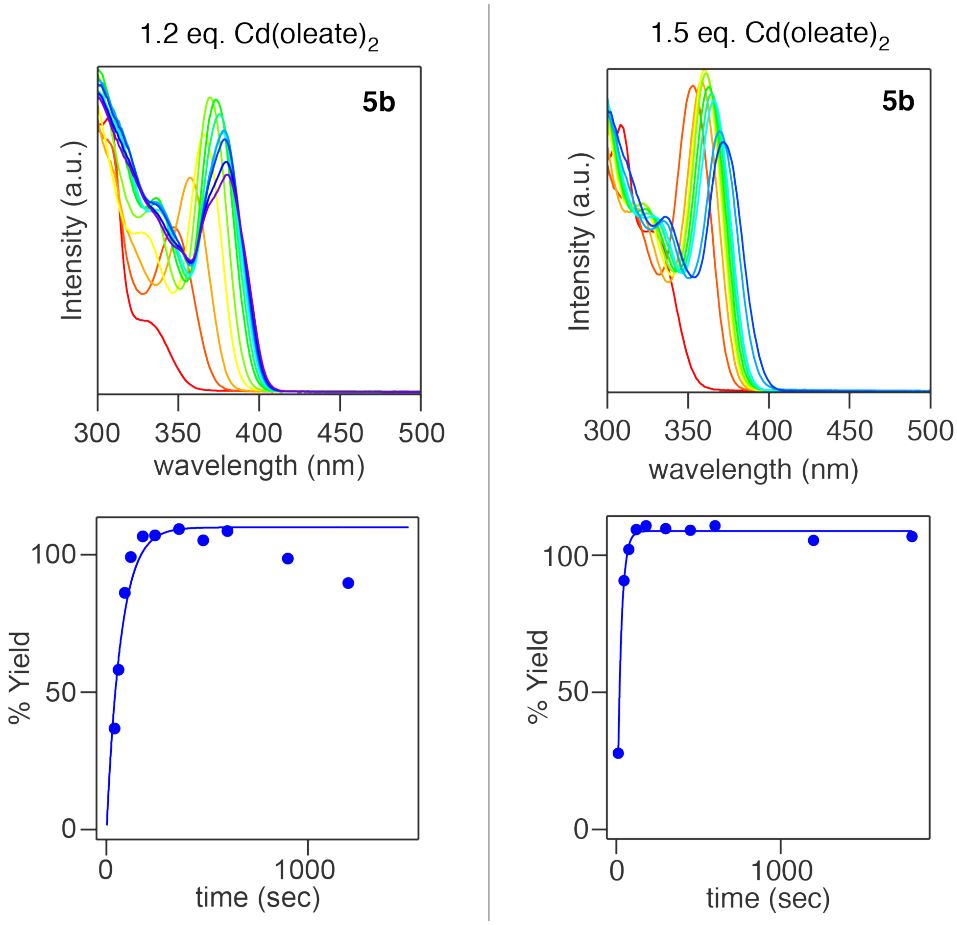

Figure 2.4.3. Comparing 1.2 and 1.5 equivalents of $Cd(oleate)_2$ precursor relative to sulfur precursor shows that more equivalents slow a ripening process that degrades the quality of the final nanocrystal product at small sizes.

2.4.2. Mechanistic Studies

To gain insight into the precursor conversion mechanism, ^1H NMR spectroscopy was used to monitor the reaction coproducts (Figure 2.4.4). For example, *N,N,N′,N′*-tetramethylthiourea (**6a**) ($\delta(CH_3)$ = 3.1 ppm) reacts with cadmium oleate to produce *N,N,N′,N′*-tetramethylurea ($\delta(CH_3)$ = 2.8 ppm) and

oleic anhydride ($\delta(\alpha$-CH_2) = 2.47 ppm) (Figure 2.4.5). Analogous *O,O'*-disubstituted carbonate and oleic anhydride coproducts form from thiocarbonates (**1c**, **1e**). In both cases, these coproducts go on to form other species, as described below.

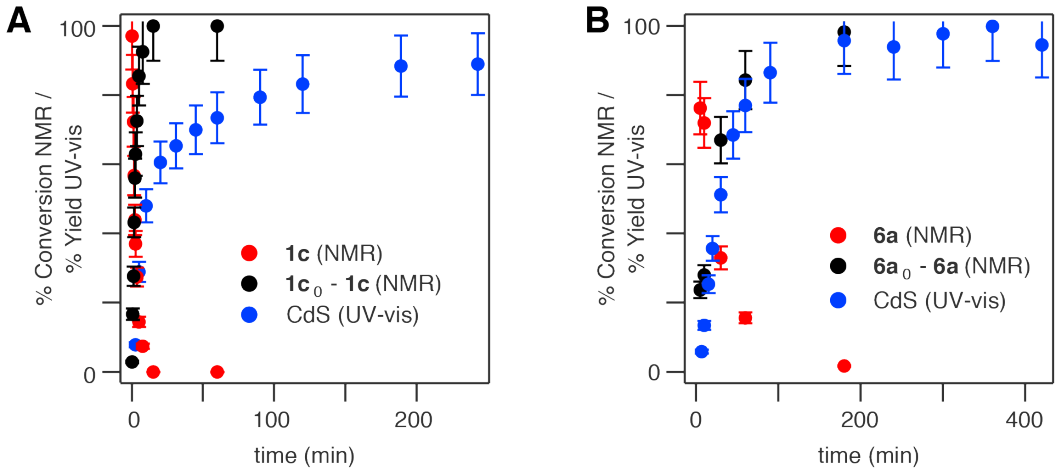

Figure 2.4.4. Reaction kinetics as measured by ^{1}H NMR spectroscopy (red), initial amount of precursor – precursor consumed (black), and UV-vis spectroscopy (blue) for A) **1c** and B) **6a**.

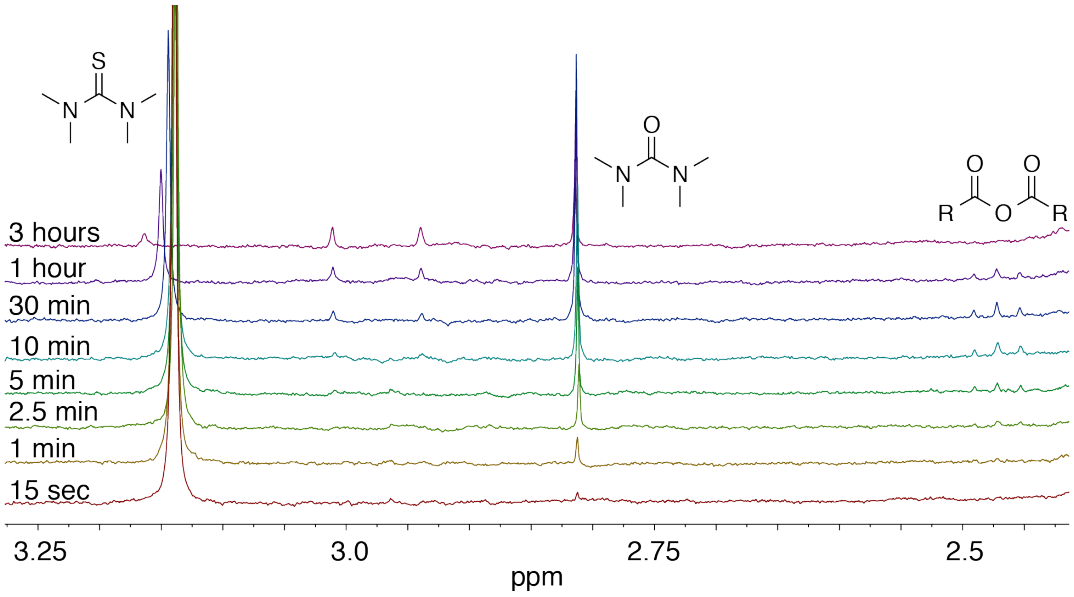

Figure 2.4.5. ^{1}H NMR spectra of the reaction of **6a** with cadmium oleate shows appearance of tetramethyl urea and oleic anhydride.

In the case of **1c**, *p*-tolyl oleate and *p*-cresol build in concentration as the initially formed di-*p*-tolyl carbonate (**8c**) and oleic anhydride disappear (Figure 2.4.6, Figure 2.4.7, and Figure 2.4.8). We infer from this observation that the carbonate coproduct reacts with oleic acid and/or moisture to form *p*-tolyl oleate and/or *p*-cresol (Figure 2.4.6). This reaction was also observed in a control experiment in the absence of nanocrystals; however, the rate is too slow to explain the results, suggesting that cadmium oleate activates the di-*p*-tolyl carbonate toward attack (Figure 2.7.1 and Figure 2.7.2). Indeed, the Lewis acid catalyzed esterification of carboxylic acids following reaction with *O,O'*-disubstituted

carbonates has been established.[37] A similar reaction between thiocarbonates and oleic acid or oleic anhydride is also observed.

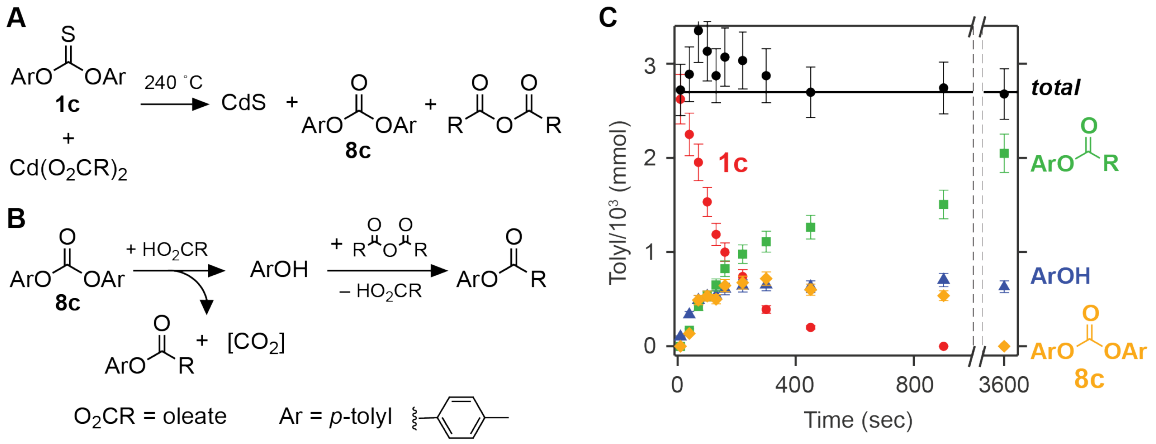

Figure 2.4.6. A) Coproducts of the precursor conversion reaction are **8c** and oleic anhydride. B) These coproducts undergo further conversion to *p*-tolyl oleate and carbon dioxide via *p*-cresol. The formation of *p*-cresol suggests the process is catalyzed by oleic acid. C) Reaction coproducts of **1c** with cadmium oleate are observed via ^{1}H NMR and evolve over time to yield *p*-tolyl oleate and *p*-cresol. ^{1}H NMR data were plotted with 10% error bars from the experiment.

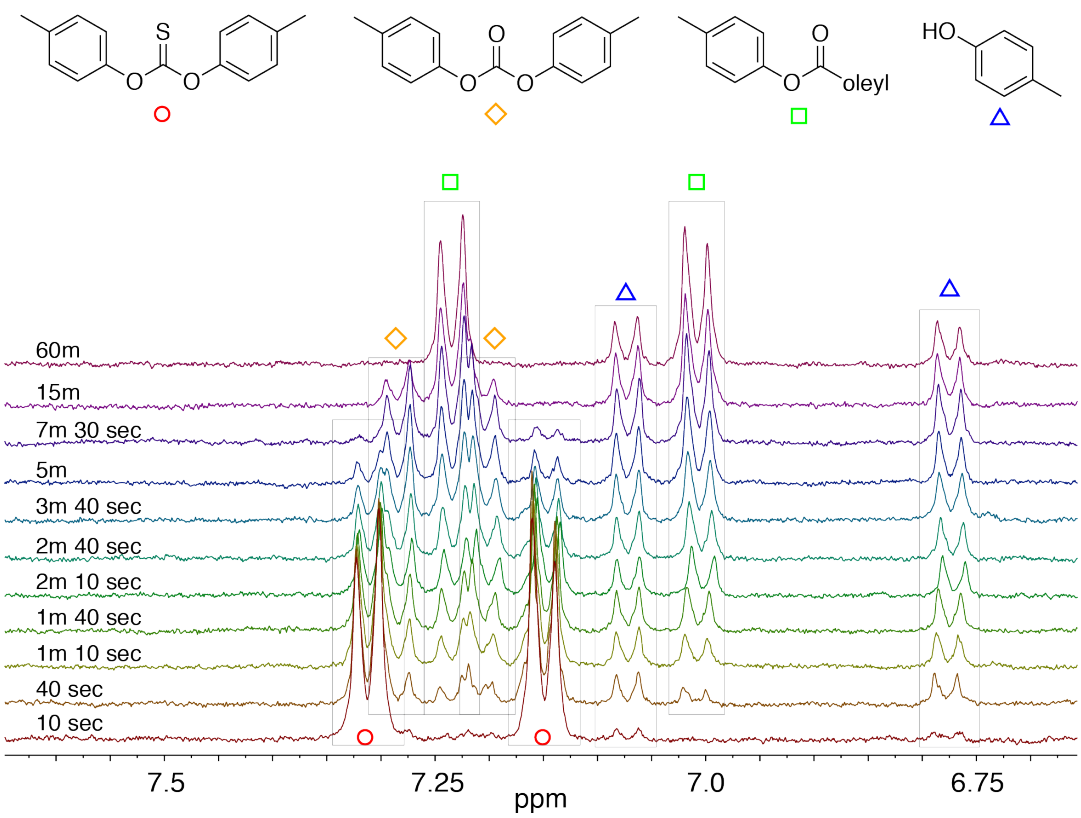

Figure 2.4.7. ^{1}H NMR for coproduct identification and tracking over the course of the reaction of **1c** with cadmium oleate.

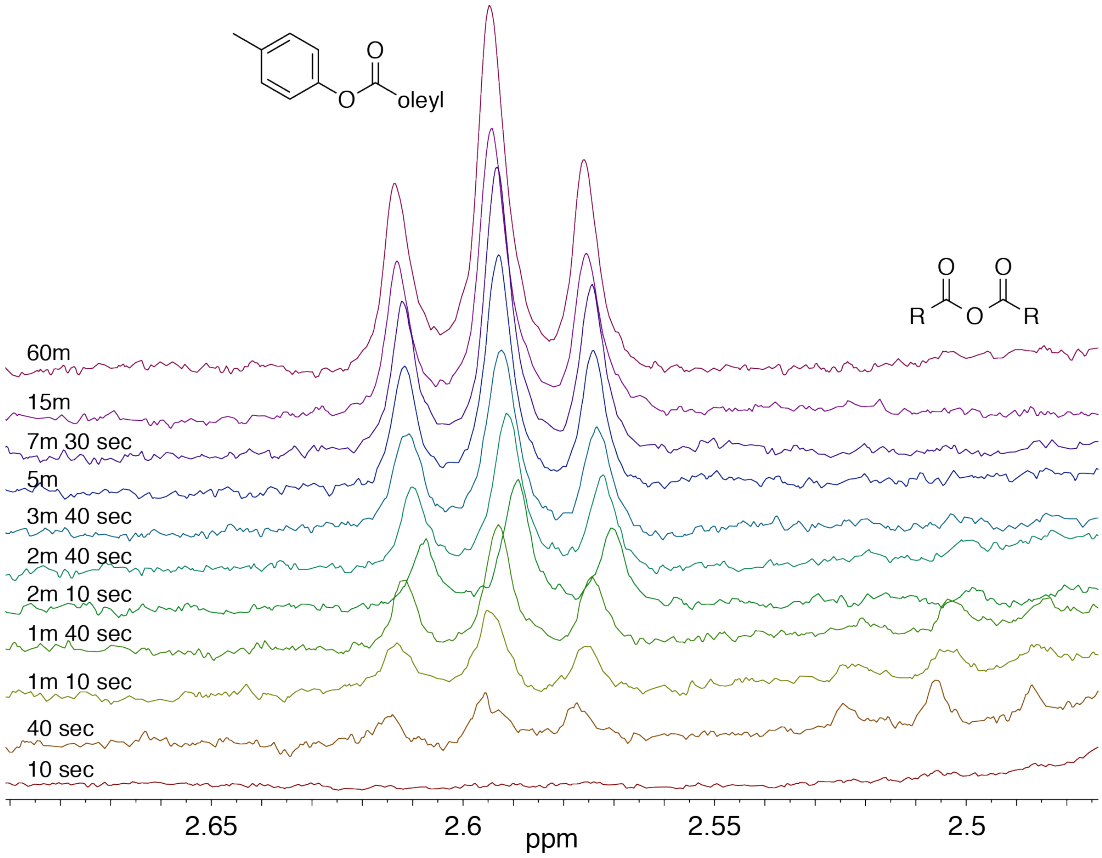

Figure 2.4.8. ^{1}H NMR for the reaction of **1c** with cadmium oleate shows appearance of oleic anhydride at early times which is consumed to produce tolyl oleate.

As the reaction proceeds and **8c** disappears, *p*-tolyl oleate continues to build in concentration and *p*-cresol persists in the product mixture. This suggests that hydrolysis of oleic anhydride and/or *p*-tolyl oleate by adventitious water also plays a role in the coproduct evolution. Cadmium carboxylates typically bind two water molecules, which is expected under our conditions because the cadmium oleate precursor was not prepared under rigorously anhydrous conditions (see Experimental Details).[7] We have not prepared anhydrous cadmium oleate to test

whether this changes the coproduct evolution. Oleic anhydride, on the other hand, is only present in low concentration and at early times, presumably because its reaction with p-cresol and moisture is rapid. This was confirmed by a control experiment, which is rapid even in the absence of Lewis acid catalysis (Figure 2.7.3). These findings are consistent with the mechanistic hypothesis in Figure 2.4.6. An analogous mechanism may explain the reaction of the *N,N,N',N'*-tetramethylthiourea.

2.5. Monitoring CdS Formation Kinetics

2.5.1. CdS Size Dependent Extinction Coefficient Correction

CdS formation was monitored using the intensity of the $1S_e - 1S_{1/2h}$ transition in the UV−vis absorption spectrum and a published size-dependent extinction coefficient.[38] However, error in this extinction coefficient, particularly at small sizes, leads to erroneous yields (as much as twice the theoretical yield) (Figure 2.5.1). Similar issues with the size-dependent extinction coefficient of CdSe nanocrystals published in that same report have been described.[39]

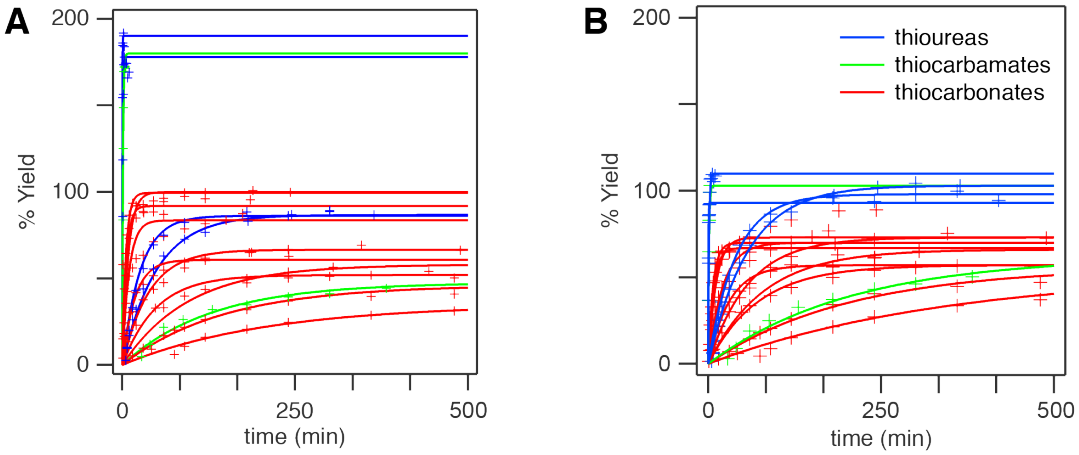

C

Diameter (nm)	Extinction Coefficient ($cm^{-1}M^{-1}$)	Fluorescence FWHM (eV)
2.18	250351	175
2.65	545334	169
3.86	562328	135
4.98	758250	138
5.63	1029210	106

Figure 2.5.1. A) % Yields of reaction aliquots using previously reported extinction coefficient,[38] B) % Yields of reaction aliquots using the size dependent extinction coefficients determined in this work. C) Properties of particles used in calibration curve.

To estimate the extinction coefficient of the $1S_e$–$1S_{1/2h}$ transition, CdS nanocrystals were synthesized from a variety of tri- and tetrasubstituted thioureas (**5a**–**6b**). We verified a near quantitative yield of CdS from **6a** by the complete disappearance of the thiourea and by measuring the empirical formula and mass of the CdS nanocrystals (see Experimental Details, Figure 2.4.1 and Figure 2.4.4). By assuming a 100% conversion of the thiourea to CdS, the extinction coefficient

of the lowest energy excitonic transition could be estimated at the end of the reaction (Figure 2.5.2).

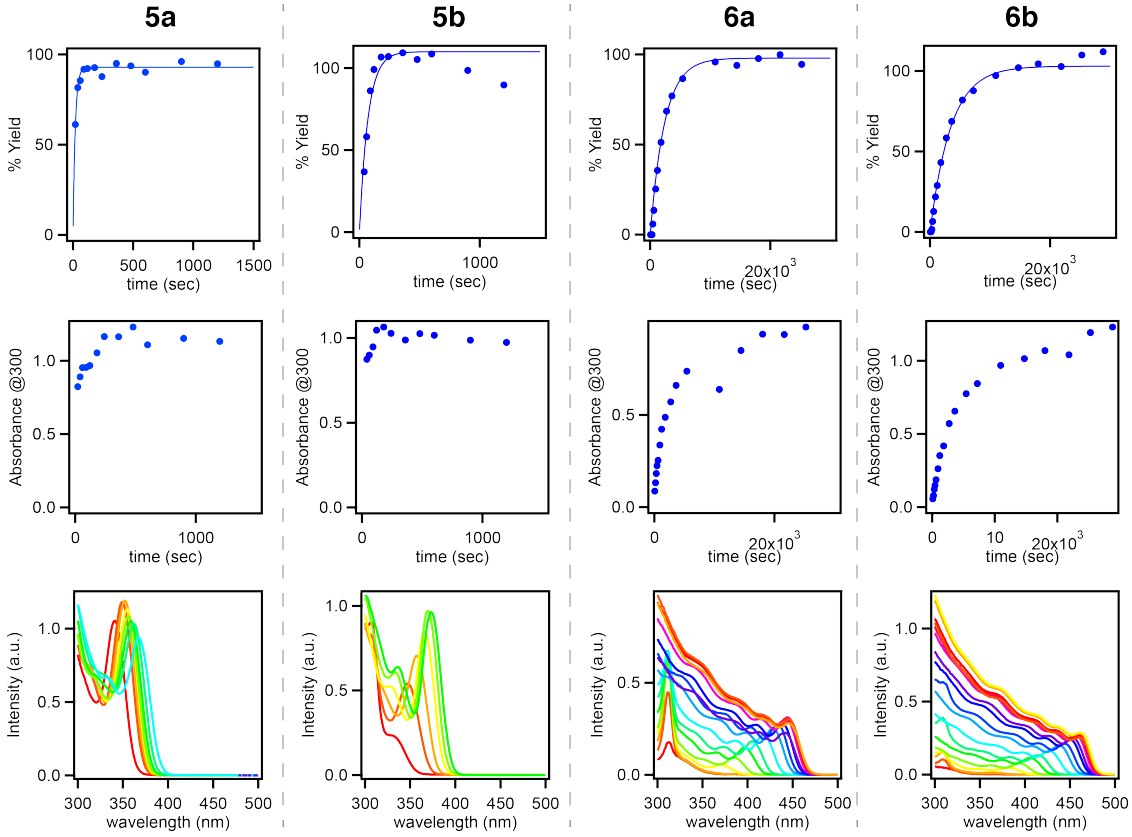

Figure 2.5.2. Yield data using corrected size dependent extinction coefficients, absorbance at 300 nm, and UV-vis spectra of reaction aliquots for thioureas **5a**-**6b**.

Selection of the endpoint for each of these reactions for incorporation into the extinction coefficient correction is nontrivial (Figure 2.5.2). In most cases, the precursor is considered done reacting when the % yield starts to plateau. However, for precursor **5b**, a decrease in % yield is observed as particles ripen

after the reaction has reached completion. Additionally, % yields are compared with the absorbance at 300 nm, which while not a perfect size-independent wavelength to measure conversion of CdS, serves as a rough measure of conversion. Precursor **6b**, shows a plateau and then increase in % yield at extended reaction times. The endpoint was selected during the plateau region since at very large sizes when the 1st excitonic feature is hard to identify, there is more error incorporated into the % yield calculation. It is also worth noting that some reactions result in the formation of magic size clusters (peak around 321 nm), however a correlation between their appearance and precursor structure could not be determined.

With the absorbance data at each reaction endpoint and a calculated theoretical concentration of CdS nanocrystals at 100% conversion, extinction coefficients could be calculated. These are plotted and compared to the previously reported size-dependent extinction coefficients[38] as a function of nanocrystal diameter (*D*) in Figure 2.5.3. Significant differences between the curves are visible at small nanocrystal sizes, which explains the erroneous yields obtained when using the previously reported extinction coefficient. A second-order polynomial fit to our data is shown in Equation 2.5.1. It is worth noting that this approach does not account for differences in the size distribution of samples. Further studies on

the intrinsic line width of single CdS nanocrystals are required before differences in the size distribution can be used to modify the extinction coefficient.

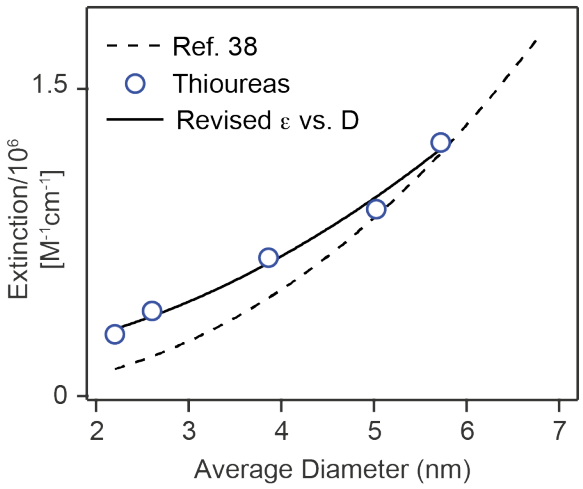

Figure 2.5.3. A) Experimentally determined extinction coefficients made using CdS nanocrystals produced from thioureas **5a**-**6b**.

$$\varepsilon\ (D)\ [\mathrm{M(CdS)^{-1}\ cm^{-1}}] = 156330 + 11522(D) + 30131(D)^2$$

Equation 2.5.1.

Using our revised size dependent extinction coefficient (Equation 2.5.1), the yield of CdS from **1a**−**6b** was monitored from timed reaction aliquots (Figure 2.5.2 and Figure 2.5.4). A single exponential fit was used to extract an observed rate constant (k_{obs}) for each precursor to understand the effect of the substitution pattern on the reactivity. However, unlike the kinetics of forming PbS and PbSe nanocrystals from thio- and selenoureas,[8-9] in most cases, the kinetics observed here are multiexponential and the k_{obs} represents an average of more complex

behavior. For example, Figure 2.5.4 contains a representative data set where some data can be fit well to a first order fit (**1a** and **1e**) but other data may be fit better by a second order fit (**1b**, **1c**, and **1d**). The reaction endpoints were determined by comparing where the % Yield data plateaus and the absorbance at 300 nm stops increasing. Despite the simplification of our kinetics analysis that masks underlying complexities, the use of a metric such as k_{obs} allows the precursor reactivities to be ordered in a semiquantitative fashion.

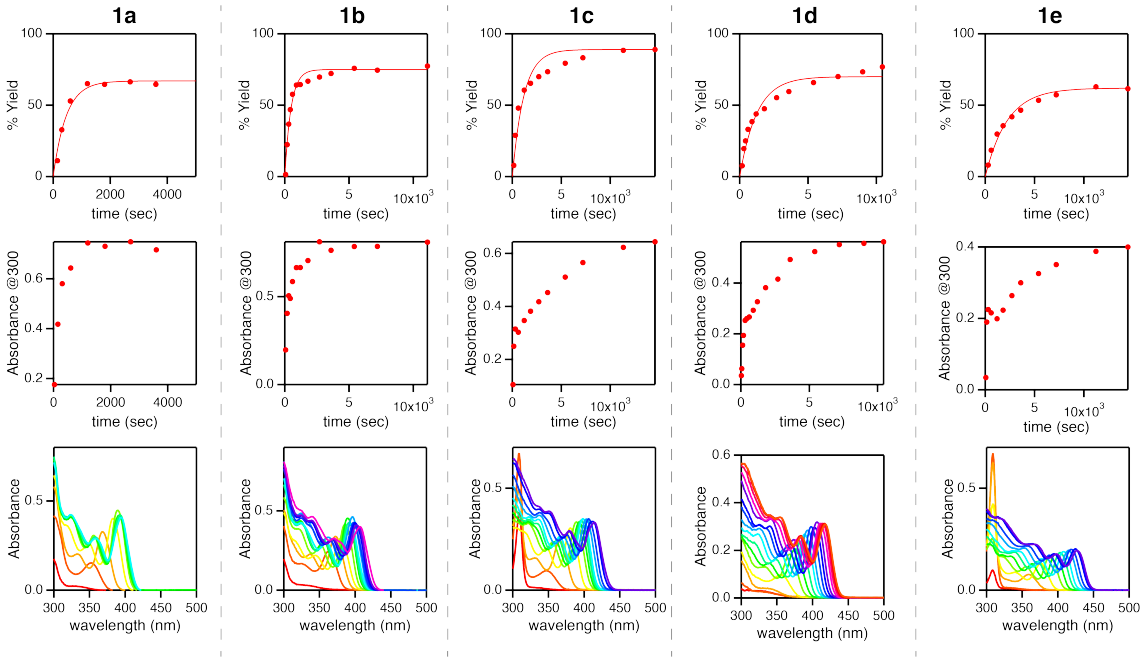

Figure 2.5.4. Yield data using corrected size dependent extinction coefficients, absorbance at 300 nm, and UV-vis spectra of reaction aliquots for thioureas **1a**-**1e**.

2.5.2. Characteristics and Relative Reactivities

The k_{obs} extracted from the UV−vis kinetics for each precursor is plotted in Figure 2.5.5, illustrating the wide range of conversion reactivity. Among disubstituted precursors, the conversion reactivity decreases from thiourea > thiocarbamate > thiocarbonate (Figure 2.5.5 and Figure 2.5.6). While cadmium oleate and *N,N'*-disubstituted thioureas react completely in a minute or less, thiocarbonate precursors convert slowly over the course of minutes to hours. Increasing the number of substituents slows the reactivity of both the thiocarbamate and the thiourea classes. For example, *N,N'*-disubstituted thioureas are more reactive than *N,N,N'*-trisubstituted thioureas by an order of magnitude, which are more reactive than *N,N,N',N'*-tetrasubstituted thioureas by an additional 2 orders of magnitude. Thus, much like in previous studies on the reaction with lead oleate, modifying the number of N−H bonds has a large effect on the reactivity.

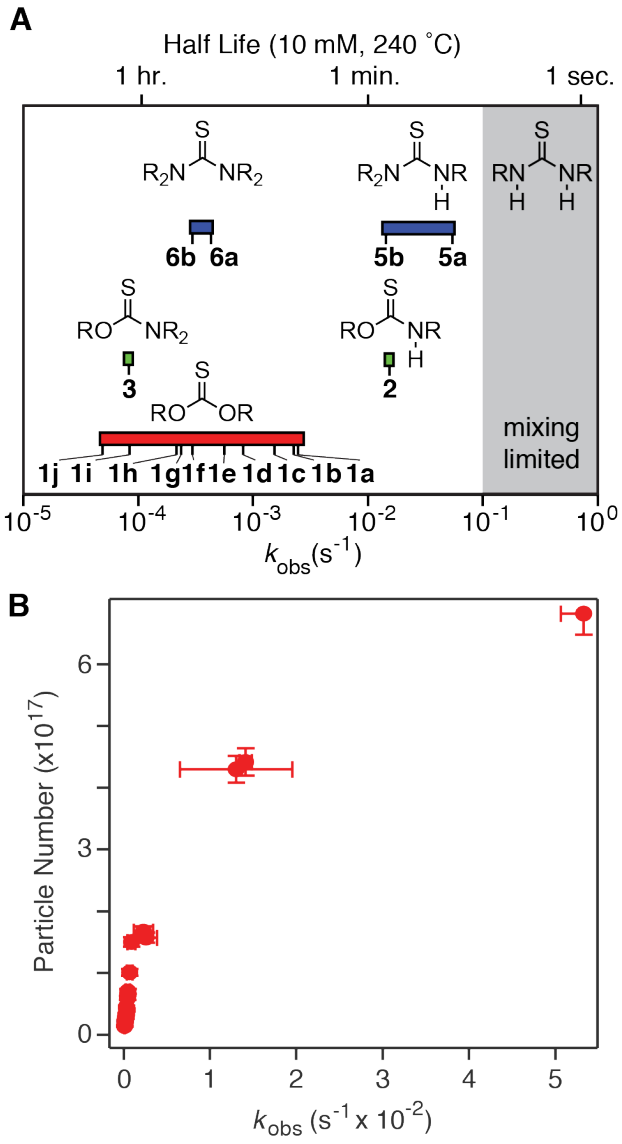

Figure 2.5.5. A) Ranges of precursor reactivity with cadmium oleate under standard reaction conditions (Figure 2.4.1B). B) Particle number versus precursor conversion rate constant.

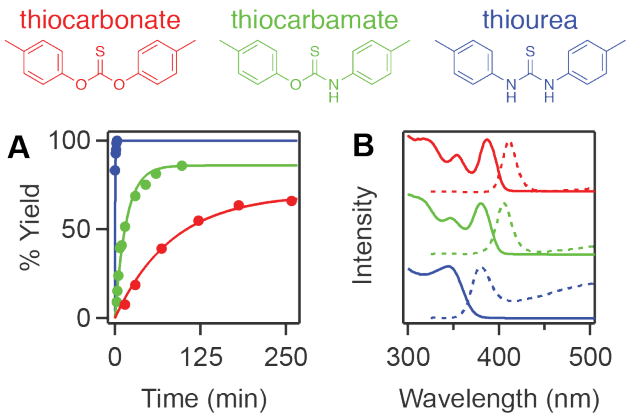

Figure 2.5.6. A) Precursor conversion kinetics of **1c**, **2**, and **4** as determined via UV-vis. B) UV-vis and fluorescence spectra of final nanocrystal products.

In addition to swapping nitrogen atoms in the thiourea derivatives for oxygen atoms to generate thiocarbonates and thiocarbamates (Figure 2.5.6), we also swapped nitrogen atoms with phosphorus atoms to generate substituted phosphanecarbothioamides. We observe that trisubstituted phosphanecarbothioamides have comparable reactivity to the trisubstituted thioureas and disubstituted thiocarbamates. Because the reaction of **7** with cadmium oleate is fast, this reaction was performed at 180 °C to slow down the precursor conversion kinetics and facilitate extraction of a relative k_{obs} value (Figure 2.5.7).

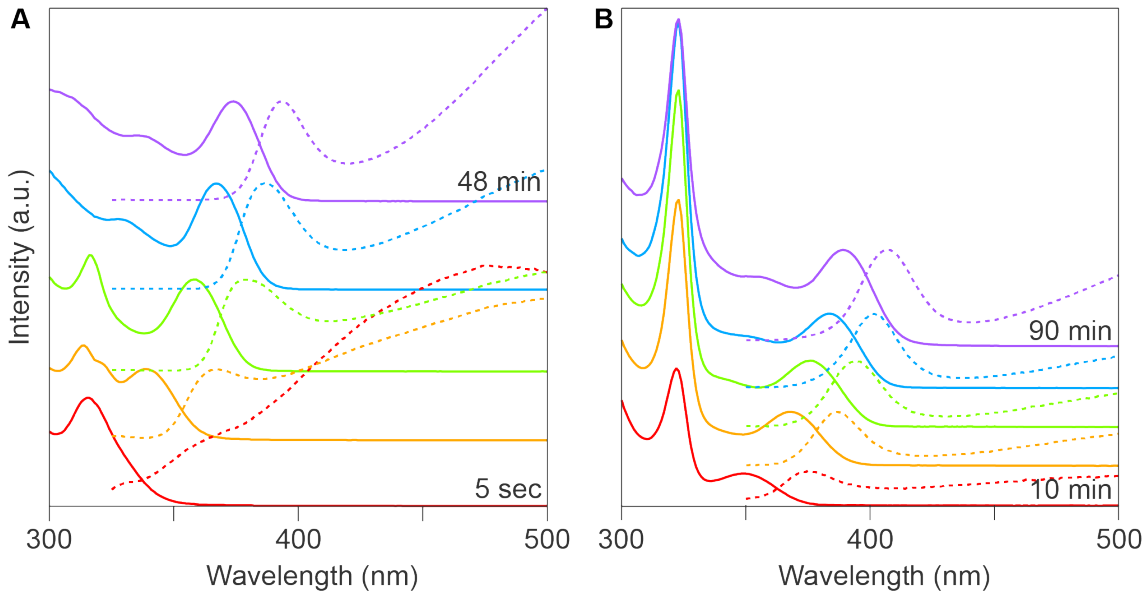

Figure 2.5.7. Absorbance and fluorescence spectra from the reaction of cadmium oleate with A) *N*,1,1-triphenylphosphanecarbothioamide (**7**) and B) phenyl isothiocyanate at 180 °C.

To further characterize the reactivity of this precursor class, the reaction between cadmium oleate and **7** at 120 °C was monitored with $^{31}P\{^{1}H\}$ NMR. We observe rapid disappearance of **7**, accompanied by the appearance of a magic size cluster intermediate in the absorbance spectra (Figure 2.5.8A). The low temperature may be responsible for favoring the formation of the magic size cluster intermediate; further experiments must be done to compare the reactivity of this compound at our standardized reaction conditions at 240 °C.

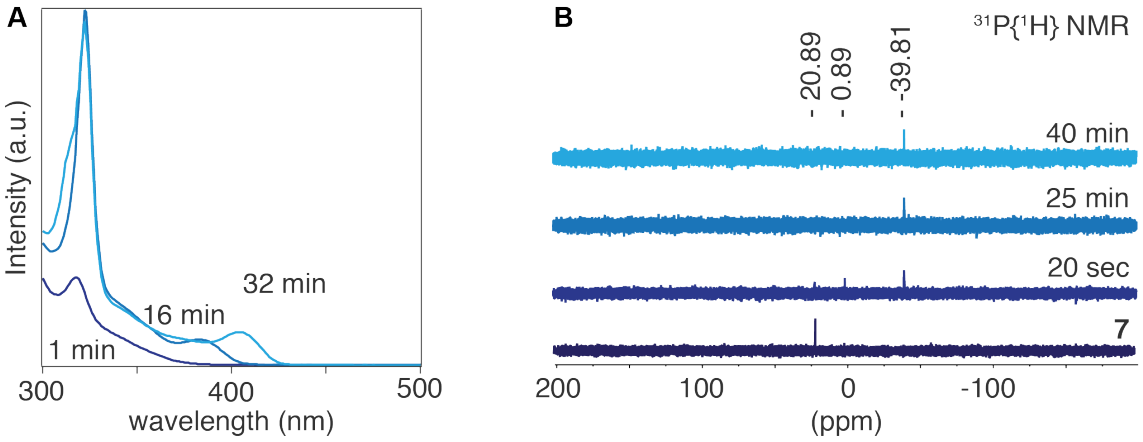

Figure 2.5.8. A) Absorbance spectra for the reaction of cadmium oleate with **7** at 120°C. The reaction was stopped before reaching completion. B) $^{31}P\{^{1}H\}$ NMR of reaction aliquots in C_6D_6 shows the disappearance of **7**, appearance of a transient species at 0.89 ppm, and eventual appearance of a species at -39.81 ppm.

We note the rapid disappearance of starting precursor and appearance of two unidentified species at 0.89 ppm and -39.81 ppm even though the nanocrystal reaction has not progressed to full yield. The chemical shift of this peak is close to that of diphenylphosphine which appears at -40.7 ppm in toluene-d8.[40] $^{31}P\{^{1}H\}$ NMR of the reaction aliquots are obtained in the presence of cadmium oleate, tetraglyme, and other reaction coproducts which render the identity of this species inconclusive. Nevertheless, in the event that the phosphanecarbothioamide immediately decomposes to isothiocyanate and diphenylphosphine under our reaction conditions, the reactivity of phenyl isothiocyanate with cadmium oleate at 180 °C was probed. Under these reaction conditions, the isothiocyanate converts

more sluggishly than **7** although CdS nanocrystals are indeed formed (Figure 2.5.7B).

Among thiocarbonate precursors, those with electron-donating substituents display faster conversion kinetics. However, *ortho*-substituted aryl groups inhibit the conversion step, making the 2,6-xylyl derivative (**1j**) much more sluggish than the related *p*-tolyl derivative (**1c**). Both observations are consistent with a conversion reaction mechanism where preequilibrium binding of the thiocarbonate to cadmium oleate precedes the cleavage of the S=C bond by attack at the thione carbon. Such a mechanism can lead to a complex temporal evolution, which is ignored by the single exponential fits used to extract k_{obs}. An analogous mechanism leads to the cleavage of phosphine chalcogenides coordinated to cadmium oleate (Figure 2.5.9).[41-42]

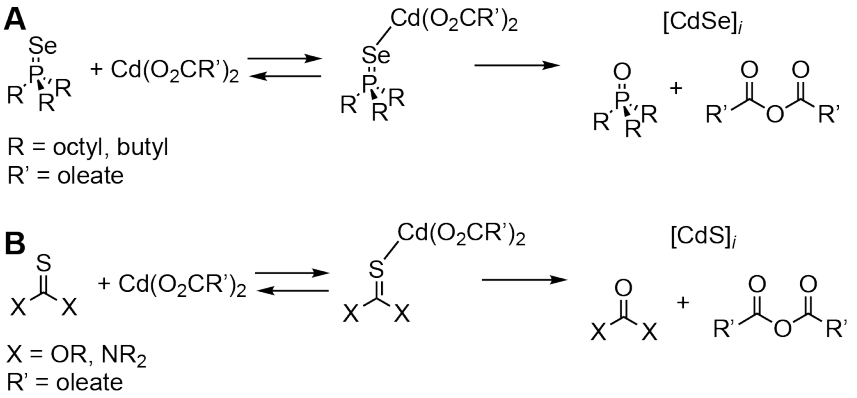

Figure 2.5.9. A) Lewis acid activation of phosphine chalogenides precedes the P=E cleavage step.[41] B) Proposed Lewis acid activation of chalcogenoureas preceding C=E cleavage.

Previous studies of CdSe, PbS, and PbSe have shown a correlation between the precursor conversion reactivity and the number of nanocrystals; faster reactions produce a higher concentration of smaller nanocrystals.[6, 8-9, 43-45] A similar trend is observed here, where less reactive precursors produce larger CdS nanocrystals (Figure 2.5.5). However, the thiocarbonate precursors used in this study produce (53–89%) ± 7% yields of CdS, which also influences the final size. Two mechanisms can explain the low yields: (1) a side reaction of thiocarbonates with oleic acid that liberates OCS in analogy to the mechanism that liberates CO_2 in Figure 2.4.6 (and Figure 2.5.10), and (2) Miyazaki–Newman–Kwart and Schönberg rearrangements for thiocarbamates and thiocarbonates respectively, which appear to compete with the conversion reaction under our reaction conditions (Figure 2.5.10).[46-49]

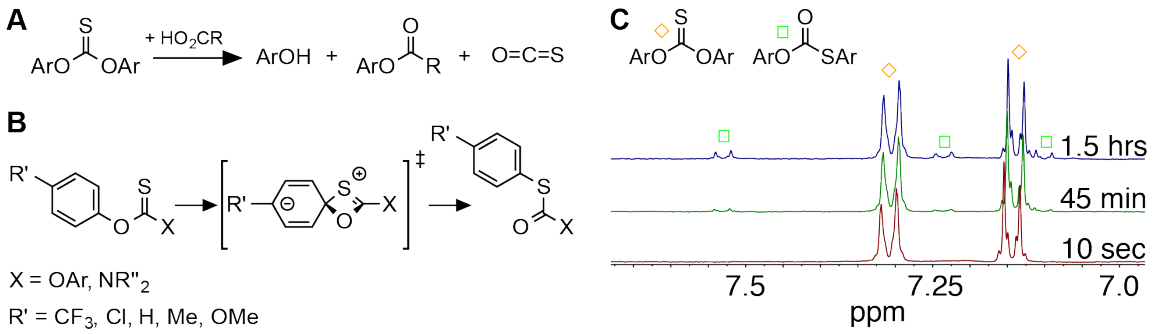

Figure 2.5.10. A) Liberation of OCS during a nanocrystal reaction. B) Isomerization of thiocarbonates and thiocarbamates via a polar transition structure.[46] C) ^{1}H NMR of thiocarbonate **1c** and oleic acid heated to 240°C shows isomerization in the absence of cadmium to *O,S*-di-*p*-tolyl thiolcarbonate.

The Miyazaki–Newman–Kwart and Schönberg rearrangements are accelerated by electron-withdrawing substituents and are known to be faster for thiocarbamates than thiocarbonates. Moreover, an independently synthesized *O,S'*-disubstituted thiolcarbonate proved unreactive toward cadmium oleate after 6 h at 240 °C (Figure 2.5.11), confirming that the formation of the rearrangement products can limit the yield of CdS. This helps explain the low yields obtained from electron-deficient thiocarbonates **1h**–**1j** (as low as 53%) and a slow reacting thiocarbamate (**3**) (yield = 62%) (other thiocarbamates proved even more problematic and are not described here). However, we were unable to detect the isomerization product in the final mixture. On the other hand, OCS was detected during a nanocrystal synthesis from **1e**, by analyzing the volatiles using FT-IR and

mass spectrometry (Figure 2.7.4). We conclude that both mechanisms can explain the partial yield of CdS. Regardless, in cases where the yield is lower than 100%, we showed that additional precursor can be added to drive the reaction forward without compromising the size distribution or nucleating a second population (Figure 2.5.12). The change in particle volume observed is consistent with a constant number of nanocrystals.

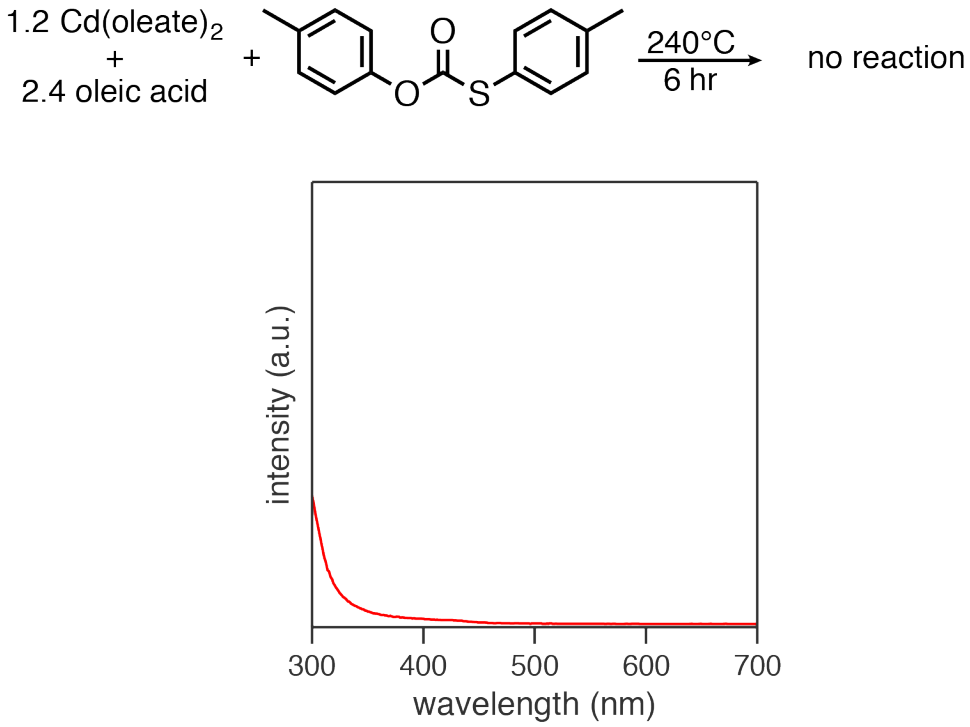

Figure 2.5.11. The reaction of cadmium oleate with *O,S*-di-*p*-tolyl thiolcarbonate shows no formation of CdS nanocrystals over the course of 6 hours.

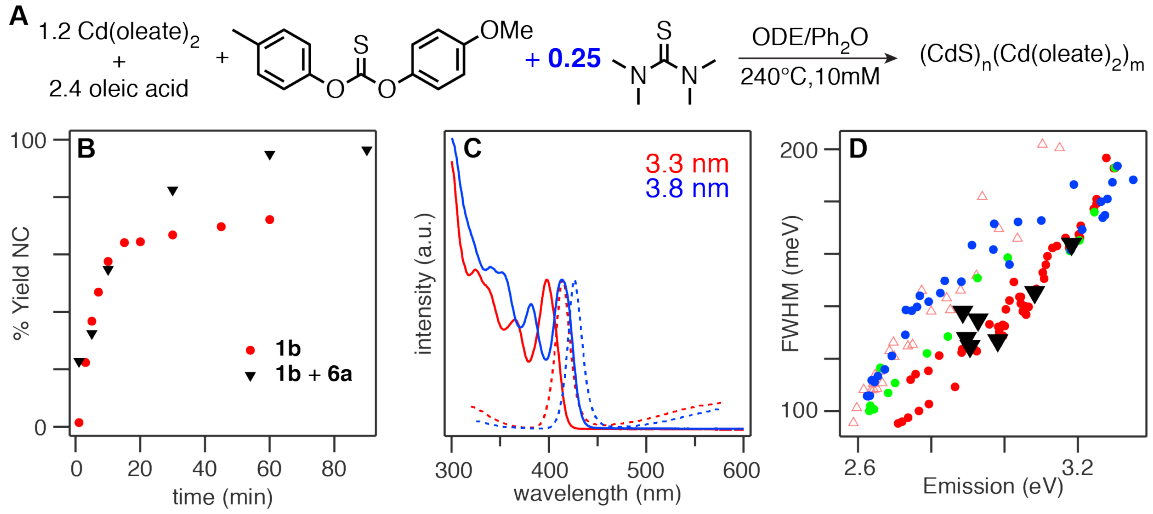

Figure 2.5.12. A) Reaction scheme for the addition of tetramethylthiourea to increase nanocrystal yield. B) Yield vs. time for thiocarbonate **1b** and the combined reaction of **1b** + thiourea **6a** for comparison. C) Absorbance and emission spectra for the nanocrystals formed via the reaction of **1b** (red) and the mixture of **1b** + **6a** (blue). D) The FWHM of particles nucleated by thiocarbonates shelled by a slow thiourea (black triangles) maintains a narrow size dispersity typical of thiocarbonate reactions.

Interestingly, nanocrystals prepared from thiocarbonates (**1a**–**1g**) display optical features that are narrower than those prepared from thiourea or thiocarbamate precursors (Figure 2.5.13). The spectra of similarly sized nanocrystals prepared from a thiocarbonate and a thiourea are compared in Figure 2.5.13, clearly showing the narrower features of the thiocarbonate sample. By plotting the FWHM of the nanocrystal photoluminescence versus the peak energy, a decreasing line width with increasing size is also visible. The trend is consistent with recent studies of PbS, PbSe, and CdSe nanocrystals where size-dependent

broadening from exciton phonon coupling and exciton fine structure account for the majority of the ensemble line width.[9, 50-55] Thus, the narrowing of 30–50 meV afforded by thiocarbonate precursors suggests a significant difference in the size distribution. Nonetheless, nanocrystals produced from thiocarbonates and thioureas, like those shown in Figure 2.5.13, possess very narrow size distributions that are not easily distinguished using transmission electron microscopy (Figure 2.5.14).

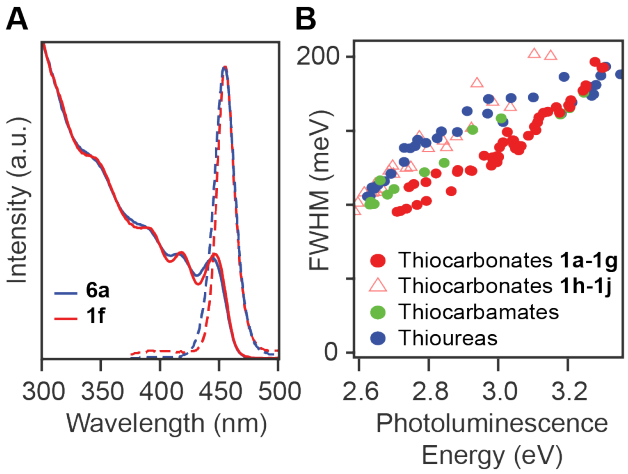

Figure 2.5.13. A) Comparison of UV-vis and fluorescence spectra of CdS nanocrystals synthesized from thiocarbonate **1f** versus thiourea **6a**. B) The FWHM versus energy of photoluminescence from aliquots of CdS syntheses using thioureas, thiocarbonates, and thiocarbamates.

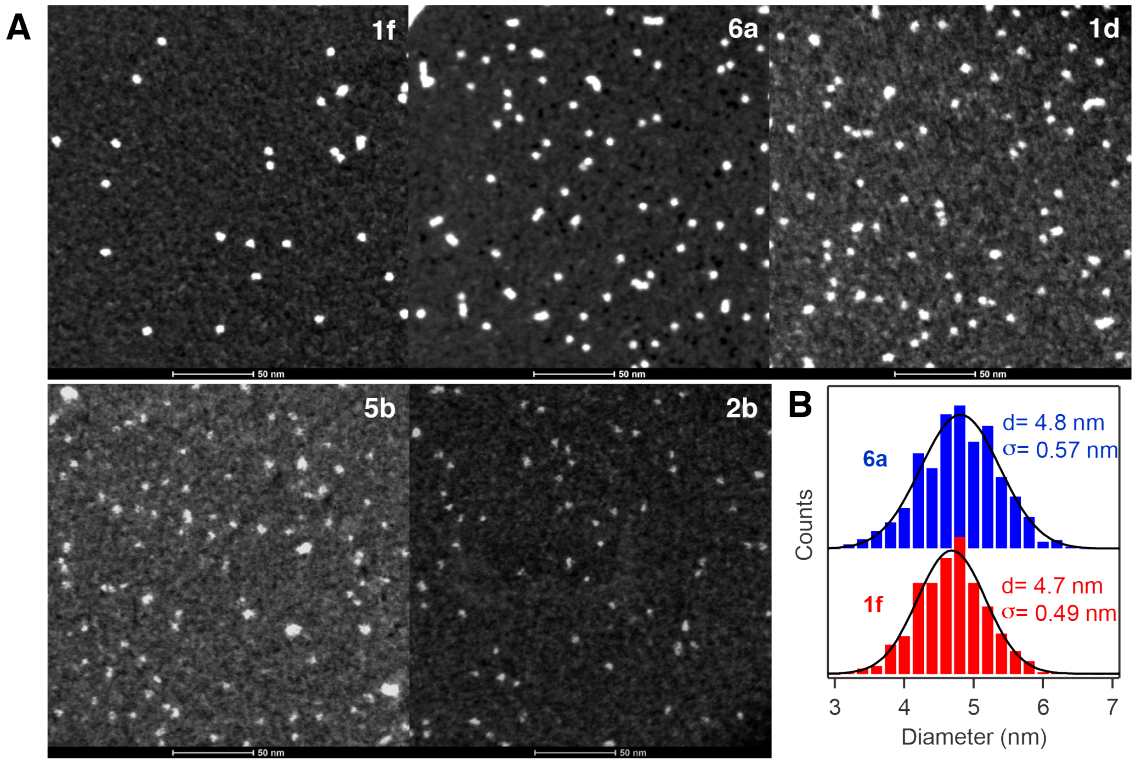

Figure 2.5.14. A) HAADF-STEM (high angle annular dark field scanning transition electron microscope) images of nanocrystal samples used for sizing and FWHM analysis. B) Size comparison of 619 and 1081 CdS nanocrystals synthesized from **1f** and **6a**, respectively.

The narrowness of the distributions obtained from thiocarbonates is apparent at early time points and persists during growth, indicating that it is a consequence of differences in the nucleation process. One possible explanation is that thiocarbonate reaction coproducts are responsible, however upon reacting tetramethyl thiourea (**6a**) with cadmium oleate in the presence of *O,O'*-di-*p*-tolyl carbonate we observed no change in the FWHM of the final nanocrystal product (Figure 2.5.15). This suggests an interaction of the sulfur precursors with the

growing nuclei or solute up to the end of the nucleation phase. While conversion byproducts could also influence the nucleation, they are minor components of the mixture at this stage. On the other hand, we found that adding the proposed rearrangement coproducts to a synthesis can negatively influence the size distribution. For example, adding *O,S*-di-*p*-tolyl thiocarbonate to a synthesis conducted with **6a** resulted in substantially more polydisperse nanocrystals with weak photoluminescence (Figure 2.5.16). This helps explain why thiocarbonates **1h**–**1j**, which undergo significant side reactions, produce broader size distributions than do the other thiocarbonate precursors. However, in the case of **1a**–**1g** where rearrangement is less significant, their beneficial impact on the size distribution may arise from a weaker Lewis basicity as compared to the thioureas. This property can reduce their coordinating power and make them less likely to interact with the growing nuclei or CdS solute.

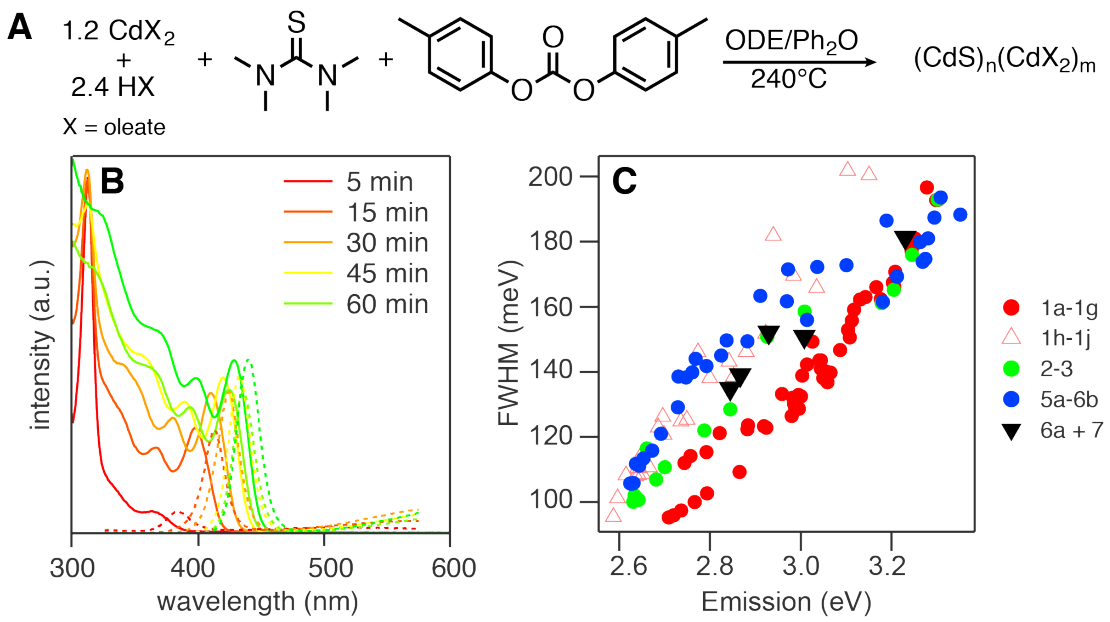

Figure 2.5.15. A) Spiking **7c** into a reaction of **6a** with cadmium oleate has no noticeable impact on B) absorbance and fluorescence spectra nor C) particle size dispersity.

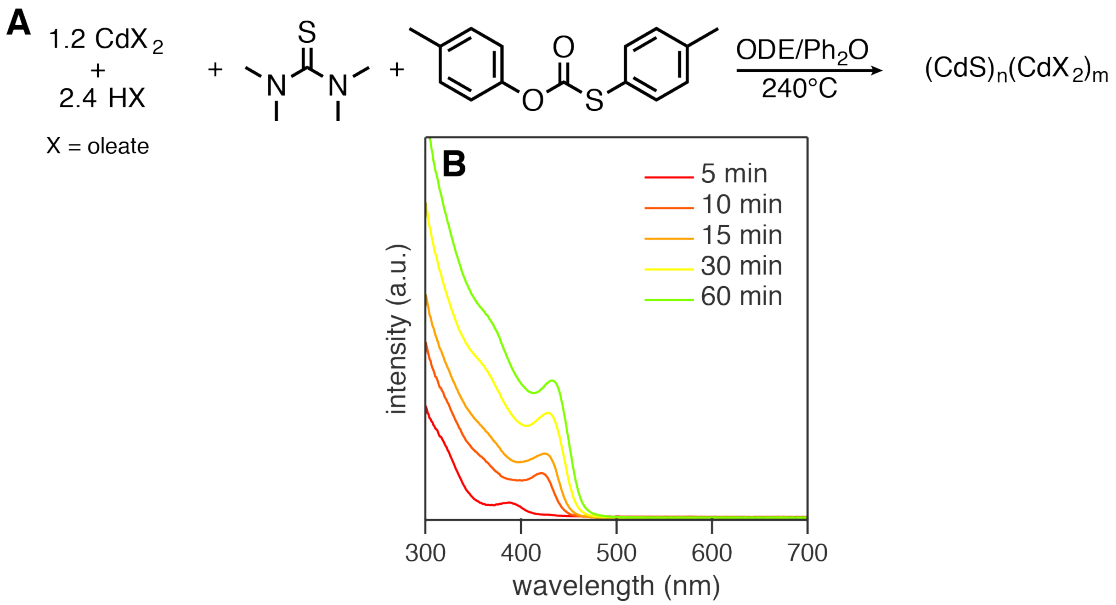

Figure 2.5.16. A) The reaction of **6a** with cadmium oleate in the presence of *O,S*-di-*p*-tolyl thiolcarbonate B) results in a decrease in the quality of the nanocrystal sample.

In principle, the precursor structure can tune the solute supply kinetics and the final nanocrystal size without simultaneously influencing factors such as the surface structure, surface tension, or monomer solubility. In this scenario, the precursor conversion reaction can be said to be "orthogonal" to the crystal nucleation and growth reactions.[56] Given the weaker Lewis basicity of **1a**–**1g**, we hypothesize that their beneficial effect on the size distribution results from an enhanced orthogonality to the nucleation phase.

Other strategies to tune the nanocrystal size, such as adjusting the reaction temperature or the surfactants, influence both the precursor conversion kinetics and the nucleation and growth steps. However, orthogonal precursor reactivity

enables separate optimization of the solute supply kinetics and the factors that influence growth kinetics such as the surfactants and temperature. In this way, orthogonal reactivity is valuable for isolating reaction variables in mechanistic studies of nanocrystal formation. Thus, the careful design of synthesis reagents and a deeper understanding of precursor reactivity will provide greater levels of control over nanocrystal synthesis.

2.6. Summary

We introduced three new classes of sulfide precursors: thiocarbonates, thiocarbamates, and phosphanecarbothioamides whose conversion kinetics to CdS nanocrystals supplement gaps in the thiourea library that now spans 5 orders of magnitude. The thiocarbonates were found to produce nanocrystals with narrower optical features than other precursor compounds with similar conversion kinetics. This finding suggests that improved material properties can be obtained if precursor reactivity can be designed that is orthogonal to the nucleation and growth processes.

2.7. Experimental Details

2.7.1. General Methods

All manipulations were performed in air unless otherwise indicated.

2.7.2. Chemicals

Toluene (99.5%), methyl acetate (99%), benzene (99.8%), hexanes (98.5%), methanol (99.8%), ethanol (≥99.8%), dichloromethane (≥99.5%), chloroform (≥99.8%), acetone (≥99.8%), acetonitrile (99.5%), cadmium nitrate tetrahydrate (98%), sodium hydroxide (≥98%), sodium bicarbonate (≥99.7%), hydrochloric acid (37%), oleoyl chloride (≥89%), sodium chloride (≥99%), sodium sulfate (≥99%), tetramethylthiourea (98%), phenyl isothiocyanate (98%), *p*-tolyl isothiocyanate (97%), triethylamine (≥99.5%), dibutylamine (99.5%), *p*-toluidine (99.6%), *O*-phenyl chlorothionoformate (99%), 4-methoxyphenol (99%), 4-(trifluoromethyl)phenol (97%), phenol (≥96.0%), *p*-cresol (≥99%), cyclohexanol (99%), pyrrolidine (99%), diphenylphosphine (98%), and dimethyl terephthalate (≥99.0%) were obtained from Sigma Aldrich and used without further purification. 4-Chlorophenol (99%) was obtained from Alfa Aesar and used without further purification. Pentafluorophenol (≥99%) was obtained from Oakwood Products and used without further purification. Oleic anhydride (>95%) was obtained from TCI Chemicals and used without further purification. Oleic acid (99%), *O*-(*p*-tolyl) chlorothionoformate (97% or ≥97%), and 1,1′- thiocarbonyldiimidazole (≥95.0% or 90%) were obtained from either Sigma-Aldrich or Alfa Aesar and used without further purification. Diphenyl ether (99%), pyridine (98%), 1-octadecene (90%), hexadecane (99%), tetraethylene glycol dimethyl ether ("tetraglyme", ≥99%),

aniline (99%), and *N*-methyl aniline (98%) were obtained from Sigma-Aldrich, stirred with calcium hydride overnight, and distilled prior to use. Chloroform-*d* (99.8%), benzene-d_6 (99.5%), and methylene chloride-d_2 (99.8%) were obtained from Cambridge Isotopes and used without further purification. Cadmium oleate was synthesized on a 60 mmol scale according to Yang et al.[57]

2.7.3. Instrumentation

UV−vis spectra were obtained using a PerkinElmer Lambda 950 spectrophotometer equipped with deuterium and halogen lamps. Photoluminescence measurements were performed using a Fluoromax 4 from Horiba Scientific, and photoluminescence quantum yields were determined using a quanta-phi integrating sphere accessory according to a previously described procedure.[26] Powder X-ray diffraction (XRD) was measured on a PANalytical X'Pert Powder X-ray diffractometer. Transmission electron microscopy (TEM) was performed on a FEI T12 BioTWIN. Scanning transmission electron microscopy (STEM) was performed on a FEI Talos F200X. FT-IR spectra were obtained using a KBr liquid cell with a Thermo Scientific Nicolet 6700 spectrometer equipped with a liquid N_2 cooled MCT-A detector.

2.7.4. Thiocarbonate Synthesis

*2.7.4.1. Thiocarbonate **1a** Synthesis*

4-Methoxyphenol (8.94 g, 72 mmol), 1,1′-thiocarbonyldiimidazole (7.06 g, 39.6 mmol), acetonitrile (144 mL), and a stir bar were added to a Teflon sealable Schlenk flask. Trifluoroacetic acid (0.41 g, 0.275 mL, 3.6 mmol) was added dropwise, and the flask was sealed, heated to 70 °C in an oil bath, and left stirring overnight. The reaction was cooled, and the volatiles were removed under vacuum. The residue was dissolved in dichloromethane, and washed with HCl (1 M), NaOH (1 M), saturated brine, and dried over Na_2SO_4. The volatiles were removed under vacuum, and the resulting solid was recrystallized from acetonitrile to yield white needles. A second crop of crystals was grown from concentrating the filtrate and crystallizing at −20 °C. Yield 5.50 g (48%).

*2.7.4.2. Synthesis of Thiocarbonates **1b**-**1j***

Thiocarbonates were synthesized using a slightly modified literature procedure[23] that is described for **1b**. It is important that pyridine is used instead of triethylamine or an undesirable side reaction results.[58]

*2.7.4.3. Example Synthesis: O-(4-Methoxyphenyl)-O′-(p-tolyl) Thiocarbonate (**1b**)*

A solution of 4-methoxyphenol (0.621 g, 5 mmol) in 10 mL of benzene was added to a solution of *O*-(*p*-tolyl) chlorothionoformate (0.933 g, 5 mmol) in 10 mL

of benzene. To this mixture, pyridine (0.56 mL, 7 mmol) was added dropwise. The solution turned from yellow to orange, and an orange oil separated. The mixture was heated to reflux for 10 min and the solution became a pale yellow color with a white crystalline precipitate. In a separatory funnel the benzene solution was washed with water, saturated brine, and then dried over Na_2SO_4. Removing the volatiles in vacuo yielded 1.11 g of a white powder. Recrystallization from methanol yielded 0.924 g (67%) of **1b** as white crystals.

2.7.5. Thiocarbamate Synthesis

Thiocarbamates are synthesized from a chlorothionoformate and aniline. ^{1}H NMR spectra show broadened lines from slow rotation about the C–N amide bond. Therefore, the NMR spectra were recorded at 273 K where two distinct sets of peaks are observed.

2.7.5.1. Example Synthesis: O-(p-*Tolyl)*-N-p-*tolyl Thiocarbamate (***2***)*

p-Toluidine (0.214 g, 2 mmol) was dissolved in 10 mL of ethyl acetate and added dropwise to a solution of ethyl acetate (10 mL) and *O*-*p*-tolyl chlorothionoformate (1 mmol, 0.187 g) cooled to 0 °C in an ice bath. The mixture was stirred 10 min, warmed to room temperature, washed with water, saturated brine, and dried over Na_2SO_4. After the volatiles were removed, 1.27 g (98%) of a white powder was collected. The compound was subsequently recrystallized from

acetonitrile to yield 0.921 g (71%) of **2** as a white powder. Because thiocarbamates begin to isomerize around 60 °C, it is important not to heat this compound during synthesis or recrystallization.

2.7.5.2. Example Synthesis: O-*Phenyl*-N-*methyl(phenyl) Thiocarbamate (**3**)*

N-Methylaniline (1.86 g, 1.88 mL, 17.37 mmol) was added dropwise to a solution of *O*-phenyl chlorothionoformate (8.69 mmol, 1.5 g) in dichloromethane (10 mL). The mixture was stirred at room temperature for 10 min, washed 3× with water and dried over $MgSO_4$. The volatiles were removed under vacuum, and the isolated powder was recrystallized from ethanol to yield 1.554 g (74%) of **3** as a white powder.

2.7.6. Thiourea Synthesis

2.7.6.1. Trisubstituted Thiourea Synthesis

N-Methyl-*N,N*′-diphenylthiourea (**5b**) was synthesized according to Hendricks et al.[8]

*2.7.6.2. Tetrasubstituted Thiourea Synthesis: Di(pyrollidin)-1-yl)methanethione (**6b**)*

Pyrrolidine (5.42 g, 6.26 mL, 75 mmol) was added to a solution of 1,1′-thiocarbonyldiimidazole (2.67 g, 15 mmol) in acetonitrile (75 mL). The solution was stirred at 70 °C for 16 h. The volatiles were removed under vacuum, and the resultant tan solid was re-dissolved in dichloromethane (50 mL) and washed with

30 mmol of HCl dissolved in 20 mL of water, saturated brine, and dried over Na_2SO_4. After the volatiles were removed, the crude product was recrystallized with hot acetonitrile to yield colorless crystals. Yield: 2.76 g (49%).

2.7.7. Phosphanecarbothioamide Synthesis

N,1,1-triphenylphosphanecarbothioamide (**7**) was synthesized according to Issleib et al.[24]

2.7.8. Carbonate Synthesis

*2.7.8.1. Example Carbonate Synthesis: Di-*p*-tolyl Carbonate (**8c**)*

Di-*p*-tolyl carbonate was synthesized according to a modified literature procedure.[59] Pyridine (0.87g, 0.88 mL, 11 mmol) was added dropwise to a solution of *p*-tolyl chloroformate (1.79 g, 10.5 mmol) and *p*-cresol (1.08 g, 10 mmol) in dichloromethane (20 mL). The mixture was then heated to reflux for 10 min. The cooled solution was washed with water, sodium hydroxide (1 M), saturated brine, and dried over Na_2SO_4. The volatiles were removed under vacuum, and the white powder was recrystallized from ethanol to yield 0.643 g (25%) of product.

2.7.9. Aryl Oleate Synthesis

2.7.9.1. Example Aryl Oleate Synthesis: p-*Tolyl Oleate*

Pyridine (0.475 g, 0.484 mL, 6 mmol) was added dropwise to a solution of oleoyl chloride (1.50 g, 5 mmol) and *p*-cresol (0.52 g, 4.8 mmol) in dichloromethane (20 mL). The mixture was heated to reflux for 10 min and subsequently washed with water, NaOH (1 M), saturated brine, and dried over Na_2SO_4 to yield 1.44 g (81%) of a brown oil.

2.7.10. Thiolcarbonate Synthesis

Thiolcarbonates were synthesized following a previously reported procedure.[60]

2.7.10.1. Example Thiolcarbonate Synthesis: O,S-*Di(*p-*tolyl) Thiolcarbonate*

A solution of *p*-tolyl chloroformate (3.41 g, 20 mmol) in chloroform (5 mL) was added dropwise to a solution of 4-methylbenzene thiol (2.48 g, 20 mmol) and potassium hydroxide (1.12 g) in chloroform (20 mL) and ethanol (15 mL). The solution was stirred for 2 h, filtered, and the volatiles were removed under vacuum, yielding a white powder (4.268 g) that was subsequently recrystallized from dichloromethane. Yield 2.6077 g (51%).

2.7.11. Synthesis of CdS Nanocrystals

In a nitrogen-filled glovebox, a three-neck round-bottom flask was loaded with cadmium oleate (0.18 mmol, 0.122 g), octadecene (14.25 mL, 11.2 g, 44.4 mmol), and oleic acid (0.102 g, 0.114 mL, 0.36 mmol). A 4 mL vial was filled with the desired sulfur precursor (0.15 mmol) and diphenyl ether (0.75 mL, 0.75 g). A polar solvent such as diphenyl ether or tetraglyme was required to dissolve the sulfur precursor. The three-neck roundbottom flask was transferred to a Schlenk line and heated to 240 °C under Ar. The sulfur precursor solution was then injected into the cadmium oleate solution and left to react for the appropriate time (Table 2.4.1Table 2.4.1. Table of all sulfur precursors, k_{obs} values, nanocrystal yields as determined via UV-vis and [a] determined by weighing the isolated product and subtracting the known mass of ligands as determined by ^{1}H NMR, diameter, particle #, 1st excitonic feature, reaction time, and FWHM of product. See Nanocrystal Formation Kinetics and Cadmium Sulfide Reaction Yield Determination sections in the experimental for details. *At 240 °C, this compound reacts with mixing limited kinetics, so a comparison was conducted at 180 °C and a relative value is reported in this table.). The resulting nanocrystals were isolated from the reaction mixture by precipitation with acetone and centrifugation. The yellow residue was redispersed in hexane (10 mL), and acetone (5–10 mL) was added in 0.5 mL portions to precipitate cadmium oleate, without precipitating the

nanocrystals. This solution was centrifuged. The supernatant was collected, and the nanocrystals precipitated with the addition of 25 mL of acetone. The nanocrystals were washed three additional times with toluene/methyl acetate.

2.7.12. Nanocrystal Formation Kinetics

Quantitative aliquots of approximately 0.1 mL were taken from a CdS nanocrystal reaction and deposited into a previously weighed vial. A mass of toluene equal to 2.5x the weight of the aliquot was added to the vial to standardize aliquot concentration. UV−vis absorption spectra were taken of each aliquot, and the concentration of CdS in the aliquot was calculated from the size-dependent extinction coefficient at the first excitonic absorption maximum using literature[38] values and Equation 2.5.1. Using a second method, the absorbance at 300 nm was monitored as a proxy for CdS conversion. This second method was used to assess the validity of our proposed correction to the size-dependent extinction coefficient for CdS. The kinetics collected from each method was fit to first-order, the rate constant of which is reported in Table 2.4.1 and Figure 2.5.5.

2.7.13. Cadmium Sulfide Reaction Yield Determination

A 2x reaction scaleup was performed in a three-neck round-bottom flask connected to a distillation head. At the end of the reaction, octadecene was distilled from the reaction solution, and the concentrated nanoparticle solution was

purified using the procedure described above. The mass of the dried nanocrystals was measured, and the sample was dispersed in $CDCl_3$ containing dimethyl terephthalate in known concentration. By integrating the dimethyl terephthalate and alkene signal of cadmium oleate, the concentration of cadmium oleate ligands could be determined. From the oleate concentration and the mass of the nanocrystals used to make the NMR sample, the mass of cadmium sulfide could be calculated by assuming the empirical formula: $(CdS)_n((Cd(O_2CR)_2)_m$.

2.7.14. Thiocarbonate Reaction Coproduct Identification

In a nitrogen-filled glovebox, a three-neck round-bottom flask is loaded with cadmium oleate (0.18 mmol, 0.122 g), octadecene (14.25 mL, 11.2 g, 44.4 mmol), and oleic acid (0.102 g, 0.114 mL, 0.36 mmol,). A 4 mL vial was filled with the desired sulfur precursor **1c** or **1e** (0.15 mmol) and tetraglyme (0.75 mL, 0.75 g). The three-neck roundbottom flask was transferred to a Schlenk line and heated to 240 °C under Ar. The sulfur precursor solution was then injected into the cadmium oleate solution and left to react for the appropriate time. 200 μL aliquots of the reaction solution were dissolved in 300 μL of CD_2Cl_2 and 100 μL of a 22.4 mM solution of dimethyl terephthalate dissolved in CD_2Cl_2. ^1H NMR spectra were collected with a relaxation delay time of 30 s. Independently synthesized samples of coproducts were spiked into the NMR tubes to verify their identities

2.7.15. Coproduct Reaction Determination

Octadecene (14.25 mL), tetraglyme (0.75 mL), and **8c** (0.0363 g, 0.15 mmol) or *p*-cresol (0.0162 g, 0.15 mmol) and oleic acid (0.102 g, 0.36 mmol) or oleic anhydride (0.082 g, 0.15 mmol) were combined in a three-neck roundbottom flask. The solution was degassed on a Schlenk line for 10 min and heated to 240 °C. A starting aliquot was taken as soon as the precursors became soluble, and time was started as soon as the solution temperature hit 240 °C. 200 μL reaction aliquots were dispersed in CD_2Cl_2 for subsequent ^1H NMR studies.

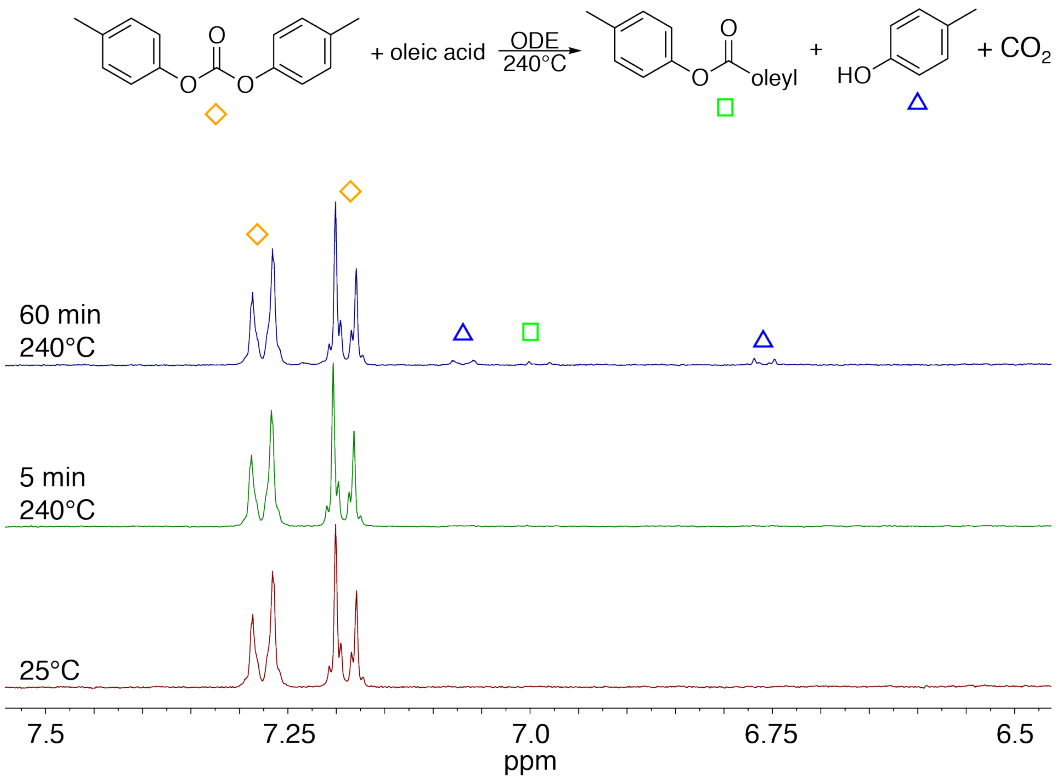

Figure 2.7.1. ^1H NMR spectra of the reaction between **8c** and oleic acid. The formation of tolyl oleate and *p*-cresol is observed.

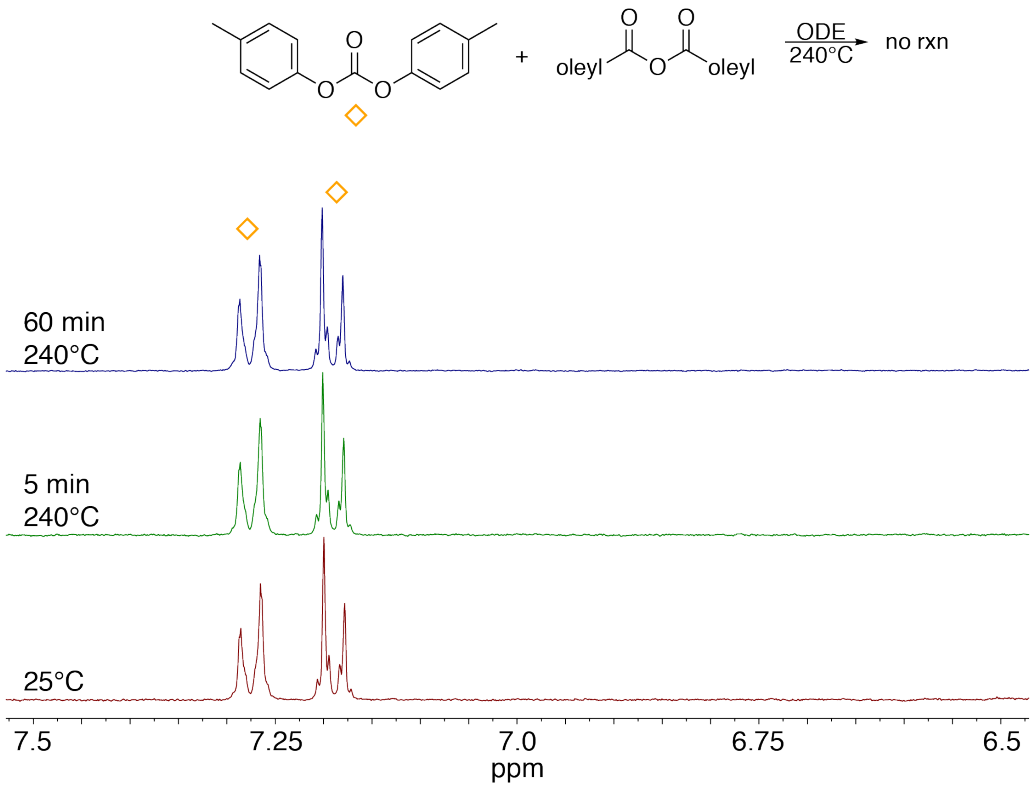

Figure 2.7.2. ^{1}H NMR to monitor the reaction of **8c** and oleic anhydride. No reaction is observed.

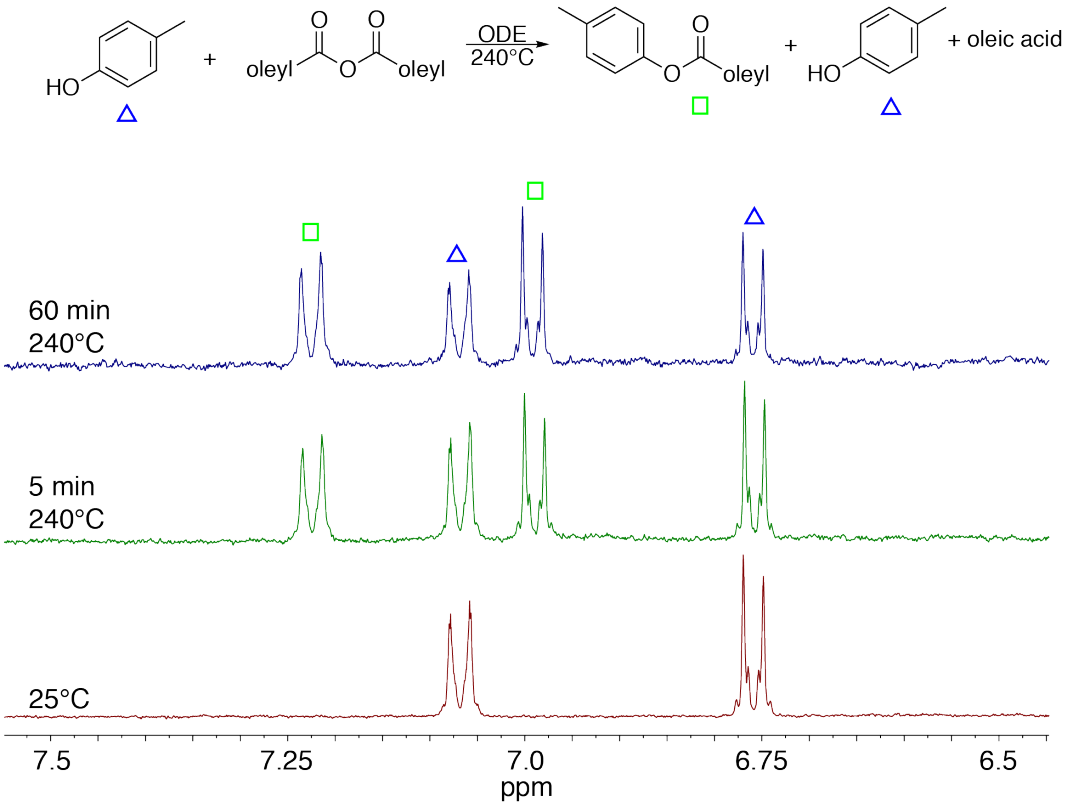

Figure 2.7.3. ^{1}H NMR spectroscopic monitoring of the reaction between *p*-cresol and oleic anhydride. The formation of *p*-tolyl oleate is observed.

2.7.16. Volatile Coproduct Collection

Cadmium oleate (1.22 g, 1.8 mmol), oleic acid (1.02 g, 3.6 mmol), **1e** (0.345 g, 1.5 mmol), diphenyl ether (7.5 mL), and octadecene (142.5 mL) were combined in a 750 mL Straus flask and degassed. The flask was sealed and heated to 200 °C in an oil bath and reacted for 3 h. Subsequently, the flask was hooked to a vacuum transfer bar and Schlenk flask. The Schlenk flask was charged with toluene and freeze pump thawed. The volatiles from the NC reaction were then vacuum

transferred over to the Schlenk flask. The gases dissolved in toluene were identified as OCS. FT-IR (KBr liquid cell): 2041 (vs). MS (ASAP) *m*/*z* calcd for [OCS^+]: 60.0. Found: 60.2.

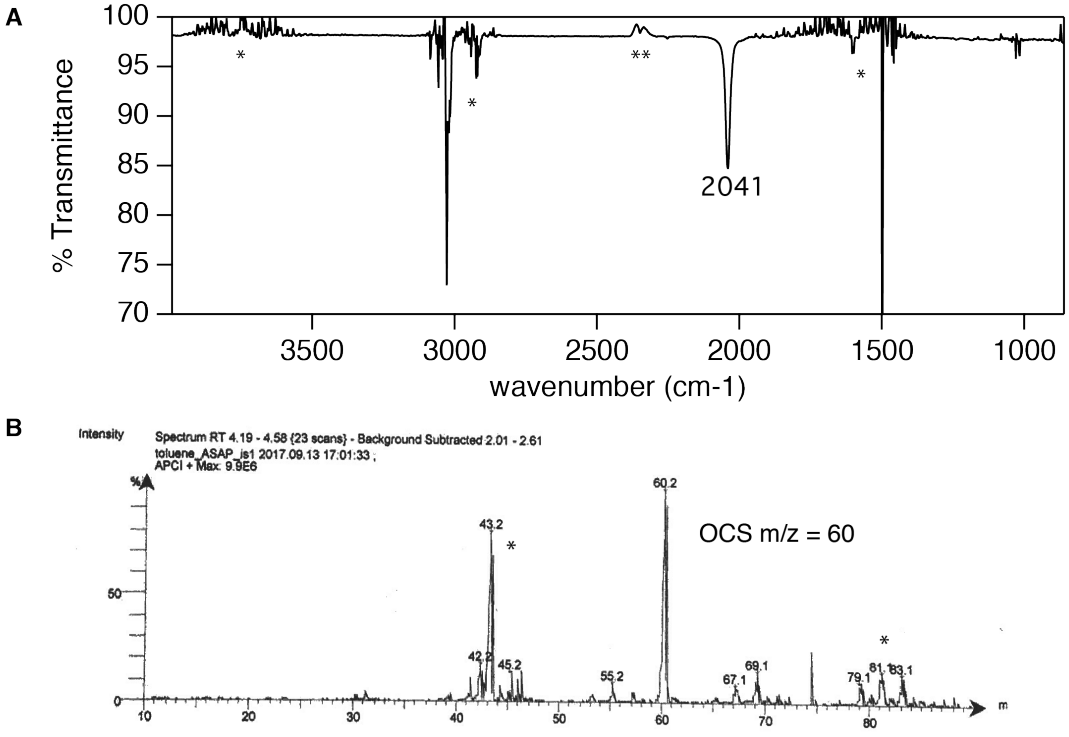

Figure 2.7.4. A) FT-IR of volatile coproducts obtained from the reaction of **1e** with cadmium oleate. The volatiles were vacuum transferred into toluene. *Instrument artifacts. **CO_2 background subtraction makes it difficult to characterize if CO_2 is present in the sample. B) ASAP+ mass spectrum of volatile coproducts dissolved in toluene. *These peaks were also present in a toluene blank and are not thought to be associated with the sample.

2.7.17. Precursor Characterization

***O,O′*-bis(4-methoxyphenyl) thiocarbonate (1a)**

Yield 5.50 g (48%). ^{1}H NMR (400 MHz, $CDCl_3$): δ = 3.82 (s, 6H), 6.92−6.98 (m, 4H), 7.10−7.16 (m, 4H). $^{13}C\{^{1}H\}$ (100 MHz, $CDCl_3$): δ = 55.72, 114.68, 122.70, 147.36, 158.0, 196.13. Anal. Calcd for $C_{15}H_{14}O_4S$: C, 62.05; H, 4.86. Found: C, 61.29; H, 4.16. MS (ASAP) *m*/*z* calcd for [$C_{15}H_{14}O_4S + H^+$]: 291.07. Found: 291.07.

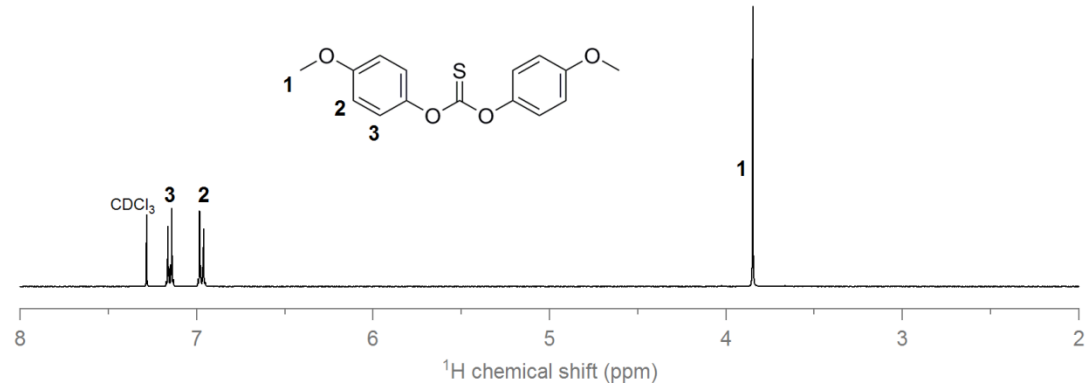

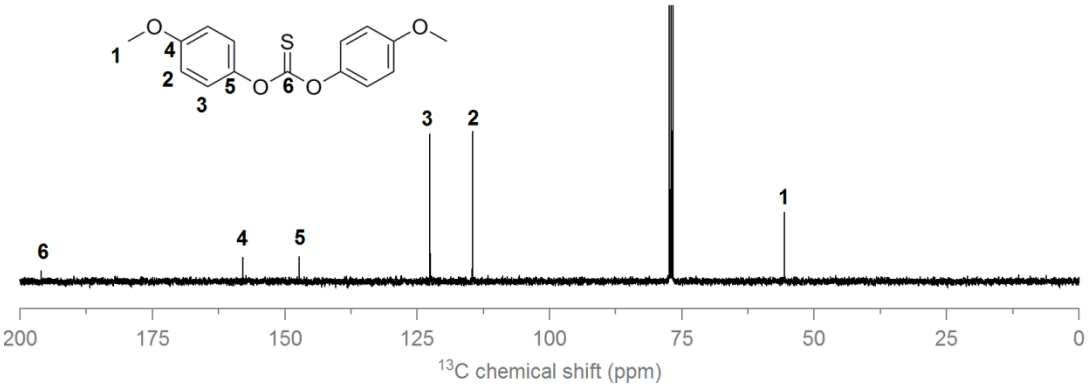

***O*-(4-Methoxyphenyl)-*O*′-(*p*-tolyl) Thiocarbonate (1b)**

The crude material (1.11 g) was recrystallized from methanol to yield 0.924 g (67%) of **1b** as white crystals. ^{1}H NMR (400 MHz, $CDCl_3$): δ = 2.42 (s, 3H), 3.86 (s, 3H), 7.02–6.94 (m, 2H), 7.20–7.10 (m, 4H), 7.31–7.25 (m, 2H). $^{13}C\{^{1}H\}$ (100 MHz, $CDCl_3$): δ = 21.13, 55.71, 114.69, 121.55, 122.70, 130.30, 136.69, 147.38, 151.66, 158.04, 195.79. Anal. Calcd for $C_{15}H_{14}O_3S$: C, 65.67; H, 5.14. Found: C, 65.60; H, 4.87. MS (ASAP) *m*/*z* calcd for [$C_{15}H_{14}O_3S + H^+$]: 275.07. Found: 275.07.

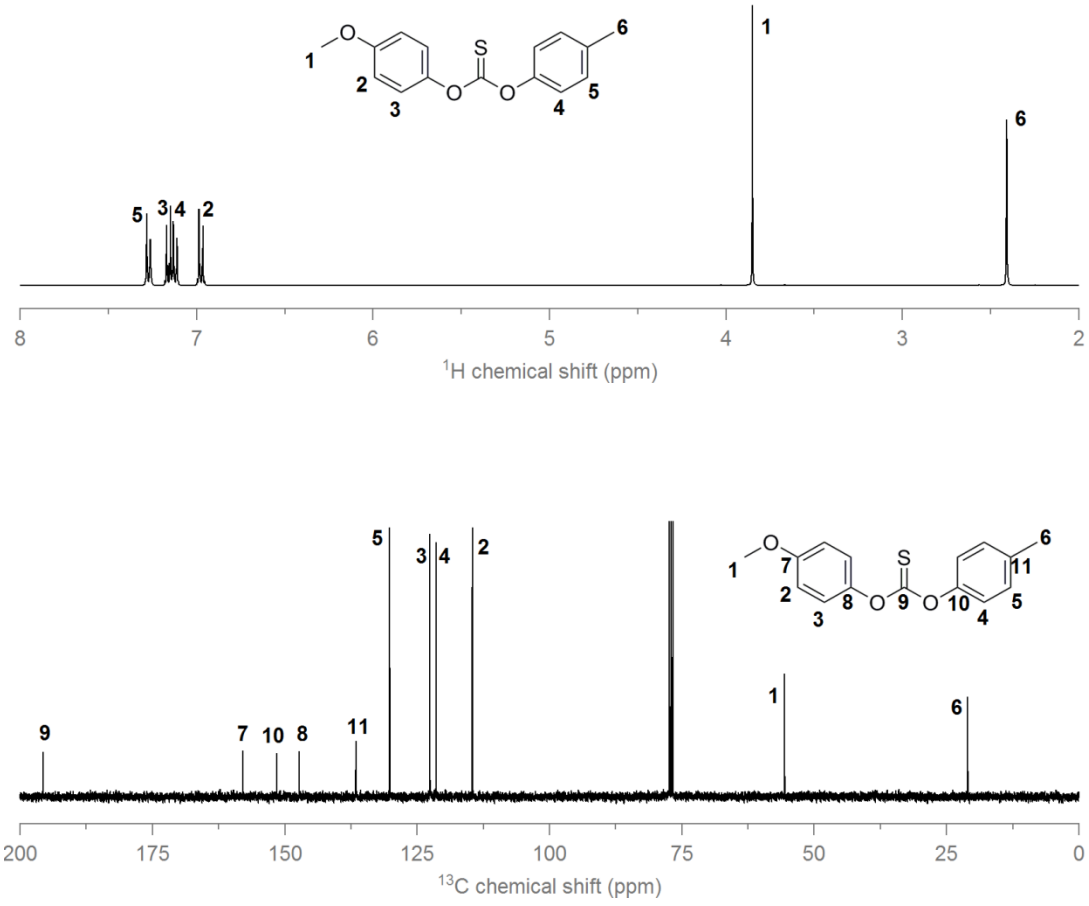

O,O′-Di-*p*-tolyl Thiocarbonate (1c)

The crude material (1.13 g) was recrystallized from methanol to yield 0.984 g (76%) of **1c** as white crystals. ^{1}H NMR (400 MHz, $CDCl_3$): δ = 2.38 (s, 6H), 7.07–7.12 (m, 4H), 7.22–7.27 (m, 4H). $^{13}C\{^{1}H\}$ (100 MHz, $CDCl_3$): δ = 21.14, 121.57, 130.31, 136.71, 151.65, 195.52. Anal. Calcd for $C_{15}H_{14}O_2S$: C, 69.74; H, 5.46. Found: C, 69.74; H, 5.24. MS (ASAP) *m*/*z* calcd for [$C_{15}H_{14}O_2S + H^+$]: 259.08. Found: 259.08.

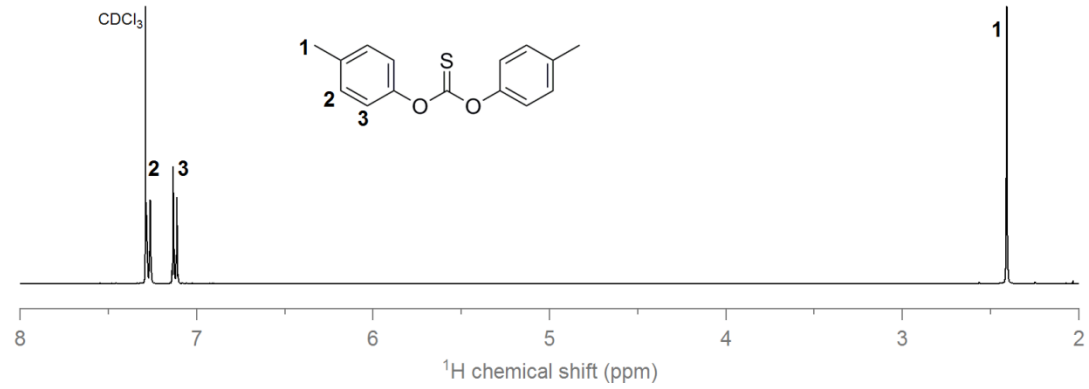

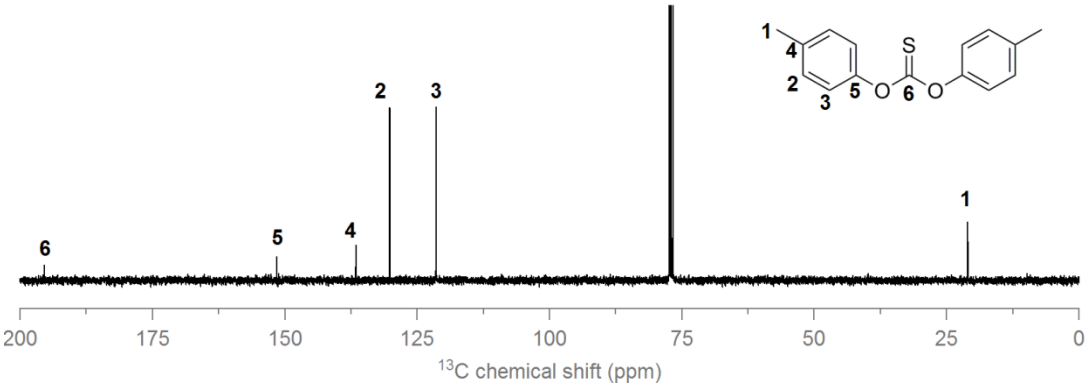

***O*-Phenyl-*O*′-(*p*-tolyl) Thiocarbonate (1d)**

The crude material (1.03 g) was recrystallized from methanol to yield 0.802 g (66%) of **1d** as white crystals. ^{1}H NMR (400 MHz, $CDCl_3$): δ = 2.43 (s, 3H), 7.13–7.19 (m, 2H), 7.24–7.33 (m, 4H), 7.34–7.40 (m, 1H), 7.47– 7.54 (m, 2H). $^{13}C\{^{1}H\}$ (100 MHz, $CDCl_3$): δ = 21.13, 121.54, 121.97, 126.91, 129.77, 130.32, 136.73, 151.62, 153.73, 195.21. Anal. Calcd for $C_{14}H_{12}O_2S$: C, 68.83; H, 4.95. Found: C, 68.61; H, 4.65. MS (ASAP) *m*/*z* calcd for [$C_{14}H_{12}O_2S + H^+$]: 245.06. Found: 245.06.

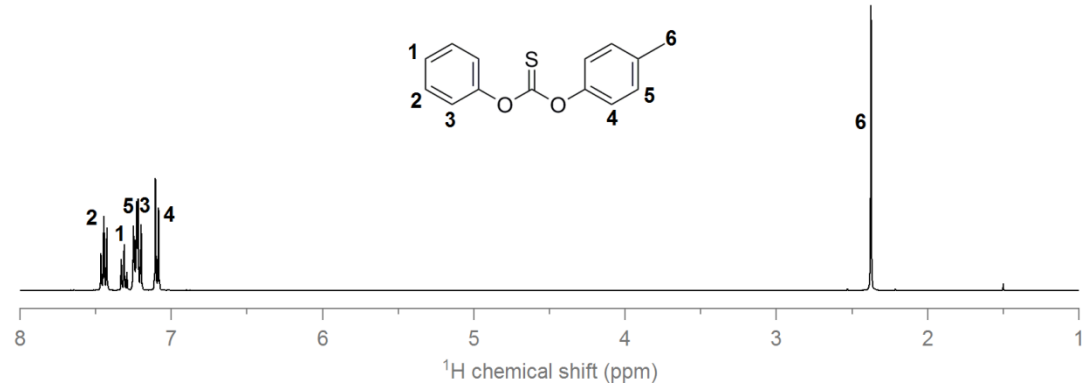

O,O'-Diphenyl Thiocarbonate (1e)

The crude material (1.01 g) was further purified by recrystallization from acetonitrile to yield 0.770 g (67%) of **1e** as white crystals. ^{1}H NMR (400 MHz, $CDCl_3$): δ = 7.20 (d, 4H), 7.30 (t, 2H), 7.43 (t, 4H). $^{13}C\{^{1}H\}$ (100 MHz, $CDCl_3$): δ = 121.97, 126.96, 129.80, 153.73, 194.94. Anal. Calcd for $C_{13}H_{10}O_2S$: C, 67.80; H, 4.38. Found: C, 67.66; H, 4.12. MS (ASAP) *m/z* calcd for [$C_{15}H_{14}O_2S + H^+$]: 231.05. Found: 231.05.

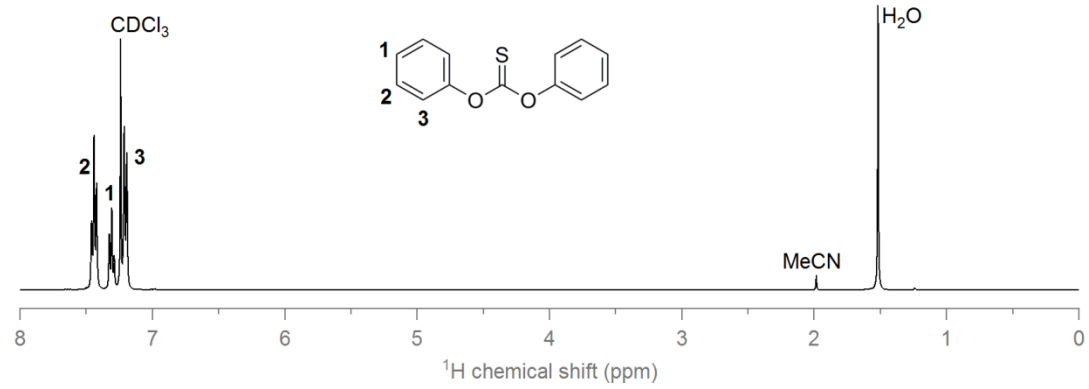

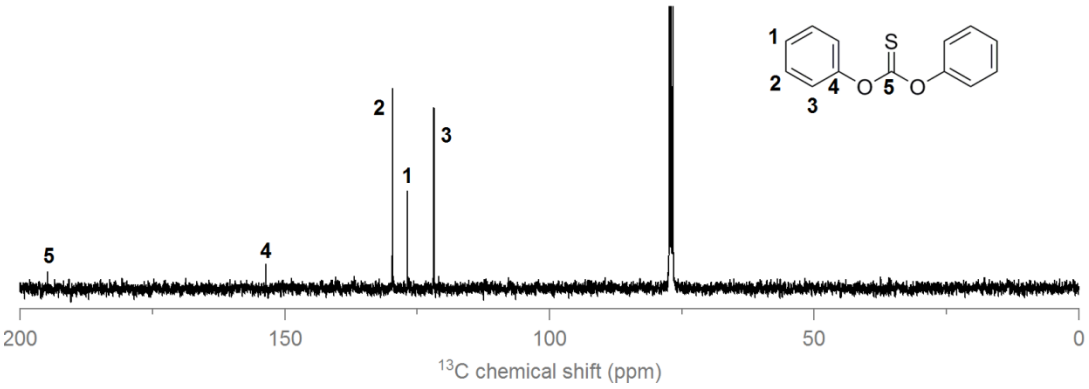

***O*-(4-Chlorophenyl)-*O*′-(*p*-tolyl) Thiocarbonate (1f)**

The crude material (1.14 g) was recrystallized from acetonitrile to yield 0.954 g (68%) of **1f** as white crystals. ^{1}H NMR (400 MHz, $CDCl_3$): δ = 2.39 (s, 3H), 7.06–7.11 (m, 2H), 7.13–7.19 (m, 2H), 7.22–7.28 (m, 2H), 2.39 (m, 2H). $^{13}C\{^{1}H\}$ (100 MHz, $CDCl_3$): δ = 21.14, 121.45, 123.46, 129.91, 130.37, 132.48, 136.89, 151.57, 152.08, 194.90. Anal. Calcd for $C_{14}H_{11}O_2SCl$: C, 60.32; H, 3.98. Found: C, 60.06; H, 3.68. MS (ASAP) *m*/*z* calcd for [$C_{14}H_{11}O_2SCl + H^+$]: 279.02. Found: 279.02.

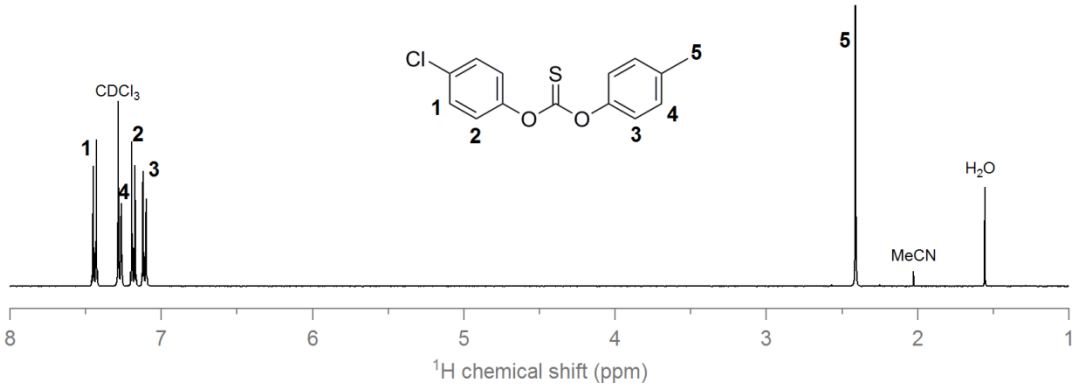

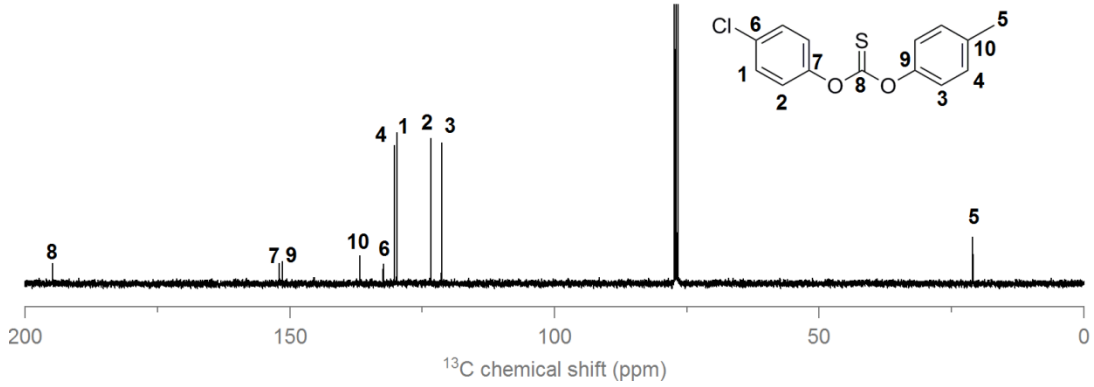

***O*-(*p*-Tolyl)-*O'*-(4-(trifluoromethyl)phenyl) Thiocarbonate (1g)**

The crude material (1.26 g) was recrystallized from acetonitrile to yield 0.949 g (61%) of **1g** as white crystals. ^{1}H NMR (400 MHz, $CDCl_3$): δ = 2.44 (s, 3H), 7.12–7.17 (m, 2H), 7.27–7.33 (d, 2H), 7.37–7.42 (d, 2H), 7.75–7.80 (d, 2H). $^{13}C\{^{1}H\}$ (100 MHz, $CDCl_3$): δ = 21.12, 121.41, 122.77, 123.86, 127.2 (q, J = 4 Hz), 129.24 (q, J = 33 Hz), 130.40, 136.98, 151.52, 155.82, 194.36. $^{19}F\{^{1}H\}$ ($CDCl_3$, 425 MHz): δ = −61.35 (s, 3F). Anal. Calcd for $C_{15}H_{11}O_2SF_3$: C, 57.69; H, 3.55. Found: C, 57.44; H, 3.25. MS (ASAP) *m*/*z* calcd for [$C_{15}H_{11}O_2SF_3$ + H^+]: 313.05. Found: 313.05.

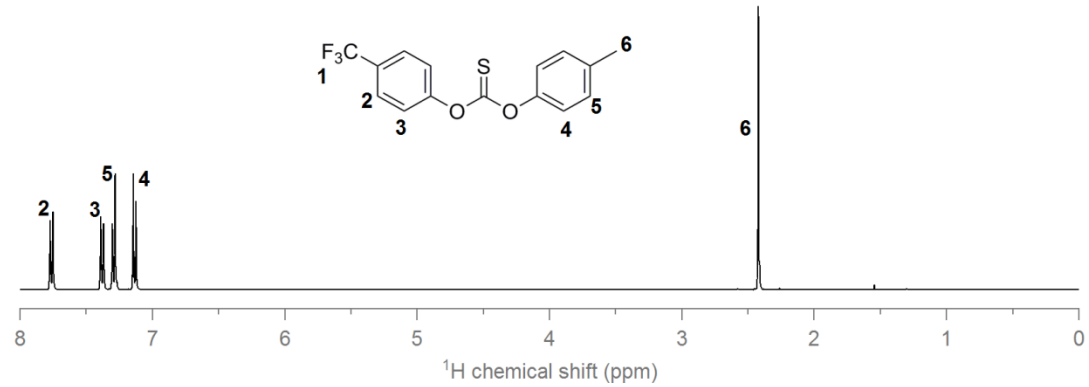

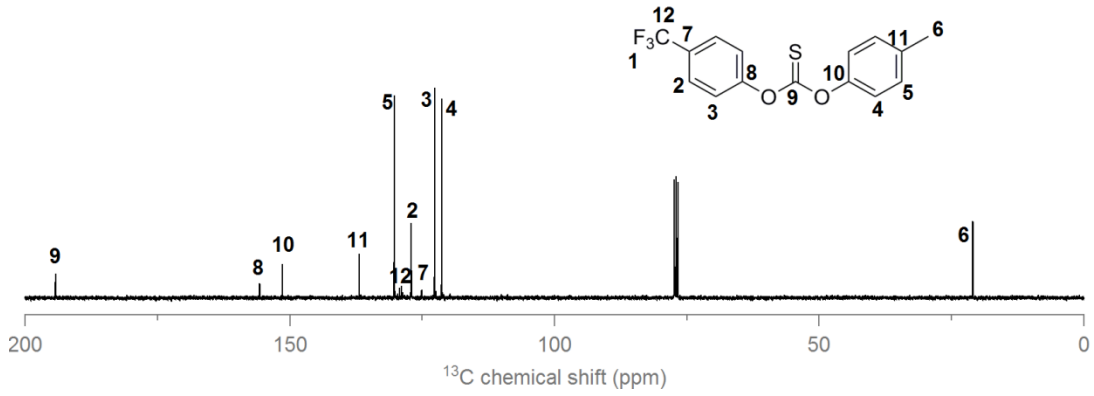

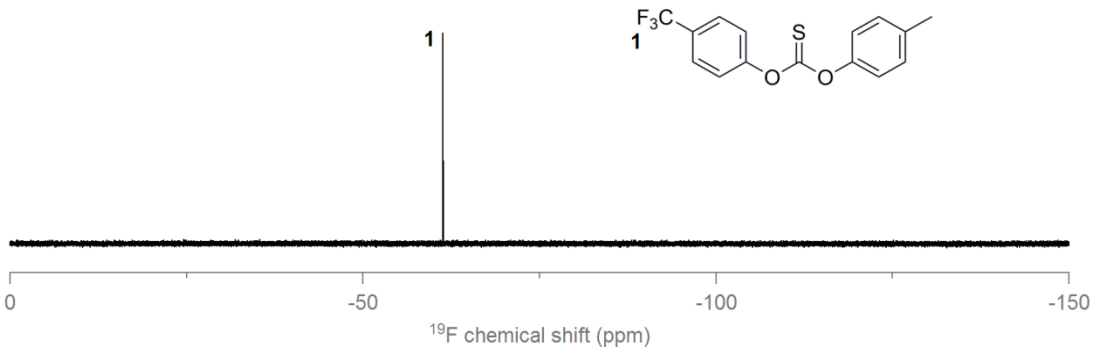
1
F3C
1
S
O
O
0
-50
-100
-150
19F chemical shift (ppm)

_O_-Cyclohexyl-_O′_-(_p_-tolyl) Thiocarbonate (1h)

The crude material was recrystallized from methanol to yield 0.159 g (62%) of **1h** as white crystals. ^{1}H NMR (400 MHz, $CDCl_3$): δ = 1.30−1.53 (m, 3H), 1.55−1.75 (m, 3H), 1.76−1.89 (m, 2H), 2.04−2.17 (m, 2H), 2.4 (s, 3H), 5.28 (sep, 1H), 7.02 (d, 2H), 7.23 (d, 2H). ^{13}C{^{1}H} (100 MHz, $CDCl_3$): δ = 21.13, 23.76, 25.36, 31.01, 83.58, 121.81, 130.14, 136.29, 151.37, 194.72. Anal. Calcd for $C_{14}H_{18}O_2S$: C, 67.16; H, 7.25. Found: C, 66.94; H, 6.97. MS (ESCI) *m*/*z* calcd for [$C_{14}H_{18}O_2S + Na^+$]: 273.09. Found: 273.09.

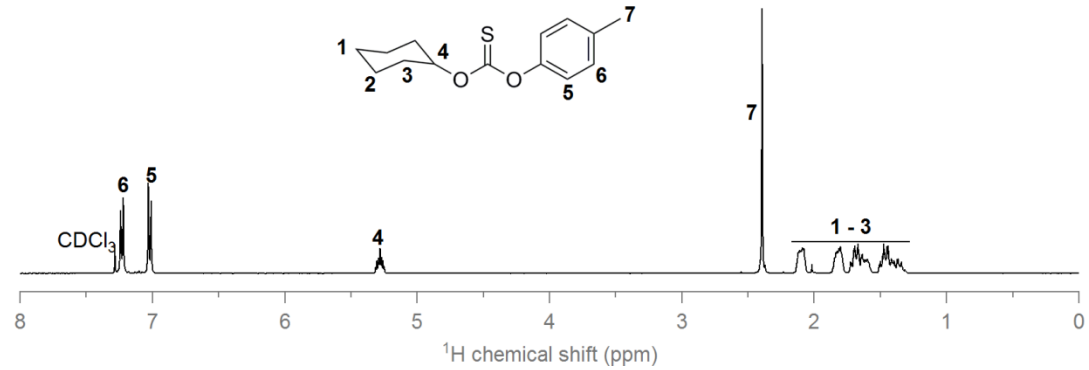

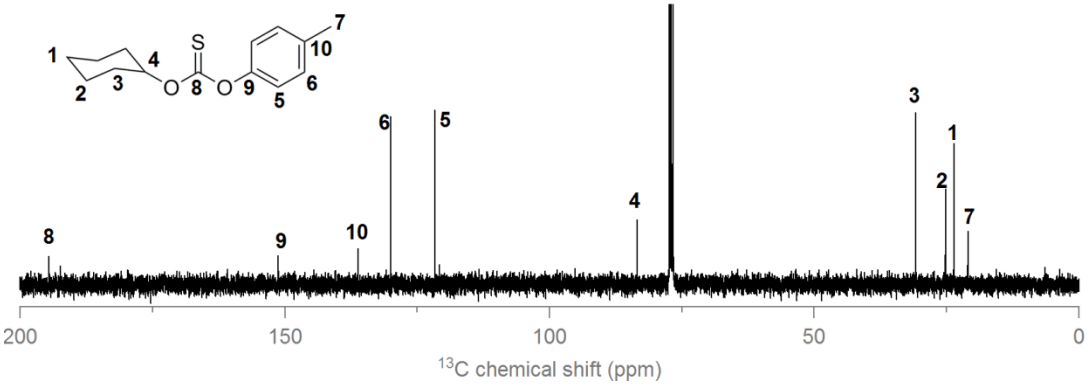

***O*-(4-Chlorophenyl)-*O*′-phenyl Thiocarbonate (1i)**

The crude material (1.081 g) was recrystallized from acetonitrile to yield 0.796 g (60%) of **1i** as white crystals. ^{1}H NMR (400 MHz, CD_2Cl_2): δ = 7.2–7.3 (m, 4H), 7.35–7.41 (m 1H), 7.45–7.54 (m, 4H). $^{13}C\{^{1}H\}$ (100 MHz, CD_2Cl_2): δ = 121.75, 123.44, 126.9, 128.34, 129.7, 132.25, 152, 153.63, 195. Anal. Calcd for $C_{13}H_9O_2SCl$: C, 58.98; H, 3.43. Found: C, 58.98; H, 3.43. MS (ASAP) *m*/*z* calcd for $[C_{13}H_9O_2SCl + H^+]$: 265.01. Found: 265.01.

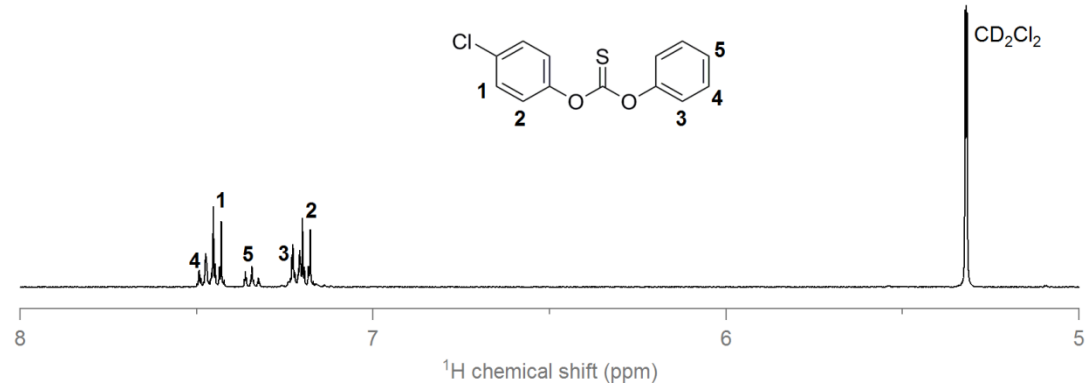

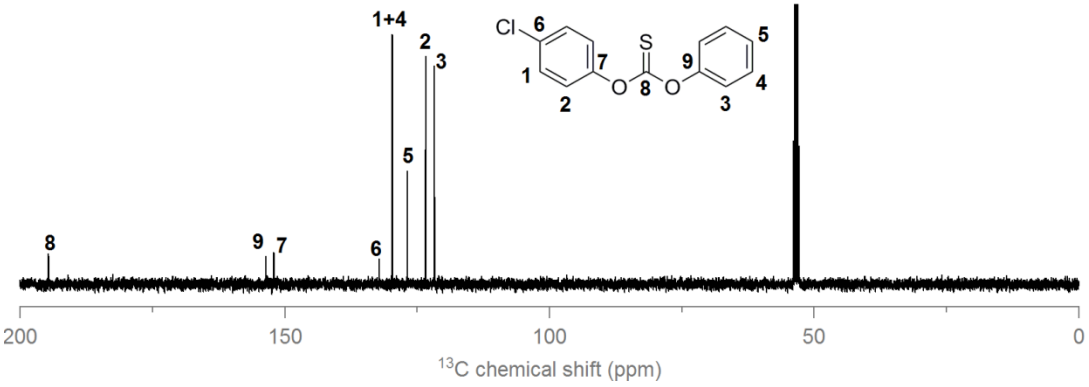

***O*-(2,6-Dimethylphenyl-*O*′-(*p*-tolyl) Thiocarbonate (1j)**

The crude material (1.175 g) was recrystallized from methanol to yield 0.6015 g (44%) of **1j** as white crystals. ^{1}H NMR (400 MHz, CD_2Cl_2): δ = 2.3 (s, 6H), 2.43 (s, 3H), 7.12 (d, 2H), 7.16 (s, 3H), 7.31 (d, 2H). $^{13}C\{^{1}H\}$ (100 MHz, CD_2Cl_2): δ = 15.9, 20.7, 121.3, 126.5, 128.8, 130.1, 130.2, 136.8, 150.8, 151.6, 193.3. Anal. Calcd for $C_{16}H_{16}O_2S$: C, 70.56; H, 5.92. Found: C, 70.24; H, 5.71. MS (ASAP) *m*/*z* calcd for [$C_{16}H_{16}O_2S + H^+$]: 273.09. Found: 273.09.

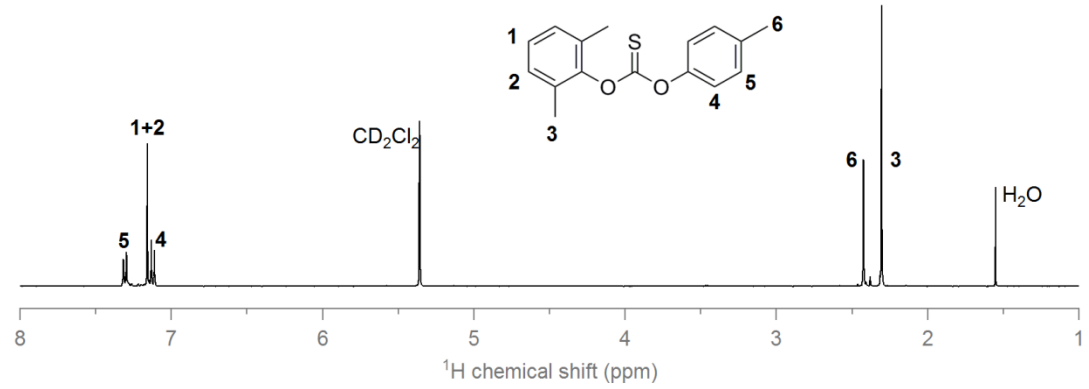

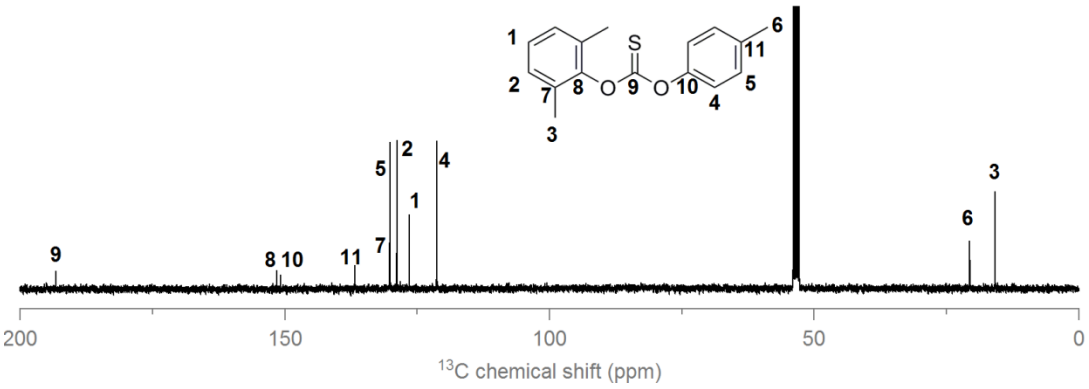

***O*-(*p*-Tolyl)-*N*-*p*-tolyl Thiocarbamate (2)**

The crude material (1.27 g) of a white powder was collected and recrystallized from acetonitrile to yield 0.921 g (71%) of **2** as a white powder. ^{1}H NMR (400 MHz, 273 K, CD_2Cl_2): δ = 2.36 + 2.39 + 2.40 (s, 6H), 7.00−7.07 (m, 2H), 7.18− 7.34 (m, 5H), 7.54 (d, 1H), 8.47 + 8.83 (s, 1H). ^{13}C{^{1}H} (100 MHz, 273 K, CD_2Cl_2): δ = 20.7, 20.8, 122.05, 122.08, 122.60, 123.67, 129.46, 129.74, 129.80, 129.83, 134.34, 134.90, 136.02, 136.13, 136.55, 150.67, 151.40, 188.00, 188.12. Anal. Calcd for $C_{15}H_{15}ONS$: C, 70.01; H, 5.87; N, 5.44. Found: C, 69.71; H, 5.79; N, 5.52. MS (ASAP) *m*/*z* calcd for [$C_{15}H_{15}ONS + H^+$]: 258.10. Found: 258.10.

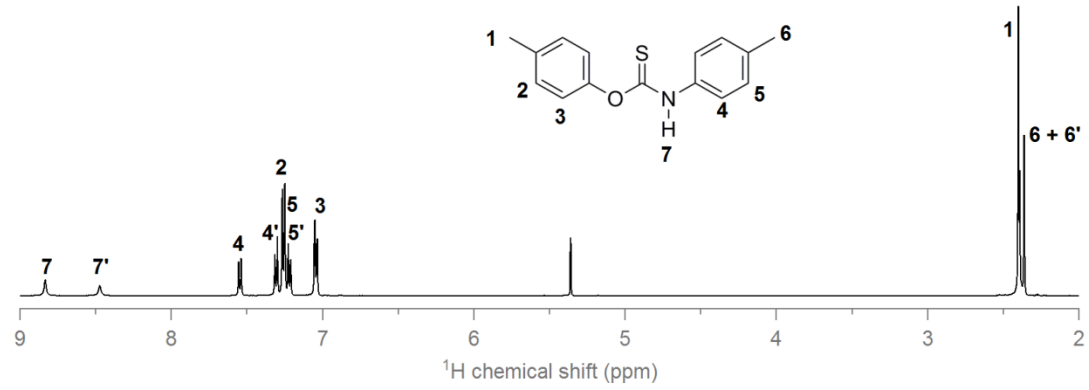

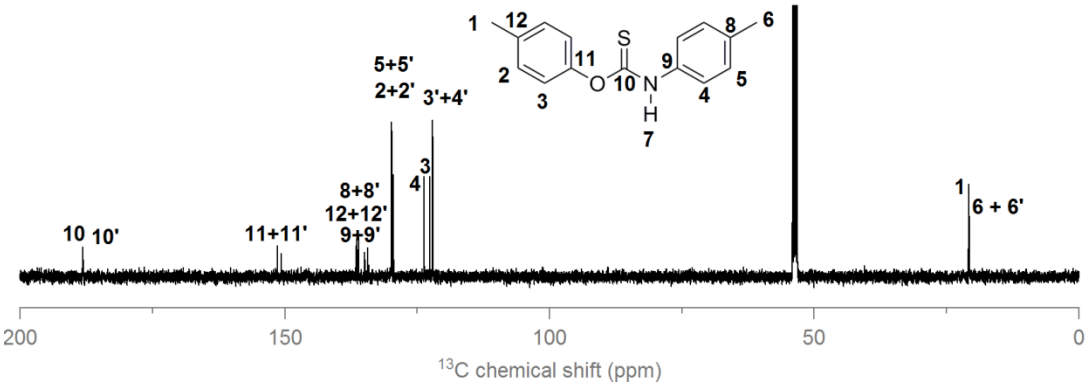

***O*-Phenyl-*N*-methyl(phenyl) Thiocarbamate (3)**

Yield 1.554 g (74%) of **3** as a white powder. ^{1}H NMR (400 MHz, 273 K, CD_2Cl_2): δ = 3.69 + 3.81 (s, 3H), 6.95–7.93 (m, 10H). ^{13}C{^{1}H} (100 MHz, 273 K, CD_2Cl_2): δ = 41, 44.8, 122.72, 123.08, 125.84, 125.99, 126.11, 127.09, 127.8, 127.84, 129.28, 129.3, 129.51, 129.61, 143.58, 146.27, 154, 154.13, 187.78, 189.07. Anal. Calcd for $C_{14}H_{13}ONS$: C, 69.11; H, 5.38; N, 5.76. Found: C, 68.96; H, 5.14; N, 5.72. MS (ASAP) *m*/*z* calcd for [$C_{14}H_{13}ONS + H^+$]: 244.08. Found: 244.08.

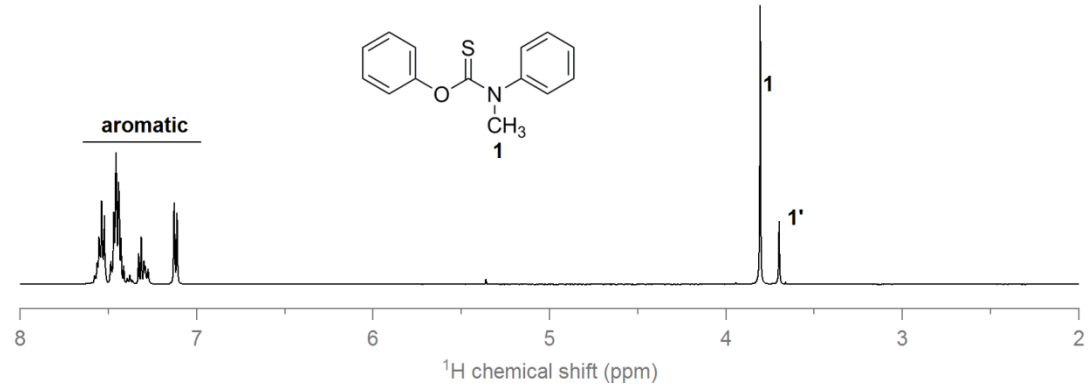

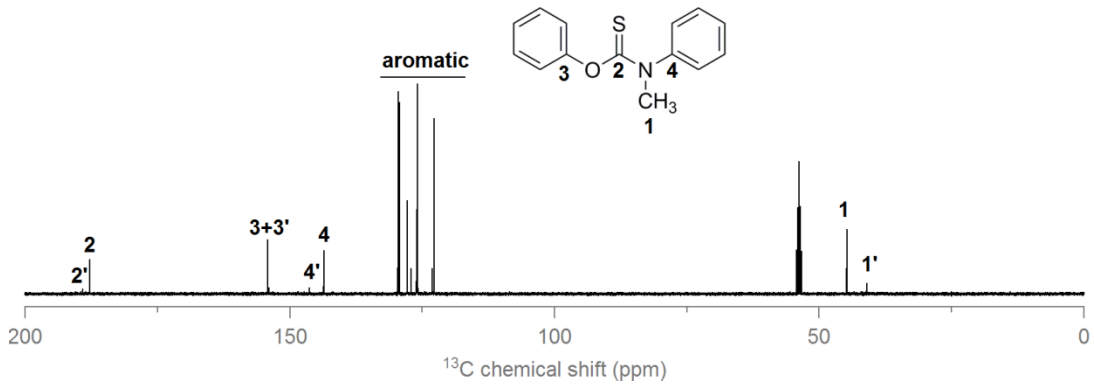

***N*-Methyl-*N,N′*-diphenylthiourea (5b)**

Yield 9.321 g (92%) of **5b** as white crystals. ^{1}H NMR (400 MHz, $CDCl_3$): δ = 3.69 (s, 3H), 6.93 (b, 1H), 7.14–7.23 (m, 1H), 7.28–7.4 (m, 6H), 7.41–7.48 (m, 1H), 7.52–7.58 (m, 2H). ^{13}C{^{1}H} (100 MHz, $CDCl_3$): δ = 43.62, 125.71, 126.04, 127.03, 128.63, 128.86, 130.84, 139.30, 143.02, 181.47. Anal. Calcd for $C_{14}H_{14}N_2S$: C, 69.39; H, 5.82; N, 11.56. Found: C, 68.63; H, 5.26; N, 11.41. MS (ASAP) *m*/*z* calcd for [$C_{14}H_{14}N2S + H^+$]: 243.10. Found: 243.10.

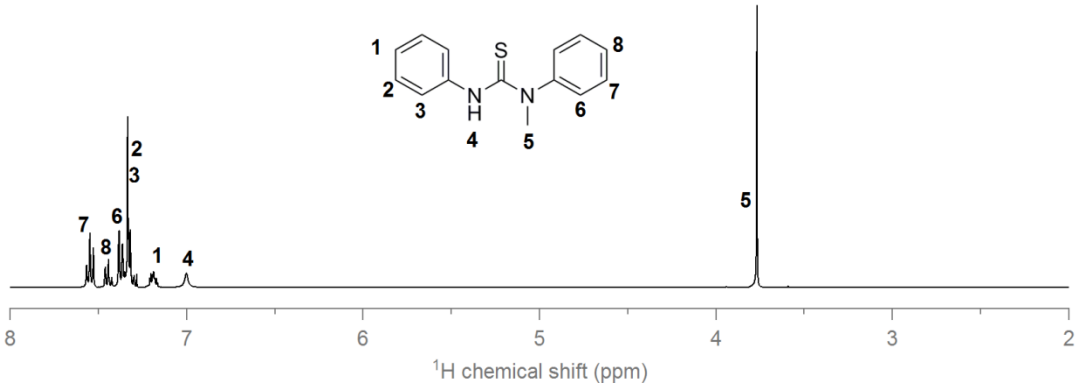

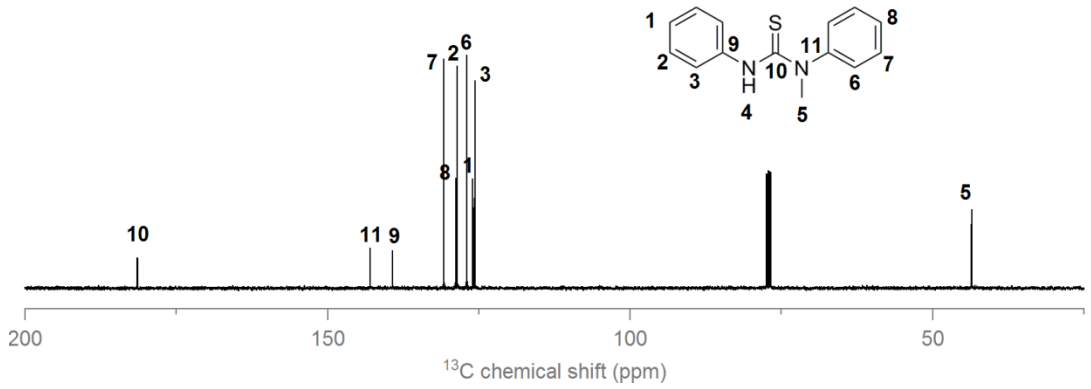

Di(pyrrolidin-1-yl)methanethione (6b)

Yield: 2.76 g (49%) of **6b** as colorless crystals. ^{1}H NMR (400 MHz, $CDCl_3$): δ = 1.94–1.84 (m, 8H), 3.65–3.55 (m, 8H). $^{13}C\{^{1}H\}$ (100 MHz, $CDCl_3$): δ = 25.84, 53.08, 184.98. Anal. Calcd for $C_9H_{16}N_2S$: C, 58.65; H, 8.75; N, 15.20. Found: C, 58.80; H, 8.56; N, 15.16. MS (ASAP) *m*/*z* calcd for [$C_9H_{16}N_2S + H^+$]: 185.11. Found: 185.11.

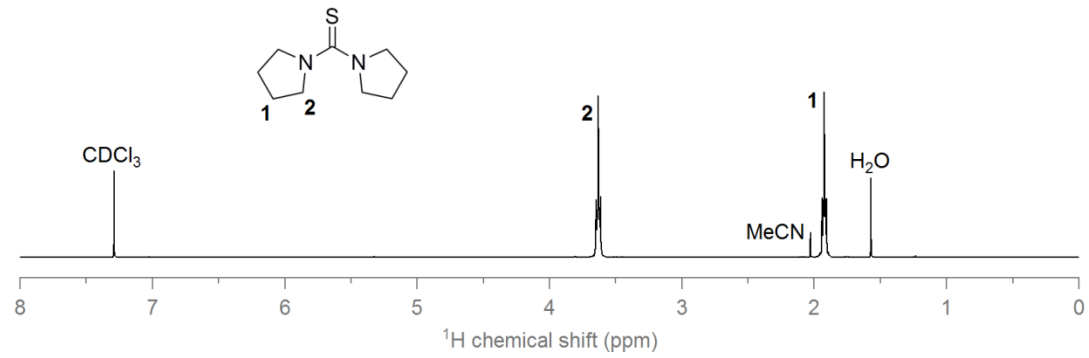

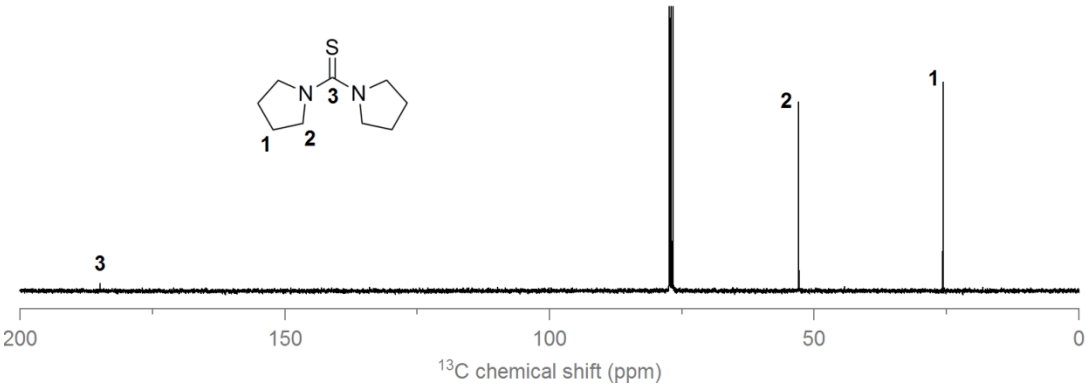

Di-*p*-tolyl Carbonate (8c)

Yield 0.643 g (25%) of **7c** as a white powder. ^{1}H NMR (400 MHz, $CDCl_3$): δ = 2.39 (s, 6H), 7.17 (d, 4H), 7.22 (d, 4H). $^{13}C\{^{1}H\}$ (100 MHz, $CDCl_3$): δ = 20.88, 120.6, 130, 136, 148.89, 152.46. Anal. Calcd for $C_{15}H_{14}O_3$: C, 74.36; H, 5.82. Found: C, 74.54; H, 6.01. MS (ASAP) *m*/*z* calcd for [$C_{15}H_{14}O_3 + H^+$]: 243.10. Found: 243.10.

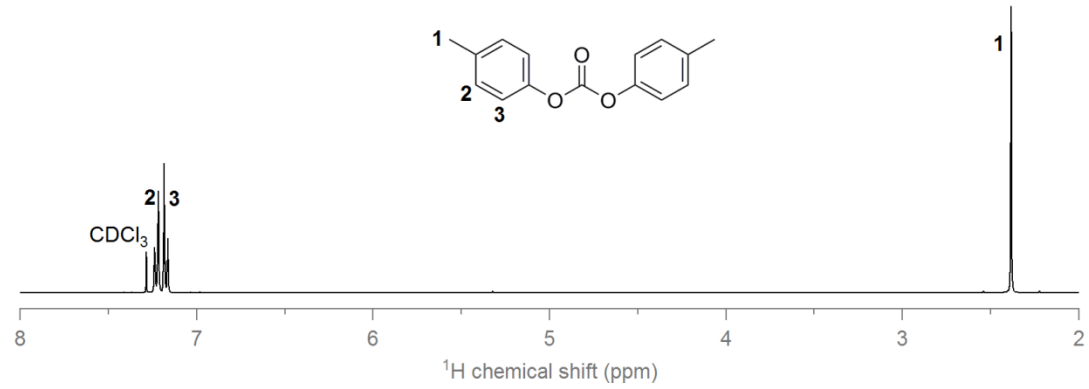

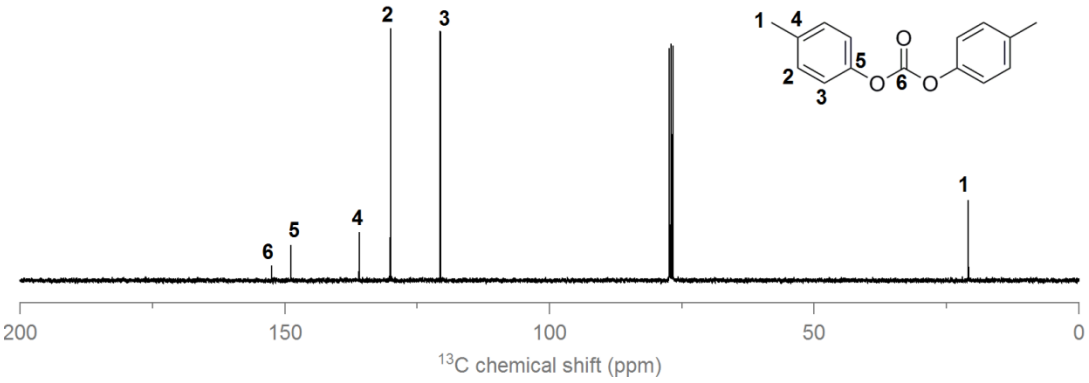

_p_-Tolyl Oleate

Brown oil. Yield 1.44 g (81%). ^{1}H NMR (400 MHz, $CDCl_3$): δ = 0.92 (t, 3H), 1.17−1.51 (m, 20H), 1.78 (quin, 2H), 1.97−2.14 (m, 4H), 2.37 (s, 3H), 2.56 (t, 2H), 5.38 (m, 2H), 6.98 (d, 2H), 7.19 (d, 2H). ^{13}C{^{1}H} (100 MHz, $CDCl_3$): δ = 14.22, 20.88, 22.77, 25.02, 27.23, 27.3, 29.16, 29.24, 29.41, 29.62, 29.76, 29.85, 32, 34.4, 121.1, 129.74, 129.88, 130.04, 135.2, 148.65, 172.37. Anal. Calcd for $C_{25}H_{40}O_2$: C, 80.59; H, 10.82. Found: C, 80.31; H, 10.54. MS (ASAP) *m*/*z* calcd for [$C_{25}H_{40}O_2$ + H^+]: 373.31. Found: 373.31.

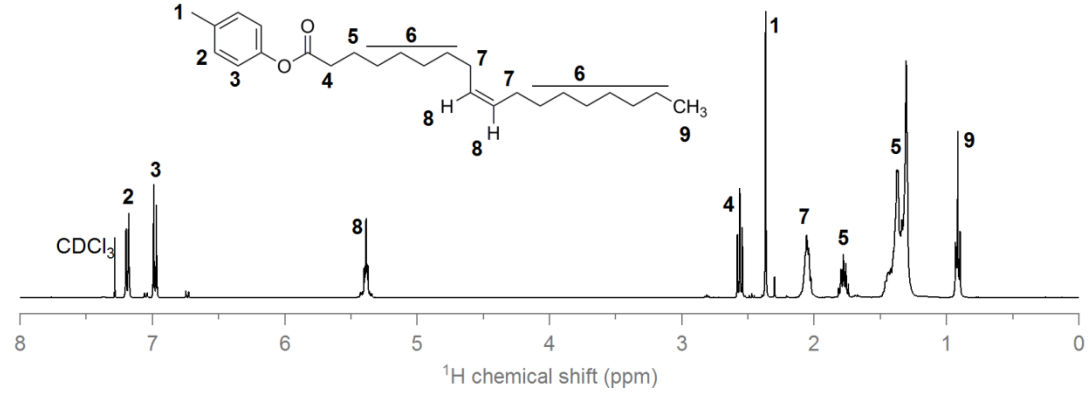

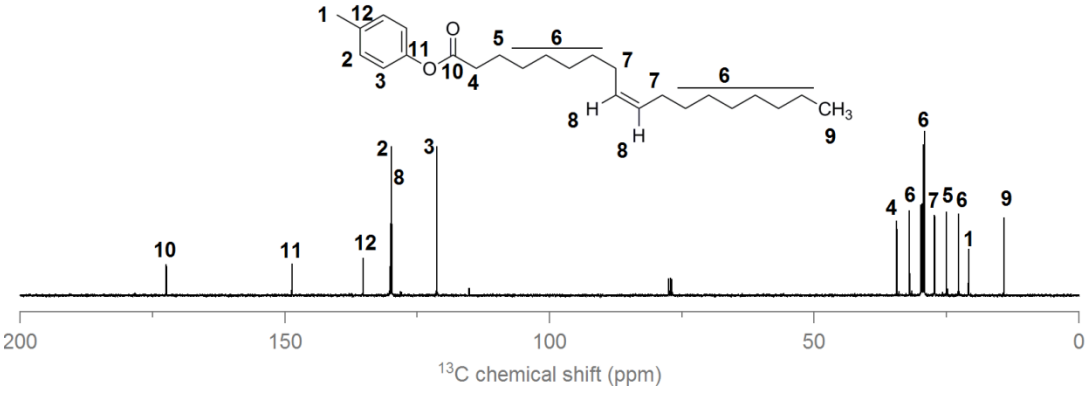

Phenyl Oleate

Brown oil. Yield 1.153 g (67%). ^{1}H NMR (400 MHz, CD_2Cl_2): δ = 0.89 (t, 3H), 1.20–1.49 (m, 20H), 1.74 (quin, 2H), 1.97–2.10 (m, 4H), 2.54 (t, 2H), 5.36 (m, 2H), 7.03–7.09 (m, 2H), 7.19–7.26 (m, 1H), 7.35–7.41 (m, 2H). ^{13}C{^{1}H} (101 MHz, CD_2Cl_2): δ = 14.32, 23.13, 25.32, 27.57, 27.61, 29.49, 29.54, 29.60, 29.76, 29.95, 30.14, 30.22, 32.35, 34.69, 122.10, 126.06, 129.74, 130.13, 130.36, 151.35, 172.67. Anal. Calcd for $C_{24}H_{38}O_2$: C, 80.39; H, 10.68. Found: C, 79.82; H, 11.27. MS (ASAP) *m*/*z* calcd for [$C_{24}H_{38}O_2$ + H^+]: 359.30. Found: 359.29.

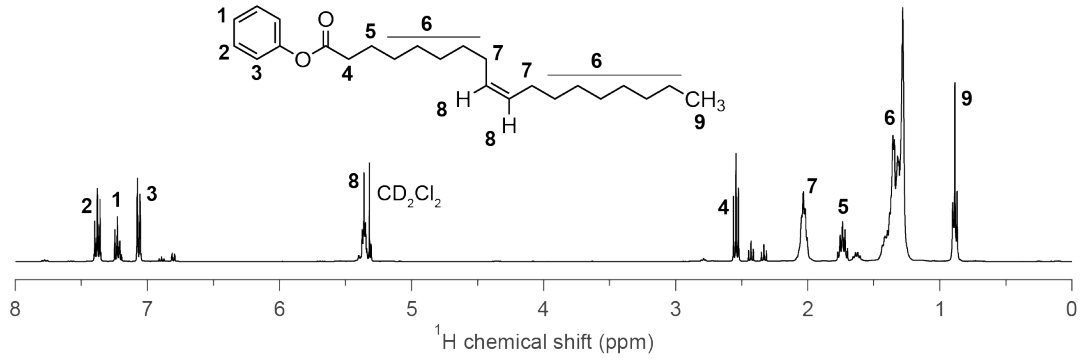

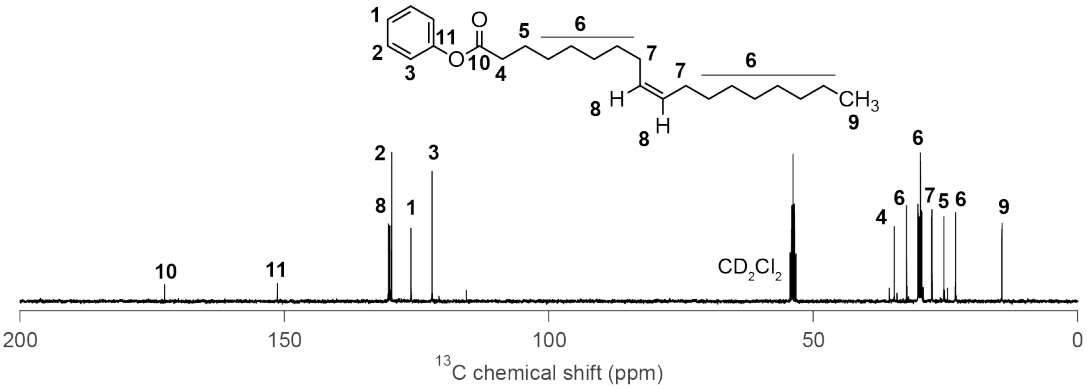

***O,S*-Di(*p*-tolyl) Thiolcarbonate**

White powder. Yield 2.6077 g (51%). ^{1}H NMR (400 MHz, CD_2Cl_2): δ = 2.34 (s, 3H), 2.39 (s, 3H), 7.01−7.07 (m, 2H), 7.16− 7.21 (m, 2H), 7.22−7.28 (m, 2H), 7.45−7.50 (m, 2H). ^{13}C{^{1}H} (100 MHz, CD_2Cl_2): δ = 20.53, 21.02, 120.88, 123.71, 129.93, 130.04, 134.86, 136.15, 140.51, 149.14, 169.14. Anal. Calcd for $C_{15}H_{14}O_2S$: C, 69.74; H, 5.46. Found: C, 69.53; H, 5.18. MS (ASAP) *m/z* calcd for [$C_{15}H_{14}O_2S$ + H^+]: 259.08. Found: 259.08.

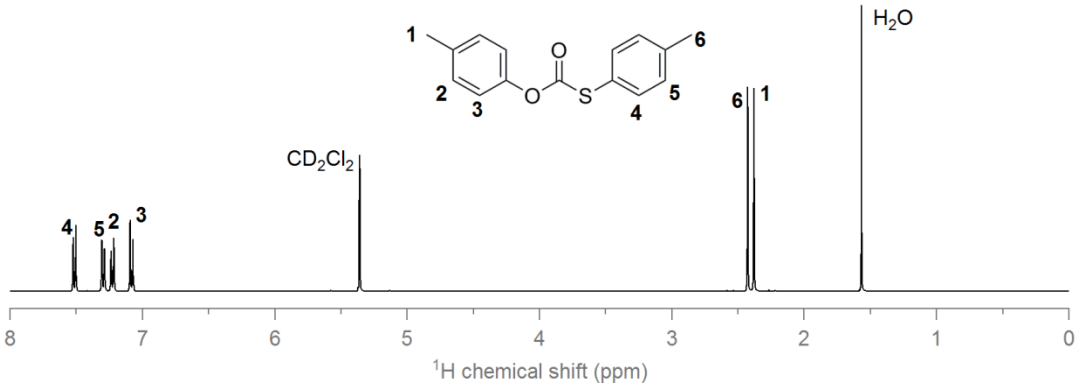

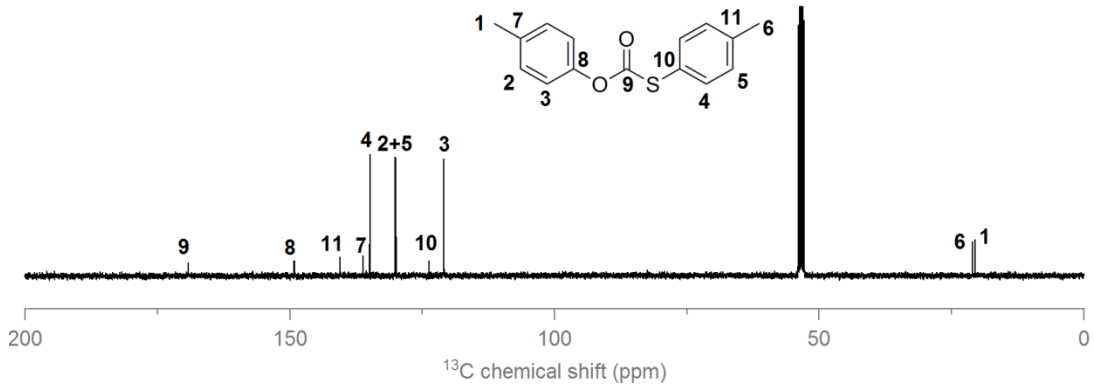

***O,S*-Di(phenyl) Thiolcarbonate**

White crystals. Yield 1.947 g (42%). ^{1}H NMR (400 MHz, CD_2Cl_2): δ = 7.15–7.21 (m, 2H), 7.24– 7.30 (m, 1H), 7.36–7.50 (m, 5H), 7.59–7.65 (m, 2H). $^{13}C\{^{1}H\}$ (101 MHz, CD_2Cl_2): δ = 121.64, 126.68, 127.63, 129.71, 129.93, 130.34, 135.31, 151.72, 169.08. Anal. Calcd for $C_{13}H_{10}O_2S$: C, 67.80; H, 4.38. Found: C, 67.53; H, 4.20. MS (ASAP) *m*/*z* calcd for $[C_{13}H_{10}O_2S + H^+]$: 231.05. Found: 231.05.

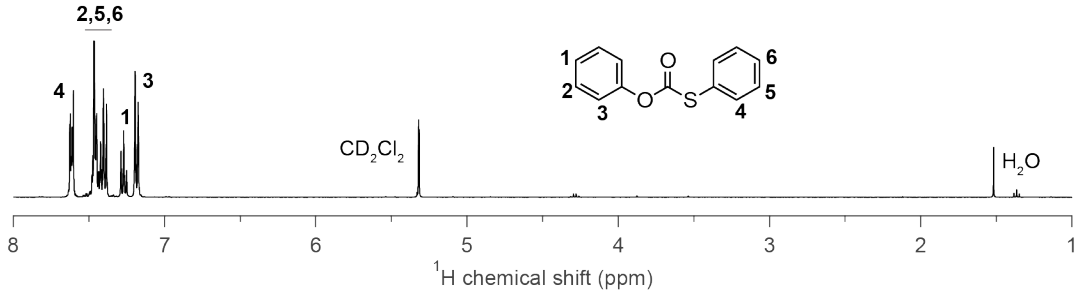

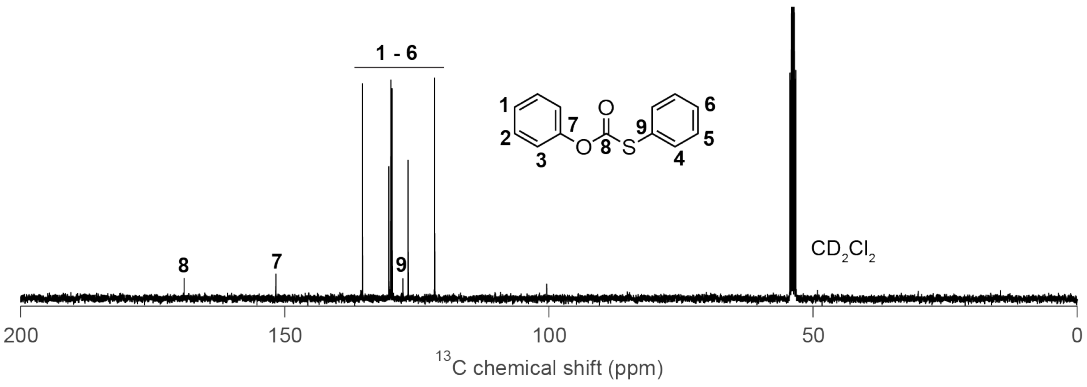

2.8. References

(1) Kamat, P. V., Quantum Dot Solar Cells. Semiconductor Nanocrystals as Light Harvesters. *J. Phys. Chem. C* **2008,** *112* (48), 18737-18753.

(2) Wilker, M. B.; Schnitzenbaumer, K. J.; Dukovic, G., Recent Progress in Photocatalysis Mediated by Colloidal II‐VI Nanocrystals. *Isr. J. Chem.* **2012,** *52* (11‐12), 1002-1015.

(3) Corsini, N. R.; Hine, N. D.; Haynes, P. D.; Molteni, C., Unravelling the Roles of Size, Ligands, and Pressure in the Piezochromic Properties of CdS Nanocrystals. *Nano Lett.* **2017,** *17* (2), 1042-1048.

(4) Talapin, D. V.; Lee, J.-S.; Kovalenko, M. V.; Shevchenko, E. V., Prospects of Colloidal Nanocrystals for Electronic and Optoelectronic Applications. *Chem. Rev.* **2009,** *110* (1), 389-458.

(5) Shirasaki, Y.; Supran, G. J.; Bawendi, M. G.; Bulović, V., Emergence of Colloidal Quantum-Dot Light-Emitting Technologies. *Nat. Photonics* **2013,** *7* (1), 13.

(6) Owen, J. S.; Chan, E. M.; Liu, H.; Alivisatos, A. P., Precursor Conversion Kinetics and the Nucleation of Cadmium Selenide Nanocrystals. *J. Am. Chem. Soc.* **2010,** *132* (51), 18206-18213.

(7) García-Rodríguez, R. l.; Hendricks, M. P.; Cossairt, B. M.; Liu, H.; Owen, J. S., Conversion Reactions of Cadmium Chalcogenide Nanocrystal Precursors. *Chem. Mater.* **2013,** *25* (8), 1233-1249.

(8) Hendricks, M. P.; Campos, M. P.; Cleveland, G. T.; Jen-La Plante, I.; Owen, J. S., A Tunable Library of Substituted Thiourea Precursors to Metal Sulfide Nanocrystals. *Science* **2015,** *348* (6240), 1226-1230.

(9) Campos, M. P.; Hendricks, M. P.; Beecher, A. N.; Walravens, W.; Swain, R. A.; Cleveland, G. T.; Hens, Z.; Sfeir, M. Y.; Owen, J. S., A Library of Selenourea Precursors to PbSe Nanocrystals with Size Distributions Near the Homogenous Limit. *J. Am. Chem. Soc.* **2017,** *139* (6), 2296-2305.

(10) Guo, Y.; Alvarado, S. R.; Barclay, J. D.; Vela, J., Shape-Programmed Nanofabrication: Understanding the Reactivity of Dichalcogenide Precursors. *ACS Nano* **2013,** *7* (4), 3616-3625.

(11) Ruberu, T. P. A.; Albright, H. R.; Callis, B.; Ward, B.; Cisneros, J.; Fan, H.; Vela, J., Molecular Control of the Nanoscale: Effect of Phosphine-Chalcogenide Reactivity on CdS-CdSe Nanocrystal Composition and Morphology. *ACS Nano* **2012,** *6* (6), 5348-5359.

(12) Hens, Z., Economical Routes to Colloidal Nanocrystals. *Science* **2015,** *348* (6240), 1211-1212.

(13) Harris, D. K.; Bawendi, M. G., Improved Precursor Chemistry for the Synthesis of III–V Quantum Dots. *J. Am. Chem. Soc.* **2012,** *134* (50), 20211-20213.
(14) Joung, S.; Yoon, S.; Han, C.-S.; Kim, Y.; Jeong, S., Facile Synthesis of Uniform Large-Sized InP Nanocrystal Quantum Dots Using Tris(*tert*-butyldimethylsilyl) Phosphine. *Nanoscale Res. Lett.* **2012,** *7* (1), 93.
(15) Gary, D. C.; Glassy, B. A.; Cossairt, B. M., Investigation of Indium Phosphide Quantum Dot Nucleation and Growth Utilizing Triarylsilylphosphine Precursors. *Chem. Mater.* **2014,** *26* (4), 1734-1744.
(16) Murray, C. B.; Norris, D. J.; Bawendi, M. G., Synthesis and Characterization of Nearly Monodisperse CdE (E= Sulfur, Selenium, Tellurium) Semiconductor Nanocrystallites. *J. Am. Chem. Soc.* **1993,** *115* (19), 8706-8715.
(17) Peng, Z. A.; Peng, X., Formation of High-Quality CdTe, CdSe, and CdS Nanocrystals Using CdO as Precursor. *J. Am. Chem. Soc.* **2001,** *123* (1), 183-184.
(18) Cao, Y. C.; Wang, J., One-Pot Synthesis of High-Quality Zinc-Blende CdS Nanocrystals. *J. Am. Chem. Soc.* **2004,** *126* (44), 14336-14337.
(19) Ouyang, J.; Kuijper, J.; Brot, S.; Kingston, D.; Wu, X.; Leek, D. M.; Hu, M. Z.; Ripmeester, J. A.; Yu, K., Photoluminescent Colloidal CdS Nanocrystals With High Quality via Noninjection One-Pot Synthesis in 1-Octadecene. *J. Phys. Chem. C* **2009,** *113* (18), 7579-7593.
(20) Schliehe, C.; Juarez, B. H.; Pelletier, M.; Jander, S.; Greshnykh, D.; Nagel, M.; Meyer, A.; Foerster, S.; Kornowski, A.; Klinke, C.; Weller, H., Ultrathin PbS Sheets by Two-Dimensional Oriented Attachment. *Science* **2010,** *329*, 550-553.
(21) Tilluck, W. R.; Morris, A. L.; Gurchiek, J. K.; Evans, A. D.; Van Patten, P. G., Rapid and Facile Syntheiss of High-Quality, Oleate-Capped PbS Nanocrystals. *RSC Adv.* **2016,** *6*, 81780-81788.
(22) Pan, D.; An, L.; Sun, Z.; Hou, W.; Yang, Y.; Yang, Z.; Lu, Y., Synthesis of Cu−In−S Ternary Nanocrystals with Tunable Structure and Composition. *J. Am. Chem. Soc.* **2008,** *130* (17), 5620-5621.
(23) Al-Kazimi, H. R.; Tarbell, D. S.; Plant, D., A Study of the Schönberg Rearrangement of Diaryl Thioncarbonates to Diaryl Thiolcarbonates. *J. Am. Chem. Soc.* **1955,** *77* (9), 2479-2482.
(24) Issleib, K.; Harzfeld, G., Alkali‐Phosphorverbindungen und Ihr Reaktives Verhalten, XXIX. [*N*‐Phenyl‐thiocarbamoyl]‐phosphine. *Chem. Ber.* **1964,** *97* (12), 3430-3435.
(25) Abe, S.; Capek, R. K.; Geyter, B. D.; Hens, Z., Reaction Chemistry/Nanocrystal Property Relations in the Hot Injection Synthesis, the Role of the Solute Solubility. *ACS Nano* **2013,** *7* (2), 943-949.

(26) Anderson, N. C.; Hendricks, M. P.; Choi, J. J.; Owen, J. S., Ligand Exchange and the Stoichiometry of Metal Chalcogenide Nanocrystals: Spectroscopic Observation of Facile Metal-Carboxylate Displacement and Binding. *J. Am. Chem. Soc.* **2013,** *135* (49), 18536-18548.
(27) Fritzinger, B.; Capek, R. K.; Lambert, K.; Martins, J. C.; Hens, Z., Utilizing Self-Exchange to Address the Binding of Carboxylic Acid Ligands to CdSe Quantum Dots. *J. Am. Chem. Soc.* **2010,** *132* (29), 10195-10201.
(28) Gomes, R.; Hassinen, A.; Szczygiel, A.; Zhao, Q.; Vantomme, A.; Martins, J. C.; Hens, Z., Binding of Phosphonic Acids to CdSe Quantum Dots: a Solution NMR Study. *J. Phys. Chem. Lett.* **2011,** *2* (3), 145-152.
(29) Owen, J. S.; Park, J.; Trudeau, P.; Alivisatos, A. P., Reaction Chemistry and Ligand Exchange at Cadmium−Selenide Nanocrystal Surfaces. *J. Am. Chem. Soc.* **2008,** *130* (37), 12279-12281.
(30) Boles, M. A.; Ling, D.; Hyeon, T.; Talapin, D. V., The Surface Science of Nanocrystals. *Nat. Mater.* **2016,** *15* (2), 141.
(31) Luther, J. M.; Pietryga, J. M., Stoichiometry Control in Quantum Dots: A Viable Analog to Impurity Doping of Bulk Materials. *ACS Nano* **2013,** *7* (3), 1845-1849.
(32) Morris-Cohen, A. J.; Frederick, M. T.; Lilly, G. D.; McArthur, E. A.; Weiss, E. A., Organic Surfactant-Controlled Composition of the Surfaces of CdSe Quantum Dots. *J. Phys. Chem. Lett.* **2010,** *1* (7), 1078-1081.
(33) Smith, D. K.; Luther, J. M.; Semonin, O. E.; Nozik, A. J.; Beard, M. C., Tuning the Synthesis of Ternary Lead Chalcogenide Quantum Dots by Balancing Precursor Reactivity. *ACS Nano* **2010,** *5* (1), 183-190.
(34) Moreels, I.; Lambert, K.; De Muynck, D.; Vanhaecke, F.; Poelman, D.; Martins, J. C.; Allan, G.; Hens, Z., Composition and Size-Dependent Extinction Coefficient of Colloidal PbSe Quantum Dots. *Chem. Mater.* **2007,** *19* (25), 6101-6106.
(35) Hughes, B. K.; Ruddy, D. A.; Blackburn, J. L.; Smith, D. K.; Bergren, M. R.; Nozik, A. J.; Johnson, J. C.; Beard, M. C., Control of PbSe Quantum Dot Surface Chemistry and Photophysics Using an Alkylselenide Ligand. *ACS Nano* **2012,** *6* (6), 5498-5506.
(36) Dai, Q.; Wang, Y.; Li, X.; Zhang, Y.; Pellegrino, D. J.; Zhao, M.; Zou, B.; Seo, J.; Wang, Y.; Yu, W. W., Size-Dependent Composition and Molar Extinction Coefficient of PbSe Semiconductor Nanocrystals. *ACS Nano* **2009,** *3* (6), 1518-1524.
(37) Gooßen, L.; Döhring, A., Lewis Acids as Highly Efficient Catalysts for the Decarboxylative Esterification of Carboxylic Acids With Dialkyl Dicarbonates. *Adv. Synth. Catal.* **2003,** *345* (8), 943-947.

(38) Yu, W. W.; Qu, L.; Guo, W.; Peng, X., Experimental Determination of the Extinction Coefficient of CdTe, CdSe, and CdS Nanocrystals. *Chem. Mater.* **2003,** *15* (14), 2854-2860.

(39) Jasieniak, J.; Smith, L.; Van Embden, J.; Mulvaney, P.; Califano, M., Re-Examination of the Size-Dependent Absorption Properties of CdSe Quantum Dots. *J. Phys. Chem. C* **2009,** *113* (45), 19468-19474.

(40) Groß, O. A.; Lauk, S.; Müller, C.; Gidt, W.; Sun, Y.; Demeshko, S.; Meyer, F.; Sitzmann, H., Iron (II) High‐Spin and Low‐Spin Complexes from Pentaisopropylcyclopentadienyliron (II) Bis (trimethylsilyl) amide. *Eur. J. Inorg. Chem.* **2017,** *2017* (30), 3635-3643.

(41) Liu, H.; Owen, J. S.; Alivisatos, A. P., Mechanistic Study of Precursor Evolution in Colloidal Group II-VI Semiconductor Nanocrystal Synthesis. *J. Am. Chem. Soc.* **2007,** *129* (2), 305-312.

(42) García-Rodríguez, R. l.; Liu, H., Mechanistic Study of the Synthesis of CdSe Nanocrystals: Release of Selenium. *J. Am. Chem. Soc.* **2012,** *134* (3), 1400-1403.

(43) Sugimoto, T.; Shiba, F.; Sekiguchi, T.; Itoh, H., Spontaneous Nucleation of Monodisperse Silver Halide Particles from Homogeneous Gelatin Solution I: Silver Chloride. *Colloids Surf. A* **2000,** *164* (2-3), 183-203.

(44) Sugimoto, T.; Shiba, F., Spontaneous Nucleation of Monodisperse Silver Halide Particles from Homogeneous Gelatin Solution II: Silver Bromide. *Colloids Surf. A* **2000,** *164* (2-3), 205-215.

(45) Abe, S.; Cabek, R. K.; De Geyter, B.; Hens, Z., Tuning the Postfocused Size of Colloidal Nanocrystals by the Reaction Rate: From Theory to Application. *ACS Nano* **2012,** *6* (1), 42-53.

(46) Zonta, C.; De Lucchi, O.; Volpicelli, R.; Cotarca, L., Thione–Thiol Rearrangement: Miyazaki–Newman–Kwart Rearrangement and Others. In *Sulfur-Mediated Rearrangements II*, Schaumann, E., Ed. Springer Berlin Heidelberg: Berlin, Heidelberg, 2007; pp 131-161.

(47) Schönberg, A.; Varga, L., Über die (Thermische) Umlagerung von Thion-Kohlensäure-Estern in Thiol-Kohlensäure-Ester. (16. Mitteil. über Organische Schwefelverbindungen.). *Ber. Dtsch. Chem. Ges. B* **1930,** *63*, 178-180.

(48) Newman, M. S.; Karnes, H. A., The Conversion of Phenols to Thiophenols via Dialkylthiocarbamates. *J. Org. Chem.* **1966,** *31* (12), 3980-3984.

(49) Kwart, H.; Evans, E. R., The Vapor Phase Rearrangement of Thioncarbonates and Thioncarbamates. *J. Org. Chem.* **1966,** *31* (2), 410-413.

(50) Weidman, M. C.; Beck, M. E.; Hoffman, R. S.; Prins, F.; Tisdale, W. A., Monodisperse, Air-Stable PbS Nanocrystals via Precursor Stoichiometry Control. *ACS Nano* **2014,** *8* (6), 6363-6371.

(51) Cui, J.; Beyler, A. P.; Marshall, L. F.; Chen, O.; Harris, D. K.; Wanger, D. D.; Brokmann, X.; Bawendi, M. G., Direct Probe of Spectral Inhomogeneity Reveals Synthetic Tunability of Single-Nanocrystal Spectral Linewidths. *Nature chemistry* **2013,** *5* (7), 602.

(52) Chen, O.; Zhao, J.; Chauhan, V. P.; Cui, J.; Wong, C.; Harris, D. K.; Wei, H.; Han, H.; Fukumura, D.; Jain, R. K.; Bawendi, M. G., Compact High-Quality CdSe-CdS Core-Shell Nanocrystals with Narrow Emission Linewidths and Suppressed Blinking. *Nat. Mater.* **2013,** *12*, 445-451.

(53) Cui, J.; Beyler, A. P.; Coropceanu, I.; Cleary, L.; Avila, T. R.; Chen, Y.; Cordero, J. M.; Heathcote, S. L.; Harris, D. K.; Chen, O., Evolution of the Single-Nanocrystal Photoluminescence Linewidth With Size and Shell: Implications for Exciton–Phonon Coupling and the Optimization of Spectral Linewidths. *Nano Lett.* **2015,** *16* (1), 289-296.

(54) Busby, E.; Anderson, N. C.; Owen, J. S.; Sfeir, M. Y., Effect of Surface Stoichiometry on Blinking and Hole Trapping Dynamics in CdSe Nanocrystals. *J. Phys. Chem. C* **2015,** *119* (49), 27797-27803.

(55) Bozyigit, D.; Yazdani, N.; Yarema, M.; Yarema, O.; Lin, W. M. M.; Volk, S.; Vuttivorakulchai, K.; Luisier, M.; Juranyi, F.; Wood, V., Soft Surfaces of Nanomaterials Enable Strong Phonon Interactions. *Nature* **2016,** *531* (7596), 618.

(56) Owen, J.; Brus, L., Chemical Synthesis and Luminescence Applications of Colloidal Semiconductor Quantum Dots. *J. Am. Chem. Soc.* **2017,** *139* (32), 10939-10943.

(57) Chen, O.; Chen, X.; Yang, Y.; Lynch, J.; Wu, H.; Zhuang, J.; Cao, Y. C., Synthesis of Metal-Selenide Nanocrystals Using Selenium Dioxide as the Selenium Precursor. *Angew. Chem. Int. Ed.* **2008,** *47* (45), 8638-8641.

(58) Millan, D. S.; Prager, R. H., The Dealkylation of Tertiary Aliphatic Amines With Phenyl Chlorothionoformate. *Tetrahedron Lett.* **1998,** *39* (24), 4387-4390.

(59) Rahmathullah, S. M.; Hall, J. E.; Bender, B. C.; McCurdy, D. R.; Tidwell, R. R.; Boykin, D. W., Prodrugs for Amidines: Synthesis and Anti-*Pneumocystis carinii* Activity of Carbamates of 2,5-Bis(4-amidinophenyl)furan. *J. Med. Chem.* **1999,** *42* (19), 3994-4000.

(60) Creighton, A.; Owen, L.; White, G., 461. Cytotoxic compounds. Part III. Some derivatives of *p*-(*N,N*-Di-2-chloroethyl-and of *p*-(*N,N*-Di-2-bromoethyl-amino)thiophenol. *J. Chem. Soc.* **1961**, 2375-2381.

CHAPTER 3. Precursor Reaction Kinetics Control Compositional Grading in $CdSe_{1-x}S_x$ Nanocrystal Heterostructures

Table of Contents

Reproduced in part from:

Hamachi, L. S.; Jen-La Plante, I.; Yang, H.; Qian, K.; Campos, M. P.; Cleveland, G. T.; De Roo, J.; Lenz, O.; Rreza, I.; Walravens, W.; Chan, E. M.; Hens, Z.; Owen, J. S. *Manuscript in Preparation*.

3.1. Abstract

3.1.1. Technical Abstract

We report a method to control the composition and microstructure of ternary $CdSe_{1-x}S_x$ nanocrystals by the simultaneous injection of sulfide and selenide precursors in a one pot synthesis. Kinetics simulations predict that precursors with a relative reactivity difference less than 10x can provide alloyed compositions, while precursors with larger reactivity differences will lead to abrupt interfaces. Substituted thio- and selenourea precursors with conversion reaction rate constants spanning 2.0×10^{-1} s^{-1} and 1.3×10^{-5} s^{-1} could be used to adjust the grading as was verified with UV-visible absorption spectroscopy and STEM-EDX elemental mapping. The faster reacting precursor dictates the number of nuclei and the final nanocrystal size at full conversion. This method provides luminescent CdSe/CdS core-shell architectures (λ= 514 to 622 nm, PLQY = 60 to 75%) in one step. Slow addition of tetramethylthiourea and cadmium oleate provides gram quantities of thick shell, brightly emissive structures with photoluminescence quantum yields between 67 and 81% when a spherical quantum well architecture (CdS/CdSe/CdS) was used. This approach provides unprecedented ability to produce highly emissive quantum dots spanning the visible (λ = 543 to 611 nm) using a one pot method.

3.1.2. Plain English Abstract

Core/shell nanocrystals composed of two distinct semiconductor materials possess brighter emissive properties than single component nanocrystals based on the alignment of their bandgaps. This architecture is used in commercial applications including fluorescent lightbulbs, television displays, and biological imaging. In this section, we introduce new classes of cyclic sulfur and selenium containing compounds as precursors for CdS and CdSe nanocrystal synthesis. As in Chapter 2, each sulfur and selenium precursor's substitution pattern and structure influences the rate of nanocrystal formation, which in turn influences the number and size of the nanocrystals produced. Here, we utilize our control of sulfur and selenium precursor reaction rates towards 1) designing easier and more reproducible core/shell nanoparticle syntheses and 2) studying inherent differences in CdS and CdSe nucleation and growth processes, uniquely enabled by our expansive precursor library.

3.2. Context

Precursor reactivity is an important tool for synthesizing precisely defined architectures by design. A well-documented relationship between the precursor conversion reactivity and the number of nanocrystals nucleated during a reaction has appeared in CdS, CdSe, PbS, and PbSe syntheses.[1-7] Libraries of precursors have been developed that provide control over the number of nanocrystals and a

mechanism to adjust the size following quantitative conversion.[5-7] This is preferable over other size tuning methods such as early reaction termination, surfactant mixture adjustment, temperature changes, and additive introduction because these all impact the final material's surface chemistry and crystallinity, and therefore final properties of interest.[8-14]

3.2.1. Three Approaches to Nanocrystal Heterostructures

Nanocrystal heterostructures, including CdSe/CdS, are among the most desirable luminescent downconverters for solid-state lighting, electronic displays, and biological imaging applications.[15-19] Compositional control of these structures is essential to achieving particular emission wavelengths, photoluminescence quantum yields (PLQYs), and exciton and multi-exciton recombination.[20-28] Presently, these heterostructures are synthesized by (1) layer-by-layer, (2) seeded growth, and (3) precursor mixtures.

Layer-by-layer methods include successive ion layer adsorption and reaction (SILAR)[24, 29] and slow precursor injections via syringe pump,[20, 25, 28] which avoid nucleation of shell precursors via either precise half monolayer precursor additions or the use of less reactive precursors at high temperatures.[20, 22, 30-31] This is not ideal; the changing precursor injection volumes in SILAR are tedious to set up, and the high temperatures (300 °C to 310 °C) used in syringe pump methods lead to undesirable $Cd(O_2CR)_2$ decomposition to CdO, Cd^0, and $CdCO_3$.[32]

Nonetheless, layer-by-layer syntheses are highly effective and have been optimized to avoid the nucleation of new nanocrystals with engineering or process controls. However, both of these methods face challenges in process reproducibility as well as practicality, especially for the growth of large shells, which are known to lead to high PLQYs.

Seeded growth reactions occur via a traditional hot injection synthesis in the presence of pre-existing nanocrystal cores. Historically, this type of reaction has been used to grow anisotropic structures such as CdSe/CdS seeded rods, tetrapods, and octapods,[33-37] although more recently the "flash" synthesis out of the Hens group has extended it towards isotropic particle growth as well.[38-39] In seeded growth reactions, the shell growth rate does not depend on the composition of the nanocrystal seed, suggesting that this process is dominated by the reactivity of new solute being produced.[40] The key to these reactions lies in balancing solute supply and solubility to disfavor homogeneous nucleation of shell precursors and favor heterogeneous growth of the shell material.

Mixed precursor syntheses proceed via a single injection of mixtures of both sulfide and selenide precursors possessing different conversion rates and rely on chemical kinetics to form heterostructures. These methods use phosphine chalcogenides,[23, 41] *bis*(trimethylsilyl)chalcogenides and elemental chalcogen precursors[42-44] to prepare $CdS_{1-x}Se_x$ graded nanorods[45] as well as $CdSe_{1-x}S_x$,[46] $CdTe_{1-}$

$_xS_x$,[47] $CdTe_{1-x}Se_x$,[48-49] $PbSe_{1-x}S_x$, $PbTe_{1-x}S_x$, and $PbTe_{1-x}Se_x$ nanoparticles.[50] Often the relative reactivity of these precursor mixtures is not well defined and it is unclear how the relative conversion of the two precursors influences the nanostructure. In theory, these mixed precursor syntheses possess immense potential to leverage chemical control over reproducibly accessing heterostructures with fine-tuned compositional changes. To expand on these efforts, there is great opportunity in developing reactions utilizing (1) rate-tunable chalcogenide precursors with appropriate conversion rates, and (2) consistent crystallization conditions and surfactant mixtures.

3.2.2. Characterization Challenges in Ternary Nanocrystals

Post-synthesis, the atomic composition of ternary quantum dots is challenging to determine with high spatial resolution. STEM-EDX and HAADF STEM profiles work well for post-synthetic characterization of elemental distributions in large ($d \geq 30$ nm) particles,[25, 51-52] but elemental mapping of small particles is much more challenging. Powder X-ray diffraction,[53] Raman spectroscopy, X-ray fluorescence, X-ray photoelectron spectroscopy (XPS), photoemission spectroscopy, energy dispersive X-ray spectroscopy (EDX), Rutherford backscattering, and solid-state ^{113}Cd and ^{77}Se NMR spectroscopy, have all been used to analyze compositional gradients.[27, 42-43, 54-55] A single injection of

mixed precursors often produces gradient structures based on elemental analysis.[56-57]

Grading the interface between CdSe and CdS is thought to reduce the rate of Auger recombination, a property of great importance to quantum dot lasers and down converting materials for solid state lighting. Large graded compositions can reduce electron-electron interactions and weaken the coupling of the biexcitons to the high energy hot excitonic states.[58] Recent theoretical and experimental studies debate whether graded alloy structures minimize Auger recombination in quantum dots.[25, 28, 58-60] We believe that a more defined means to access interface grading—such as via kinetic control of precursor conversion—is required to settle this debate.

Controlled precursor reactivity presents the opportunity to finely grade the interfaces of CdSe/CdS heterostructures in a single synthetic step. The tunable solute supply provided by recently reported chalcogenourea and carbonate precursors spans several orders of magnitude in reactivity. Leveraging this precursor library could enable systematic structural changes such as introducing graded interfacial regions or altering the precise ratio of sulfur and selenium in the nanocrystal core. This new methodology affords an unprecedented level of control over nanocrystal heterostructure synthesis and will enable synthetic access to the next generation of nanocrystals for use in LEDs and displays.

3.3. Precursor Synthesis

3.3.1. Chalcogenourea Precursor Synthesis

To access reaction temperatures where CdSe nanocrystals can be prepared, we synthesized *N*-monosubstituted and *N,N′*-disubstituted imidazolidine (SI) and pyrimidine (Pym) thiones and selones and studied their reaction with cadmium oleate at 240 ˚C (Figure 3.3.1 and Table 3.3.1). Our naming scheme for these compounds draws inspiration from the cyclic selenourea literature.[61-62]

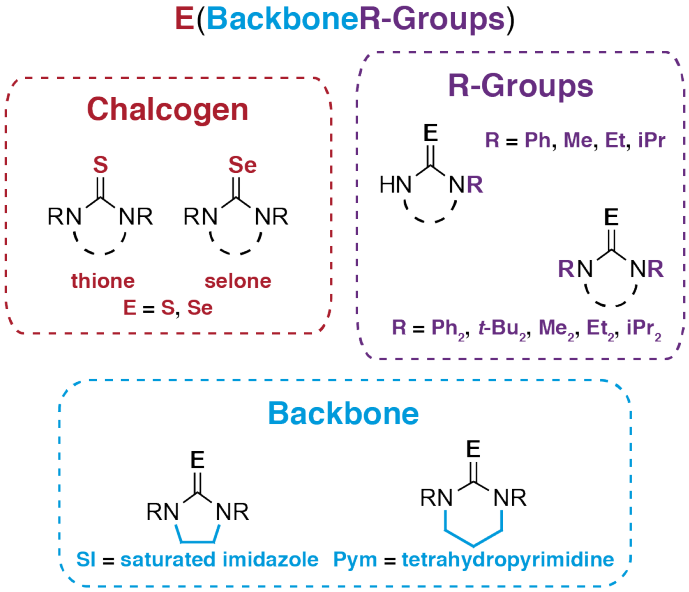

Figure 3.3.1. Compound nomenclature for cyclic thione and selone compounds.

N-substituted cyclic selones are prepared in moderate to good yields in a single step by refluxing diamines with triethyl orthoformate and elemental selenium.[63] *N*-substituted cyclic thiones can be synthesized from carbon disulfide

or thiophosgene and substituted diamines,[64-66] however due to the flammability and toxicity of these reagents, cyclic thiones were synthesized from thiocarbonyldiimidazole.[66-67] The majority of cyclic thiones and selones are readily prepared in this way, with the *tert*-butyl and tetrahydropyrimidine derivatives as notable exceptions, reacting to low yields. We hypothesize that difficulties with the di-*tert*-butyl substituted selone and thione arise from steric crowding that inhibits the cyclization process. Additionally, reactions with propanediamines are conducted under dilute conditions to prevent oligomerization, which is known to compete with the cyclization step.[65]

Table 3.3.1. Synthesis of a library of N-monosubstituted and N,N'-disubstituted cyclic thiones and selenones. Recrystallized compound yields are reported.

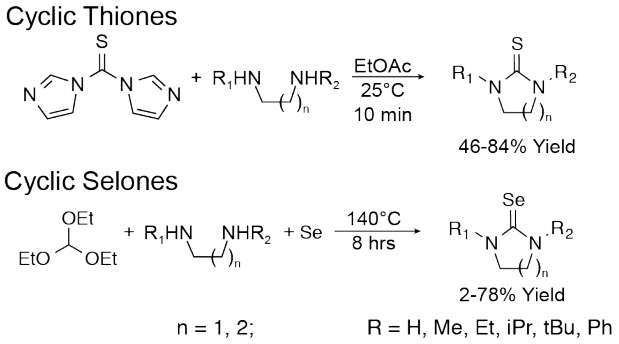

Compound	E	R_2	R_2	Yield (%)
S(SIPh)	S	H	Ph	84
S(SIMe)	S	H	Me	71
S(SIEt)	S	H	Et	73
S(SIiPr)	S	H	iPr	74

S(SIPh$_2$)	S	Ph	Ph	78
S(SIMe$_2$)	S	Me	Me	60
S(SIEt$_2$)	S	Et	Et	59
S(SIiPr$_2$)	S	iPr	iPr	66
S(PymMe)	S	H	Me	54
S(PymiPr)	S	H	iPr	46
S(PymMe$_2$)	S	Me	Me	72
S(PymEt$_2$)	S	Et	Et	74
S(PymiPr$_2$)	S	iPr	iPr	76
Se(SIPh)	Se	H	Ph	25
Se(SIEt)	Se	H	Et	38
Se(SIiPr)	Se	H	iPr	21
Se(SIPh$_2$)	Se	Ph	Ph	44
Se(SI*t*-Bu$_2$)	Se	*t*-Bu	*t*-Bu	3
Se(SIMe$_2$)	Se	Me	Me	50
Se(SIEt$_2$)	Se	Et	Et	77
Se(SIiPr$_2$)	Se	iPr	iPr	56
Se(PymMe)	Se	H	Me	11
Se(PymMe$_2$)	Se	Me	Me	8
Se(PymEt$_2$)	Se	Et	Et	2
Se(PymiPr$_2$)	Se	iPr	iPr	3

3.3.2. Cadmium Oleate Synthesis

In order to standardize our nanoparticle reactions and eliminate the production of water or acetic acid generated by *in situ* cadmium carboxylate synthesis,[32] we synthesize cadmium oleate on 50 g scales from the reaction of cadmium trifluoroacetate with triethylammonium oleate (Section 3.10.4). After

isolating cadmium oleate as a white powder it can be pumped into a glove box and stored airfree. Benefits of this method include standardization of the chemical composition of the starting metal oleate and easy reaction setup. The shelf stable cadmium oleate enabled us to perform high throughput reaction condition screenings at WANDA in order to perform kinetics experiments and one-pot core/shell reactions described in Chapter 5.

3.4. CdS and CdSe Nanoparticle Synthesis

Cyclic thiones and selones react with cadmium oleate at 240 °C producing CdSe and CdS nanocrystals over the course of minutes to hours depending on their substituents (Figure 3.4.1). Reaction kinetics are monitored by quantitative aliquoting of the reaction mixture. The disappearance of the precursors and the formation of corresponding urea and carboxylic anhydride coproducts are followed using ^{1}H NMR spectroscopy.[4-7] Nanocrystal formation is monitored with UV-visible absorption spectroscopy. Extinction coefficients for CdSe[68] and CdS[7] are known that allow the yield of semiconductor to be compared with the disappearance of the starting material.

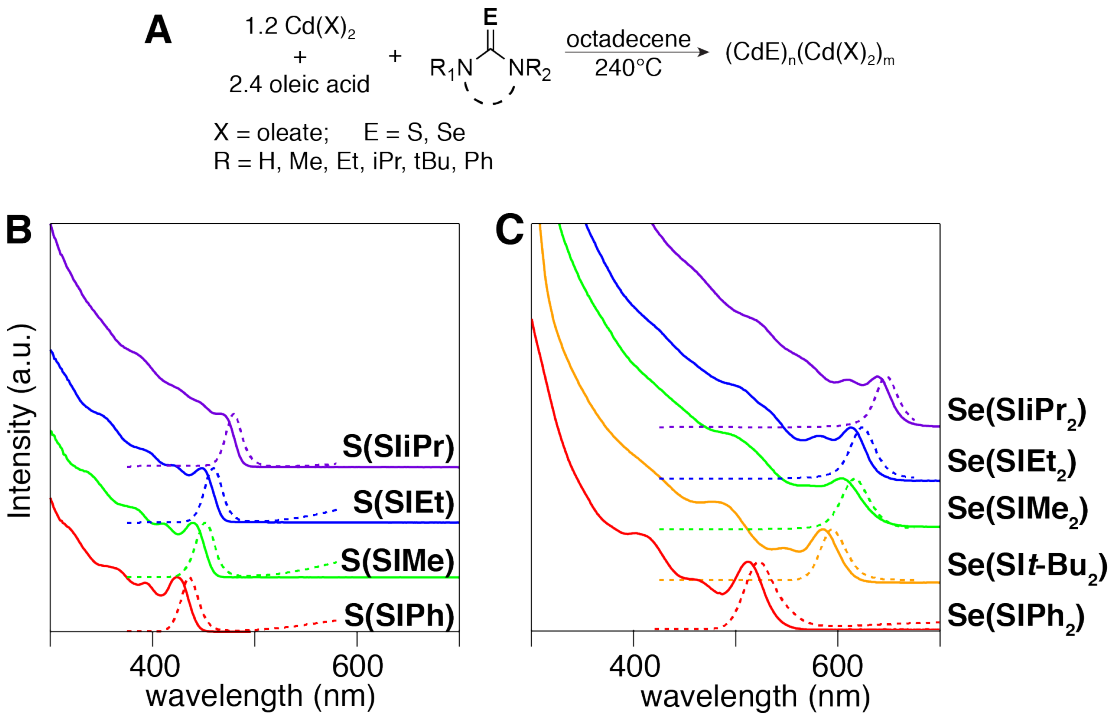

Figure 3.4.1. A) Standard reaction scheme for the substituted cyclic thiones and selones used in this study. Final absorption and fluorescence spectra from reactions with several cyclic thiones and selones to produce B) CdS nanocrystals and C) CdSe nanocrystals.

Among the classes of new precursors, some cyclic thiones proved relatively unreactive and produce few nanocrystals that quickly reach a size that precipitated from the reaction solution. In those cases, the conversion was monitored in the presence of CdS seeds at a concentration that maintains a small nanocrystal size and a homogeneous dispersion. Classes **S(SIR), Se(SIR), Se(SIR$_2$), Se(PymR), and Se(PymR$_2$)** (Table 3.4.1) however, can be used to nucleate nanocrystals at desirable concentrations.

In all cases studied here, kinetics measurements performed with NMR spectroscopy and UV-vis spectroscopy agree within measurement error (Figure 3.4.2). A single exponential fit of the conversion and yield was used to extract a reactivity exponent (k_r) for each precursor, analogous to a first order conversion reaction rate constant (sec^{-1}). However, k_r is distinct from a first order rate constant because the kinetics are not run under pseudo-first order conditions and may follow a preequilibrium binding and rate determining C=E bond cleavage. Nonetheless, the exponents provide a way to conveniently order the relative precursor reactivity. Reactivity coefficients are plotted for the new cyclic thione and selone precursor classes as well as previously reported precursors measured under identical conditions (Figure 3.4.3). Five orders of magnitude in reactivity are apparent, with many pairs of sulfur and selenium precursors within an order of magnitude of each other (Figure 3.4.3 and Table 3.4.1).

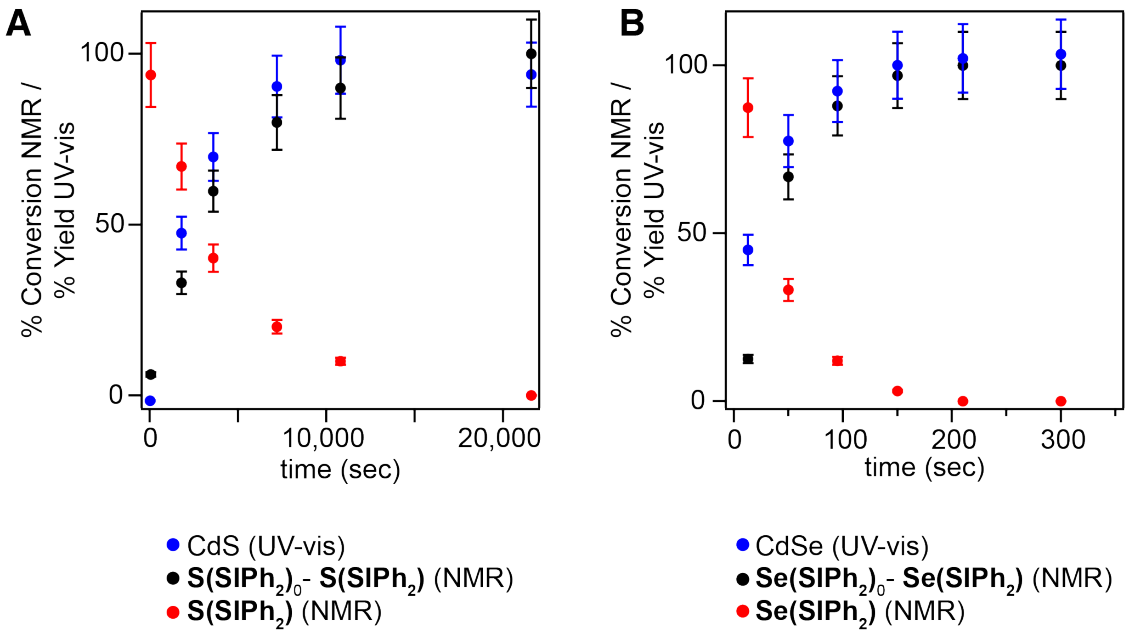

Figure 3.4.2. Comparison of conversion kinetics as measured by UV-vis and 1H NMR show nice agreement for A) **S(SIPh2)** and B) **Se(SIPh2)**.

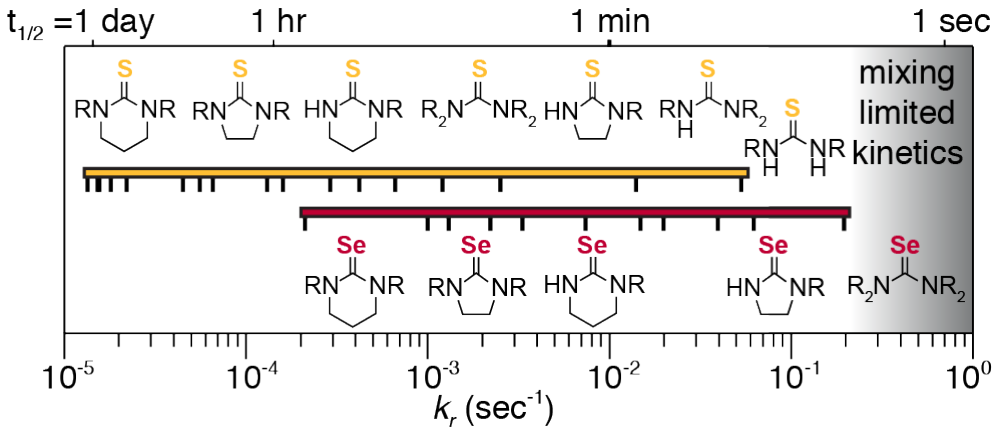

Figure 3.4.3. Relative rate constants of chalcogenourea precursor library with cadmium oleate at 240 °C.

Table 3.4.1. A list of the relative conversion rate constants for the cyclic thiones and selones used in this study.

Precursor	k_r (s^{-1})	Precursor	k_r (s^{-1})
S(SIPh)	2.5×10^{-3}	**Se(SIPh)**	2.0×10^{-1}
S(SIMe)	1.2×10^{-3}	**Se(SIEt)**	6.3×10^{-2}
S(SIEt)	6.6×10^{-4}	**Se(SIiPr)**	4.0×10^{-2}
S(SIPh$_2$)	2.2×10^{-4}	**Se(SIPh$_2$)**	2.0×10^{-2}
S(PymMe)	1.6×10^{-4}	**Se(PymMe)**	1.5×10^{-2}
S(SIiPr)	1.3×10^{-4}	**Se(SI*t*-Bu$_2$)**	7.4×10^{-3}
S(SIMe$_2$)	6.5×10^{-5}	**Se(SIMe$_2$)**	3.3×10^{-3}
S(PymMe$_2$)	5.5×10^{-5}	**Se(PymMe$_2$)**	2.2×10^{-3}
S(SIEt$_2$)	2.2×10^{-5}	**Se(SIEt$_2$)**	1.3×10^{-3}
S(PymEt$_2$)	1.8×10^{-5}	**Se(PymEt$_2$)**	1.0×10^{-3}
S(PymiPr)	1.6×10^{-5}	**Se(PymiPr$_2$)**	9.5×10^{-4}
S(SIiPr$_2$)	1.5×10^{-5}	**Se(SIiPr$_2$)**	2.1×10^{-4}
S(PymiPr$_2$)	1.3×10^{-5}		

3.4.1. Reactivity Trends

Several reactivity trends emerge from the range of k_r. Sterically encumbered precursors are typically less reactive, causing an order of magnitude reduction in reactivity on going from methyl to isopropyl. Precursors with *tert*-butyl groups, however, are anomalously reactive and likely follow a different conversion mechanism. Aryl substituted precursors tend to be more reactive, although ortho-substitution dramatically reduces the conversion reactivity. Both effects are

consistent with a mechanism involving Lewis acidic activation of the chalcogen. Cyclic precursors are substantially less reactive than acyclic structures with the same substituents. For example, tetramethyl thiourea is more reactive than *N,N'*-dimethylimidazolinethione by an order of magnitude. Likewise, the larger ring size of the pyrimidine chalcogenones further reduces their reactivity, perhaps by orienting their substituents toward the chalcogen atom and weakening its binding with cadmium oleate.

3.4.2. Additional Precursors

Several additional cyclic precursor classes were explored whose utility under our reaction conditions is variable.

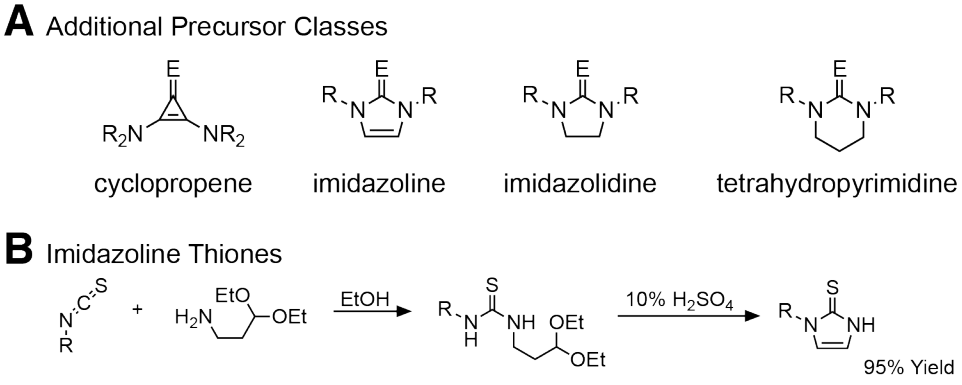

Figure 3.4.4. A) Summary of all cyclic precursor classes whose reactivity with cadmium oleate was investigated and B) synthetic scheme for the synthesis of *N*-monosubstituted imidazoline thiones.

We synthesized *N*-monosubstituted cyclic imidazoline thiones by reacting substituted isothiocyanates with aminoacetaldehyde diethyl acetal followed by cyclization in the presence of acid (Figure 3.4.4B).[69] When used as CdS precursors, these *N*-monosubstituted imidazoline thione precursors did not form CdS even after several hours of reaction.

Cyclopropene thiones and selones synthesized by M. A. Radtke from Tristan Lambert's lab were used as CdS and CdSe precursors. These molecules are good sources of CdS and CdSe that allow for the accessibility of intermediate precursor conversion rates. Under our standardized reaction conditions, 2,3-bis(dicyclohexylamino)cycloprop-2-ene-1-selenone has a k_r = 4.8 x 10^{-4} which possesses reactivity between **Se(PymiPr$_2$)** and **Se(SIiPr$_2$)**.

Due to changes in C=E bond strengths, telluroureas should possess greater reactivity than selenoureas and thioureas of a given substitution pattern. Thus, we reacted a tellurium analogue of our slowest dialkyl selone precursors (1,3-diisopropyl-4,5-dimethyl-1,3-dihydro-2*H*-imidazole-2-telluorone synthesized by B. Choi from Xavier Roy's lab) with cadmium oleate under our standard reaction conditions. Mixing limited kinetics were observed. In order to further reduce tellurourea precursor reactivity, the *N,N'*-dimesityl derivative is a promising future target.

3.4.3. Nanocrystal Nucleation as a Function of Conversion Rate

As has been observed in several other nanocrystal publications, more reactive precursors increase the number of nanocrystals nucleated.[2-3, 5-6] However, under otherwise identical reaction conditions and precursor conversion rates, we observe that more CdS than CdSe nanocrystals nucleate (Figure 3.4.5). A notable exception is **Se(SIPh$_2$)** which nucleates more CdSe nanocrystals compared to the other selenourea precursors. Notably, this is the only diaryl cyclic selone tested that could possess a different reaction mechanism than the alkyl substituted selones. Differences in precursor structure are likely to affect the reaction mechanism; for example, disubstituted and trisubstituted thioureas will likely react via an initial deprotonation to form a metal thioureate complex, whereas tetrasubstituted compounds and thiocarbonates cannot. Interestingly, across a wide variety of structures, CdS tends to nucleate more nanocrystals than CdSe which we tentatively attribute to a slower material growth rate.

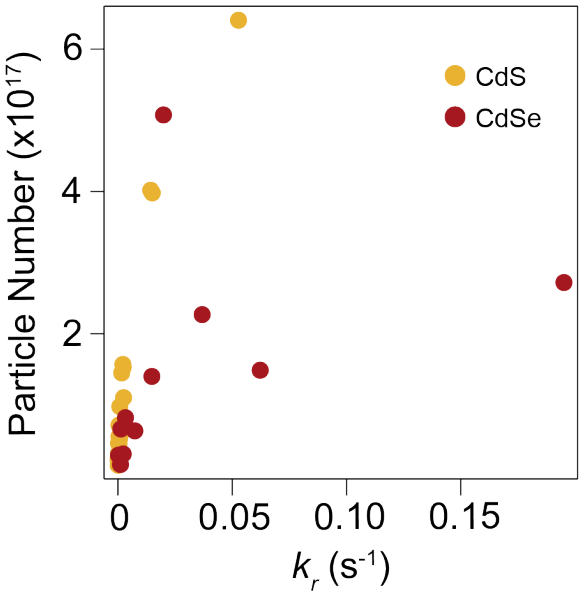

Figure 3.4.5. Particle number vs. precursor conversion rate constant for the library of sulfur and selenium precursors all run under the standard cadmium chalcogenide reaction conditions.

To further explore the effect precursor class has on nucleation, we compare the number of nuclei produced by selones based on the saturated imidazole backbone with the number of nuclei produced by selones based on the tetrahydropyrimidine backbone (Figure 3.4.6). We observe that fewer particles nucleate for the tetrahydropyrimidine selone precursors compared to the imidazolidine selone precursors. Interestingly, for these two classes of compounds and conditions, the CdSe growth rates should be identical, indicating that precursor structure exerts an additional level of control over the number of particles nucleated.

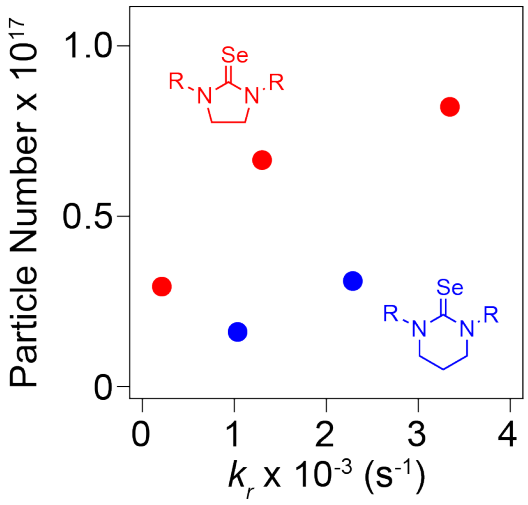

Figure 3.4.6. Particle number vs. precursor conversion rate constant for the cyclic dialkyl imidazolidine selones **Se(SIR$_2$)** and cyclic dialkyl tetrahydropyrimidine selones **Se(PymR$_2$)** show that six membered ring compounds nucleate fewer particles than the five membered ring compounds at similar precursor conversion rates.

3.4.4. CdS and CdSe Critical Concentrations

With our expanded library of chalcogen precursors, we sought to compare the critical concentrations of CdS and CdSe nanocrystal reactions. In order to extract critical concentrations for these two materials, we analyzed the induction delay observed in the time period between precursor conversion into soluble solute before reaching supersaturation and undergoing nucleation processes. This induction delay is defined as the first stage, or pre-nucleation stage, in the LaMer model where monomers build up in solution until they supersaturate and trigger the second stage, a burst of nucleation.[70-71] We notice that as sulfur and selenium

precursors decrease in k_r, an increase in induction delay before the formation of nanocrystals is observed. This makes sense because slower precursors should take longer to reach supersaturating conditions (Figure 3.4.7).

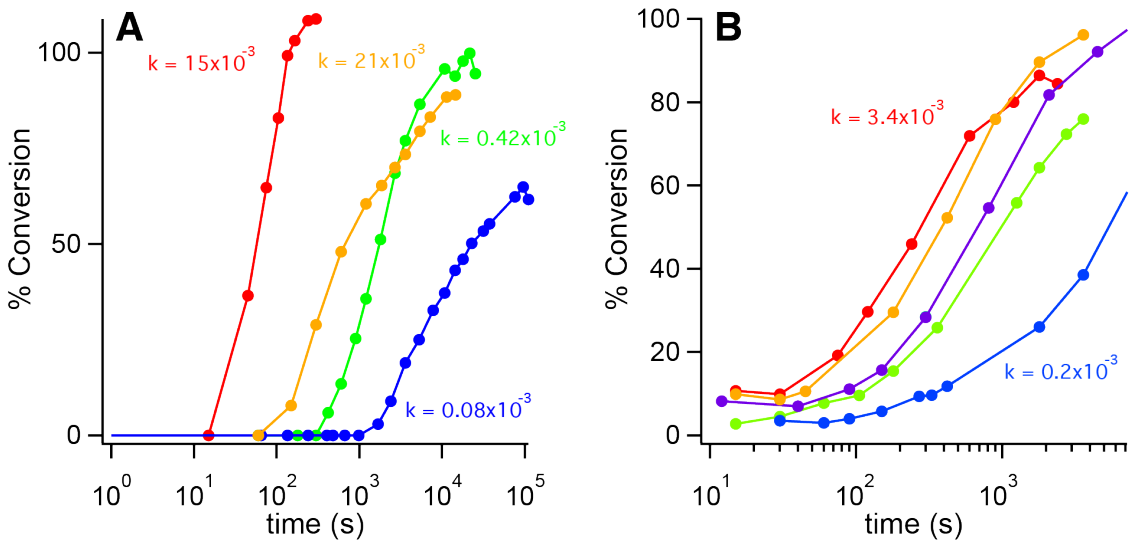

Figure 3.4.7. % conversion vs. time for various A) sulfur and B) selenium precursors all run under the standard cadmium chalcogenide nanocrystal reaction conditions shows an induction delay in nucleation that tracks roughly with precursor conversion rate.

We extract the critical concentration two ways: (1) plotting induction delays vs. $1/k_r$ and (2) calculating the fraction of precursor converted at nucleation, f_{con}, from each individual experiment as a product of the induction delay (t_{ind}) and precursor conversion rate constant (k_r). Using the first method, we rearrange the first order rate law

$$f_{con} = \frac{[M]}{[M]_{max}} = 1 - e^{-k_r t_{ind}}$$

Equation 3.4.1.

to

$$t_{ind} = -ln\,(1 - f_{con})\frac{1}{k_r}$$

Equation 3.4.2.

The slope of the plot of induction time vs. $1/k_r$ is equal to $-\ln(1-f_{con})$ where f_{con} equals the fraction of the total chalcogen precursor added that has converted at the time of nucleation. For CdS run at our reaction conditions, we extract that $f_{con} = 0.09$, and for CdSe we extract 0.023. We multiply this by the total reaction concentration of 10 mM to get that $[CdS]_{crit} = 0.91$ mM and $[CdSe]_{crit} = 0.23$ mM. Comparing the results obtained via method 2, we get that $[CdS]_{crit} = 1.4$ mM and $[CdSe]_{crit} = 0.23$ mM. Regardless of method, we extract that the $[CdSe]_{crit} < [CdS]_{crit}$ which illustrates that there is more to think about in kinetically controlled nanocrystal syntheses than simply precursor conversion rates (Figure 3.4.8).

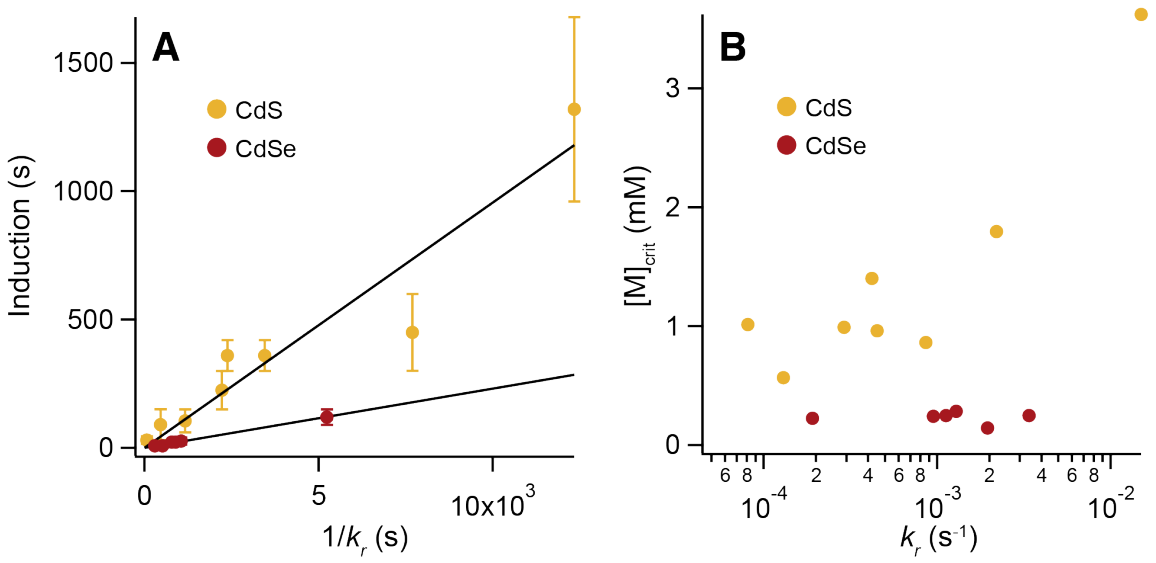

Figure 3.4.8. Plot of A) induction time (s) vs. $1/k_r$ (s) and B) [M]crit vs. k_r for CdS and CdSe.

3.5. One-Pot Core/Shell Reactions

The wide range of reactivity for both thiones and selones provides several matched pairs of precursors with which to synthesize alloy and heterostructured nanocrystals in a single step (Figure 3.5.1). Kinetics simulations performed by Dr. H. Yang were used to study the influence of reactivity on the distribution of chalcogen atoms (Section 3.10.8).

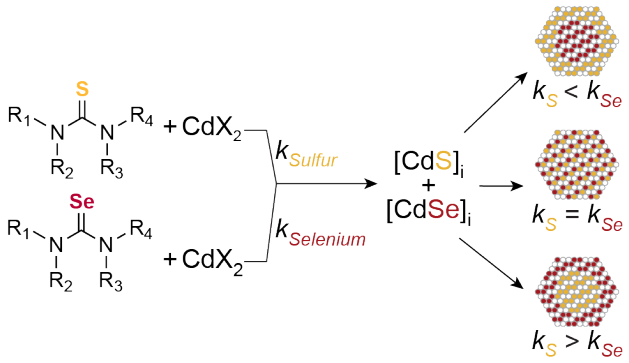

Figure 3.5.1. General principle for kinetic control over the formation of alloyed and heterostructured nanocrystals in a single injection of chalcogen precursors.

3.5.1. Kinetics Modeling

Elemental distributions of nanoparticles synthesized by a simultaneous injection of two chalcogen precursors could be calculated following several assumptions: (1) solute generation kinetics are single exponential, i.e. first order in the chalcogen precursors and zero order in the metal, (2) the elemental composition of the nanocrystal is equal to the instantaneous solute generation rate ($M^{-1}s^{-1}$), and (3) the nanocrystals are spherical and grow isotropically. Using these inputs, we simulated the radial profile of nanocrystals produced across a wide range of compositions and relative rate constants (Figure 3.5.3A).

For an example reaction where $k_{Se} > k_S$, the extent of reaction of each precursor at different stages of the synthesis gives rise to changes in radial composition, as shown in Figure 3.5.2A. At early times, the fast Se compound

reacts to generate CdSe-rich cores. At intermediate times, the slower S compound starts to react while the faster Se compound has not fully been consumed yet, which results in the simultaneous deposition of CdS and CdSe onto the particles to form a graded interfacial layer. In the final stage of the reaction, the faster Se compound has almost been depleted, leaving only the reaction of the remaining slower S compound, which produces a CdS-rich outer shell.

The simulated elemental profile of a representative heterogeneous particle is shown in Figure 3.5.2B. The composition change from the center to the surface of the particle follows a sigmoidal curve, in which the percentage of CdSe is highest at the center, and lowest on the surface. We divided the curve into three regions. The core region is defined as the sphere from the center outwards in which the compositional change is less than 5% of the total compositional change over the whole radius. Similarly, the outer shell region is defined as the shell from the surface inwards in which the compositional change is also less than 5% of the total compositional change. The inner layer between the core and the outer shell is defined as the graded alloyed interfacial region, inside which 90% of the total compositional change happens.

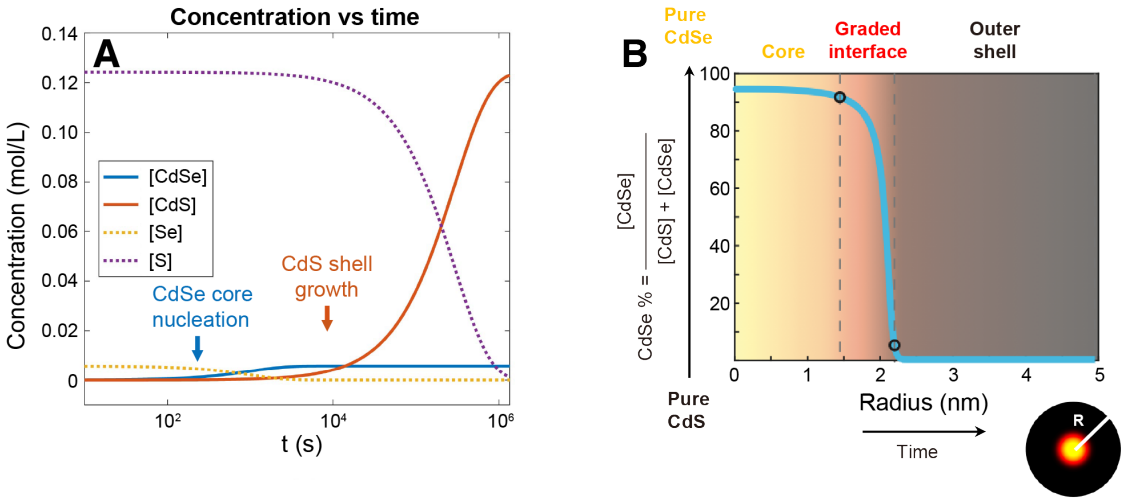

Figure 3.5.2. A) Calculated temporal evolution of the concentrations of crystallized CdSe and CdS, Se and S precursors in a typical heterostructure synthesis reaction. B) The simulated radial distribution of a representative core/shell nanoparticle.

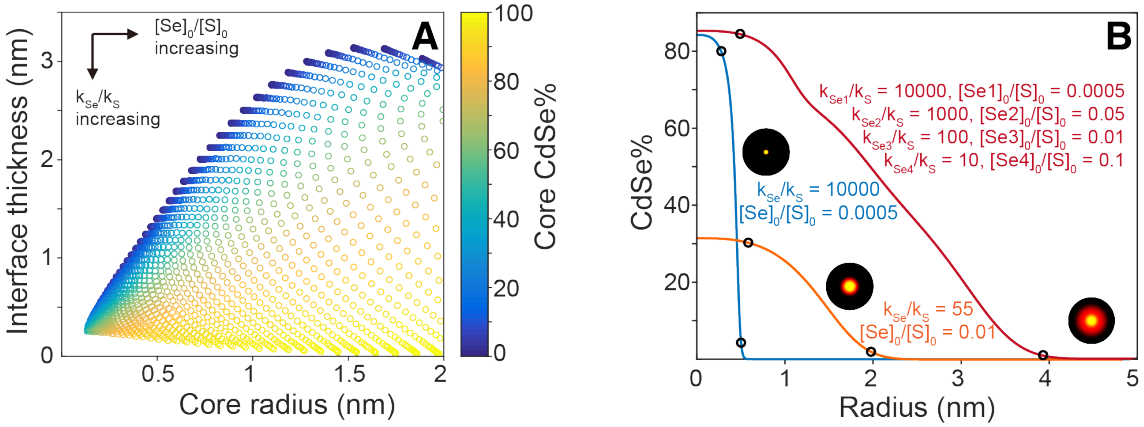

Figure 3.5.3. A) A summary of simulation results showing three heterostructure features of interest. Each point represents one set of parameters. X-axis represents the radius of the core, Y-axis represents the thickness of the interfacial region, and the color of the points represents the composition of the core. B) The simulated radial distributions of three types of heterostructures.

A number of important observations can be made from these simulations. (1) Reactivity exponents within an order of magnitude are needed to substantially grade the core and shell interface or produce alloys. (2) Heterostructures with thick outer shells require a greater amount of shell precursor, and therefore a greater difference in reactivity is required to obtain distinct core and shell regions. The large amount of precursor needed to obtain a thick shell, also increases the instantaneous rate of production at early times. This increases the tendency to form an alloyed core. For example, a QD heterostructure with a 4 nm CdSe core and a 3 nm thick CdS shell is 95% CdS and requires ~20x the amount of sulfide precursor. Thus, to obtain a heterostructure with distinct core and shell regions, the reactivity of the core precursor must be 200x greater than the shell precursor. Thicker shells require even greater differences. (3) Higher fidelity structures (e.g. with pure phase cores, a thick graded interface, and a pure phase shell) require more than two precursors to obtain distinct regions. A series of precursors with "laddered" reactivity can lead to such a structure. Such a scenario is depicted in Figure 3.5.3B. However, as the dimensions of the nanocrystal grow, and the outer layers make up a greater fraction of the whole, the differences in reactivity must be magnified. The resulting range of required reactivity is large and leads to impractically long total reaction times. We estimate that reaction times of several

days are required to produce pure core-graded interface-pure shell structures with radii >10 nm (Figure 3.5.4).

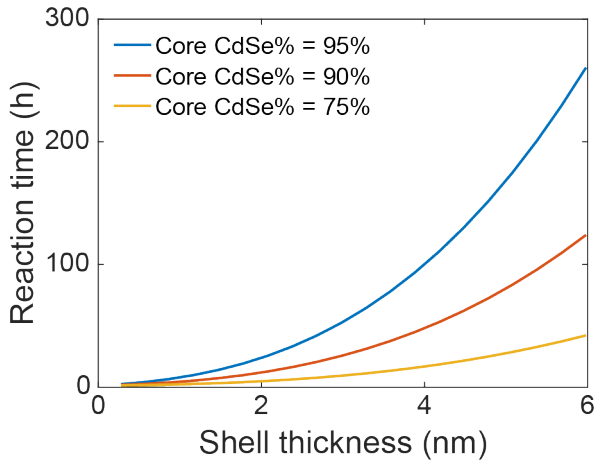

Figure 3.5.4. Reaction times required to grow heterostructures as a function of shell thickness. Impractically long reaction times are needed for thick-shell particles, especially when a high percentage of CdSe in the core is sought after.

3.5.2. Experimental Core/Shell Results

Using these principles as a guide we selected pairs of precursors to prepare CdSe/CdS, $CdSe_{1-x}S_x$, and CdS/CdSe heterostructures in a single synthetic step (Figure 3.5.5).

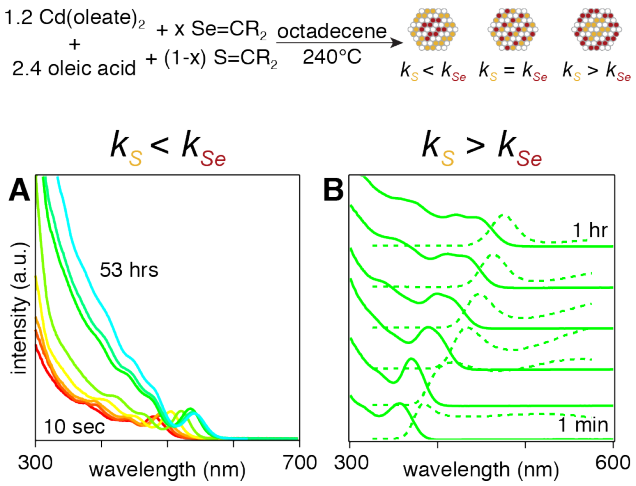

Figure 3.5.5. Synthetic scheme for the kinetically controlled formation of core/shell nanocrystals. A) UV-vis spectra of CdSe/CdS core/shell and B) UV-vis and fluorescence spectra of CdS/CdSe core/shell nanocrystals synthesized via kinetic control.

When using a Se precursor (**Se(SI*t*-Bu$_2$)**) that is 100x more reactive than a sulfide precursor partner (**S(SIMe$_2$)**), a CdSe nanocrystal appears and grows to ~4 nm, followed by a slow deposition of a CdS shell that increases the absorbance at high energies (< 400 nm) (Figure 3.5.5A and Figure 3.5.6). During the CdS formation, the photoluminescence quantum yield (PLQY) increases and the luminescence lifetime shortens, signs that CdS is depositing on the CdSe nucleus (Figure 3.5.7). Scanning transmission electron microscopy and energy dispersive

x-ray spectroscopy (STEM EDX) support the expected CdSe/CdS microstructure (Figure 3.5.8).

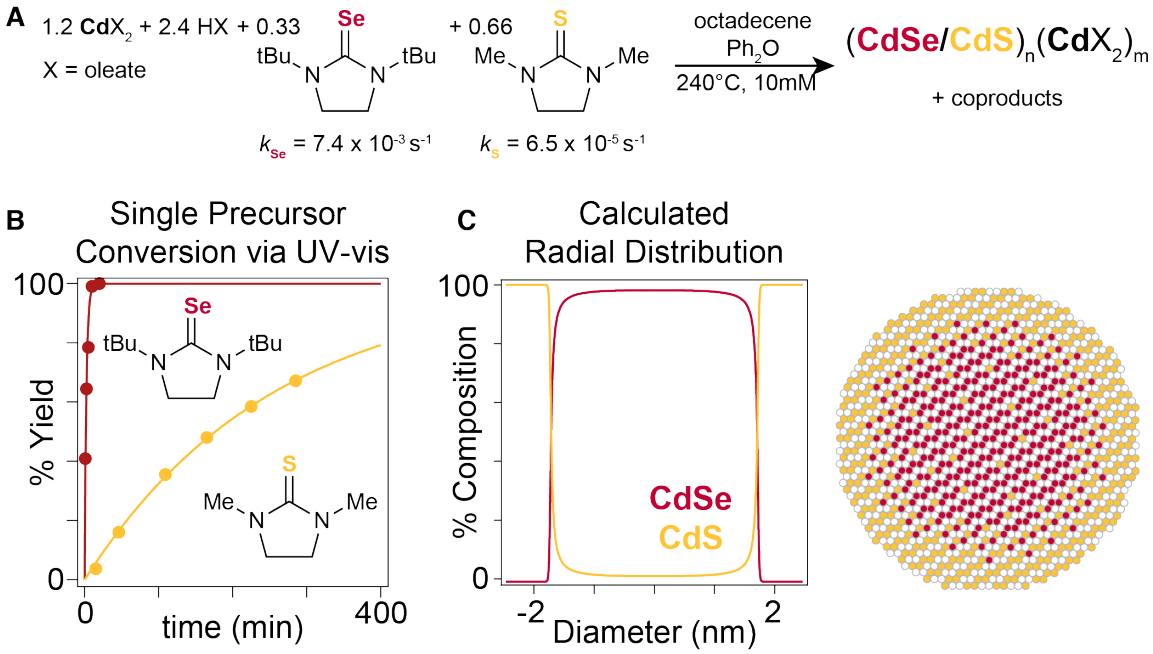

Figure 3.5.6. A) Scheme for the synthesis of red emitting CdSe/CdS nanocrystals, B) their individual precursor conversion rates as monitored via UV-vis absorbance spectra and C) predicted radial distribution.

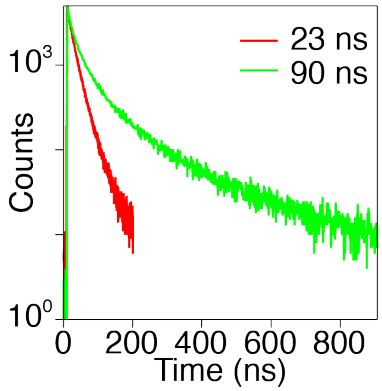

Precursors		$\tau_{1/2}$	PLQY
0.33 eq.	Se(SI*t*-Bu$_2$)	23 ns	60%
0.66 eq.	S(SIMe$_2$)		
0.5 eq.	*N*-hexyl, *N'*-dodecyl thiourea	90 ns	18%
0.5 eq.	Se(SIEt$_2$)		

Figure 3.5.7. Fluorescence lifetimes and PLQY of CdSe/CdS and CdS/CdSe core/shell nanoparticles are indicative of the predicted structures.

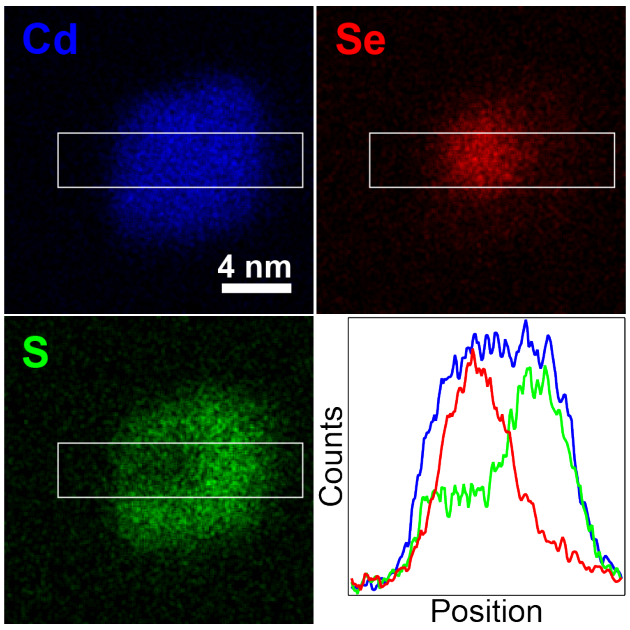

Figure 3.5.8. STEM EDX elemental map of predicted CdSe/CdS nanocrystal confirms elemental distributions with blue = cadmium, red = selenium, green = sulfur.

The reverse architecture is obtained when a reactive CdS precursor (*N*-dodecyl-*N'*-hexylthiourea) is paired with a 100x slower selenium precursor

(**Se(SIEt$_2$)**): CdS rapidly nucleates (d = 2.1 nm, λ_{max} = 351 nm) upon which CdSe deposits over an hour. Growth of the CdSe layer causes lower energy absorption features to appear and shift across the visible (Figure 3.5.5B and Figure 3.5.9). Long photoluminescence lifetimes ($\tau_{1/2}$) and low PLQY are consistent with the CdS/CdSe core/shell heterostructure (Figure 3.5.7). ^{1}H NMR spectroscopy of reaction aliquots taken from these mixtures suggests that the conversion reactivity is unchanged from the single component reactions. Thus, in the cases studied here where k_r of the two precursors differ by more than an order of magnitude, the precursors do not have a strong effect on each other's reactivity. (Figure 3.5.10).

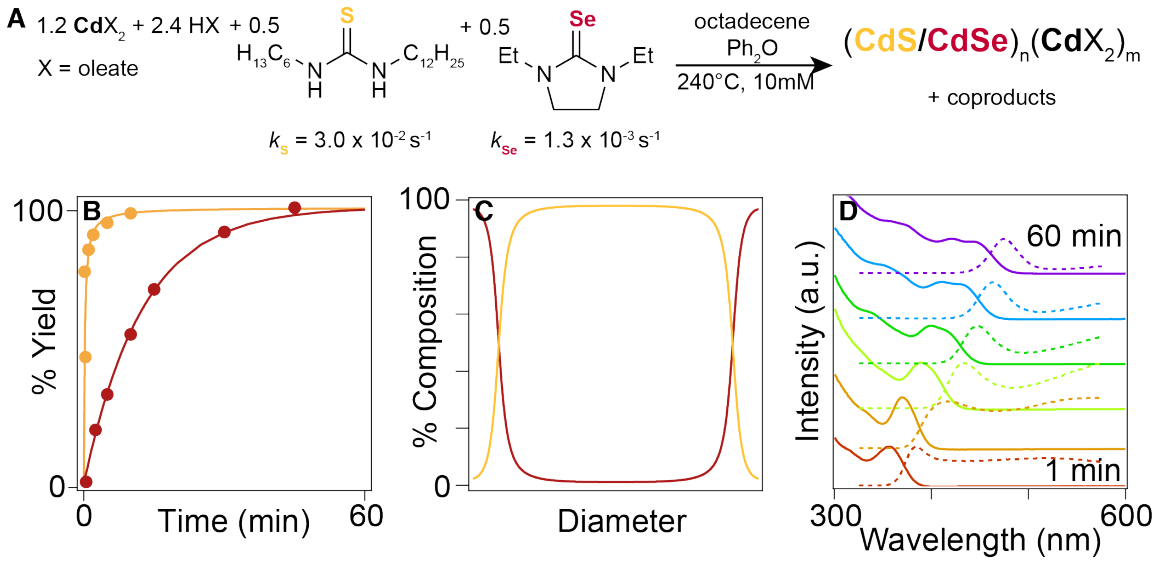

Figure 3.5.9. A) Scheme for the synthesis of blue emitting CdS/CdSe nanocrystals, B) their individual precursor conversion rates as monitored via UV-vis absorbance spectra, C) predicted radial distribution, and D) UV-vis and fluorescence spectra.

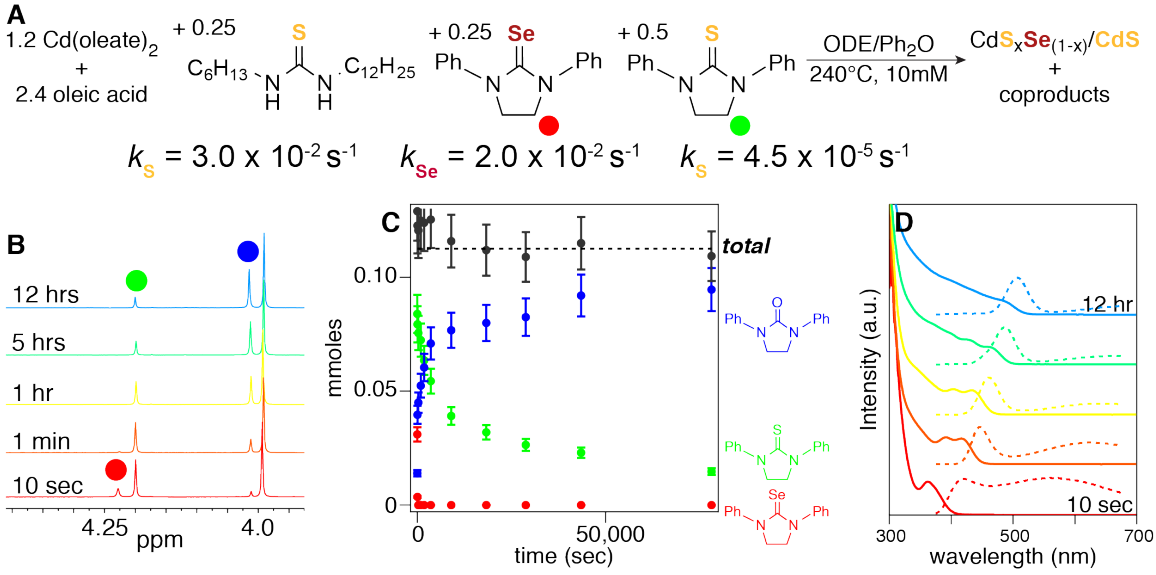

Figure 3.5.10. A) Reaction to form CdS_xSe_{1-x}/CdS with a single injection of three precursors, B) ^1H NMR kinetics of precursor conversion, C) quantification of conversion via ^1H NMR, and D) UV-vis and fluorescence spectra of reaction aliquots. Observed rate constants determined via ^1H NMR match well with single component precursor conversion rates.

3.5.3. Experimental Alloy Synthesis

When we react two precursors possessing conversion rates that are within one order of magnitude of each other, we predict the formation of an alloyed $CdSe_{1-x}S_x$ nanoparticle (Figure 3.5.11). Ongoing Raman and pair distribution function analysis experiments must be performed to confirm the alloyed structure of these nanocrystals.

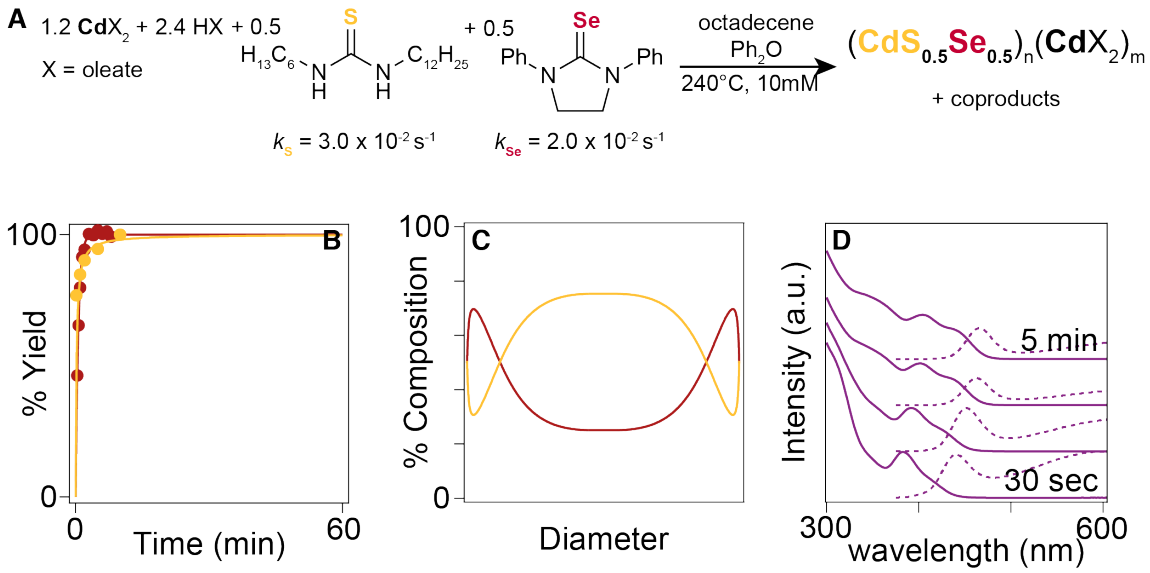

Figure 3.5.11. A) Scheme for the synthesis of blue emitting CdS_xSe_{1-x} nanocrystals, B) their individual precursor conversion rates as monitored via UV-vis absorbance spectra, C) predicted radial distribution, and D) UV-vis and fluorescence spectra of reaction aliquots.

3.5.4. Color Tunability

Both the concentration of nanocrystals (set by the more reactive precursor) and the Se:S ratio can be used to control the final emission wavelength. The more reactive precursor typically controls the nucleation phase and determines the number of nanocrystals and therefore, the final size at full conversion. For example, several selenium precursors were paired with a slow (≤ 10x) sulfur precursor to prepare CdSe/CdS core/shell nanocrystals. The selenium conversion kinetics control the nucleation phase, and much like single component reactions, faster reactivity leads to bluer emission wavelengths, and slower reactivity

produces a larger particle possessing redder emission. A wide range of colors can be accessed in this way depending on the precursor employed (λ_{max} = 515 – 622 nm, Figure 3.5.12), including blue-green emitters that are otherwise challenging to synthesize.

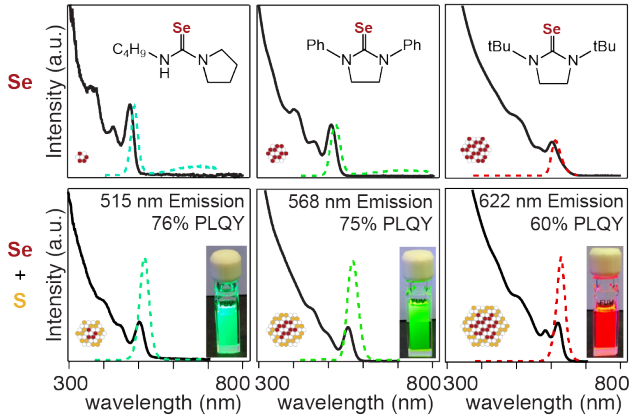

Figure 3.5.12. Color tunability of CdSe/CdS core/shell nanocrystals made via this method is accomplished by changing the fast selenium precursor. The identity of this precursor sets the CdSe core size. Paired with a slower sulfur precursor, high PLQY products can be synthesized with a single injection of chalcogen precursors.

Adjusting the S:Se ratio provides another method to tune the emission spectrum. However, adjusting the S:Se ratio impacts the final nanocrystal product color by changing both number and composition in sometimes counterintuitive ways (Figure 3.5.13). For example, as the amount of sulfur precursor is increased and the amount of selenium precursor injected is decreased, the particle should blue shift because CdS has a higher energy band gap than CdSe. However,

changing the S:Se precursor ratio also changes the number of particles nucleated. Particle number ${p_T}'^{\infty}$ can be modeled according to Equation 3.5.1

$$ {p_T}'^{\infty} = 2\left(\frac{Q}{G}\right)'\left(\frac{\sqrt{1+4a'}-1}{2a'}\right) $$

Equation 3.5.1.

where

$$ \left(\frac{Q}{G}\right)' = x\left(\frac{Q}{G}\right)_{CdS} + (1-x)\left(\frac{Q}{G}\right)_{CdSe} $$

Equation 3.5.2.

and

$$ (a)' = x(a)_{CdS} + (1-x)(a)_{CdSe} $$

Equation 3.5.3.

and Q is the solute supply rate per volume, G is the growth rate in solutes attached per time nucleus, x is the fraction of sulfur precursor injected, and a is a constant dependent on Q and G but expected to be a very small number.[72] Equation 3.5.2 suggests that in reactions involving a simultaneous injection of sulfur and selenium precursors, decreasing the concentration of whichever semiconductor has a higher Q/G will decrease the particle number which in turn increases particle size. For a single precursor, it is experimentally observed that lowering the equivalents of precursor injected has a linear relationship to the number of particles nucleated (Figure 3.5.14).

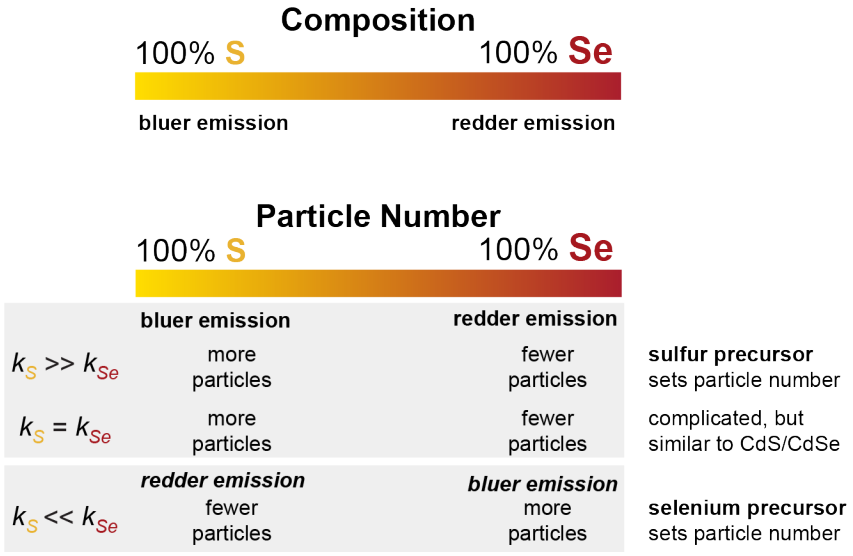

Figure 3.5.13. Changing the S:Se ratio in one-pot core/shell reactions impacts both composition and particle number, causing the nanocrystal reaction to redshift or blueshift in ways that sometimes oppose each other.

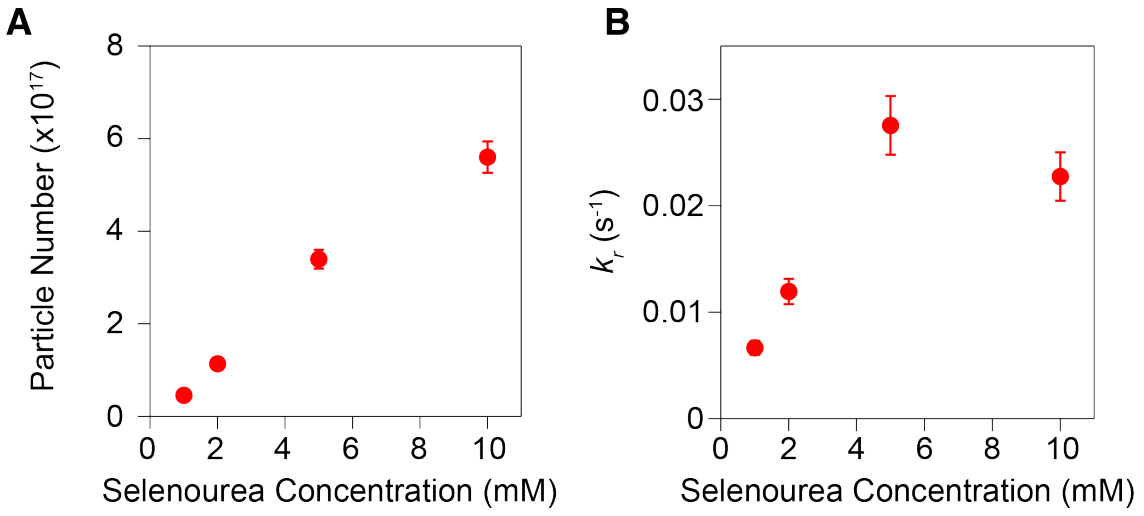

Figure 3.5.14. Selenourea **Se(SIPh$_2$)** concentration dependence on A) particle number and B) k_r.

Thus, as the number of cores decreases when increasing S:Se ratio for k_S << k_{Se}, the particles should grow larger and red shift the particle emission. On the

other hand, when $k_S = k_{Se}$ or $k_S >> k_{Se}$, an increase in the S:Se ratio should increase the number of particles nucleated and blue shift the particle emission in an effect cooperative with composition effects (Figure 3.5.15 and Figure 3.5.16). Interestingly, the number of particles nucleated for sulfur precursors is approximately 2x higher than the number of particles nucleated for selenium precursors at any given k_{rel} with the notable exception of **Se(SIPh$_2$)** (Figure 3.4.5). This is likely due to differences in CdS and CdSe growth rates as illustrated by the k_{rel} vs. *particle #* plot (Figure 3.4.5) whose slopes are proportional to $2/G$.[72]

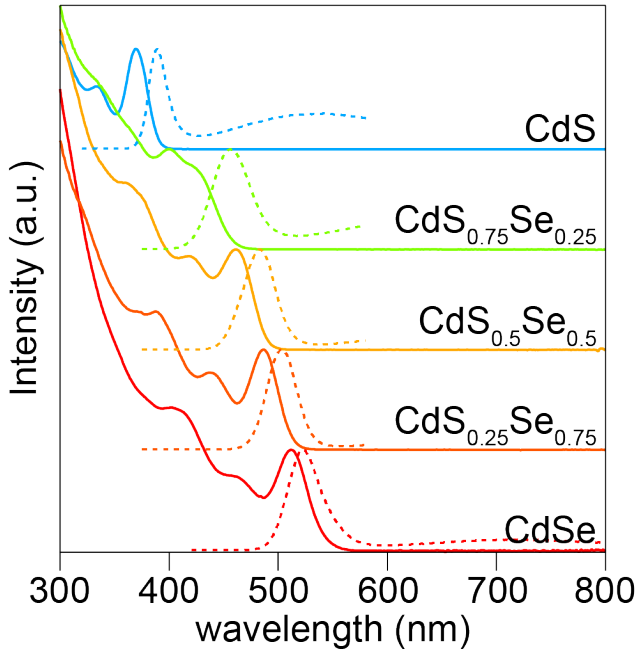

Figure 3.5.15. UV-vis and fluorescence spectra of CdS, $CdS_{0.75}Se_{0.25}$, $CdS_{0.5}Se_{0.5}$, $CdS_{0.25}Se_{0.75}$, and CdSe nanocrystals.

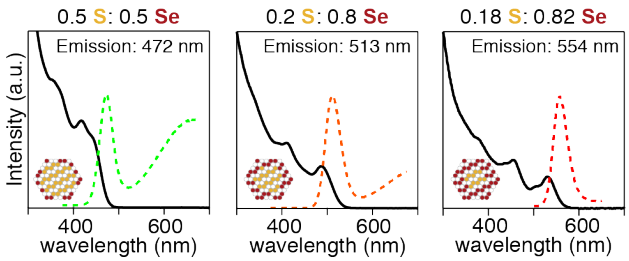

Figure 3.5.16. Color tunability of CdS/CdSe core/shell nanocrystals can also be accomplished by changing the ratios of *N*-hexyl, *N'*-dodecyl thiourea and **Se(SIEt$_2$)**.

We predict the particle numbers for alloys of varying composition will lie between that of the 100% sulfur and 100% selenium precursor reactions. In order to test this, pairs of precursors with nearly matched conversion reactivity (*N*-methyl, *N,N'*-diphenyl thiourea and **Se(SIPh$_2$)**) were used to prepare alloys over a range of Se:S ratios (Figure 3.5.15). These conditions provide a wide range of emission colors spanning the blue-green region of the spectrum in this case. Our hypothesis is supported by changes in alloyed nanocrystal size observed by preliminary pair distribution function analysis experiments.

Adding additional complexity, more than two precursors may also be used to push the accessible color range out to 499 nm in emission energy (Figure 3.5.10). Conditions for accessing these CdSe/CdS, CdS/CdSe, and CdS_xSe_{1-x} nanocrystals are described in detail in the experimental (Sections 3.10.13, 3.10.14, and 3.10.15).

3.6. Synthetic Challenges

3.6.1. Heterogeneity in the Nucleation of CdSe

Although the precursor combinations described above provide access to a wide range of architectures and emission wavelengths, many combinations attempted result in heterogeneous products. Issues with (1) the nucleation of CdSe, (2) homogeneous nucleation of the shell material and (3) crystallization issues under low solute supply rates were all documented. In the first case, we observe that the nucleation of CdSe is sensitive to the total reaction concentration and to the presence of added carboxylic acid. At 10 mM **Se(SIEt$_2$)** produces a single population of emitters, while cutting the chalcogen concentration in half produces a second population of emitters (Figure 3.6.1). Although the origin of these effects is unclear, heterogeneity can be avoided by optimizing the selenourea concentration for each precursor. Addition of a slow reacting thiourea to deposit a shell still results in the appearance of two populations of emitters (Figure 3.6.2A). The concentration of acid also impacts the nucleation of CdSe and can be used to reduce the presence of multiple populations of emitters (Figure 3.6.2B).

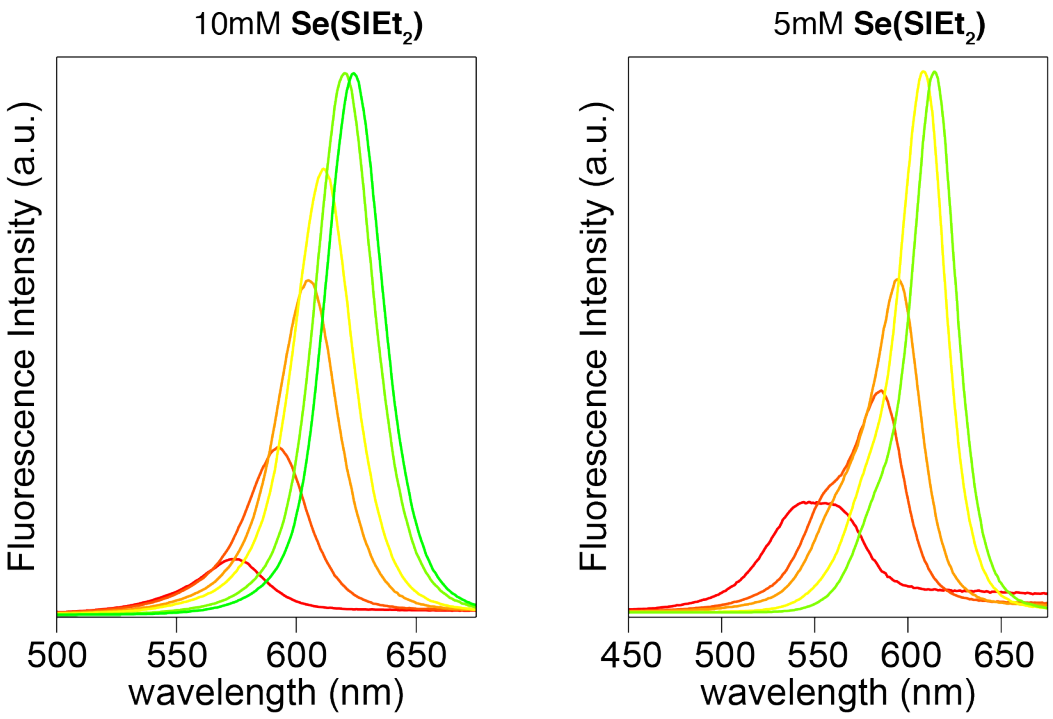

Figure 3.6.1. Fluorescence spectra of a CdSe nanocrystal reaction shows one population of emitters for a selone run at 10 mM, whereas 5 mM in selone results in the presence of two emitting populations.

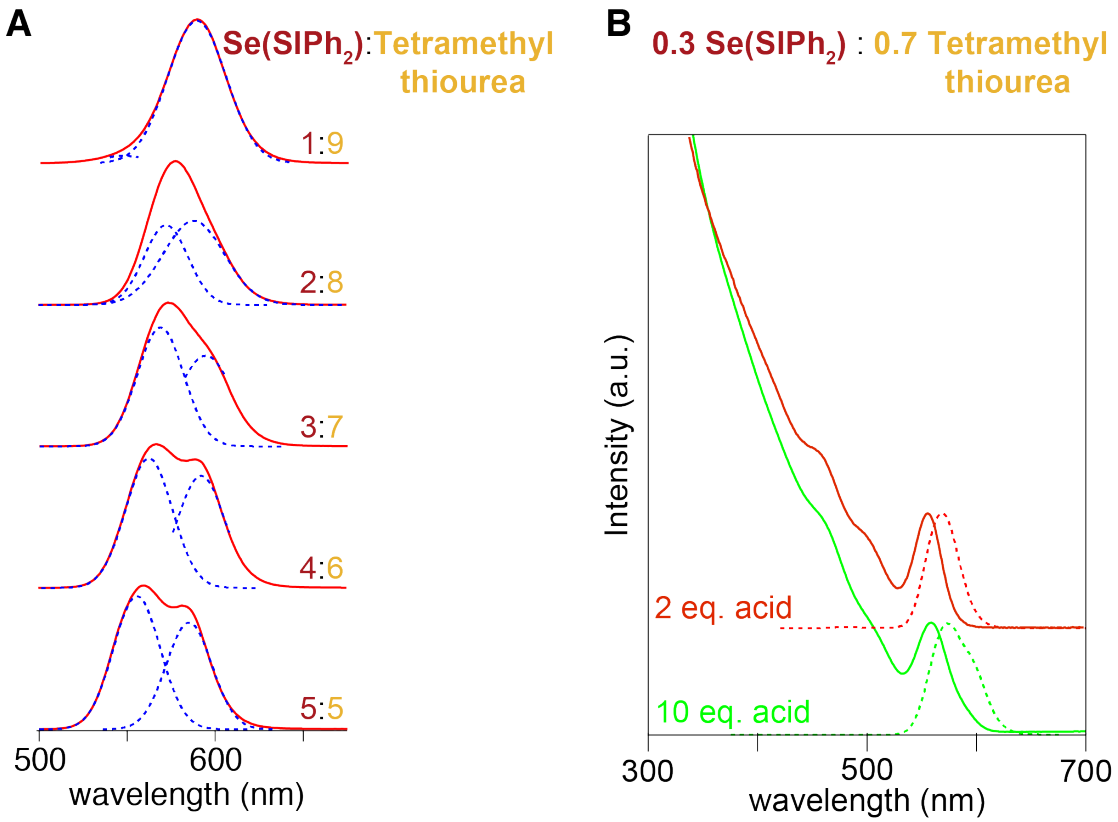

Figure 3.6.2. A) Sulfur to selenium precursor ratio dependence on the appearance of a second population of emitters in the nanocrystal fluorescence spectra and B) acid dependence on the appearance of the second population of emitters.

While nucleation of CdSe proved complicated under our standard conditions, reactions that nucleate CdS routinely produce single populations of emitters with a narrow FWHM. For reasons yet unclear, the CdS nucleation is remarkably robust across 0.1-1 eq. of thiourea and 0-10 eq. of oleic acid.[7] Thus, from our methods, we favor the synthesis of CdS/CdSe/CdS quantum wells that

rely on CdS nucleation in lieu of CdSe/CdS particles that rely on often problematic CdSe nucleation.

3.6.2. Homogeneous Nucleation of Shell Material

Nucleation of a second population of shell material was observed in both CdSe/CdS and CdS/CdSe core/shell reactions (Figure 3.6.3). Preventing nucleation of this type of impurity is controlled by the relationship between solute supply rate which is equal to k_r*[chalcogen], the number of nanocrystals nucleated, and shell material growth rates (G) at a given set of reaction conditions. Homogeneous nucleation of a second population of shell material results from supersaturation of solute units because (1) the solute supply rate is too high, (2) there are not enough cores to grow onto, and/or (3) the inherent material growth rate is too slow. Previous studies have shown that material growth rates can be increased by the addition of acid.[11] While this is an effective way to shut down nucleation of shell precursors, here, we seek to control its appearance by controlling (1) solute supply rate and (2) particle number.

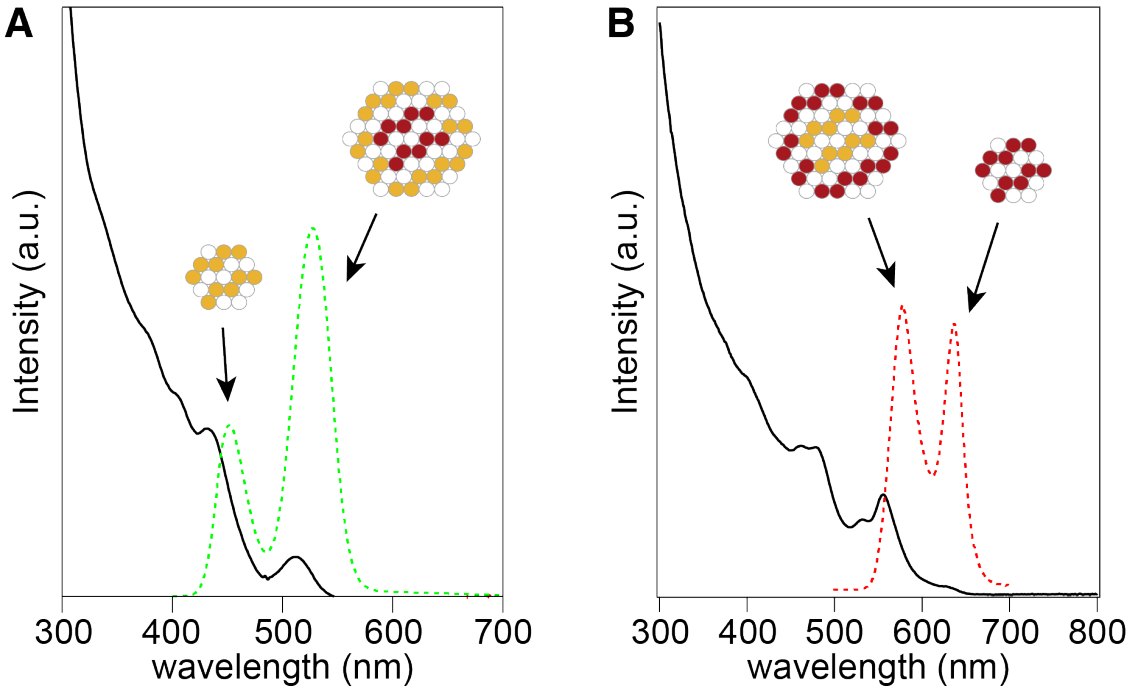

Figure 3.6.3. Example UV-vis and fluorescence spectra of observed homogeneous nucleation of shell material in A) CdSe/CdS and B) CdS/CdSe one-pot core/shell reactions.

We demonstrate suppression of CdS nucleation in a typical CdSe/CdS core/shell system. When 0.1 eq. of *N*-butyl, *N'*-pyrrolidine selenourea is combined with 0.9 eq. of tetramethylthiourea, there is nucleation of a second population of CdS nanocrystals (Figure 3.6.4A). Because solute supply rate depends on [thiourea]*k_r, lowering the solute supply rate can be accomplished by decreasing the concentration of tetramethylthiourea to 0.4 eq. OR switching to a precursor with a slower k_r such as **S(SIMe$_2$)**. Both of these methods are successful in eliminating the nucleation of a second population (Figure 3.6.4A). Both of these changes do impact the final nanocrystal product; we observe that adding fewer eq.

of tetramethylthiourea leads to a blue shifted spectrum because the CdS shell is thinner. Additionally, the reaction with **S(SIMe$_2$)** also takes longer to reach completion due to slower kinetics. Nevertheless, this example successfully illustrates how to avoid nucleation of shell precursors by considering solute supply rate.

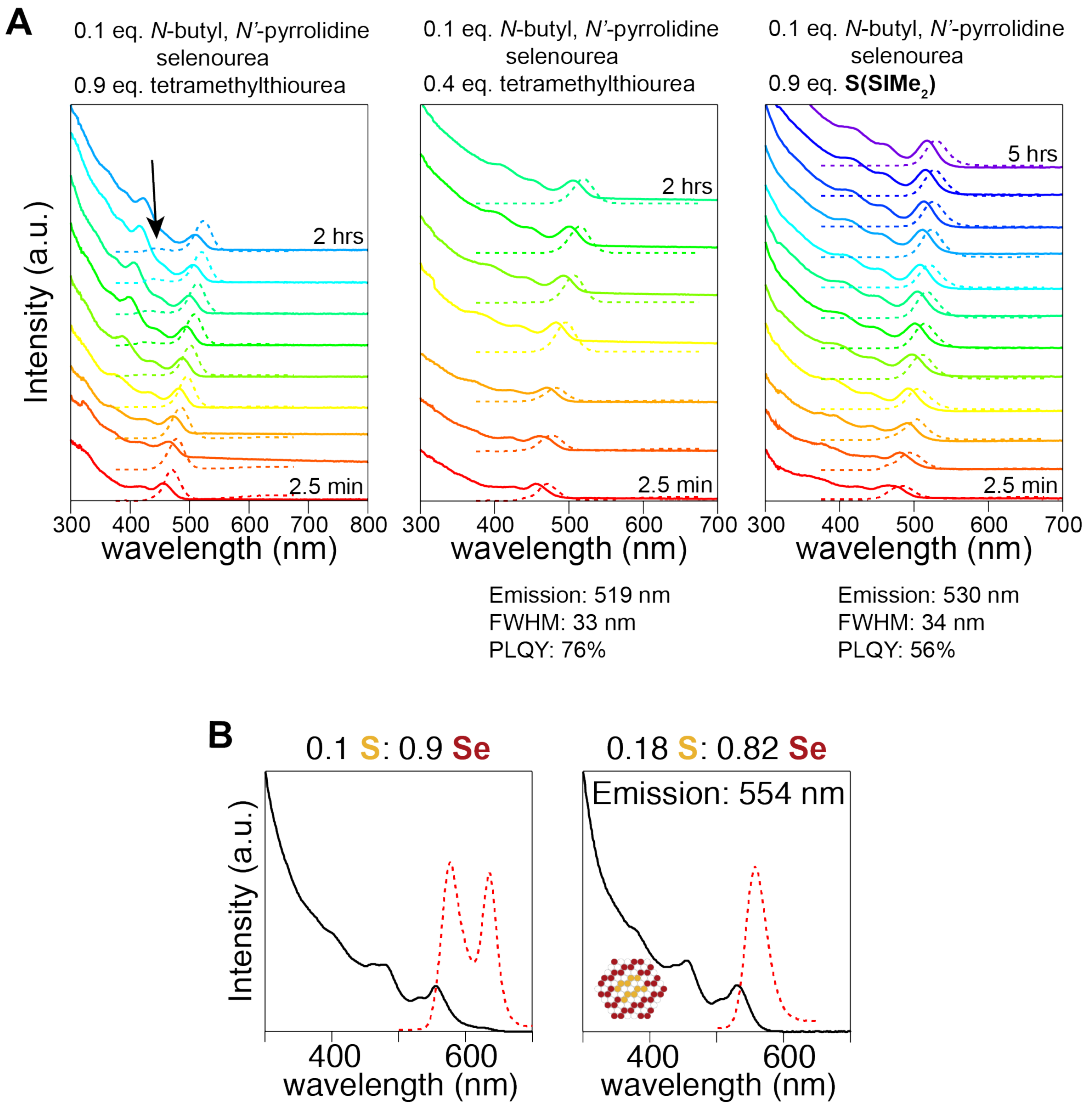

Figure 3.6.4. UV-vis and fluorescence data of A) growing a CdS shell on CdSe nuclei results in a second population of CdS nanocrystals for 0.9 eq. of tetramethylthiourea. Adding fewer eq. of tetramethyl thiourea (0.4 eq.) or swapping to a slower precursor such as **S(SIMe2)** reduces the appearance of the second population. B) UV-vis and fluorescence data depicting CdSe nucleation when S:Se ratios are 0.1:0.9. The second population of nanocrystals is eliminated by switching to a higher ratio.

Increasing the number of cores nucleated can also suppress nucleation of a second population of CdSe in a CdS/CdSe core/shell system. When 0.1 eq. of *N*-

hexyl, *N'*-dodecyl thiourea are injected with 0.9 eq. of **Se(SIiPr$_2$)**, we observe nucleation of CdSe nanocrystals. Upon increasing the number of CdS cores in the reaction by changing the sulfur to selenium ratio to 0.2 eq. S : 0.9 eq. Se, we see that the second population of particles is eliminated (Figure 3.6.4B).

Further studies must be performed to rigorously explore the conditions that cause nucleation of shell precursors. We believe that this behavior may be precursor class dependent; we observe precursor structure dependent nucleation behavior between tetrasubstituted cyclic imidazolidine selones and tetrahydropyrimidine selones (Figure 3.4.6).

3.6.3. Issues Growing Large Structures via Kinetic Control

While alloy and core/shell nanocrystals with a small diameter (d < 3 nm) are reproducibly obtained under our conditions, larger structures are more difficult to synthesize. Often, multiple populations of emitters appear and anisotropic growth is observed (Figure 3.5.8, Figure 3.6.5, and Figure 3.6.6). Here we observe that the shell does not grow isotropically around the core. This is consistent with EELS data taken on CdSe/ZnS core/shell nanocrystals.[73]

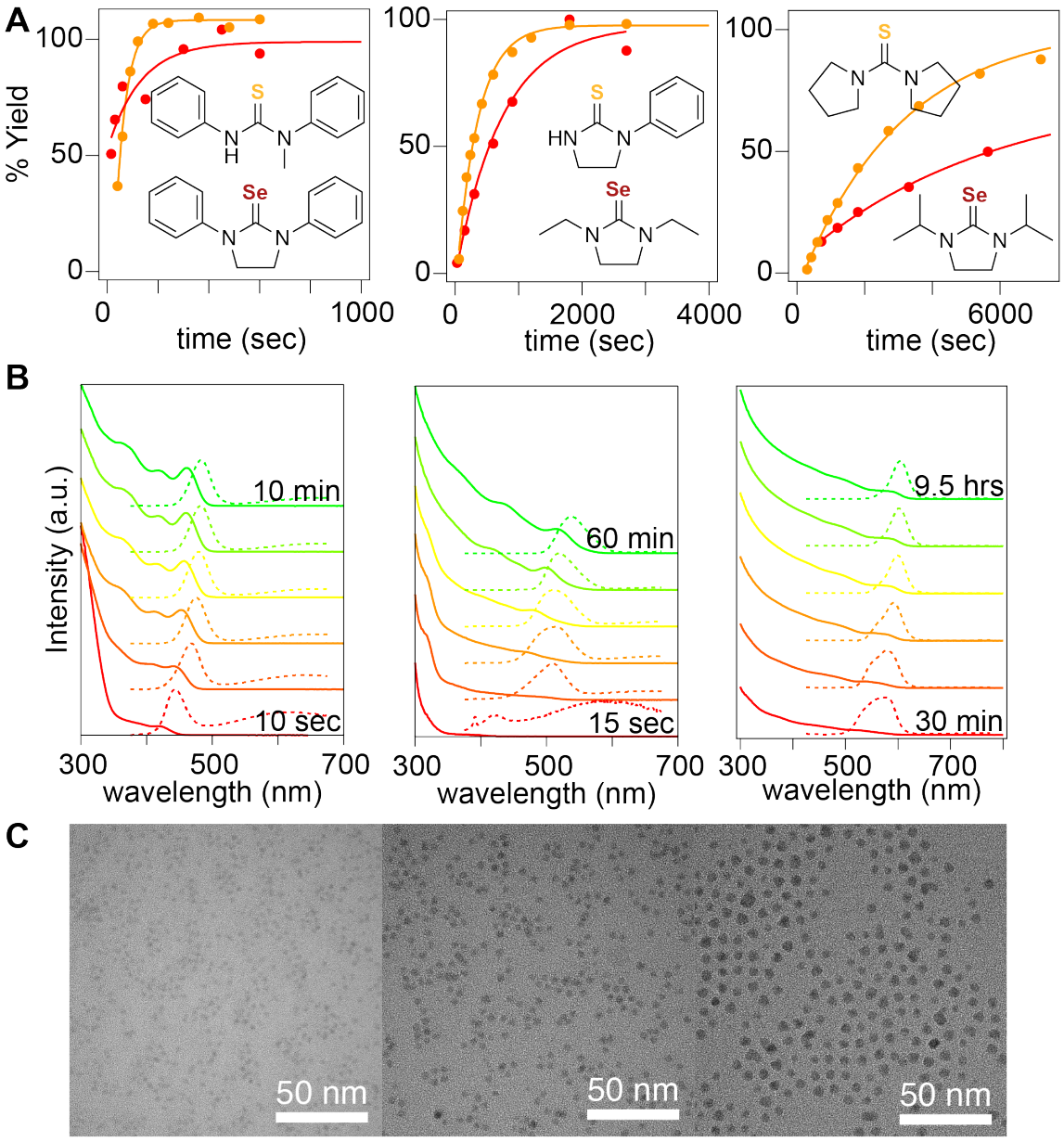

Figure 3.6.5. A) Precursor conversion rates for three matched pairs of precursors. B) Absorbance and fluorescence spectra. C) TEM of $CdS_{0.5}Se_{0.5}$ alloyed nanocrystals.

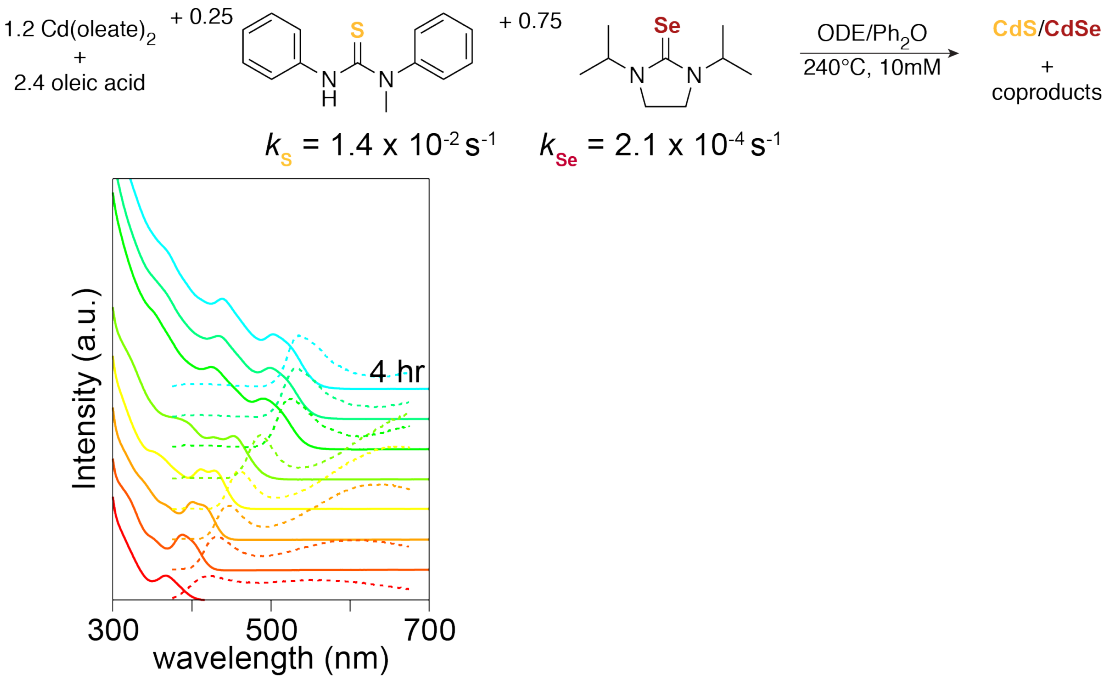

Figure 3.6.6. Reaction scheme and UV-vis/fluorescence spectra of a reaction to make medium sized CdS/CdSe core/shell nanocrystals that shows broad absorbance and fluorescence spectra.

3.7. Syringe Pump Shelling Method, to Access Thick CdS Shells

In order to get around the kinetic limitations of growing thick outer CdS shells where the shell material comprises > 95% of the final particle material, we developed two syringe pump shelling methods. The low reactivity of our precursors at room temperature allows tetramethylthiourea and cadmium oleate to be mixed at room temperature and added via syringe pump. Dropwise addition of this mixture into crude CdS/CdSe synthesis mixtures produces CdS shells up to 6 nm in diameter. Beyond this diameter the nanocrystals become insoluble. To

achieve thicker shells, trioctylphosphine and 2-hexyldecanoic acid are added to the shelling solution and the temperature increased to 290 °C (Figure 3.7.1). We select an injection speed based on the number of nanocrystals present in the shelling reaction. If the number of seeds is too low then shell precursors will supersaturate and nucleate a separate population of nanocrystals.

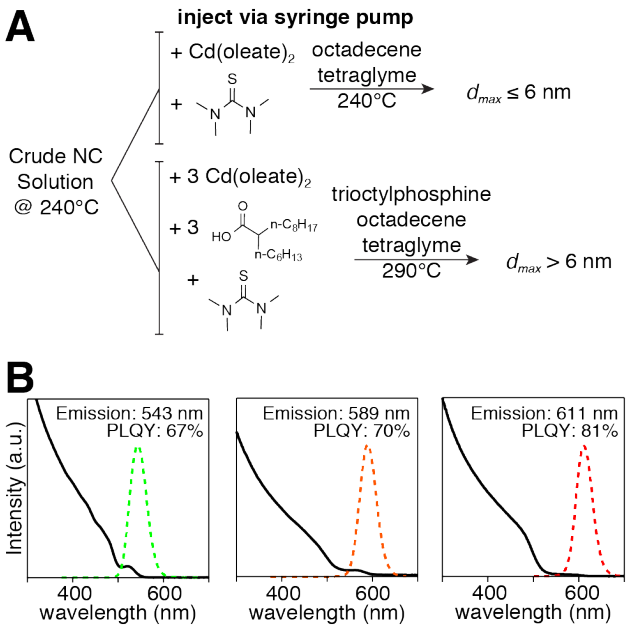

Figure 3.7.1. A) Synthetic scheme for the syringe pump injection of CdS precursors to grow thick outer shells. B) UV-vis and fluorescence spectra of CdS/CdSe/CdS SQWs synthesized using a one-pot core/shell reaction to form a CdS/CdSe nanocrystal and shelled further with CdS using a slow syringe pump method. Resulting nanocrystals exhibit high PLQY over a range of colors from green to red.

With this method, we can grow CdS/CdSe/CdS spherical quantum wells (SQWs)[22] with facile color tunability and high PLQY in a single pot. Incidentally, we can grow CdS/CdSe/CdS with a single injection of three chalcogen precursors,

but this approach is limited by constraints previously described (Figure 3.7.2). Additionally, upon elemental characterization of SQWs made via method 2 (Section 3.10.17.2), we observe that the CdSe region is off-centered, much like the CdSe/CdS core/shell (Figure 3.7.3). Nevertheless, these materials possess high PLQYs and are synthesized completely in one-pot avoiding the need for intermediate purification steps.

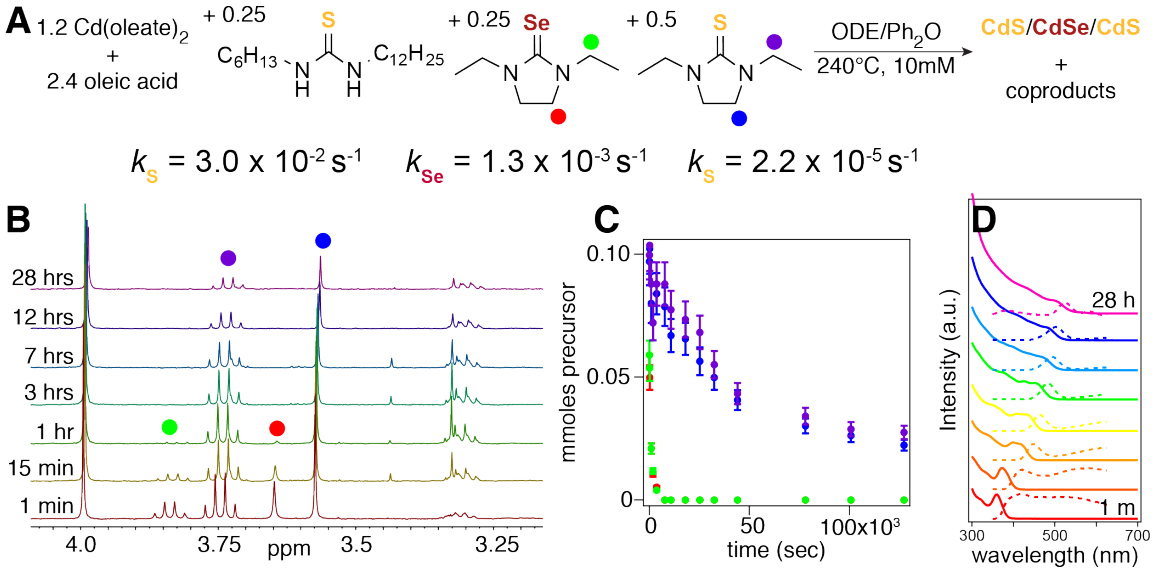

Figure 3.7.2. A) One pot/single precursor injection synthesis of CdS/CdSe/CdS. B) The reaction of cyclic thione and selenone precursors can be monitored by ^{1}H NMR and C) quantified. D) UV-vis and fluorescence spectra of reaction aliquots.

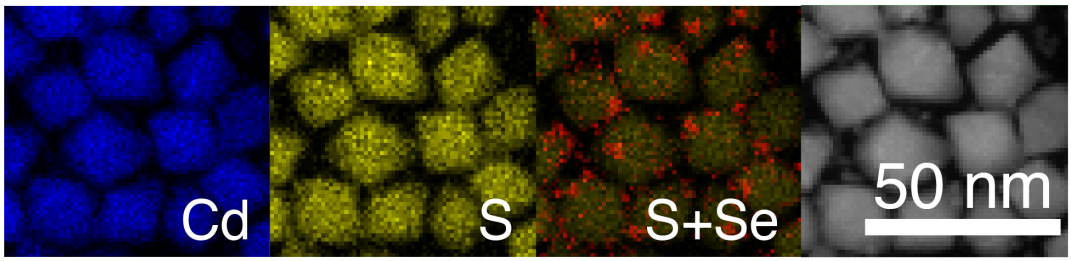

Figure 3.7.3. Elemental mapping of a CdS/CdSe/CdS nanocrystal with an outer shell grown via Method 2 (Section 3.10.17.2) shows the distribution of Se located anisotropically near a tip of the nanocrystals.

3.8. Extinction Coefficient Determination for CdS-CdSe Composites

To use CdS-CdSe composite nanocrystals in concentration dependent studies, it is useful to quantify the particle concentration via UV-vis. However, the extinction coefficients of CdS-CdSe composites are not well defined, despite numerous thorough investigations of core and shell layer thicknesses on optical spectra.[21] Although the intrinsic absorption coefficient has been determined experimentally for CdSe,[74] PbS,[75] PbSe[76] and $CsPbBr_3$ NCs,[77] this is not as straightforward for core-shell nanocrystals[78] and the yield of such syntheses has been monitored by theoretical values determined from the bulk dielectric function.[79] Here, we calculate the intrinsic absorption coefficient of CdS-CdSe composites using the intrinsic absorption coefficients of CdS and CdSe (Section 3.10.18). Indeed, for two materials with relatively similar optical constants, the intrinsic absorption coefficient of the core-shell nanocrystals μ_{i_cs} has been

approximated as a volume-weighted average of the intrinsic absorption coefficient of core μ_{i_c} and shell μ_{i_s}.[80]

$$\mu_{i\_cs} = \phi_c \mu_{i\_c} + \phi_s \mu_{i\_s}$$

Equation 3.8.1.

We estimate the molar ratio of core and shell material using the amount of selenoureas and thioureas initially injected and convert it to a volume fraction using the molar volume of CdSe and CdS. This is a reasonable estimate since the selenoureas and thioureas convert quantitatively to semiconductor. As such, we calculate the intrinsic absorption coefficient of various heterostructures. The intrinsic absorption coefficient can be converted to a molar extinction coefficient via

$$\varepsilon = \frac{N_A V_{NC}}{\ln 10 \times 10^{24}} \mu_i$$

Equation 3.8.2.

with N_A being Avogradro's number, V_{NC} the volume of one nanocrystal in nm^3 and ε in $cm^{-1}\,M^{-1}$ (Table 3.8.1). Together with the quantification of the bound oleate concentration via NMR, we were able to calculate ligand densities of 3.7 nm^{-2} for 5.4 nm CdS/CdSe/CdS quantum wells (Section 3.10.18). The excellent agreement of the ligand density with previous reported surface coverages for single component nanocrystals supports the accurateness of both the UV-vis and the NMR quantification.

Table 3.8.1. Calculated Extinction Coefficients for $CdSe_{1-x}S_x$ Composites.

Diameter (nm)	Emission (nm)	χ_{CdS}	$\mu_{i_{CdS_xSe_{1-x}}}$ (cm^{-1})	ε (cm^{-1} M^{-1})
5.4	543	0.952	1.41×10^5	3.04×10^6
6.1	589	0.867	1.44×10^5	4.48×10^6
10.9	611	0.955	1.41×10^5	2.50×10^6

3.9. Summary

We report the synthesis of new cyclic thione and selone precursors possessing appropriate reaction rates with cadmium oleate at 240 °C. These new chalcogen precursors expand our kinetic control over precursor conversion to span five orders of magnitude. Here we use kinetic control to synthesize CdS/CdSe, CdS_xSe_{1-x} alloys, and CdSe/CdS core/shell nanocrystals in a single hot injection. Towards further characterization of small cadmium chalcogenide nanocrystals of mixed composition, known precursor conversion kinetics can provide additional insight into the elemental composition. Inherent limitations of kinetic control require the synthesis of thick outer CdS shells with a syringe pump. We obtain color control and high PLQY of CdSe/CdS and CdS/CdSe/CdS particles synthesized via this method.

3.10. Experimental Details

3.10.1. General Methods

All manipulations were performed in air unless otherwise indicated.

3.10.2. Chemicals

Toluene (99.5%), methyl acetate (99%), ethyl acetate (≥99.8%), benzene (99.8%), hexanes (98.5%), methanol (99.8%), ethanol (≥99.8%), dichloromethane (≥99.5%), chloroform (≥99.8%), acetone (≥99.8%), acetonitrile (99.5%), cadmium nitrate tetrahydrate (98%), sodium hydroxide (≥98%), sodium bicarbonate (≥99.7%), hydrochloric acid (37%), sodium chloride (≥99%), sodium sulfate (≥99%), tetramethylthiourea (98%), phenyl isothiocyanate (98%), pyrrolidine (99%), dimethyl terepthalate (≥99.0%), triethyl orthoformate (98%), trifluoroacetic anhydride (≥99%), trifluoroacetic acid (99%), Selenium powder ~100 mesh (99.99%), and trioctylphosphine (97%) were obtained from Sigma Aldrich and used without further purification. Oleic acid (99%) and 1,1'-thiocarbonyldiimidazole (≥95.0% or 90%) were obtained from either Sigma Aldrich or Alfa Aesar and used without further purification. Diphenyl ether (99%), 1-octadecene (90%), hexadecane (99%), and tetraethylene glycol dimethyl ether ("tetraglyme" ≥99%) were obtained from Sigma Aldrich, stirred with calcium hydride overnight, and distilled prior to use. 2-hexyldecanoic acid (96%) was

obtained from Sigma Aldrich, stirred with sodium sulfate overnight, and distilled prior to use. Chloroform-*d* (99.8%), benzene-d_6 (99.5%), and methylene chloride-d_2 (99.8%) were obtained from Cambridge Isotopes and used without further purification. Cadmium oxide (99.99%) was obtained from Strem and used without further purification. *N*-Methylethylenediamine (95%), *N*-isopropylethylenediamine (98%), *N,N'*-Dimethylethylenediamine (99%), *N,N'*-Diphenyl ethylenediamine (98%), *N,N'*-Diisopropylethylenediamine (99%), *N*-Methyl-1,3-propanediamine (98%), *N*-isopropyl-1,3-propanediamine (95%), *N,N'*-Dimethyl-1,3-propanediamine (97%), *N,N'*-Diethyl-1,3-propanediamine (97%), and *N,N'*-Diisopropyl-1,3-propanediamine (96%) were obtained from Sigma Aldrich and used without further purification. *N*-Ethylethylenediamine (98%), and *N,N'*-Diethylethylenediamine (96%) were obtained from Alfa Aesar and used without further purification. *N*-phenylethylenediamine (98% or 99%) was obtained from either Sigma Aldrich or Acros Organics and used without further purification. Column Chromatography was performed with 40-63 μm Silica Gel (230-400 mesh).

3.10.3. Instrumentation

UV-vis spectra were obtained using a Perkin-Elmer Lambda 950 spectrophotometer equipped with deuterium and halogen lamps. Photoluminescence measurements were performed using a Fluoromax 4 from

Horiba Scientific, and photoluminescence quantum yields were determined using a quanta-phi integrating sphere accessory according to a previously described procedure.[81] Powder X-ray diffraction (XRD) was measured on a PANalytical X'Pert Powder X-ray diffractometer. Transmission electron microscopy (TEM) was performed on a FEI T12 BioTWIN and a FEI Talos F200X. Scanning transmission electron microscopy (STEM and EDX) was performed on a FEI Talos F200X.

3.10.4. Cadmium Oleate Synthesis

Cadmium oxide (99.99%) (9.5 g, 74 mmol, 1 eq.) and acetonitrile (95 mL) are stirred at room temperature. Trifluoroacetic acid (1.6 mL, 20.9 mmol, 0.28 eq.) and trifluoroacetic anhydride (11 mL, 79 mmol, 1.1 eq.) are added slowly and stirred for one hour. The cadmium oxide fully dissolves, yielding a clear colorless solution. To a 4 L Erlenmeyer flask, oleic acid (46.7 mL, 148 mmol, 2 eq.), dichloromethane (740 mL), and triethylamine (26.3 mL, 188.7 mmol, 2.55 eq.) are added. The cadmium trifluoroacetate solution is then added dropwise to the oleic acid solution with stirring. An additional 600 mL of acetonitrile are added resulting in the formation of a white precipitate. The mixture is heated to 60 °C in order to dissolve the precipitate, and the flask is slowly cooled to room temperature and then put in a -22 °C freezer. The resulting white powder is isolated by vacuum filtration and washing with 1 L acetonitrile, being careful to

thoroughly stir the slurry and break up large chunks. The product is dried under vacuum to yield a fine white powder. Typical yields are 49 g (98%).

3.10.5. Tetrasubstituted, Trisubstituted, and Disubstituted Thiourea and Selenourea Synthesis

These compounds were prepared as described previously.[5-7]

3.10.6. Imidazolidine and Tetrahydropyrimidine Thione Synthesis

N,N'-dialkyl- and *N,N'*-diarylsubstituted imidazolidine thiones are prepared from 1,1'-thiocarbonyldiimidazole and the corresponding *N,N'*-substituted ethylenediamines. The reaction with alkyl-substituted diamines proceeds rapidly at room temperature with the evolution of heat, while the less nucleophilic *N,N'*-diarylethylenediamines convert over the course of an hour at 70 °C.

3.10.6.1. Example Synthesis of Mono-Aryl Imidazolidine Thiones: 1-phenylimidazolidine-2-thione ***(S(SIPh))***

1,1'-Thiocarbonyldiimidazole (1.09 g, 1.1 eq, 6.14 mmol) was dissolved in 10 mL of ethyl acetate. *N*-phenylethylenediamine (0.760 g, 1 eq, 5.58 mmol) was added dropwise to the solution. The solution was heated to 70 °C and reacted for 1 hour. After cooling, the resulting precipitate is collected via filtration and washed with hexanes to yield 0.905 g (91%) of **S(SIPh)**. The product was further purified

by recrystallization from ethyl acetate and hexanes to produce off-white crystals. Recrystallized yield: 0.835 g (84%).

3.10.6.2. Example Synthesis of Mono-Alkyl Imidazolidine Thiones and Tetrahydropyrimidine Thiones: 1-methylimidazolidine-2-thione ***(S(SIPh))***

N-methyl-ethylenediamine (1.22 g, 1 eq, 16.4 mmol) was dissolved in 100 mL of ethyl acetate. A suspension of 1,1′-thiocarbonyldiimidazole (3.23 g, 1.1 eq, 18.1 mmol) in 100 mL of ethyl acetate was added to the diamine solution slowly over the course of 10 minutes. The mixture was allowed to stir at room temperature for 1 hour. The reaction solution was gravity filtered to remove a red precipitate, and the filtrate was evaporated to produce an orange solid. This solid was dissolved in a minimal amount of dichloromethane and was loaded onto a column where product was eluted out with ethyl acetate. The fractions were consolidated and evaporated to yield **S(SIMe)** as white crystals.

3.10.6.3. Example Synthesis of Di-Aryl Imidazolidine Thiones: 1,3-diphenylimidazolidine-2-thione ***(S(SIPh$_2$))***

1,1′-Thiocarbonyldiimidazole (1.09 g, 1.1 eq, 6.14 mmol) was dissolved in 10 mL of ethyl acetate. *N,N′*-diphenylethylenediamine (1.19 g, 1 eq, 5.58 mmol) was added dropwise to the solution. The solution was heated to 70 °C and reacted for 1 hour. After cooling, the resulting precipitate is collected via filtration and

washed with hexanes to yield 1.20 g (85%) of **S(SIPh$_2$)**. The product was further purified by recrystallization from ethyl acetate and hexanes to produce pale off-white crystals.

3.10.6.4. Example Synthesis of Di-Alkyl Imidazolidine Thiones: 1,3-dimethylimidazolidine-2-thione ***(S(SIMe$_2$))***

1,1'-Thiocarbonyldiimidazole (1.09,g, 1.1 eq, 6.14 mmol) was dissolved in 10 mL of ethyl acetate. *N,N'*-dimethylethylenediamine (0.492 g, 1 eq, 5.58 mmol) was added dropwise to the solution, producing heat. The reaction was extracted with 10% HCl (10 mL), saturated $NaHCO_3$ (10 mL), and then dried over Na_2SO_4. The resulting solution was evaporated to yield 0.56 g (77%) of **S(SIMe$_2$)** as a pale off white powder. The product was further purified by recrystallization from ethyl acetate and hexanes to produce colorless crystals of **S(SIMe$_2$)**.

3.10.7. Imidazolidine and Tetrahydropyrimidine Selenone Synthesis

Adapting a procedure from Zhou et. al.,[63] selenium (97.5 mmol), triethyl orthoformate (195 mmol), and diamine (97.5 mmol) were added to a Straus tube equipped with a distillation apparatus. The reaction mixture was degassed by the freeze-pump-thaw method, placed under an argon atmosphere, and heated to 130 °C with stirring for 8 hours. Over this period, the selenium dissolved and a small amount of liquid condensed in the receiving flask. The reaction mixture was then

allowed to cool to room temperature and the triethyl orthoformate was evaporated off. The remaining solid was dissolved in dichloromethane in air, filtered through celite, and was recrystallized once outside of the glovebox in dichloromethane. The resulting solid residue was brought into a nitrogen-filled glove box, where it was dissolved in acetonitrile and syringe filtered (PTFE, 0.2 μm), and then purified by recrystallization from acetonitrile. The container was stored in a –40 °C freezer for > 2 hours to precipitate product. The resulting solid was isolated by suction filtration using a glass fritted funnel and washing thoroughly with pentane, and then dried under vacuum for > 6 hours.

3.10.7.1. Example Synthesis: 1,3-diethylimidazolidine-2-selenone ***(Se(SIEt$_2$))***

1,3-Diethylimidazolidine-2-selenone was prepared according to the general procedure from *N,N'*-diethylethylenediamine (11.330 g, 13.97 mL, 97.5 mmol), selenium (7.699 g, 97.5 mmol), and triethyl orthoformate (28.899 g, 32.43 mL, 195 mmol).

3.10.8. Kinetics Modeling

Our nanoparticle composition modeling is based on a kinetic scheme where selenium and sulfur precursors simultaneously react with cadmium precursors that form nuclei which grow larger through the co-deposition of CdSe and CdS. According to previous experimental observations, the growth of our nanocrystals

can be fit well to first order reaction kinetics, where the reaction of the chalcogen precursors to form soluble solute is the rate-limiting step:

$$CdX_2 \quad + \quad \begin{matrix} Se-precursor \\ S-precursor \end{matrix} \quad \begin{matrix} \overset{k_{Se}}{\longrightarrow} \\ \overset{k_{Se}}{\longrightarrow} \end{matrix} \quad \begin{matrix} [CdSe]_i \\ [CdS]_i \end{matrix} \quad \rightarrow \quad CdS_xSe_{1-x}\ nanocrystal$$

Equation 3.10.1.

The rate equations are written as:

$$\frac{d[CdSe]}{dt} = -\frac{d[Se]}{dt} = k_{Se} \cdot [Se]$$

Equation 3.10.2.

$$\frac{d[CdS]}{dt} = -\frac{d[S]}{dt} = k_S \cdot [S]$$

Equation 3.10.3.

where $[CdSe]$, $[CdS]$, $[Se]$ and $[S]$ are the concentrations of crystalized CdSe and CdS, selenium and sulfur precursors, respectively, and k_{Se} and k_S are the first order rate constants of selenium and sulfur precursors.

Based on the Sugimoto nucleation model, the number of nuclei at the end of the reaction (n_∞) is proportional to the initial monomer generation rate, which is consistent with previous experiments. In our case, n_∞ is given by:

$$n_\infty = A \cdot (k_{Se} \cdot [Se]_0 \ + \ k_S \cdot [S]_0)$$

Equation 3.10.4.

where $[Se]_0$ and $[S]_0$ are the initial precursor concentrations, and A is a constant that can be experimentally determined.

Assuming the nucleation happens instantly in the beginning of the reaction and the number of nuclei stays constant throughout the reaction, we can calculate the size evolution of the particle based on:

$$\frac{dV_{QD}}{dt} = (\frac{d[CdSe]}{dt} \cdot V_{m,CdSe} + \frac{d[CdS]}{dt} \cdot V_{m,CdS}) \cdot V_{Reaction}/n_{\infty}$$

Equation 3.10.5.

where $V_{m,CdSe}$ and $V_{m,CdS}$ are the molar volume of CdSe and CdS, respectively, V_{QD} is the volume of each QD, and $V_{Reaction}$ is the volume of the reaction solution. Solving this differential equation gives the time evolution of the volume of the QD, $V_{QD}(t)$. Assuming the particle is spherical in shape, the radius evolution with time, R_{QD}(t), can be calculated.

Meanwhile, the local composition (molar percentage of CdSe in CdE) at the surface of the particle at time t can be calculated by:

$$CdSe\%(t) = \frac{k_{Se} \cdot [CdSe](t)}{k_{Se} \cdot [CdSe](t) + k_S \cdot [CdS](t)} \cdot 100\%$$

Equation 3.10.6.

Now, the radial elemental profile within a particle can be presented by CdSe% versus R_{QD}.

3.10.9. General Synthesis of CdS, CdSe, and $CdSe_{1-x}S_x$ Nanocrystals

In a nitrogen-filled glove box, a three-neck round bottom flask is loaded with cadmium oleate (0.18 mmol, 0.122 g), 1-octadecene (14.25 mL, 11.2 g, 44.4

mmol), and oleic acid (0.102 g, 0.114 mL, 0.36 mmol,). A 4mL vial is filled with the desired sulfur and/or selenium precursor (0.15 mmol) and diphenyl ether or tetraglyme (0.75 mL, 0.75 g). Most compounds are more soluble in tetraglyme, however diphenyl ether is necessary to monitor reactions by ^{1}H NMR spectroscopy in the 3-4 ppm range. The three-neck round bottom flask is transferred to a Schlenk line and heated to 240 °C under Ar. The sulfur and/or selenium precursor solution is then injected into the cadmium oleate solution and left to react for the appropriate time. The resulting nanocrystals were isolated from the reaction mixture by precipitation with acetone and centrifugation. The yellow residue is redispersed in hexane (10 mL) and acetone (5–10 mL) is added in 0.5mL portions to precipitate cadmium oleate, without precipitating the nanocrystals. This solution was centrifuged. The supernatant was collected and the nanocrystals precipitated with the addition of 25 mL of acetone. The nanocrystals were washed three additional times with toluene/methyl acetate.

3.10.10. Nanocrystal Formation Kinetics via Absorption Spectra

Quantitative aliquots of approximately 0.1 mL were taken from a CdS or CdSe nanocrystal reaction and deposited into a previously weighed vial. A mass of toluene equal to 2.5x the weight of the aliquot was added to the vial to standardize aliquot concentration. UV-vis absorption spectra were taken of each aliquot and the concentration of cadmium chalcogenide in the aliquot was

calculated from the size dependent extinction coefficient at the first excitonic absorption maximum for CdS[7] or the size independent absorption coefficient of CdSe at 350 nm.[68] The kinetics collected from each method was fit to a first order fit whose rate constant is reported in Figure 3.4.3 and Table 3.4.1. Induction delays are obtained via this method and are reported in Figure 3.4.7.

3.10.11. Precursor Conversion Kinetics via ^{1}H NMR

Quantitative aliquots of 200 μL were taken from a CdS, CdSe, or mixed precursor reaction and diluted with 300 μL of CD_2Cl_2 and 100μL of a 22.4 mM solution of dimethyl terephthalate dissolved in CD_2Cl_2. Quantitative ^{1}H NMR spectra were collected with a relaxation delay time of 30 s. Diphenyl ether must be used as the injection solvent instead of tetraglyme in order to monitor precursor disappearance kinetics between 3.0-4.5 ppm. Precursor disappearance was quantified based on integrating against the dimethyl terephthalate internal standard and compared with the appearance of nanocrystal as determined by UV-vis absorbance spectra.

3.10.12. Determination of Number of Nanocrystals Nucleated

Reaction aliquots were analyzed by UV-vis. The percent conversion of precursor was determined from the concentration of CdSe, which was found by using the size-independent extinction coefficient of CdSe at 350 nm.[68] The λ_{max} was

selected at maximum conversion and was used to find the particle diameter, from which the total number of moles of CdSe per particle was calculated. The product of percent conversion and the total number of moles of precursor injected divided by the calculated number of moles of CdSe per particle yields the total number of particles.

3.10.13. CdSe/CdS Nanocrystal Synthesis

3.10.13.1. Emission = 514 nm

A three-neck round bottom flask is loaded with cadmium oleate (0.9 mmol, 0.608 g), 1-octadecene (148 mL), and oleic acid (0.508 g, 1.14 mL, 1.8 mmol) and degassed on a Schlenk line. In a nitrogen filled glovebox, a 4 mL vial is filled with *N*-butyl, *N'*-pyrrolidine selenourea (0.075 mmol, 0.0174 g), tetramethylthiourea (0.3 mmol, 0.030 g) and diphenyl ether (2.0 mL, 2.0 g). The three-neck round bottom flask is heated to 240 °C under Ar. The chalcogen precursor solution is injected into the cadmium oleate solution and reacted for 2 hours. Upon completion of the reaction, 1-octadecene may be distilled off *in vacuo* to reduce the reaction volume and facilitate cleaning. The resulting nanocrystals are isolated from the reaction mixture by precipitation and centrifugation as described above. This reaction is run at a lower concentration than standard conditions to prevent

mixing limited kinetics of the selenourea. This reaction does not scale to larger volumes particularly well due to fast selenourea conversion kinetics.

3.10.13.2. Emission = 622 nm

In a nitrogen-filled glove box, a three-neck round bottom flask is loaded with cadmium oleate (0.18 mmol, 0.122 g), 1-octadecene (14.25 mL), and oleic acid (0.102 g, 0.114 mL, 0.36 mmol). A 4 mL vial is filled with **Se(SI*t*-Bu$_2$)** (0.05 mmol, 0.013 g), **S(SIMe$_2$)** (0.1 mmol, 0.013 g) and diphenyl ether (0.75 mL, 0.75 g). The three-neck round bottom flask is transferred to a Schlenk line and heated to 240 °C under Ar. The chalcogen precursor solution is injected into the cadmium oleate solution and reacted for 8 hours. The resulting nanocrystals are isolated from the reaction mixture by precipitation and centrifugation as described above.

3.10.14. CdS/CdSe Nanocrystal Synthesis

3.10.14.1. Emission = 472 nm

In a nitrogen-filled glove box, a three-neck round bottom flask is loaded with cadmium oleate (0.18 mmol, 0.122 g), 1-octadecene (14.25 mL), and oleic acid (0.102 g, 0.114 mL, 0.36 mmol). A 4 mL vial is filled with *N*-hexyl, *N'*-dodecyl thiourea (0.075 mmol, 0.025 g), **Se(SIEt$_2$)** (0.075 mmol, 0.015 g) and tetraglyme (0.75 mL, 0.75 g). The three-neck round bottom flask is transferred to a Schlenk line and heated to 240 °C under Ar. The chalcogen precursor solution is injected into the

cadmium oleate solution and reacted for 1 hour. The resulting nanocrystals are isolated from the reaction mixture by precipitation and centrifugation as described above.

3.10.14.2. Emission = 513 nm

In a nitrogen-filled glove box, a three-neck round bottom flask is loaded with cadmium oleate (0.12 mmol, 0.081 g), 1-octadecene (9.5 mL), and oleic acid (0.068 g, 0.076 mL, 0.24 mmol). A 4 mL vial is filled with *N*-hexyl, *N'*-dodecyl thiourea (0.02 mmol, 0.0066 g), **Se(SIEt$_2$)** (0.08 mmol, 0.0164 g) and tetraglyme (0.5 mL, 0.5 g). The three-neck round bottom flask is transferred to a Schlenk line and heated to 240 °C under Ar. The chalcogen precursor solution is injected into the cadmium oleate solution and reacted for 1 hour. The resulting nanocrystals are isolated from the reaction mixture by precipitation and centrifugation as described above.

3.10.14.3. Emission = 544 nm

In a nitrogen-filled glove box, a three-neck round bottom flask is loaded with cadmium oleate (0.12 mmol, 0.081 g), 1-octadecene (9.5 mL), and oleic acid (0.068 g, 0.076 mL, 0.24 mmol). A 4 mL vial is filled with *N*-hexyl, *N'*-dodecyl thiourea (0.02 mmol, 0.0066 g), **Se(SIiPr$_2$)** (0.09 mmol, 0.021 g) and tetraglyme (0.5 mL, 0.5 g). The three-neck round bottom flask is transferred to a Schlenk line and

heated to 240 °C under Ar. The chalcogen precursor solution is injected into the cadmium oleate solution and reacted for 9.5 hours. The resulting nanocrystals are isolated from the reaction mixture by precipitation and centrifugation as described above.

3.10.14.4. CdS/CdSe With Larger CdS Core

In a nitrogen-filled glove box, a three-neck round bottom flask is loaded with cadmium oleate (0.18 mmol, 0.122 g), octadecene (14.25 mL), and oleic acid (0.102 g, 0.114 mL, 0.36 mmol). A 4 mL vial is filled with *N*-methyl, *N,N'*-diphenyl thiourea (0.0375 mmol, 0.009 g), **Se(SIiPr$_2$)** (0.1125 mmol, 0.026 g) and diphenyl ether (0.75 mL, 0.75 g). *N*-methyl, *N,N'*-diphenyl thiourea has slower conversion kinetics than *N*-hexyl, *N'*-dodecyl thiourea which is typically used for CdS/CdSe core/shell reactions and should nucleate a CdS larger core. The three-neck round bottom flask is transferred to a Schlenk line and heated to 240 °C under Ar. The chalcogen precursor solution is injected into the cadmium oleate solution and reacted for 9.5 hours. The resulting nanocrystals are isolated from the reaction mixture by precipitation and centrifugation as described above.

3.10.15. Alloy Nanocrystal Synthesis

3.10.15.1. D = 2.5 nm CdS_xSe_{1-x} Alloy Nanocrystal Synthesis

In a nitrogen-filled glove box, a three-neck round bottom flask is loaded with cadmium oleate (0.18 mmol, 0.122 g), 1-octadecene (14.25 mL), and oleic acid (0.102 g, 0.114 mL, 0.36 mmol). A 4 mL vial is filled with *N*-methyl, *N*,*N*′-diphenyl thiourea (0.0375-0.1125 mmol, 0.009-0.027 g), **Se(SIPh$_2$)** (0.0375-0.1125 mmol, 0.011-0.034 g) and diphenyl ether (0.75 mL, 0.75 g). The three-neck round bottom flask is transferred to a Schlenk line and heated to 240 °C under Ar. The chalcogen precursor solution is injected into the cadmium oleate solution and reacted for 10 minutes. The resulting nanocrystals are isolated from the reaction mixture by precipitation and centrifugation as described above.

3.10.15.2. D = 3.7 nm CdS_xSe_{1-x} Alloy Nanocrystal Synthesis

In a nitrogen-filled glove box, a three-neck round bottom flask is loaded with cadmium oleate (0.18 mmol, 0.122 g), octadecene (14.25 mL), and oleic acid (0.102 g, 0.114 mL, 0.36 mmol). A 4 mL vial is filled with **S(SIPh)** (0.075 mmol, 0.013 g), **Se(SIEt$_2$)** (0.075 mmol, 0.015 g) and diphenyl ether (0.75 mL, 0.75 g). The three-neck round bottom flask is transferred to a Schlenk line and heated to 240 °C under Ar. The chalcogen precursor solution is injected into the cadmium oleate solution and reacted for 1 hour. The resulting nanocrystals are isolated from the

reaction mixture by precipitation and centrifugation as described in the experimental.

3.10.15.3. D = 5.7 nm CdS_xSe_{1-x} Alloy Nanocrystal Synthesis

In a nitrogen-filled glove box, a three-neck round bottom flask is loaded with cadmium oleate (0.18 mmol, 0.122 g), octadecene (14.25 mL), and oleic acid (0.102 g, 0.114 mL, 0.36 mmol). A 4 mL vial is filled with dipyrroline thiourea (0.075 mmol, 0.014 g), **Se(SIiPr$_2$)** (0.075 mmol, 0.017 g) and diphenyl ether (0.75 mL, 0.75 g). The three-neck round bottom flask is transferred to a Schlenk line and heated to 240 °C under Ar. The chalcogen precursor solution is injected into the cadmium oleate solution and reacted for 9.5 hours. The resulting nanocrystals are isolated from the reaction mixture by precipitation and centrifugation as described above.

3.10.15.4. $CdS_{0.5}Se_{0.5}$/CdS Alloy/Shell Nanocrystal Synthesis

In a nitrogen-filled glove box, a three-neck round bottom flask is loaded with cadmium oleate (0.18 mmol, 0.122 g), 1-octadecene (14.25 mL), and oleic acid (0.102 g, 0.114 mL, 0.36 mmol). A 4 mL vial is filled with *N*-hexyl, *N'*-dodecyl thiourea (0.0375 mmol, 0.009 g), **Se(SIPh$_2$)** (0.0375 mmol, 0.011 g), **S(SIPh$_2$)** (0.075 mmol, 0.019 g) and diphenyl ether (0.75 mL, 0.75 g). The three-neck round bottom flask is transferred to a Schlenk line and heated to 240 °C under Ar. The chalcogen precursor solution is injected into the cadmium oleate solution and reacted for 12

hours. The resulting nanocrystals are isolated from the reaction mixture by precipitation and centrifugation as described above.

3.10.16. Shell Material Nucleation Experiments

3.10.16.1. CdSe/CdS Shell Nucleation Experiment

In a nitrogen-filled glove box, a three-neck round bottom flask is loaded with cadmium oleate (0.09 mmol, 0.061 g), octadecene (14.25 mL), and oleic acid (0.050 g, 0.057 mL, 0.18 mmol). A 4 mL vial is filled with *N*-butyl, *N'*-pyrrolidine selenourea (0.0075 mmol, 0.0017 g), tetramethylthiourea or **S(SIMe$_2$)** (0.03-0.0675 mmol) and diphenyl ether (0.75 mL, 0.75 g). The three-neck round bottom flask is transferred to a Schlenk line and heated to 240 °C under Ar. The chalcogen precursor solution is injected into the cadmium oleate solution and reacted for 2-5 hours. The resulting nanocrystals are isolated from the reaction mixture by precipitation and centrifugation as described in the experimental.

3.10.16.2. CdS/CdSe Shell Nucleation Experiment

In a nitrogen-filled glove box, a three-neck round bottom flask is loaded with cadmium oleate (0.06 mmol, 0.041 g), octadecene (4.75 mL), and oleic acid (0.034 g, 0.038 mL, 0.12 mmol). A 4 mL vial is filled with *N*-hexyl, *N'*-dodecyl thiourea (0.005 mmol, 0.0016 g), **Se(SIiPr$_2$)** (0.045 mmol, 0.0105 g) and diphenyl ether (2.5 mL, 2.5 g). The three-neck round bottom flask is transferred to a Schlenk

line and heated to 240 °C under Ar. The chalcogen precursor solution is injected into the cadmium oleate solution and reacted for 9.5 hours. The resulting nanocrystals are isolated from the reaction mixture by precipitation and centrifugation as described above.

The synthesis of the CdS/CdSe core/shell (right panel) is the CdS/CdSe Emission = 554 nm synthesis reported in the experimental.

3.10.17. Syringe Pump Shelling Methods

3.10.17.1. Syringe Pump Shelling Method 1

3.10.17.1.1. Shelling Solution Preparation

A solution of cadmium oleate (1.4 mmol, 0.945 g), and 1-octadecene (17.75 mL) is prepared in a three-neck round bottom flask in a nitrogen filled glovebox. The solution is transferred to a Schlenk line and heated to 100°C to dissolve the cadmium oleate. After full dissolution, the cadmium oleate solution is cooled to room temperature. In a 20 mL vial in a nitrogen filled glovebox, tetramethylthiourea (1.4 mmol, 0.185 g) is dissolved in tetraglyme (3.51 mL, 3.51 g). The tetramethylthiourea solution is added to the cooled cadmium oleate solution and mixed well to dissolve. This mixture is stable under argon at room temperature for at least 10 days.

3.10.17.1.2. Shelling Procedure

A nanocrystal reaction such as CdS/CdSe with Emission = 472 nm is prepared as described above. When the reaction is nearly complete, the shelling solution is dripped in at a rate of 1.7 mL/hr. Once the desired volume of shell solution has been injected, the reaction is held at 240 °C for 30 additional minutes before cooling to room temperature. Note, the syringe pump addition rate is dependent on the number of cores present in the reaction solution to avoid nucleation of shell precursors.

3.10.17.2. Syringe Pump Shelling Method 2

3.10.17.2.1. Shelling Solution Preparation

A solution of cadmium oleate (4.49 mmol, 3.03 g), 2-hexyldecanoic acid (4.5 mmol, 1.32 mL, 1.155 g), trioctylphosphine (2.24 mmol, 1.0 mL, 0.83 g), and 1-octadecene (41.25 mL) is prepared in a three-neck round bottom flask in a nitrogen filled glovebox. This solution may also be prepared outside of a glovebox and degassed on a Schlenk line. The solution is transferred to a Schlenk line and heated to 150°C in an oil bath to dissolve the cadmium oleate. After full dissolution, the cadmium oleate solution is cooled to room temperature. In a 20 mL vial in a nitrogen filled glovebox, tetramethylthiourea (1.5 mmol, 0.198 g) and tetraglyme

(2.175 mL, 2.175 g) are combined. The tetramethylthiourea solution is added to the cooled cadmium oleate solution and mixed well to dissolve.

3.10.17.2.2. Shelling Procedure

A nanocrystal reaction such as CdS/CdSe with Emission = 513 nm is prepared as described above. When the reaction is nearly complete, the shelling solution is dripped in at a rate of 7.5 mL/hr with a syringe pump. Once the first few drops of shelling solution hit the reaction solution, the temperature is raised to 290 °C and held there for the remainder of the reaction. Note, the syringe pump addition rate is dependent on the number of cores present in the reaction solution to avoid nucleation of shell precursors.

3.10.17.3. CdS/CdSe/CdS Emission: 543 nm

CdS/CdSe with Emission = 472 nm are prepared as described above. 21.5 mL of shell precursor solution are prepared and injected via method 1 at a rate of 1.7 mL/hr keeping the temperature constant at 240 °C. Once the injection is finished, the reaction is held at the reaction temperature for an additional 30 minutes before cooling. The resulting nanocrystals are isolated from the reaction mixture by precipitation and centrifugation as described above.

3.10.17.4. CdS/CdSe/CdS Emission: 589 nm

CdS/CdSe with Emission = 513 nm are prepared as described above but on a 2x scale. 46 mL of shell precursor solution are prepared and injected via method 2 at a rate of 7.5 mL/hr. Once the injection finished, the reaction is held at the reaction temperature for an additional 30 minutes before cooling. The resulting nanocrystals are isolated from the reaction mixture by precipitation and centrifugation as described above.

3.10.17.5. CdS/CdSe/CdS Emission: 611 nm

CdS/CdSe with Emission = 554 nm are prepared as described above. 57.5 mL of shell precursor solution are prepared and injected via method 2 at a rate of 5 mL/hr. Once the injection finished, the reaction is held at the reaction temperature for an additional 30 minutes before cooling. The resulting nanocrystals are isolated from the reaction mixture by precipitation and centrifugation as described above.

3.10.18. Extinction Coefficients for CdS-CdSe Composites

UV-vis absorption spectroscopy has been established as a convenient tool to determine the nanocrystal concentration.[82] The volume fraction f of nanocrystals in solution is calculated from the absorbance A using the size-independent intrinsic absorption coefficient μ_i:

$$f = \frac{\ln 10 \times A}{\mu_i}$$

Equation 3.10.7.

The molar extinction coefficient of a nanocrystal ε is related to the intrinsic absorption coefficient by:

$$\varepsilon = \frac{N_A V_{NC}}{\ln 10 \times 10^{24}} \mu_i$$

Equation 3.10.8.

with N_A being Avogradro's number, V_{NC} the volume of one nanocrystal in nm^3 and ε in $cm^{-1}\ M^{-1}$. We use the recently reported size-dependent molar extinction coefficient of zincblende CdS NCs to calculate the intrinsic absorption coefficient of CdS at 320 nm: μ_i = 1.39 10^5 M^{-1}. Furthermore, we know the intrinsic absorption coefficient of zincblende CdSe at 320 nm: μ_i = 1.74 10^5 M^{-1}.[83] For two materials with relatively similar optical constants, the intrinsic absorption coefficient of the core-shell nanocrystals μ_{i_cs} is a volume weighted average of the intrinsic absorption coefficient of core μ_{i_c} and shell μ_{i_s}.[80]

$$\mu_{i\_cs} = \phi_c \mu_{i\_c} + \phi_s \mu_{i\_s}$$

Equation 3.10.9.

We estimate the molar ratio χ of core and shell material based on the amount of selenoureas and thioureas. This is a reasonable assumption as they go to full yield. Using the molar volumes, the molar ratios are converted in volume ratios resulting in

$$\mu_{i_{CdS_xSe_{1-x}}} = \frac{\chi_{CdSe} \times 32.9}{\chi_{CdSe} \times 32.9 + \chi_{CdS} \times 29.9} \mu_{i_{CdSe}} + \frac{\chi_{CdS} \times 29.9}{\chi_{CdSe} \times 32.9 + \chi_{CdS} \times 29.9} \mu_{i_{CdS}}$$

Equation 3.10.10.

Finally the molar extinction coefficient is calculated for a particular size, according to the above relation between molar extinction coefficient and intrinsic absorption coefficient. Table 3.8.1 in the main text provides four examples of this calculation.

Using these molar extinction coefficients and quantifying the number of oleate ligands via ^{1}NMR, we find reasonable ligand densities for these nanocrystals:

Table 3.10.1. A table of CdS-CdSe nanocrystal properties, nanocrystal concentration, oleate ligand concentration, and ligand density as determined from the calculated CdS-CdSe composite extinction coefficients.

Diameter (nm)	Emission (nm)	Concentration of NCs (μM)	Concentration of oleates (μM)	Ligand Density (nm^{-2})
5.4	543	105	34	3.7

3.10.19. Precursor Characterization

1-phenylimidazolidine-2-thione (S(SIPh)).

Yield: 0.835 g (84%). ^{1}H NMR (400 MHz, CD_2Cl_2): δ = 3.69-3.78 (m, 2H, -CH_2), 4.14-4.24 (m, 2H, -CH_2), 6.35 (br, 1H, NH), 7.24-7.32 (m, 1H, *p*-CH), 7.39-7.48 (m, 2H, *m*-CH), 7.58-7.65 (m, 2H, *o*-C); ^{13}C{^{1}H} (125 MHz, $CDCl_3$): δ = 41.71 (-CH_2), 52.16 (-CH_2), 124.56 (*m*-CH), 126.44 (*p*-C), 128.86 (*o*-C), 140.02 (*i*-C), 182.75 (C(S)); Anal. Calcd for $C_9H_{10}N_2S$: C, 60.64; H, 5.65; N, 15.72. Found: C, 60.41; H, 5.41; N, 15.67. MS (ASAP) *m*/*z* Calcd for [$C_9H_{10}N_2S$ + H^+]: 179.06. Found: 179.06.

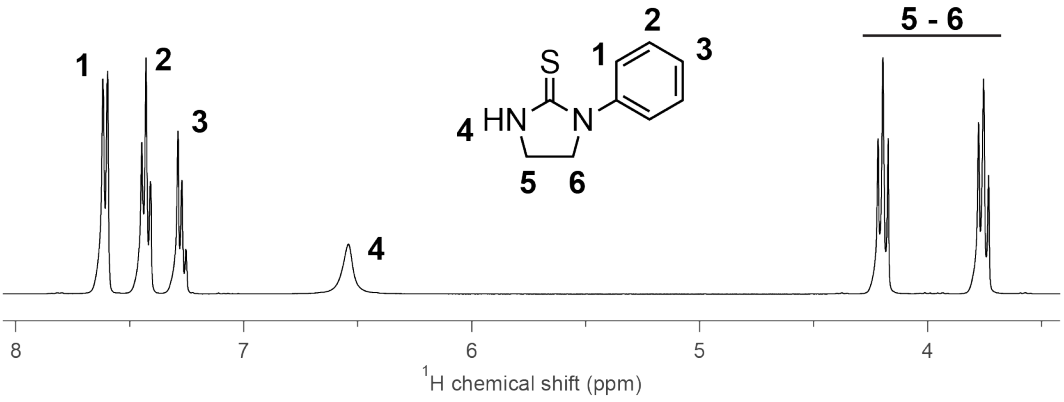

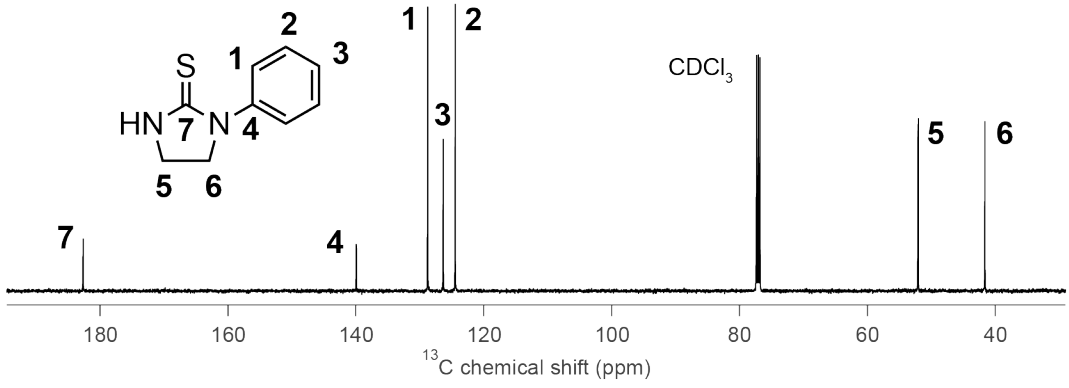

1-methylimidazolidine-2-thione (S(SIMe)).

Yield: 1.346 g (71%)). ^{1}H NMR (400 MHz, $CDCl_3$): δ = 3.13 (s, 3H, -CH_3), 3.56 (t, 2H, -CH_2), 3.71 (t, 2H, -CH_2) 5.88 (br, 1H, NH);^{13}C{^{1}H} (100 MHz, $CDCl_3$): δ = 34.30 (-CH_3), 41.17 (-CH_2), 51.19 (-CH_2), 184.07 (C(S)); Anal. Calcd for $C_4H_8N_2S$: C, 41.35; H, 6.94; N, 24.11. Found: C, 41.88; H, 6.88; N, 24.05. MS (ASAP) *m/z* Calcd for [$C_4H_8N_2S$ + H^+]: 117.05. Found: 117.05.

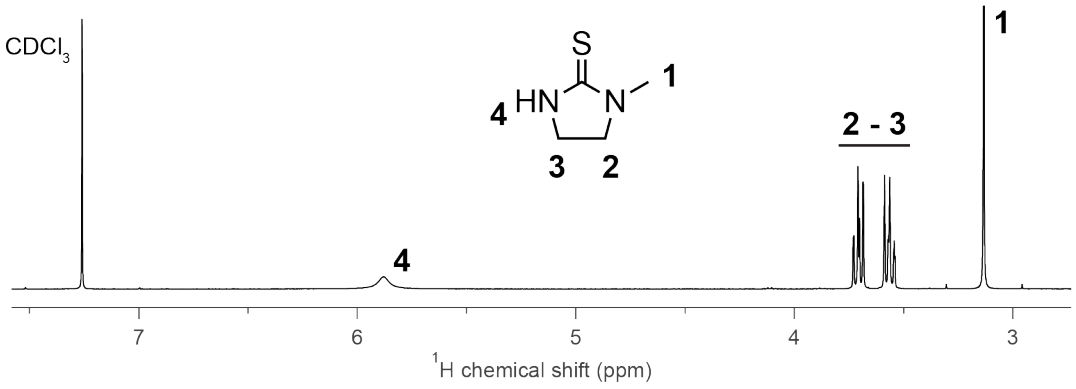

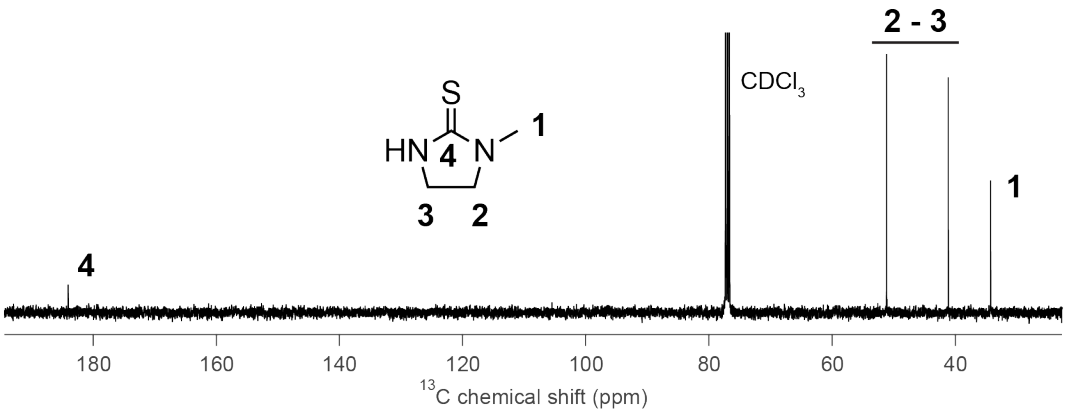

1-ethylimidazolidine-2-thione (S(SIEt)).

Yield: 1.56 g (73%). ^{1}H NMR (400 MHz, $CDCl_3$): δ = 1.19 (t, 3H, -CH_3), 3.66 (m, 6H, -CH_2 & -$\underline{CH_2}CH_3$), 5.83 (br, 1H, NH); $^{13}C\{^{1}H\}$ (100 MHz, $CDCl_3$): δ = 12.13 (-CH_3), 41.31 (-CH_2), 41.57 ($\underline{CH_2}CH_3$), 47.90 (-CH_2), 182.90 (C(S)); Anal. Calcd for $C_5H_{10}N_2S$: C, 46.12; H, 7.74; N, 21.51. Found: C, 45.86; H, 7.57; N, 21.29. MS (ASAP) *m*/*z* Calcd for [$C_5H_{10}N_2S + H^+$]: 131.06. Found: 131.06.

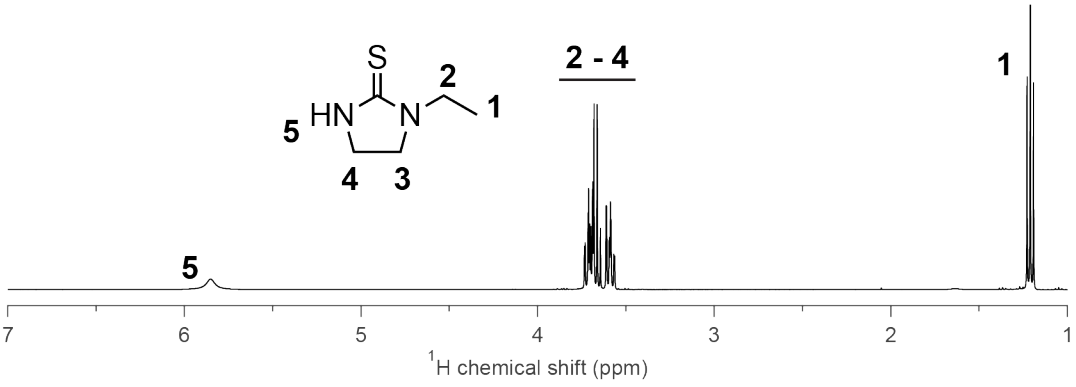

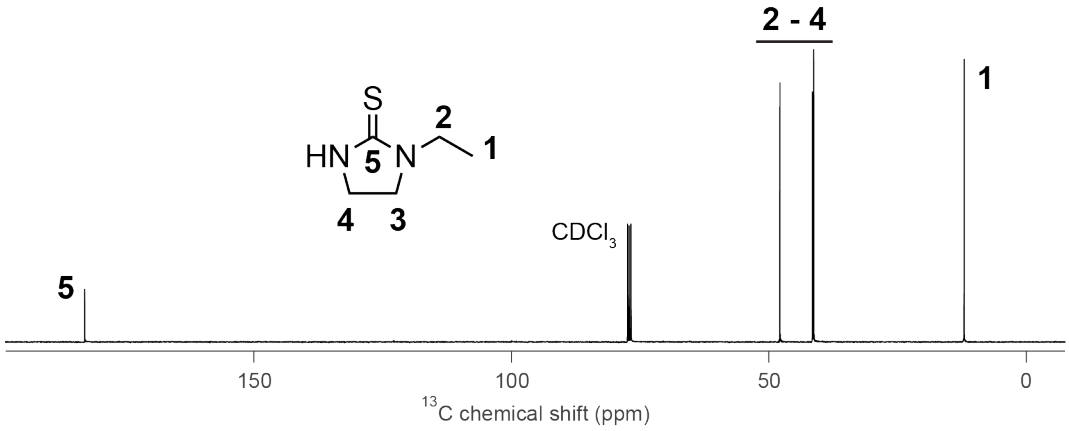

1-isopropylimidazolidine-2-thione (S(SIiPr)).

Yield: 1.05 g (74%). ^{1}H NMR (400 MHz, $CDCl_3$): δ = 1.17 (d, 6H, -CH_3), 3.59 (m, 4H, CH_2), 4.78 (m, 1H, -CH), 5.91 (br, 1H, NH); $^{13}C\{^{1}H\}$ (100 MHz, $CDCl_3$): δ = 19.36 (-CH_3), 41.52 (-CH_2), 42.88 (-CH_2), 46.92 (-CH) 182.54 (C(S)); Anal. Calcd for $C_6H_{12}N_2S$: C, 49.96; H, 8.39; N, 19.42. Found: C, 50.25; H, 8.18; N, 19.36. MS (ASAP) *m*/*z* Calcd for [$C_6H_{12}N_2S + H^+$]: 145.08. Found: 145.08.

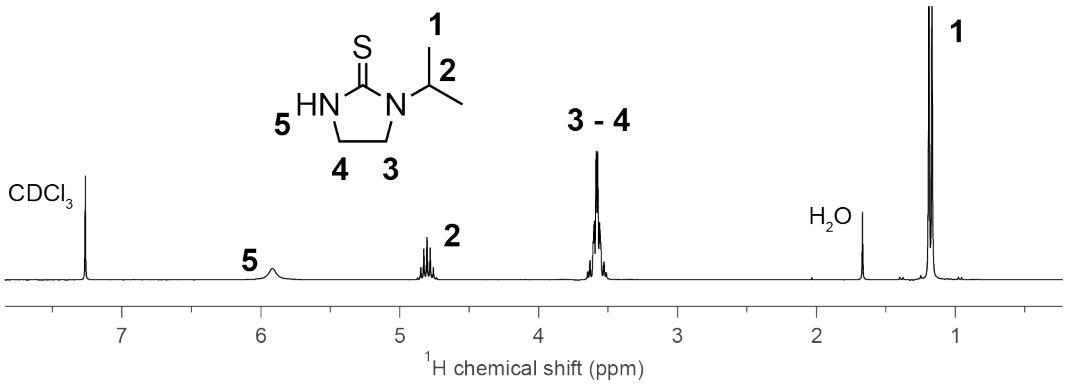

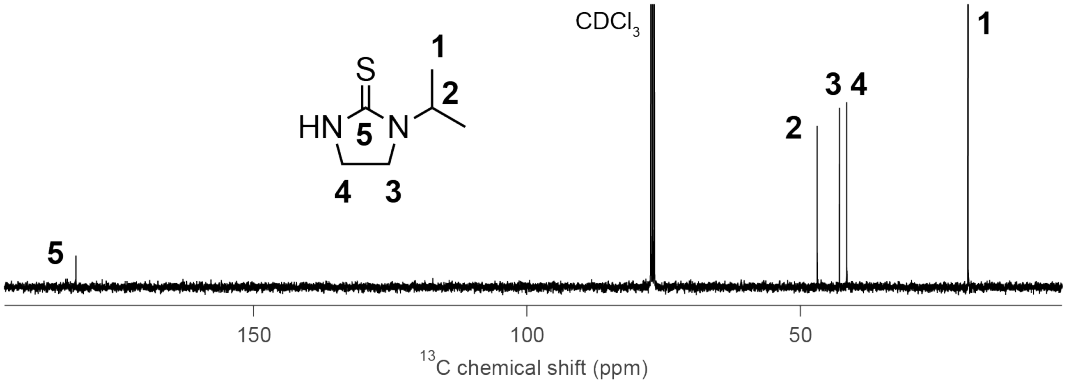

1,3-diphenylimidazolidine-2-thione (S(SIPh$_2$)).

Yield: 1.10 g (78%). ^{1}H NMR (400 MHz, C_6D_6): δ = 3.07 (s, 4H, -CH_2), 6.97-7.03 (m, 2H, *p*-CH), 7.14-7.23 (m, 4H, *m*-CH), 7.56-7.62 (m, 4H, *o*-CH); ^{13}C{^{1}H} (125 MHz, $CDCl_3$): δ = 49.41 (-CH_2), 125.47 (*m*-CH), 126.67 (*p*-CH), 128.89 (*o*-CH), 140.85 (*i*-CH), 181.27 (C(S)); Anal. Calcd for $C_{15}H_{14}N_2S$: C, 70.83; H, 5.55; N, 11.01. Found: C, 70.77; H, 5.57; N, 10.26. MS (ASAP) *m*/*z* Calcd for [$C_{15}H_{14}N_2S$ + H^+]: 255.10. Found: 255.10.

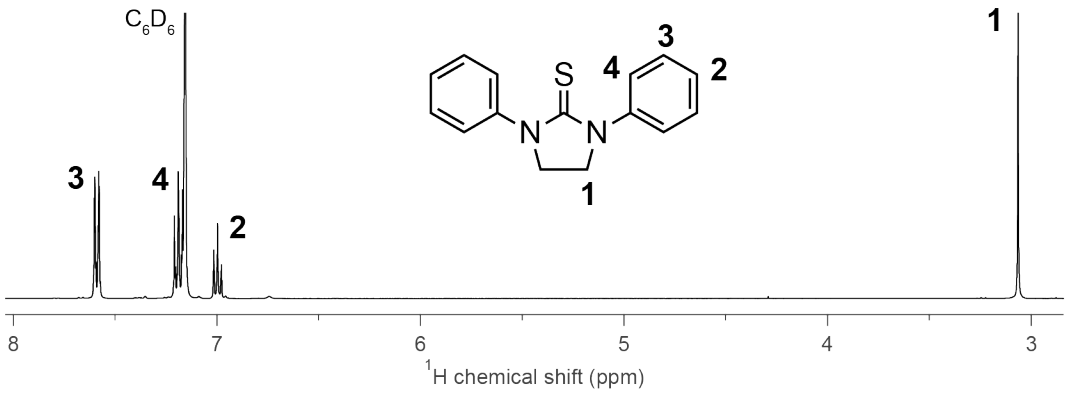

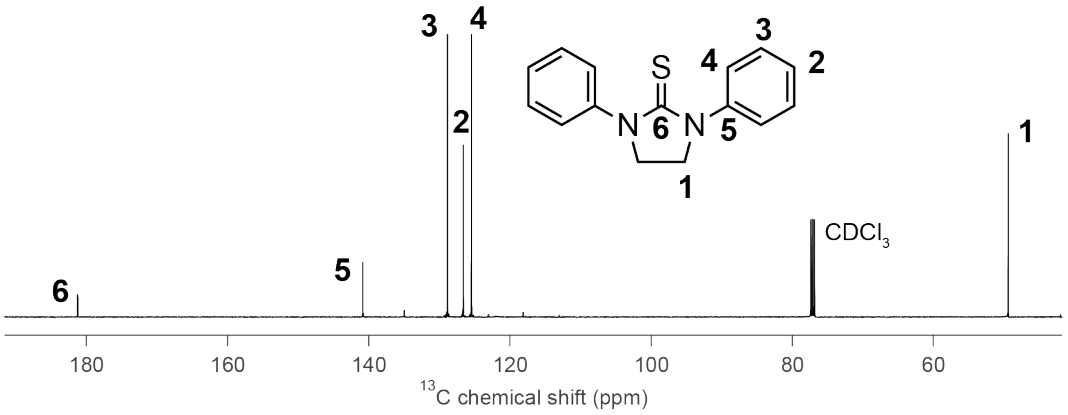

1,3-dimethylimidazolidine-2-thione (S(SIMe$_2$)).

Yield 0.436 g (60%). ^{1}H NMR (400 MHz, C_6D_6): δ = 2.38 (s, 4H, -CH_2), 2.81(s, 6H, -CH_3); $^{13}C\{^1H\}$ (100 MHz, C_6D_6): δ = 24.51 (-CH_3), 47.27 (-CH_2), 184.25 (C(S)); Anal. Calcd for $C_5H_{10}N_2S$: C, 46.12; H, 7.74; N, 21.51. Found: C, 46.25; H, 7.73; N, 21.45. MS (ASAP) *m*/*z* Calcd for [$C_5H_{10}N_2S + H^+$]: 131.06. Found: 131.06.

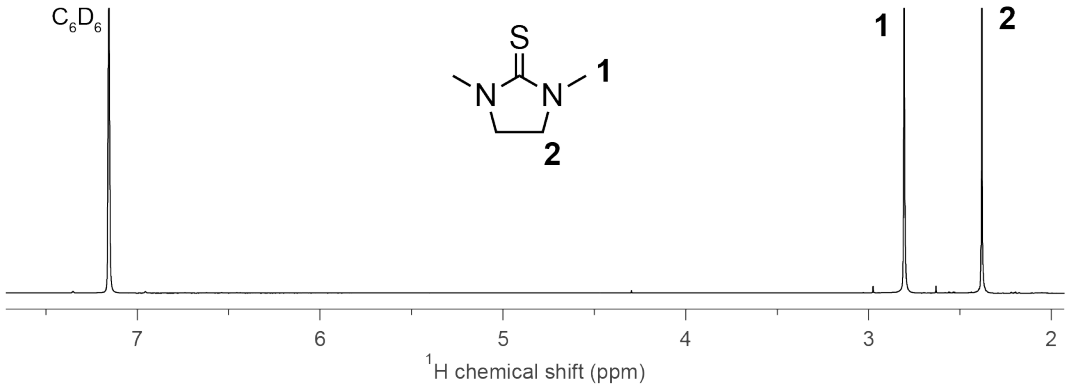

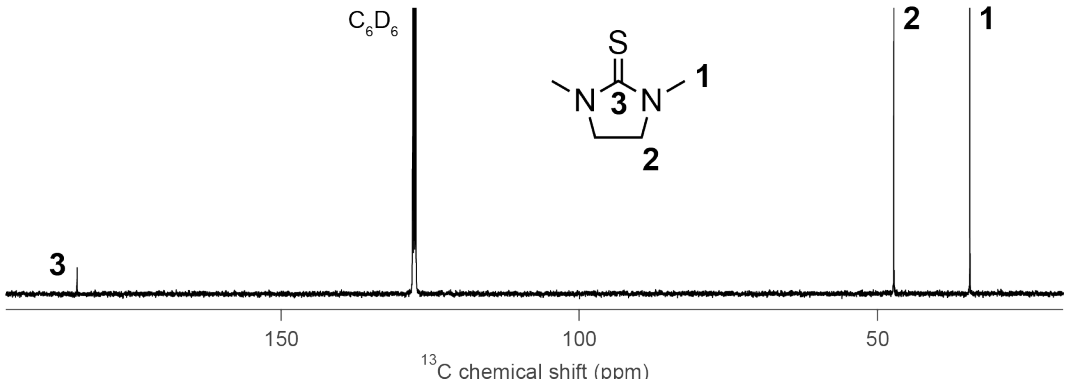

1,3-diethylimidazolidine-2-thione (S(SIEt$_2$)).

Yield: 0.657 g (74%). ^{1}H NMR (500 MHz, C_6D_6): δ = 0.87 (t, 6H, -CH_3), 2.54 (s, 4H, -CH_2), 3.52 (q, 4H, -$\underline{CH_2}CH_3$); $^{13}C\{^1H\}$ (125 MHz, $CDCl_3$): δ = 12.06 (-CH_3), 42.20 (-$\underline{CH_2}CH_3$), 45.35 (-CH_2), 181.82 (C(S)); Anal. Calcd for $C_7H_{14}N_2S$: C, 53.12; H, 8.92; N, 17.70. Found: C, 53.25; H, 8.75; N, 17.56. MS (ASAP) *m*/*z* Calcd for [$C_7H_{14}N_2S + H^+$]: 159.10. Found: 159.10.

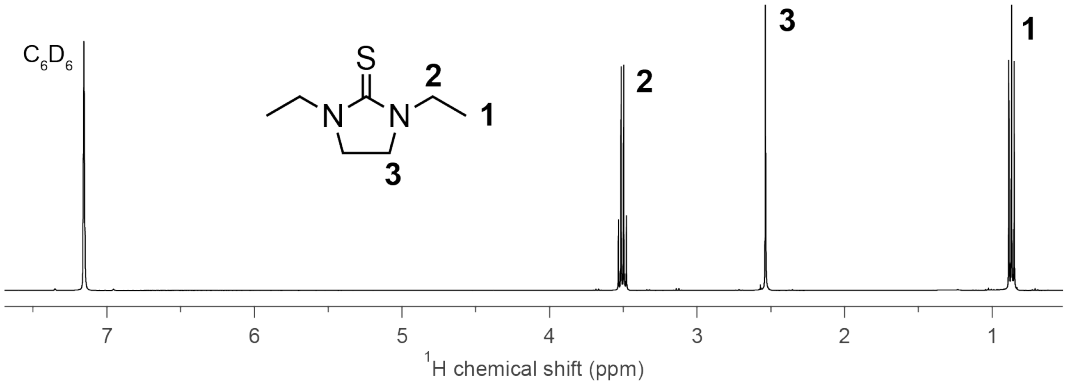

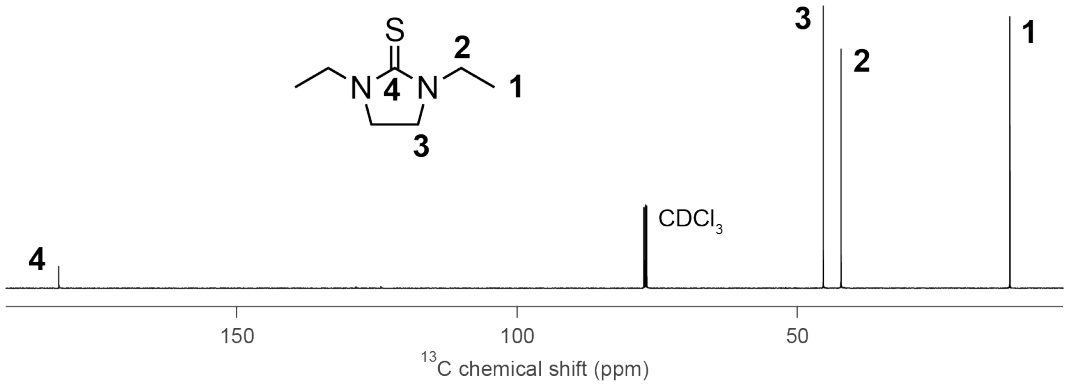

1,3-diisopropylimidazolidine-2-thione (S(SIiPr$_2$)).

Yield: 0.826 g (79%). ^{1}H NMR (400 MHz, C_6D_6): δ = 0.89 (d, 12H, -CH_3), 2.65 (s, 4H, -CH_2), 5.19 (m, 2H, -CH); ^{13}C{^{1}H} (100 MHz, C_6D_6): δ = 18.64 (-CH_3), 39.88 (-CH_2), 46.35 (-CH), 182.06 (C(S)); Anal. Calcd for $C_9H_{18}N_2S$: C, 58.02; H, 9.74; N, 15.04. Found: C, 58.12; H, 9.52; N, 15.02. MS (ASAP) *m*/*z* Calcd for [$C_9H_{18}N_2S + H^+$]: 187.13. Found: 187.13.

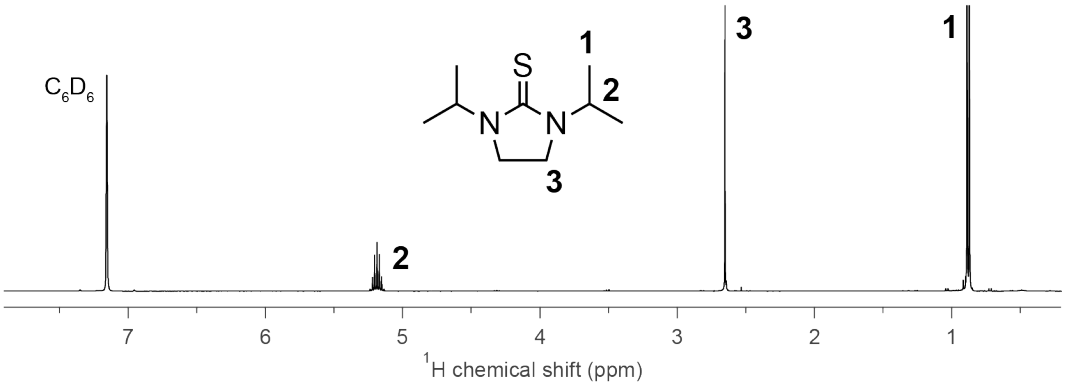

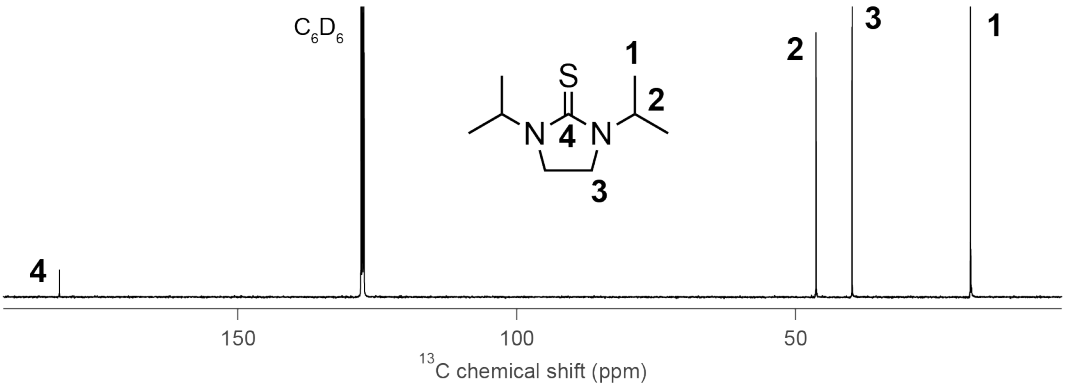

1-methyltetrahydropyrimidine-2(1*H*)-thione (S(PymMe)).

Yield: 1.16 g (54%). ^{1}H NMR (400 MHz, $CDCl_3$): δ = 2.01 (m, 2H, -CH_2), 3.28 (t, 2H, -CH_2), 3.35 (t, 2H, -CH_2), 3.39 (s, 3H, -CH_3), 6.35 (br, 1H, NH); ^{13}C{^{1}H} (100 MHz, $CDCl_3$): δ =21.12 (-CH_2), 40.75 (-CH_2), 42.12 (-CH_2), 48.35 (-CH_3), 178.04 (C(S)); Anal. Calcd for $C_5H_{10}N_2S$: C, 46.12; H, 7.74; N, 21.51. Found: C, 47.37; H, 7.62; N, 20.96. MS (ASAP) *m*/*z* Calcd for [$C_5H_{10}N_2S$ + H^+]: 131.06. Found: 131.06.

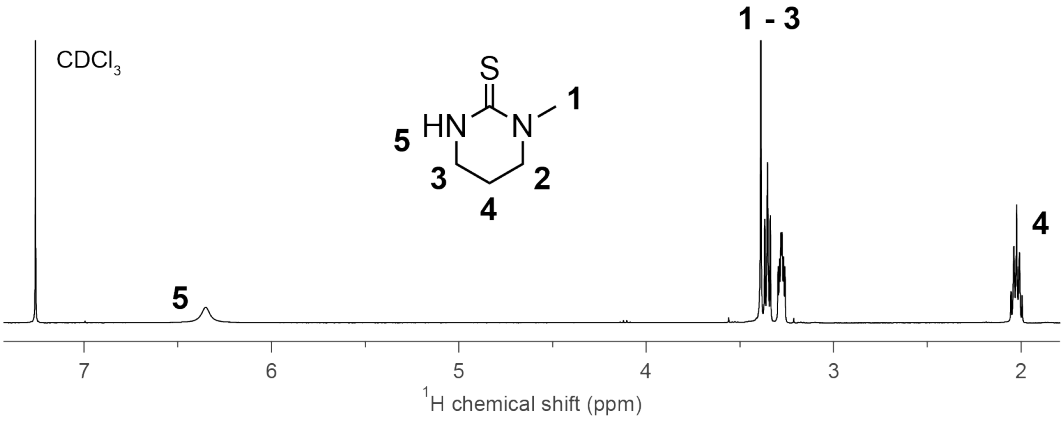

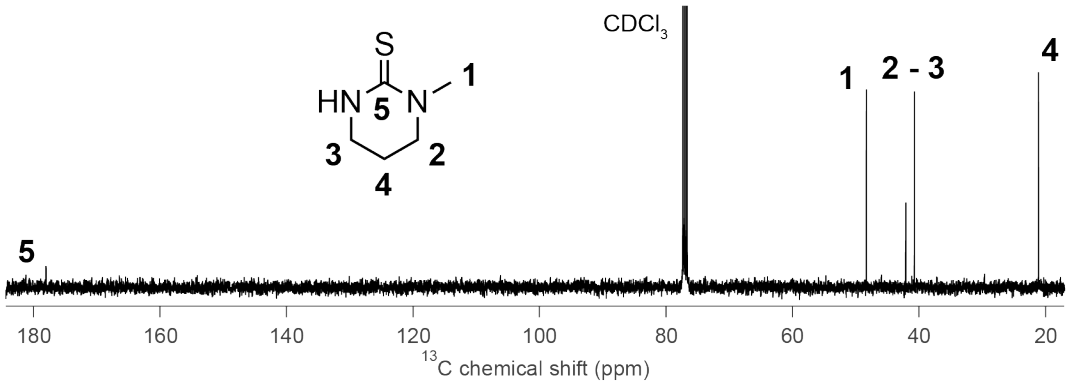

1-isopropyltetrahydropyrimidine-2(1*H*)-thione (S(PymiPr)).

Yield: 0.0263 g (46%). ^{1}H NMR (400 MHz, $CDCl_3$): δ = 1.16 (d, 6H, CH_3), 1.96 (m, 2H, CH_2), 3.24 (m, 4H, CH_2), 5.64 (m, 1H, CH), 6.25 (br, 1H, NH); ^{13}C{^{1}H} (100 MHz, $CDCl_3$): δ = 19.07 ($-CH_3$), 21.11 ($-CH_2$), 38.99 ($-CH_2$), 40.85 ($-CH_2$), 51.87 (-CH), 177.05 (C(S)); Anal. Calcd for $C_7H_{14}N_2S$: C, 53.12; H, 8.92; N, 17.70. Found: C, 53.32; H, 8.76; N, 17.72. MS (ASAP) *m*/*z* Calcd for [$C_7H_{14}N_2S + H^+$]: 159.10. Found: 159.10.

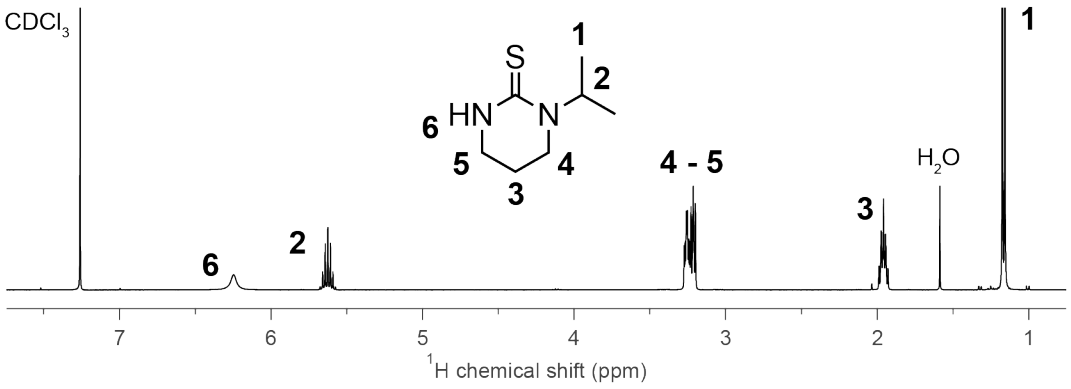

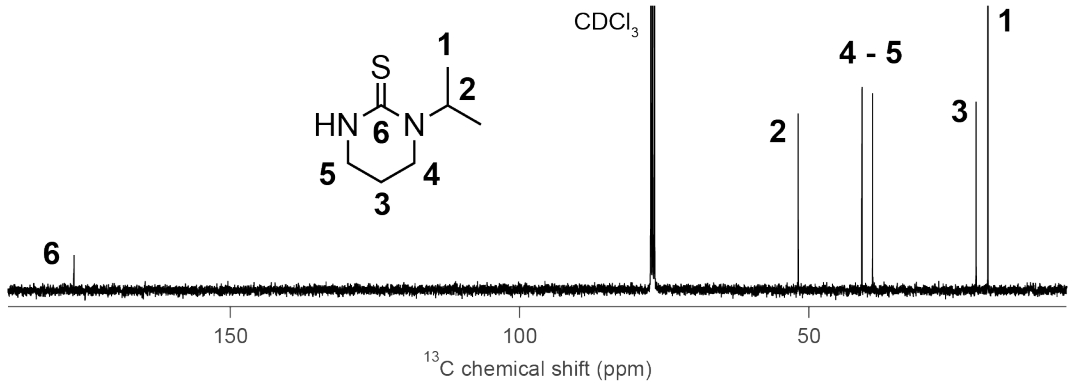

1,3-dimethyltetrahydropyrimidine-2(1*H*)-thione (S(PymMe$_2$)).

Yield: 0.373 g (72%). ^{1}H NMR (400 MHz, $CDCl_3$): δ = 2.04 (m, 2H, -CH_2), 3.38 (t, 4H, -CH_2), 3.43 (s, 6H, -CH_3); $^{13}C\{^1H\}$ (100 MHz, $CDCl_3$): δ = 21.15 (-CH_2), 43.46 (-CH_2), 48.87 (-CH_3) 179.38 (C(S)); Anal. Calcd for $C_6H_{12}N_2S$: C, 49.96; H, 8.39; N, 19.42. Found: C, 50.73; H, 8.27; N, 19.32. MS (ASAP) *m*/*z* Calcd for [$C_6H_{12}N_2S$ + H^+]: 145.08. Found: 145.08.

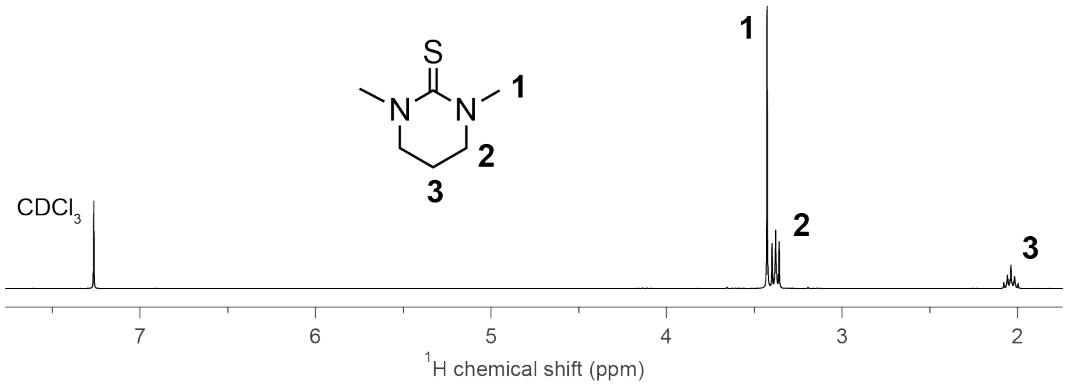

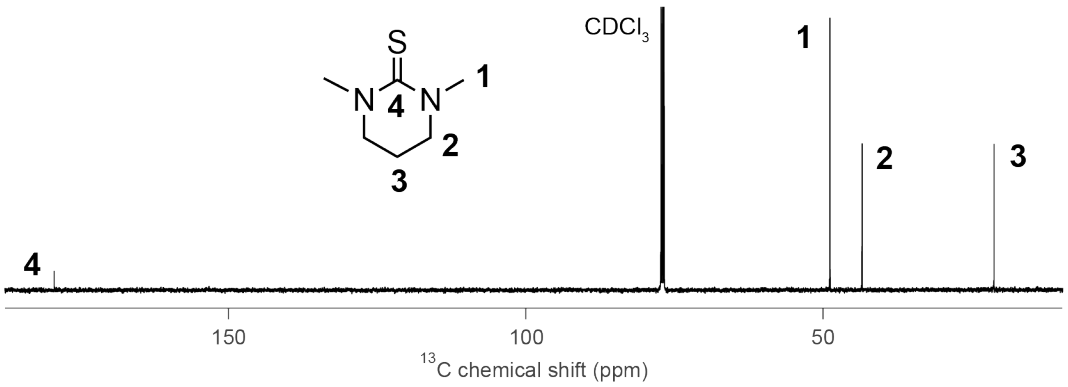

1,3-diethyltetrahydropyrimidine-2(1*H*)-thione (S(PymEt$_2$)).

Yield: 2.09 g (74%). ^{1}H NMR (400 MHz, $CDCl_3$): δ = 1.23 (t, 6H, -CH_3), 1.99 (m, 2H, -CH_2), 3.33 (t, 4H, -CH_2), 3.97 (q, 4H, -$\underline{CH_2}CH_3$); $^{13}C\{^1H\}$ (100 MHz, $CDCl_3$): δ = 12.13 (-CH_3), 21.38 (-CH_2), 46.08 (-CH_2), 49.86 (-$\underline{CH_2}CH_3$), 177.59 (C(S)); Anal. Calcd for $C_8H_{16}N_2S$: C, 55.77; H, 9.36; N, 16.26. Found: C, 56.03; H, 9.22; N, 16.29. MS (ASAP) *m*/*z* Calcd for [$C_8H_{16}N_2S + H^+$]: 173.11. Found: 173.11.

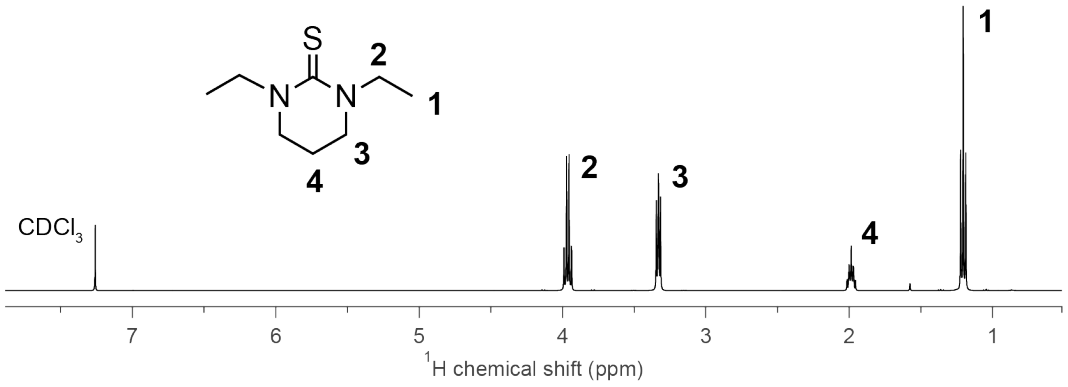

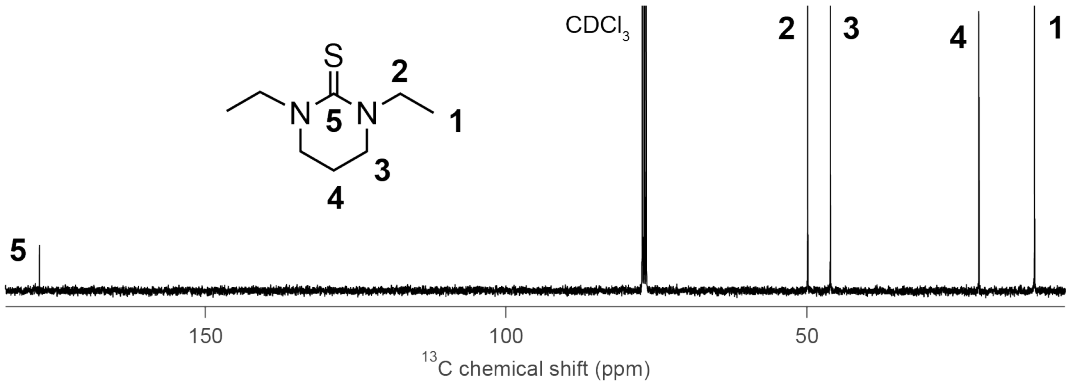

1,3-diisopropyltetrahydropyrimidine-2(1*H*)-thione (S(PymiPr$_2$)).

Yield: 1.16 g (76%). ^{1}H NMR (400 MHz, $CDCl_3$): δ = 1.16 (d, 12H, -CH_3), 1.91 (m, 2H, -CH_2), 3.18 (t, 4H, -CH_2), 5.91 (m, 2H, -CH); $^{13}C\{^1H\}$ (100 MHz, $CDCl_3$): δ = 19.23 (-CH_3), 21.76 (-CH_2), 39.59 (-CH_2), 52.19 (-CH), 177.88 (C(S)); Anal. Calcd for $C_{10}H_{20}N_2S$: C, 59.95; H, 10.06; N, 13.98. Found: C, 61.14; H, 10.11; N, 12.79. MS (ASAP) *m*/*z* Calcd for [$C_{10}H_{20}N_2S + H^+$]: 201.14. Found: 201.14.

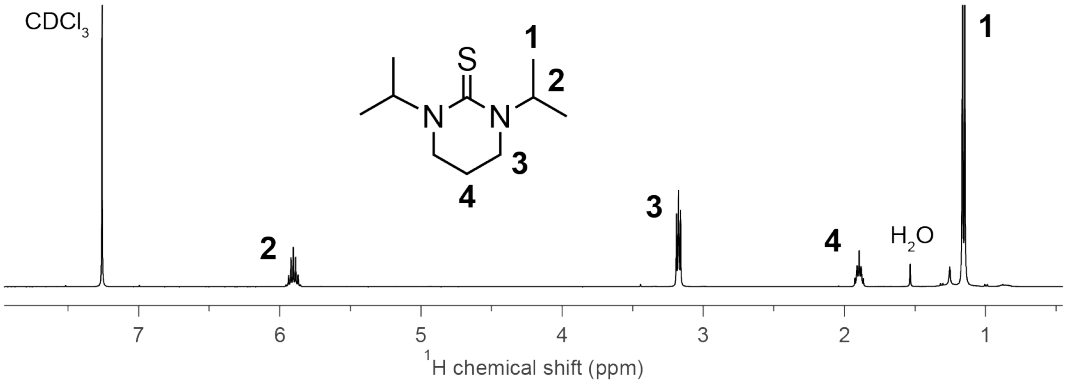

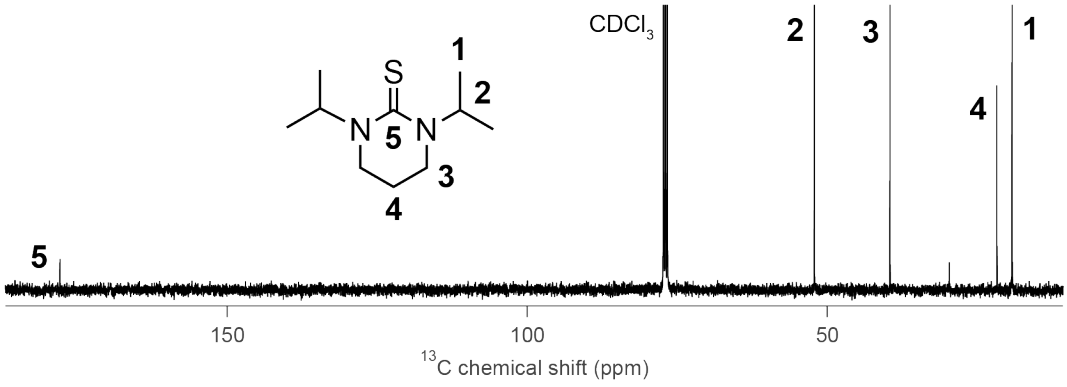

1-phenylimidazolidine-2-selenone (Se(SIPh)).

Yield: 6.85 g (25%). ^{1}H NMR (400 MHz, CD_2Cl_2): δ = 3.76 (t, 2H, -CH_2), 4.18 (t, 2H, -CH_2), 6.66 (br, 1H, NH), 7.34 (t, 1H, *p*-CH), 7.46 (t, 2H, *o*-CH), 7.61 (d, 2H, *m*-CH); ^{13}C{^{1}H} (101 MHz, CD_2Cl_2): δ = 43.16 (-CH_2), 52.91 (-CH_2), 125.36 (*m*-CH), 126.83 (*p*-CH), 128.67 (*o*-CH), 140.64 (*i*-C), 180.32 (C(Se)); ^{77}Se {^{1}H} (76 MHz, CD_2Cl_2): δ = 133.52; Anal. Calcd for $C_9H_{10}N_2Se$: C, 48.01; H, 4.48; N, 12.44. Found: C, 47.90; H, 4.49; N, 12.37. MS (ASAP) *m*/*z* Calcd for [$C_9H_{10}N_2Se + H^+$]: 227.01. Found: 227.01.

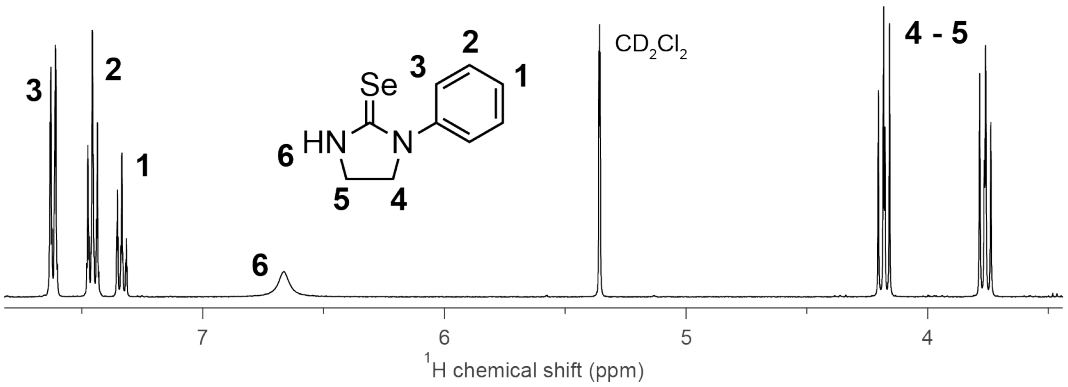

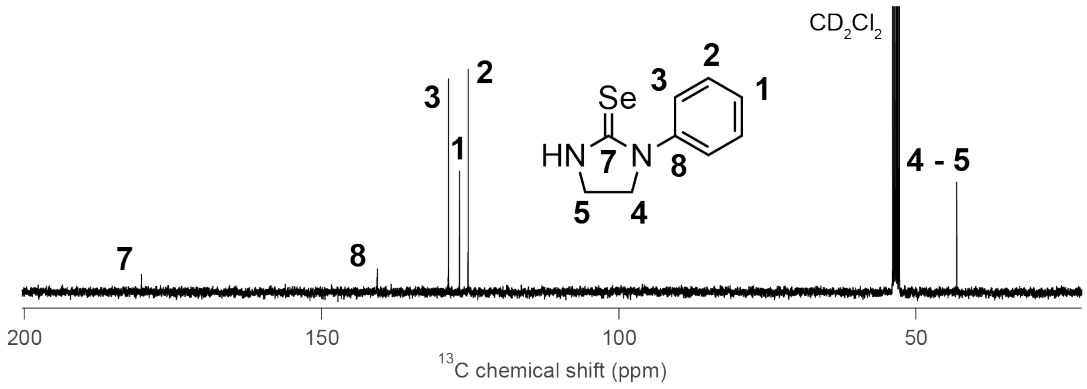

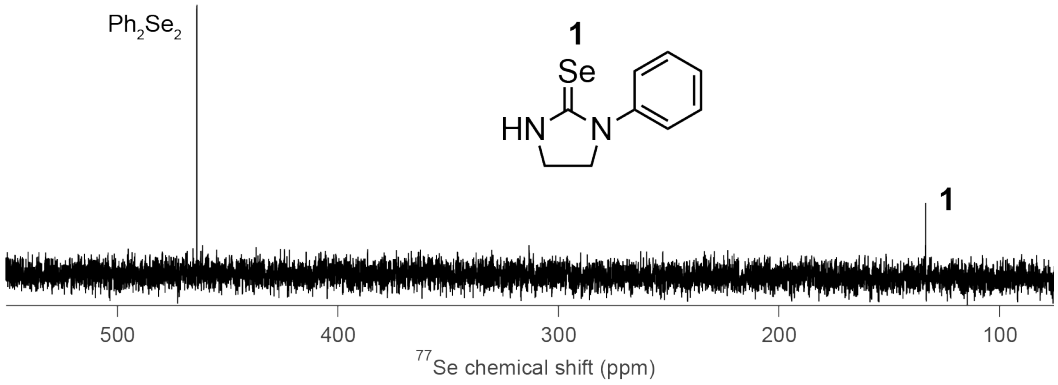

1-ethylimidazolidine-2-selenone (Se(SIEt)).

Yield: 2.01 g (38%). ^{1}H NMR (400 MHz, $CDCl_3$): δ = 1.17 (t, 3H, -CH_3), 3.58 (m, 2H, -CH_2), 3.67 (m, 4H, -CH_2), 6.83 (br, 1H, NH); ^{13}C{^{1}H} (101 MHz, $CDCl_3$): δ = 12.24 (-CH_3), 42.66 (-CH_2), 43.51 (-CH_2), 48.08 (-CH_2), 179.09 (C(Se)); ^{77}Se{^{1}H} (76 MHz, CD_2Cl_2):δ = 67.70; Anal. Calcd for $C_5H_{10}N_2Se$: C, 33.91; H, 5.69; N, 15.82. Found: C, 33.98; H, 5.49; N, 15.75. MS (ASAP) *m*/*z* Calcd for [$C_5H_{10}N_2Se$ + H^+]: 179.01. Found: 179.01.

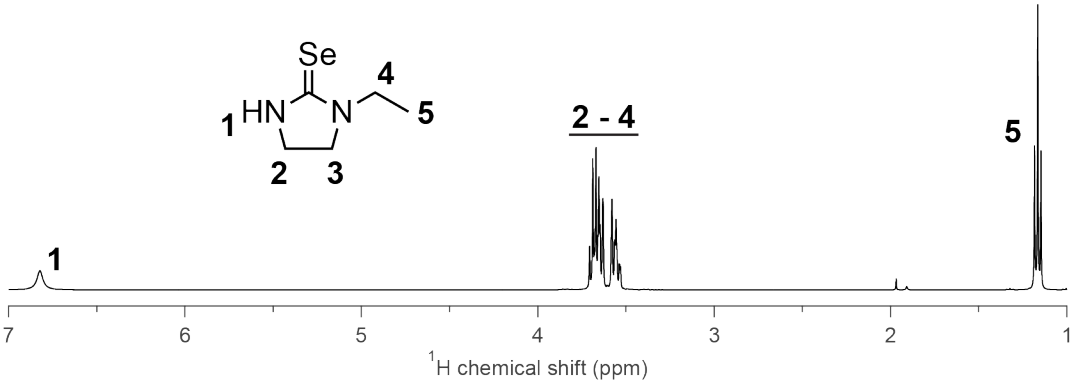

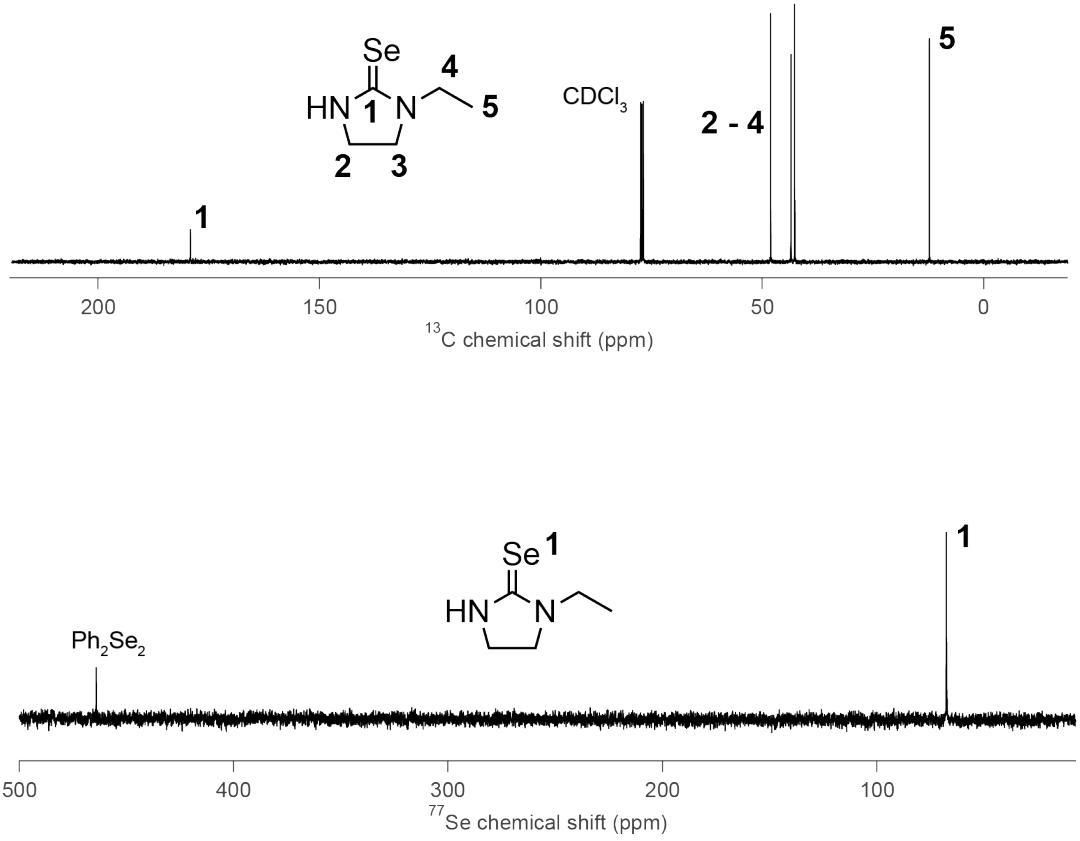

1-isopropylimidazolidine-2-selenone (Se(SIiPr)).

Yield: 0.84 g (21%). ^{1}H NMR (400 MHz, $CDCl_3$): δ = 1.16 (d, 6H, -CH_3), 3.56 (m, 4H, -CH_2), 4.85 (m, 1H, -CH), 6.68 (br, 1H, NH); ^{13}C{^{1}H} (101 MHz, $CDCl_3$): δ = 19.53 (-CH_3), 42.79 (-CH_2), 43.07 (-CH_2), 49.08 (-CH), 178.60 (C(Se)); ^{77}Se{^{1}H} (76 MHz, CD_2Cl_2): δ =70.24; Anal. Calcd for $C_6H_{12}N_2Se$: C, 37.70; H, 6.33; N, 14.66. Found: C, 37.74; H, 6.12; N, 14.64. MS (ASAP) *m*/*z* Calcd for [$C_6H_{12}N_2Se$ + H^+]: 193.02. Found: 193.02.

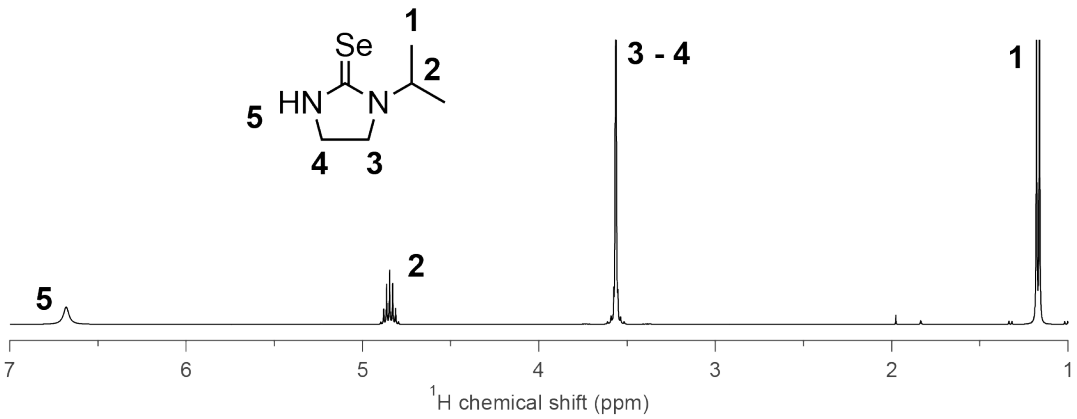
Se
HN
N
1
2
3 - 4
1
5
2
5
7
6
5
4
3
2
1
^{1}H chemical shift (ppm)

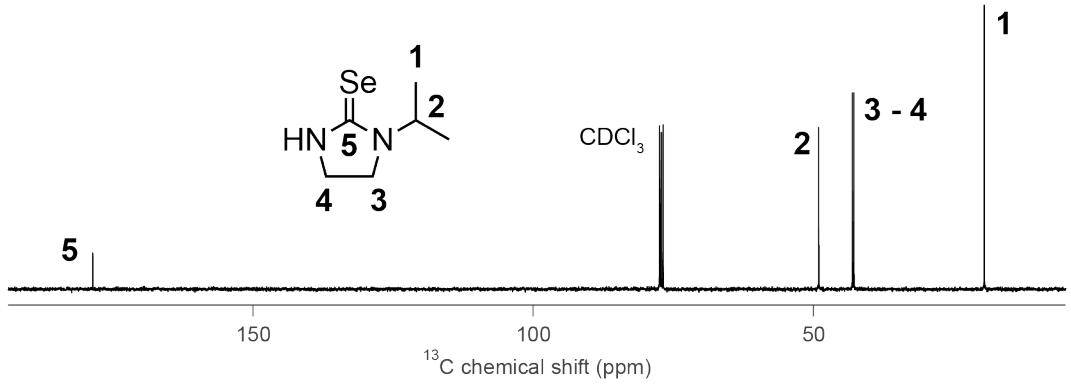
Se
HN
5
N
1
2
4
3
CDCl$_3$
1
3 - 4
2
5
150
100
50
^{13}C chemical shift (ppm)

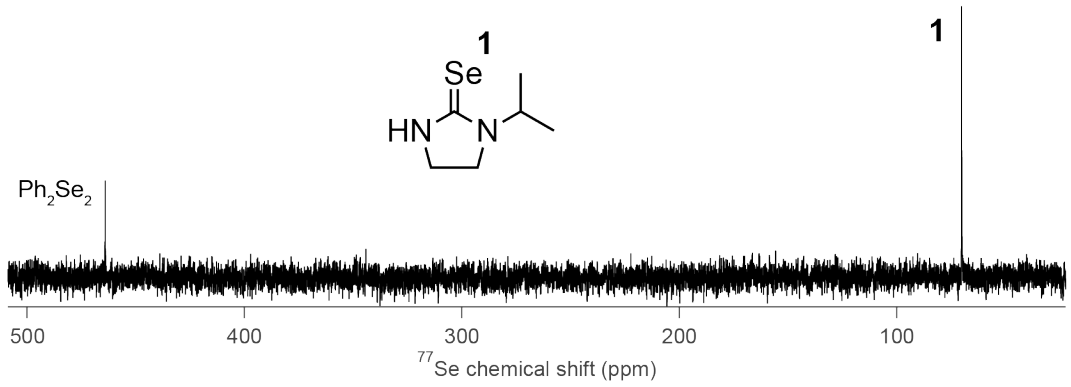
Se
HN
N
1
1
Ph$_2$Se$_2$
500
400
300
200
100
^{77}Se chemical shift (ppm)

1,3-diphenylimidazolidine-2-selenone (Se(SIPh$_2$))

Yield: 19.67 g (44%). ^{1}H NMR (400 MHz, CD_2Cl_2): δ = 4.15 (s, 4H, -CH_2), 7.30-7.36 (m, 2H, *p*-CH), 7.41-7.49 (m, 4H, *m*-CH), 7.53-7.59 (d, 4H, *o*-CH); ^{13}C{^{1}H} (101 MHz, CD_2Cl_2): δ = 51.44 (-CH_2), 126.96 (*o*-CH), 127.50 (*p*-CH), 129.20 (*m*-CH), 142.08 (*i*-C), 181.38 (C(Se)); ^{77}Se {^{1}H} (76 MHz, CD_2Cl_2): δ = 174.28; Anal. Calcd for $C_{15}H_{14}N_2Se$: C, 59.81; H, 4.68; N, 9.30. Found: C, 59.68; H, 4.58; N, 9.24. MS (ASAP) *m*/*z* Calcd for [$C_{15}H_{14}N_2Se + H^+$]: 303.04. Found: 303.04.

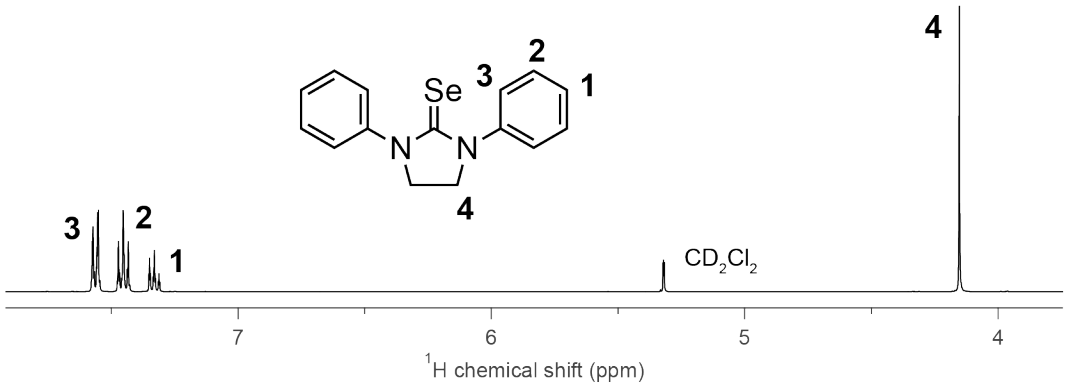

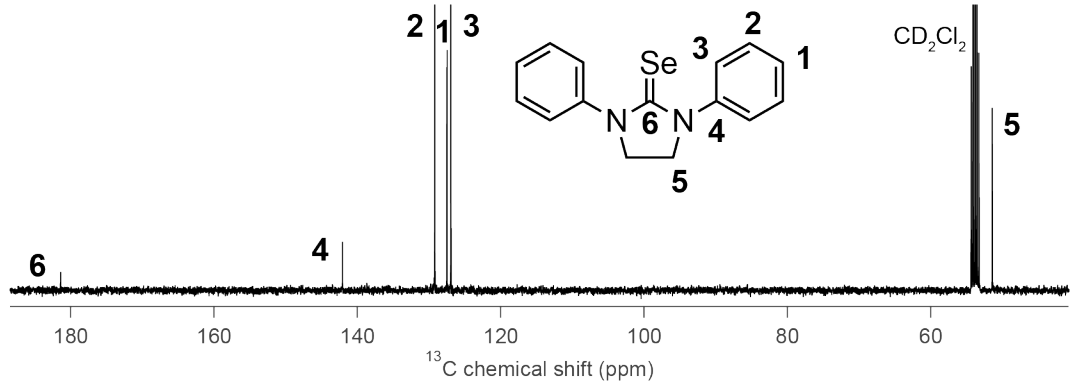

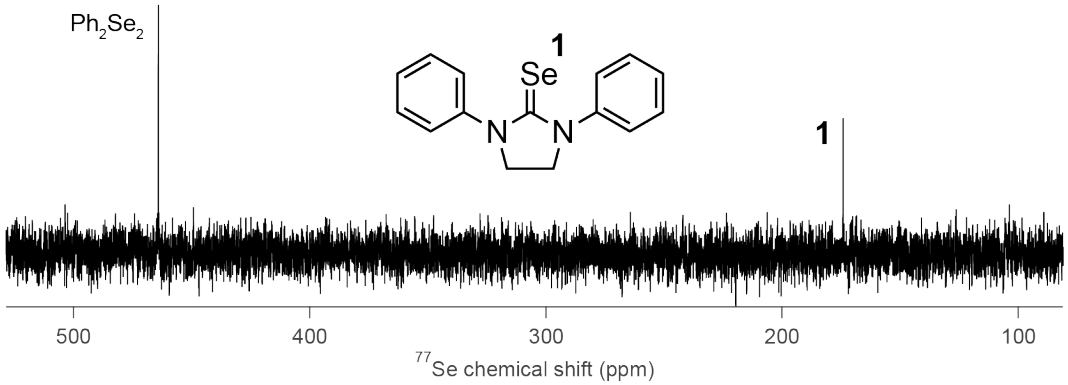

1,3-ditertbutylimidazolidine-2-selenone (Se(SI*t*-Bu$_2$))

Yield: 0.81 g (3%). ^{1}H NMR (400 MHz, $CDCl_3$): δ = 1.69 (s, 18H, -CH_3), 3.47 (s, 4H, -CH_2); ^{13}C{^{1}H} (101 MHz, $CDCl_3$): δ = 28.92 (-CH_3), 45.71 (-CH_2), 58.07 (-$\underline{C}(CH_3)_3$), 179.09 (C(Se)); ^{77}Se {^{1}H} (76 MHz, $CDCl_3$): δ = 274.39; Anal. Calcd for $C_{11}H_{22}N_2Se$: C, 50.57; H, 8.49; N, 10.72. Found: C, 50.66; H, 8.10; N, 10.79. MS (ASAP) *m*/*z* Calcd for [$C_{11}H_{22}N_2Se + H^+$]: 263.10. Found: 263.10.

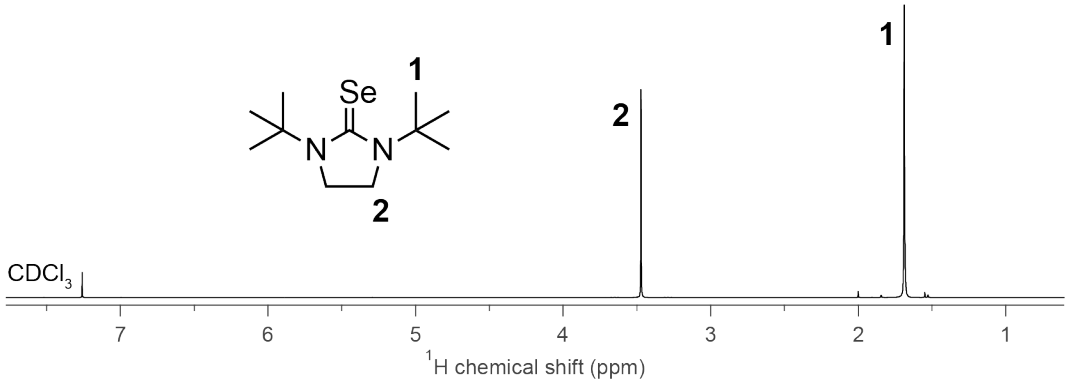

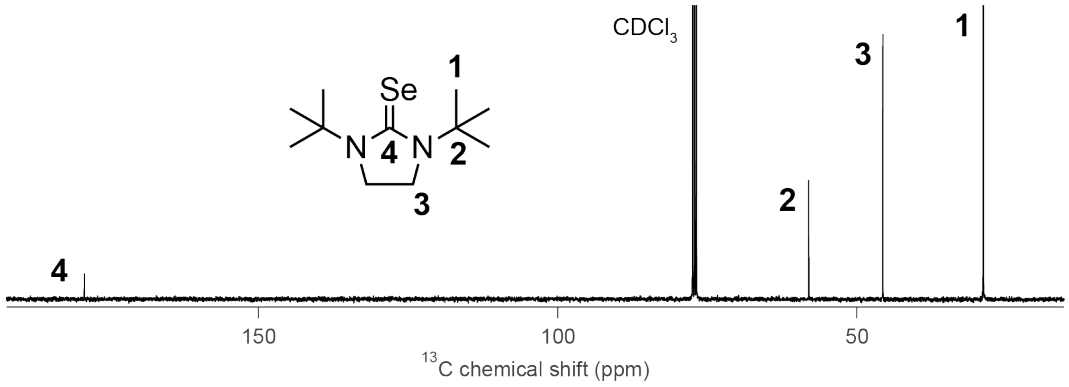

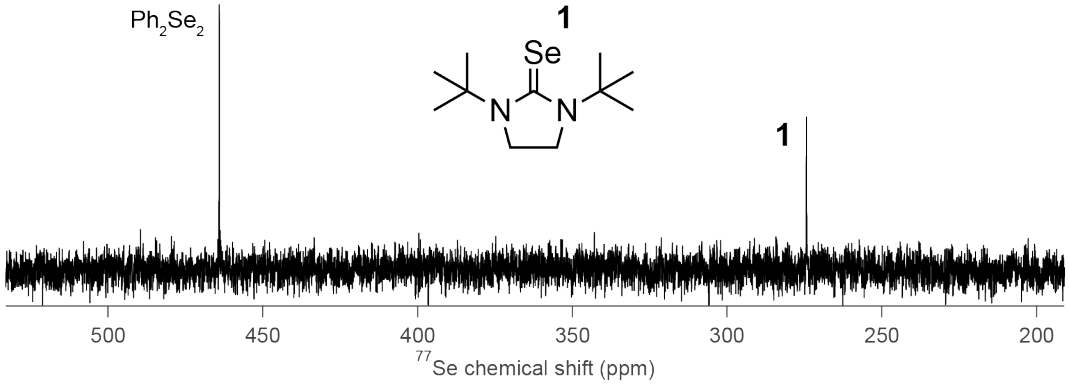

1,3-dimethylimidazolidine-2-selenone (Se(SIMe$_2$))

Yield: 15.01 g (50%). ^{1}H NMR (400 MHz, C_6D_6): δ = 2.38 (s, 4H, -CH_2), 2.89 (s, 6H, -CH_3); ^{13}C{^{1}H} (101 MHz, C_6D_6): δ = 36.62 (-CH_3), 48.50 (-CH_2), 183.46 (C(Se)); ^{77}Se {^{1}H} (76 MHz, C_6D_6): δ = 110.90; Anal. Calcd for $C_5H_{10}N_2Se$: C, 33.91; H, 5.69; N, 15.82. Found: C, 33.93; H, 5.47; N, 15.77. MS (ASAP) *m*/*z* Calcd for [$C_5H_{10}N_2Se$ + H^+]: 179.01. Found: 179.01.

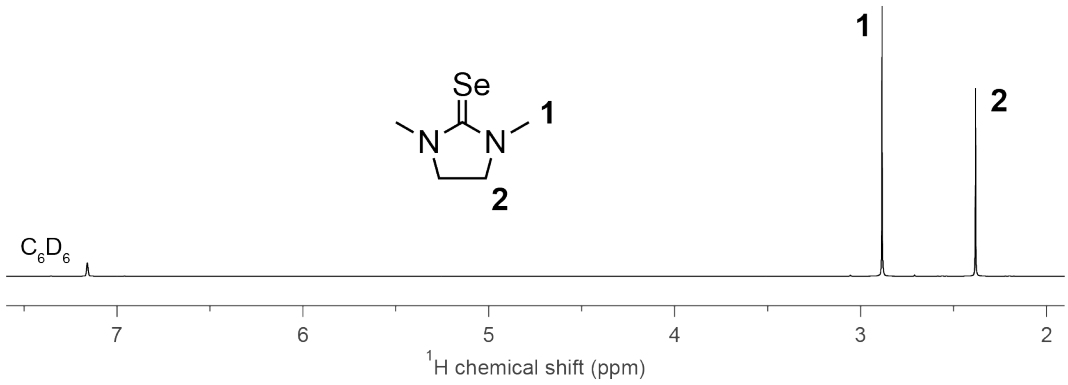
Se
1
2
1
2
C6D6
7
6
5
4
3
2
1H chemical shift (ppm)

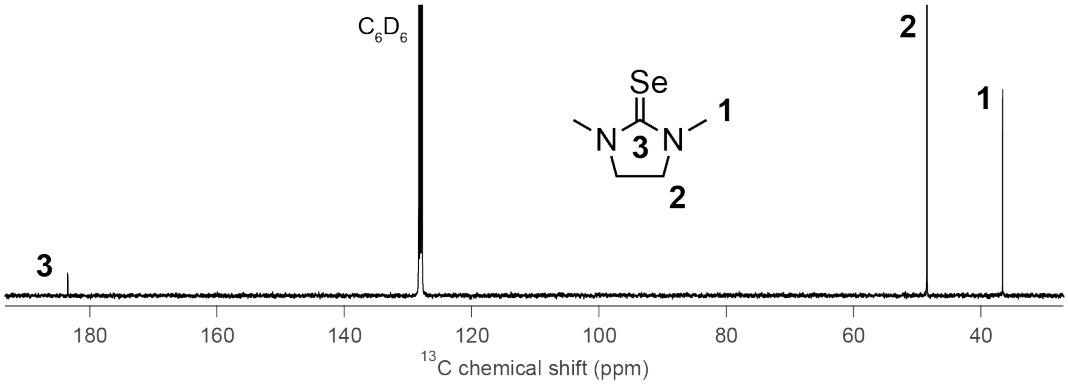
C6D6
Se
1
3
2
2
1
3
180
160
140
120
100
80
60
40
13C chemical shift (ppm)

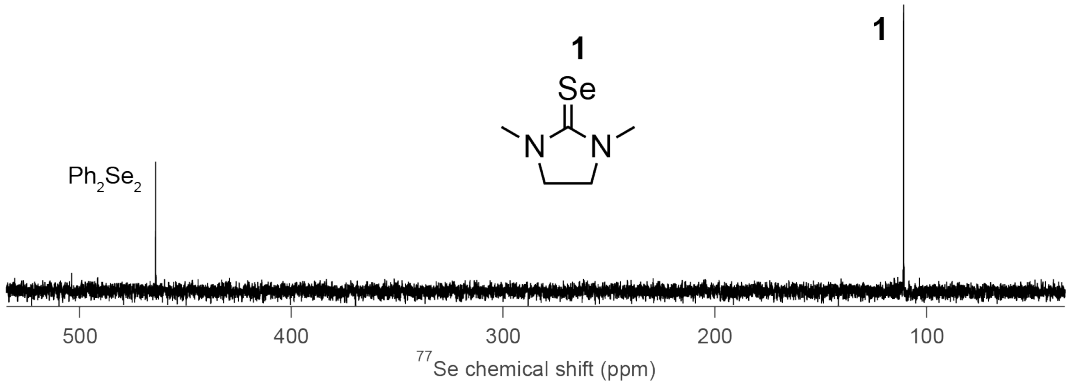
1
Se
1
Ph2Se2
500
400
300
200
100
77Se chemical shift (ppm)

1,3-diethylimidazolidine-2-selenone (Se(SIEt$_2$))

Yield: 15.30 g (76.5%). ^{1}H NMR (400 MHz, $CDCl_3$): δ = 1.17 (t, 6H, -CH_3), 3.55 (s, 4H, -CH_2), 3.75 (q, 4H, -$\underline{CH_2}CH_3$); $^{13}C\{^1H\}$ (101 MHz, $CDCl_3$): δ = 12.28 (-CH_3), 44.16 (-$\underline{CH_2}CH_3$), 46.37 (-CH_2), 179.86 (C(Se)); $^{77}Se\ \{^1H\}$ (76 MHz, $CDCl_3$): δ = 62.14; Anal. Calcd for $C_7H_{14}N_2Se$: C, 40.98; H, 6.88; N, 13.65. Found: C, 41.19; H, 6.57; N, 13.70. MS (ASAP) *m*/*z* Calcd for [$C_7H_{14}N_2Se + H^+$]: 207.04. Found: 207.04.

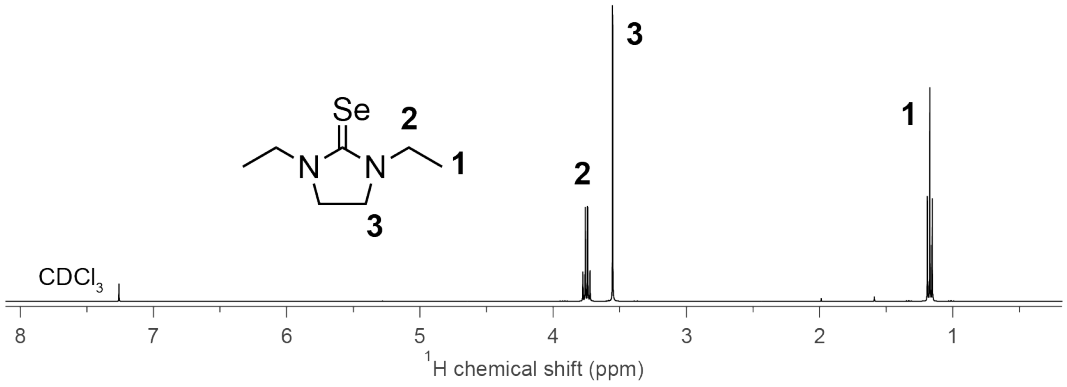

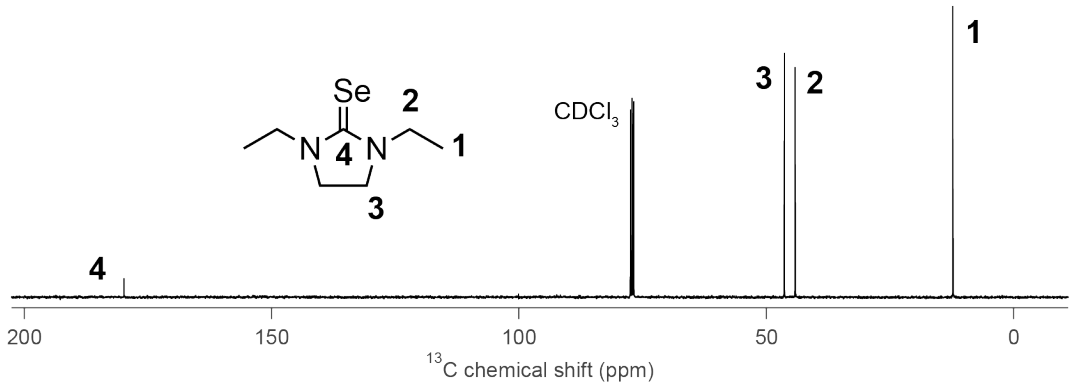

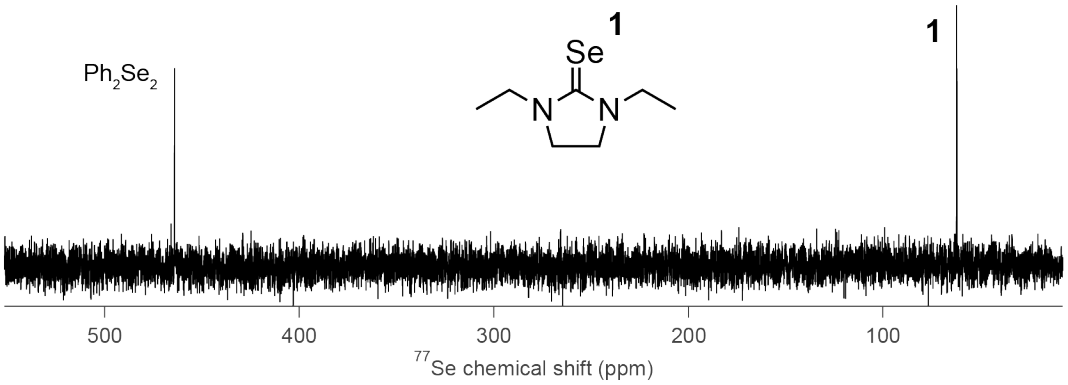

1,3-diisopropylimidazolidine-2-selenone (Se(SIiPr$_2$))

Yield: 11.17 g (55.9%). ^{1}H NMR (400 MHz, C_6D_6): δ = 0.88 (d, 12H, -CH_3), 2.63 (s, 4H, -CH_2), 5.33 (m, 2H, -CH); ^{13}C{^{1}H} (101 MHz, C_6D_6): δ = 19.11 (-CH_3), 41.05 (-CH_2), 48.70 (-CH), 181.30 (C(Se)); ^{77}Se {^{1}H} (76 MHz, C_6D_6): δ = 107.23; Anal. Calcd for $C_9H_{18}N_2Se$: C, 46.35; H, 7.78; N, 12.01. Found: C, 46.41; H, 7.51; N, 12.14. MS (ASAP) *m*/*z* Calcd for [$C_9H_{18}N_2Se$ + H^+]: 235.07. Found: 235.07.

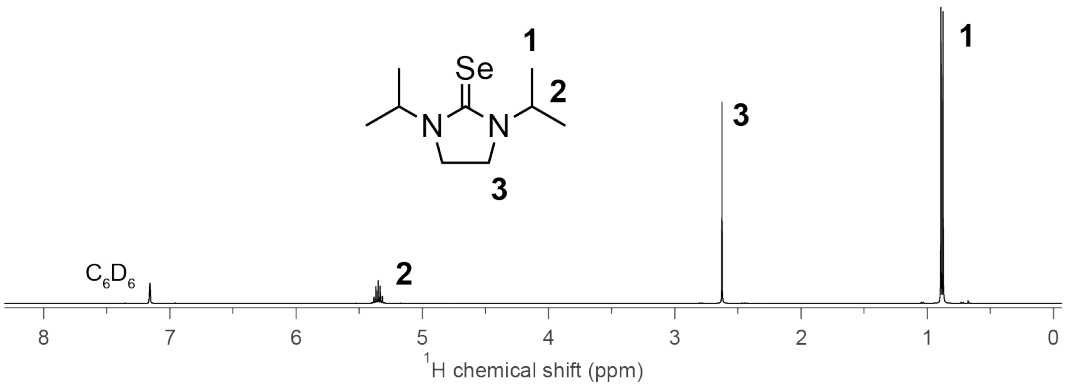

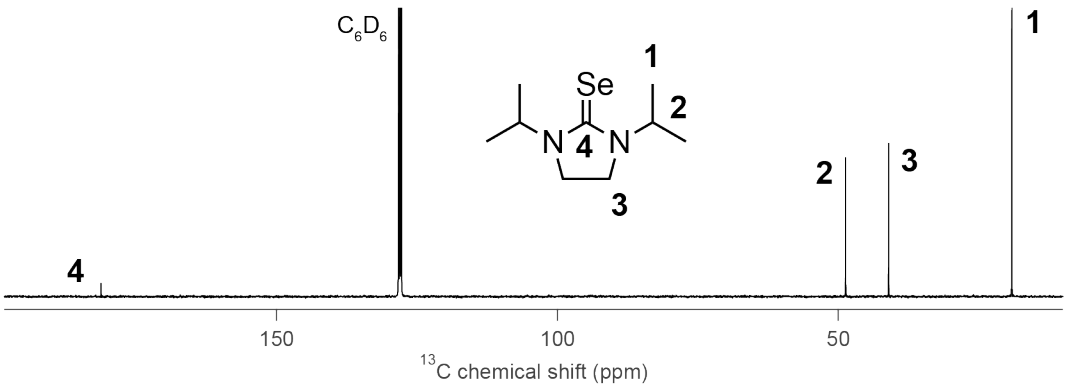

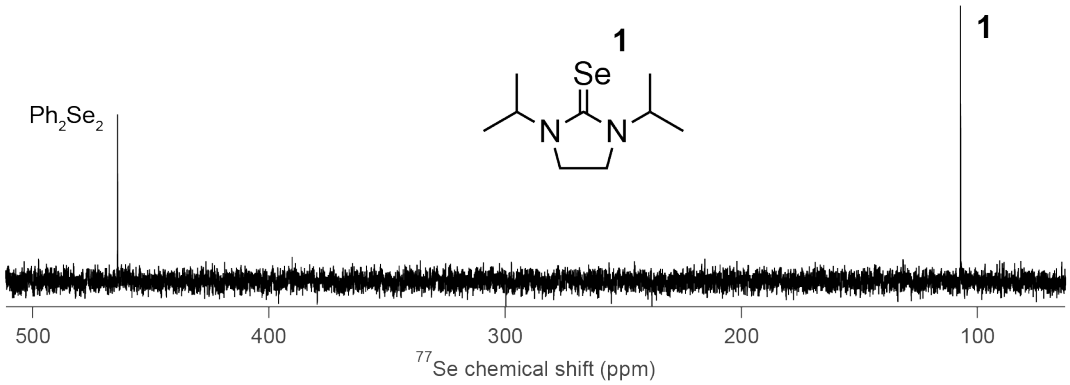

1-methyltetrahydropyrimidine-2(1*H*)-selenone (Se(PymMe)).

Yield: 0.62 g (11%). ^{1}H NMR (400 MHz, $CDCl_3$): δ = 2.07 (m, 2H, -CH_2), 3.23 (m, 2H, -CH_2), 3.36 (t, 2H, -CH_2), 3.50 (s, 3H, -CH_3), 6.70 (br, 1H, NH); ^{13}C{^{1}H} (101 MHz, $CDCl_3$): δ = 20.71 (-CH_2), 40.57 (-CH_2), 45.08 (-CH_2), 48.04 (-CH_3), 173.35 (C(Se)); ^{77}Se {^{1}H} (76 MHz, C_6D_6): δ = 205.43; Anal. Calcd for $C_5H_{10}N_2Se$: C, 33.91; H, 5.69; N, 15.82. Found: C, 3.99; H, 5.48; N, 15.80. MS (ASAP) *m*/*z* Calcd for [$C_5H_{10}N_2Se$ + H^+]: 179.01. Found: 179.01.

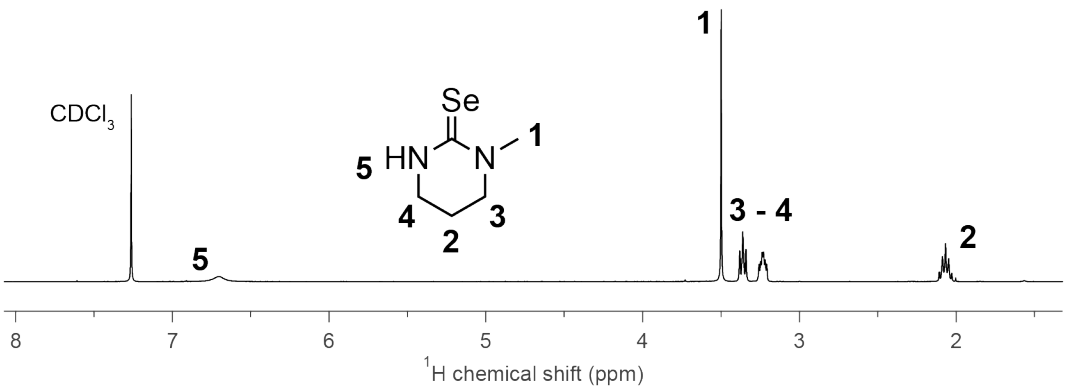
CDCl3
Se
HN
N
1
5
4
3
2
1
3 - 4
2
5
8
7
6
5
4
3
2
1H chemical shift (ppm)

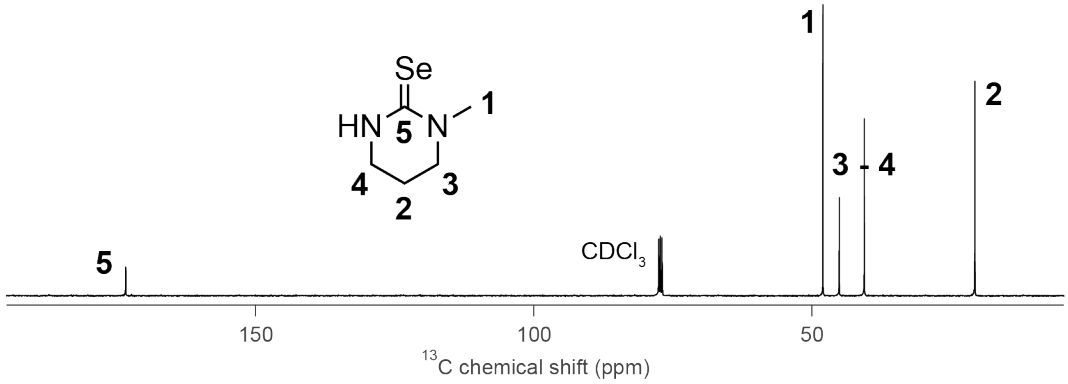
Se
HN
5
N
1
4
3
2
1
3 - 4
2
5
CDCl3
150
100
50
13C chemical shift (ppm)

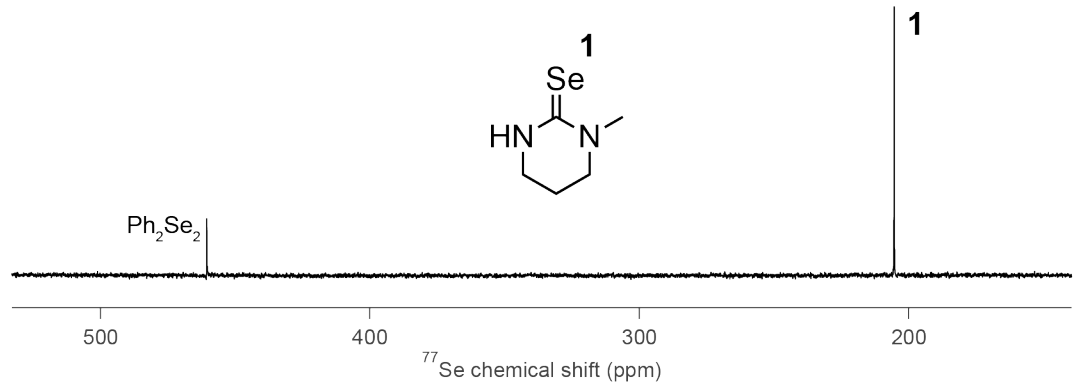
1
Se
HN
N
1
Ph2Se2
500
400
300
200
77Se chemical shift (ppm)

1,3-dimethyltetrahydropyrimidine-2(1*H*)-selenone (Se(PymMe$_2$)).

Yield: 0.69 g (8%). ^{1}H NMR (400 MHz, $CDCl_3$): δ = 2.05 (m, 2H, -CH_2), 3.36 (t, 4H, -CH_2), 3.55 (s, 6H, -CH_3); $^{13}C\{^1H\}$ (101 MHz, $CDCl_3$): δ = 20.92 (-CH_2), 46.94 (-CH_2), 48.46 (-CH_3), 177.76 (C(Se)); $^{77}Se\{^1H\}$ (76 MHz, C_6D_6): δ = 221.22; Anal. Calcd for $C_6H_{12}N_2Se$: C, 37.70; H, 6.33; N, 14.66. Found: C, 37.72; H, 6.16; N, 14.63. MS (ASAP) *m*/*z* Calcd for [$C_6H_{12}N_2Se$ + H^+]: 193.02. Found: 193.02.

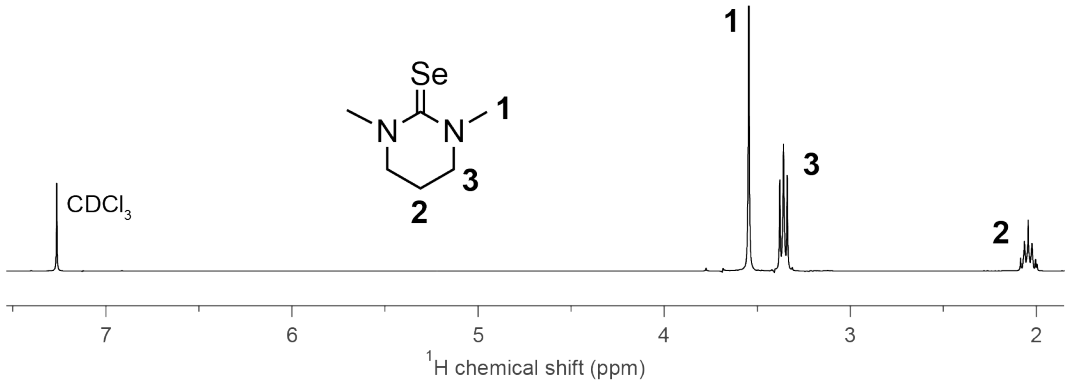

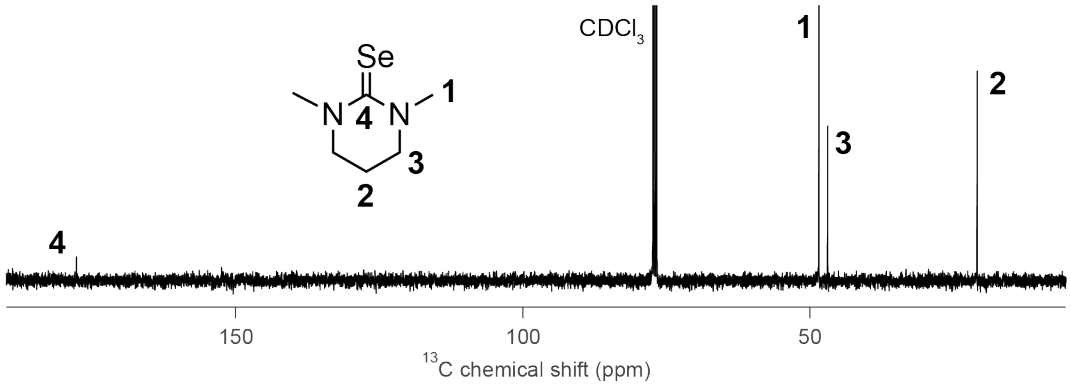

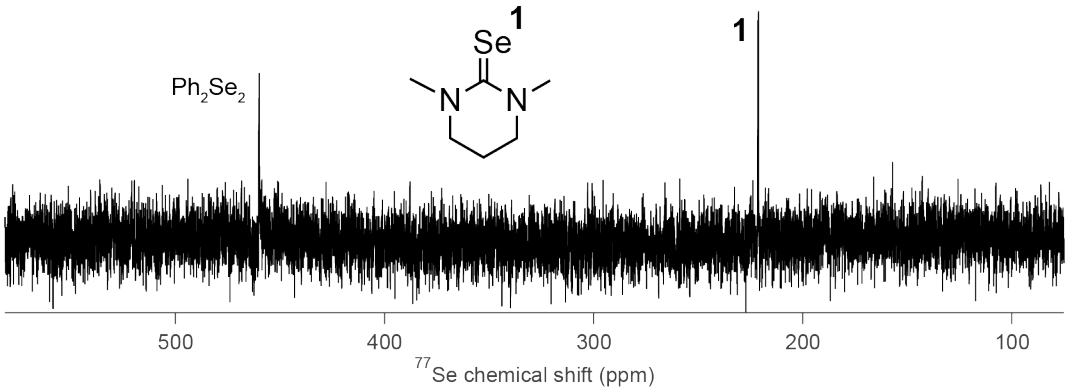

1,3-diethyltetrahydropyrimidine-2(1*H*)-selenone (Se(PymEt$_2$)).

Yield: 0.23 g (2%). ^{1}H NMR (400 MHz, $CDCl_3$): δ = 1.24 (t, 6H, -CH_3), 2.00 (m, 2H, -CH_2), 3.31 (t, 4H, -CH_2), 4.07 (q, 4H, -CH_2); ^{13}C{^{1}H} (101 MHz, $CDCl_3$): δ = 12.31 (-CH_3), 21.06 (-CH_2), 45.68 (-CH_2), 53.26 (-CH_2), 175.65 (C(Se)); ^{77}Se {^{1}H} (76 MHz, C_6D_6): δ = 175.18; Anal. Calcd for $C_8H_{16}N_2S$: C, 43.84; H, 7.36; N, 12.78. Found: C, 43.88; H, 7.31; N, 12.74. MS (ASAP) *m*/*z* Calcd for [$C_8H_{16}N_2S$ + H^+]: 221.06. Found: 221.06.

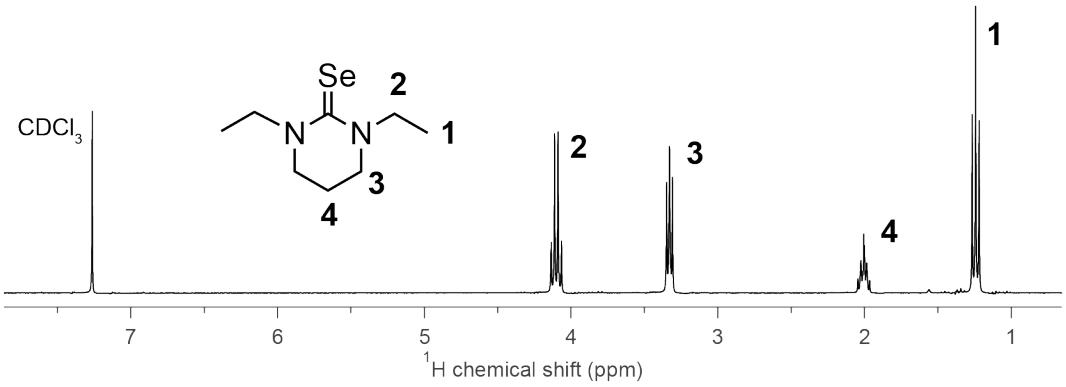

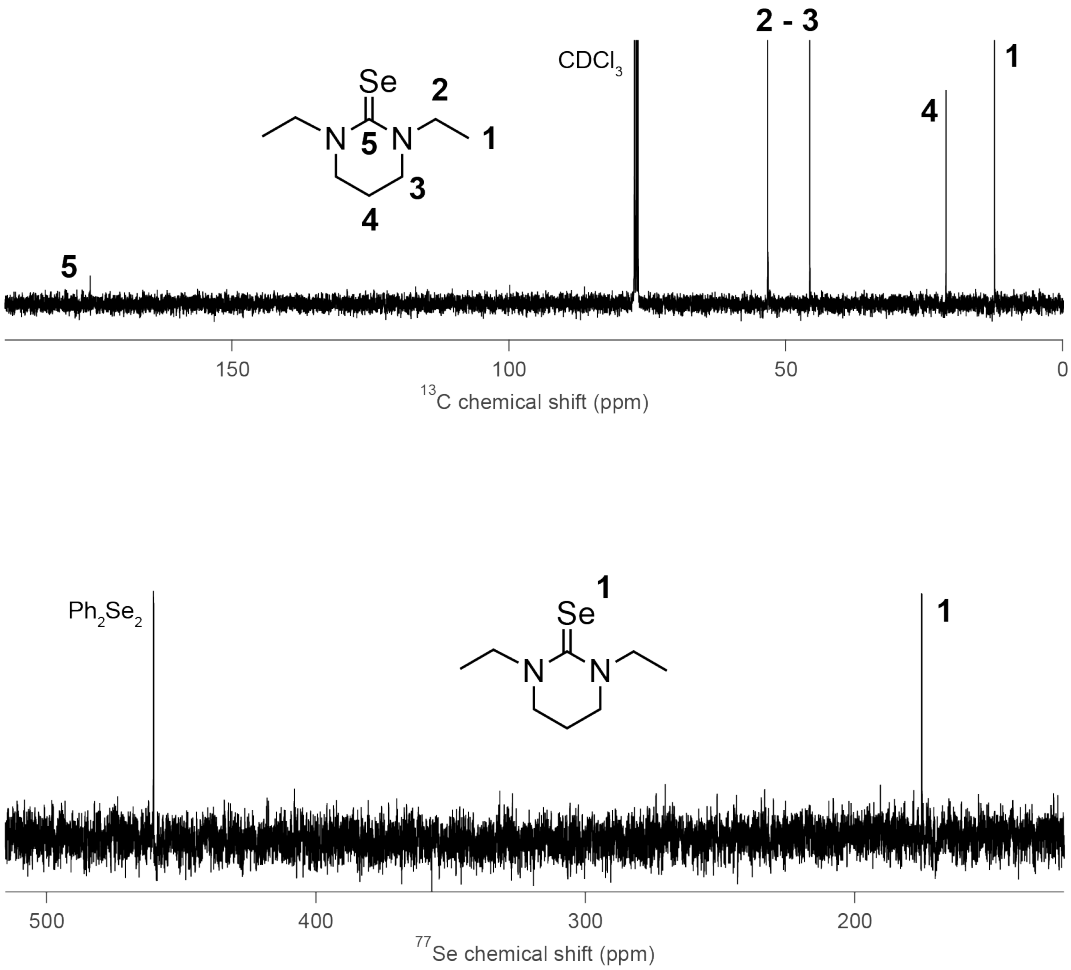

1,3-diisopropyltetrahydropyrimidine-2(1*H*)-selenone (Se(PymiPr$_2$)).

Yield: 0.15 g (3%) ^{1}H NMR (400 MHz, $CDCl_3$): δ = 1.21 (d, 12H, -CH_3), 1.92 (m, 2H, -CH_2), 3.18 (t, 4H, -CH_2), 6.08 (m, 2H, -CH); ^{13}C{^{1}H} (101 MHz, $CDCl_3$): δ = 19.25 (-CH_3), 21.41 (-CH_2), 39.77 (-CH_2), 56.20 (-CH), 176.12 (C(Se)); ^{77}Se {^{1}H} (76 MHz, C_6D_6): δ = 175.96; Anal. Calcd for $C_{10}H_{20}N_2Se$: C, 48.58; H, 8.15; N, 11.33. Found: C, 49.51; H, 8.93; N, 10.91. MS (ASAP) *m*/*z* Calcd for [$C_{10}H_{20}N_2Se + H^+$]: 249.09. Found: 249.09.

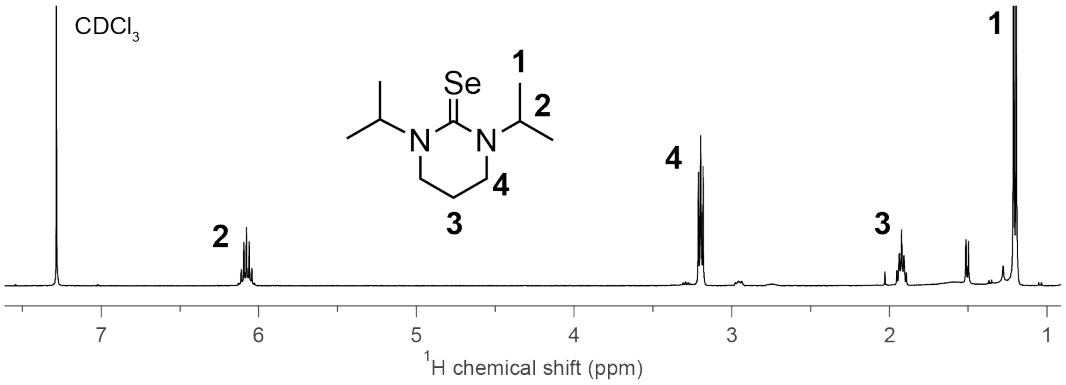
CDCl3
Se
1
2
3
4
1
2
3
4
7
6
5
4
3
2
1
1H chemical shift (ppm)

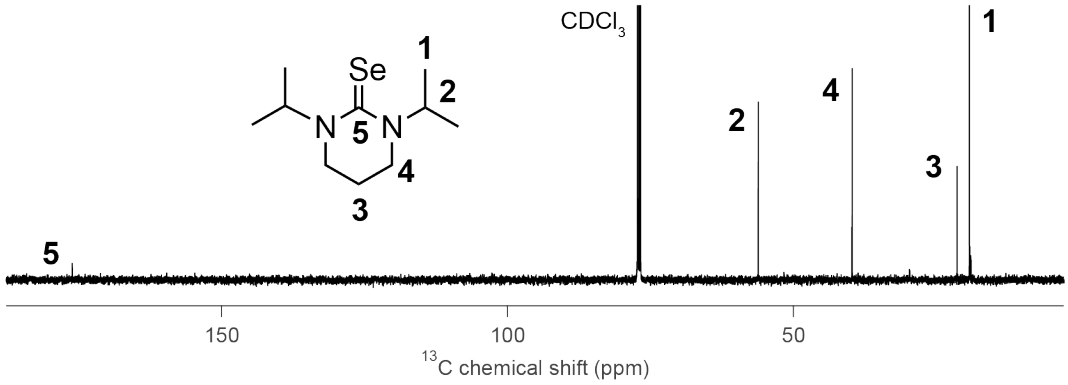
CDCl3
Se
1
2
3
4
5
1
2
3
4
5
150
100
50
13C chemical shift (ppm)

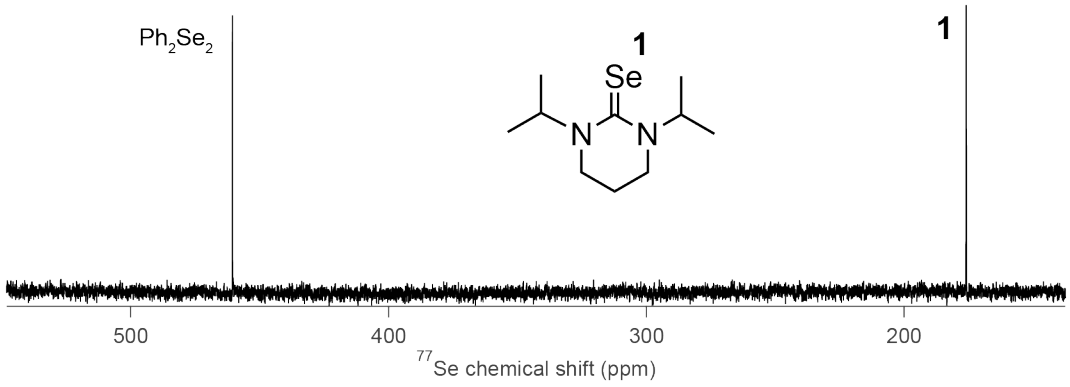
Ph2Se2
Se
1
1
500
400
300
200
77Se chemical shift (ppm)

3.11. References

(1) Abe, S.; Cabek, R. K.; De Geyter, B.; Hens, Z., Tuning the Postfocused Size of Colloidal Nanocrystals by the Reaction Rate: From Theory to Application. *ACS Nano* **2012,** *6* (1), 42-53.

(2) Sugimoto, T.; Shiba, F., Spontaneous Nucleation of Monodisperse Silver Halide Particles from Homogeneous Gelatin Solution II: Silver Bromide. *Colloids Surf. A* **2000,** *164* (2-3), 205-215.

(3) Sugimoto, T.; Shiba, F.; Sekiguchi, T.; Itoh, H., Spontaneous Nucleation of Monodisperse Silver Halide Particles from Homogeneous Gelatin Solution I: Silver Chloride. *Colloids Surf. A* **2000,** *164* (2-3), 183-203.

(4) Owen, J. S.; Chan, E. M.; Liu, H.; Alivisatos, A. P., Precursor Conversion Kinetics and the Nucleation of Cadmium Selenide Nanocrystals. *J. Am. Chem. Soc.* **2010,** *132* (51), 18206-18213.

(5) Hendricks, M. P.; Campos, M. P.; Cleveland, G. T.; Jen-La Plante, I.; Owen, J. S., A Tunable Library of Substituted Thiourea Precursors to Metal Sulfide Nanocrystals. *Science* **2015,** *348* (6240), 1226-1230.

(6) Campos, M. P.; Hendricks, M. P.; Beecher, A. N.; Walravens, W.; Swain, R. A.; Cleveland, G. T.; Hens, Z.; Sfeir, M. Y.; Owen, J. S., A Library of Selenourea Precursors to PbSe Nanocrystals with Size Distributions Near the Homogenous Limit. *J. Am. Chem. Soc.* **2017,** *139* (6), 2296-2305.

(7) Hamachi, L. S.; Jen-La Plante, I.; Coryell, A. C.; De Roo, J.; Owen, J. S., Kinetic Control over CdS Nanocrystal Nucleation Using a Library of Thiocarbonates, Thiocarbamates, and Thioureas. *Chem. Mater.* **2017,** *29* (20), 8711-8719.

(8) Yu, W. W.; Peng, X., Formation of High-Quality CdS and Other II-VI Semiconductor Nanocrystals in Noncoordinating Solvents: Tunable Reactivity of Monomers. *Angew. Chem. Int. Ed.* **2002,** *41* (13), 2368-2371.

(9) Bullen, C. R.; Mulvaney, P., Nucleation and Growth Kinetics of CdSe Nanocrystals in Octadecene. *Nano Lett.* **2004,** *4* (12), 2303-2307.

(10) van Embden, J.; Mulvaney, P., Nucleation and Growth of CdSe Nanocrystals in a Binary Ligand System. *Langmuir* **2005,** *21* (22), 10226-10233.

(11) Abe, S.; Capek, R. K.; Geyter, B. D.; Hens, Z., Reaction Chemistry/Nanocrystal Property Relations in the Hot Injection Synthesis, the Role of the Solute Solubility. *ACS Nano* **2013,** *7* (2), 943-949.

(12) De Nolf, K.; Capek, R. K.; Abe, S.; Sluydts, M.; Jang, Y.; Martins, J. C.; Cottenier, S.; Lifshitz, E.; Hens, Z., Controlling the Size of Hot Injection Made Nanocrystals by Manipulating the Diffusion Coefficient of the Solute. *J. Am. Chem. Soc.* **2015,** *137* (7), 2495-2505.

(13) Nose, K.; Fujita, H.; Omata, T.; Otsuka-Yao-Matsuo, S.; Nakamura, H.; Maeda, H., Chemical Role of Amines in the Colloidal Synthesis of CdSe Quantum Dots and Their Photoluminescence Properties. *J. Lumin.* **2007,** *126* (1), 21-26.

(14) Mahler, B.; Lequeux, N.; Dubertret, B., Ligand-Controlled Polytypism of Thick-Shell CdSe/CdS Nanocrystals. *J. Am. Chem. Soc.* **2010,** *132* (3), 953-959.

(15) Mangum, B. D.; Landes, T. S.; Theobald, B. R.; Kurtin, J. N., Exploring the Bounds of Narrow-Band Quantum Dot Downconverted LEDs. *Photon. Res.* **2017,** *5* (2), A13-A22.

(16) Kang, Y.; Song, Z.; Jiang, X.; Yin, X.; Fang, L.; Gao, J.; Su, Y.; Zhao, F., Quantum Dots for Wide Color Gamut Displays From Photoluminescence to Electroluminescence. *Nanoscale Res. Lett.* **2017,** *12* (1), 154.

(17) Dai, X.; Zhang, Z.; Jin, Y.; Niu, Y.; Cao, H.; Liang, X.; Chen, L.; Wang, J.; Peng, X., Solution-Processed, High-Performance Light-Emitting Diodes Based on Quantum Dots. *Nature* **2014,** *515* (7525), 96.

(18) McHugh, K. J.; Jing, L.; Behrens, A. M.; Jayawardena, S.; Tang, W.; Gao, M.; Langer, R.; Jaklenec, A., Biocompatible Semiconductor Quantum Dots as Cancer Imaging Agents. *Adv. Mater.* **2018**.

(19) Mazumder, S.; Dey, R.; Mitra, M.; Mukherjee, S.; Das, G., Biofunctionalized Quantum Dots in Biology and Medicine. *J. Nanomater.* **2009,** *2009*, 38.

(20) Chen, O.; Zhao, J.; Chauhan, V. P.; Cui, J.; Wong, C.; Harris, D. K.; Wei, H.; Han, H.; Fukumura, D.; Jain, R. K.; Bawendi, M. G., Compact High-Quality CdSe-CdS Core-Shell Nanocrystals with Narrow Emission Linewidths and Suppressed Blinking. *Nat. Mater.* **2013,** *12*, 445-451.

(21) van Embden, J.; Jasieniak, J.; Mulvaney, P., Mapping the Optical Properties of CdSe/CdS Heterostructure Nanocrystals: The Effects of Core Size and Shell Thickness. *J. Am. Chem. Soc.* **2009,** *131* (40), 14299-14309.

(22) Jeong, B. G.; Park, Y.; Chang, J. H.; Cho, I.; Kim, J. K.; Kim, H.; Char, K.; Cho, J.; Klimov, V. I.; Park, P.; Lee, D. C.; Bae, W. K., Colloidal Spherical Quantum Wells with Near-Unity Photoluminescence Quantum Yield and Suppressed Blinking. *ACS Nano* **2016,** *10* (10), 9297-9305.

(23) Zhang, J.; Yang, Q.; Cao, H.; Ratcliffe, C. I.; Kingston, D.; Chen, Q. Y.; Ouyang, J.; Wu, X.; Leek, D. M.; Riehle, F. S.; Yu, K., Bright Gradient-Alloyed $CdSe_xS_{1-x}$ Quantum Dots Exhibiting Cyan-Blue Emission. *Chem. Mater.* **2016,** *28* (2), 618-625.

(24) Chen, Y.; Vela, J.; Htoon, H.; Casson, J. L.; Werder, D. J.; Bussian, D. A.; Klimov, V. I.; Hollingsworth, J. A., "Giant" Multishell CdSe Nanocrystal Quantum Dots with Suppressed Blinking. *J. Am. Chem. Soc.* **2008,** *130* (15), 5026-5027.

(25) Nasilowski, M.; Spinicelli, P.; Patriarche, G.; Dubertret, B., Gradient CdSe/CdS Quantum Dots with Room Temperature Biexciton Unity Quantum Yield. *Nano Lett.* **2015,** *15* (6), 3953-3958.

(26) Reiss, P.; Protière, M.; Li, L., Core/Shell Semiconductor Nanocrystals. *Small* **2009,** *5* (2), 154-168.

(27) Sarma, D. D.; Nag, A.; Santra, P. K.; Kumar, A.; Sapra, S.; Mahadevan, P., Origin of the Enhanced Photoluminescence from Semiconductor CdSeS Nanocrystals. *J. Phys. Chem. Lett.* **2010,** *1* (14), 2149-2153.

(28) Bae, W. K.; Padilha, L. A.; Park, Y.; McDaniel, H.; Robel, I.; Pietryga, J. M.; Klimov, V. I., Controlled Alloying of the Core-Shell Interface in CdSe/CdS Quantum Dots for Suppression of Auger Recombination. *ACS Nano* **2013,** *7* (4), 3411-3419.

(29) Li, J. J.; Wang, Y. A.; Guo, W.; Keay, J. C.; Mishima, T. D.; Johnson, M. B.; Peng, X., Large-Scale Synthesis of Nearly Monodisperse CdSe/CdS Core/Shell Nanocrystals Using Air-Stable Reagents via Successive Ion Layer Adsorption and Reaction. *J. Am. Chem. Soc.* **2003,** *125* (41), 12567-12575.

(30) Boldt, K.; Kirkwood, N.; Beane, G. A.; Mulvaney, P., Synthesis of Highly Luminescent and Photo-Stable, Graded Shell CdSe/$Cd_xZn_{1-x}S$ Nanoparticles by In Situ Alloying. *Chem. Mater.* **2013,** *25* (23), 4731-4738.

(31) Ghosh, Y.; Mangum, B. D.; Casson, J. L.; Williams, D. J.; Htoon, H.; Hollingsworth, J. A., New Insights Into the Complexities of Shell Growth and the Strong Influence of Particle Volume in Nonblinking "Giant" Core/Shell Nanocrystal Quantum Dots. *J. Am. Chem. Soc.* **2012,** *134* (23), 9634-9643.

(32) García-Rodríguez, R. l.; Hendricks, M. P.; Cossairt, B. M.; Liu, H.; Owen, J. S., Conversion Reactions of Cadmium Chalcogenide Nanocrystal Precursors. *Chem. Mater.* **2013,** *25* (8), 1233-1249.

(33) Carbone, L.; Nobile, C.; De Giorgi, M.; Sala, F. D.; Morello, G.; Pompa, P.; Hytch, M.; Snoeck, E.; Fiore, A.; Franchini, I. R., Synthesis and Micrometer-Scale Assembly of Colloidal CdSe/CdS Nanorods Prepared by a Seeded Growth Approach. *Nano Lett.* **2007,** *7* (10), 2942-2950.

(34) Talapin, D. V.; Nelson, J. H.; Shevchenko, E. V.; Aloni, S.; Sadtler, B.; Alivisatos, A. P., Seeded growth of highly luminescent CdSe/CdS nanoheterostructures with rod and tetrapod morphologies. *Nano Lett.* **2007,** *7* (10), 2951-2959.

(35) Fiore, A.; Mastria, R.; Lupo, M. G.; Lanzani, G.; Giannini, C.; Carlino, E.; Morello, G.; De Giorgi, M.; Li, Y.; Cingolani, R., Tetrapod-Shaped Colloidal Nanocrystals of II−VI Semiconductors Prepared by Seeded Growth. *J. Am. Chem. Soc.* **2009,** *131* (6), 2274-2282.

(36) Zhong, H.; Scholes, G. D., Shape Tuning of Type II CdTe-CdSe Colloidal Nanocrystal Heterostructures Through Seeded Growth. *J. Am. Chem. Soc.* **2009,** *131* (26), 9170-9171.

(37) Deka, S.; Miszta, K.; Dorfs, D.; Genovese, A.; Bertoni, G.; Manna, L., Octapod-Shaped Colloidal Nanocrystals of Cadmium Chalcogenides Via "One-Pot" Cation Exchange and Seeded Growth. *Nano Lett.* **2010,** *10* (9), 3770-3776.

(38) Cirillo, M.; Aubert, T.; Gomes, R.; Van Deun, R.; Emplit, P.; Biermann, A.; Lange, H.; Thomsen, C.; Brainis, E.; Hens, Z., "Flash" Synthesis of CdSe/CdS Core–Shell Quantum Dots. *Chem. Mater.* **2014,** *26* (2), 1154-1160.

(39) Drijvers, E.; De Roo, J.; Geiregat, P.; Fehér, K.; Hens, Z.; Aubert, T., Revisited Wurtzite CdSe Synthesis: A Gateway for the Versatile Flash Synthesis of Multishell Quantum Dots and Rods. *Chem. of Mater.* **2016,** *28* (20), 7311-7323.

(40) Nakonechnyi, I.; Sluydts, M.; Justo, Y.; Jasieniak, J.; Hens, Z., Mechanistic Insights in Seeded Growth Synthesis of Colloidal Core/Shell Quantum Dots. *Chem. Mater.* **2017,** *29* (11), 4719-4727.

(41) Hsia, C.; Wuttig, A.; Yang, H., An Accessible Approach to Preparing Water-Soluble Mn^{2+}-Doped (CdSSe)ZnS (Core)Shell Nanocrystals for Ratiometric Temperature Sensing. *ACS Nano* **2011,** *5* (12), 9511-9522.

(42) Aubert, T.; Cirillo, M.; Flamee, S.; Van Deun, R.; Lange, H.; Thomsen, C.; Hens, Z., Homogeneously Alloyed $CdSe_{1-x}S_x$ Quantum Dots ($0 \le x \le 1$): An Efficient Synthesis for Full Optical Tunability. *Chem. Mater.* **2013,** *25* (12), 2388-2390.

(43) Ouyang, J.; Vincent, M.; Kingston, D.; Descours, P.; Boivineau, T.; Zaman, M. B.; Wu, X.; Yu, K., Noninjection, One-Pot Synthesis of Photoluminescent Colloidal Homogeneously Alloyed CdSeS Quantum Dots. *J. Phys. Chem. C* **2009,** *113* (13), 5193-5200.

(44) Cao, H.; Ma, J.; Huang, L.; Qin, H.; Meng, R.; Li, Y.; Peng, X., Design and Synthesis of Antiblinking and Antibleaching Quantum Dots in Multiple Colors via Wave Function Confinement. *J. Am. Chem. Soc.* **2016,** *138* (48), 15727-15735.

(45) Ruberu, T. P. A.; Vela, J., Expanding the One-Dimensional CdS-CdSe Composition Landscape: Axially Anisotropic $CdS_{1-x}Se_x$ Nanorods. *ACS Nano* **2011,** *5* (7), 5775-5784.

(46) Al-Salim, N.; Young, A. G.; Tilley, R. D.; McQuillan, A. J.; Xia, J., Synthesis of CdSeS Nanocrystals in Coordinating and Noncoordinating Solvents: Solvent's Role in Evolution of the Optical and Structural Properties. *Chem. Mater.* **2007,** *19* (21), 5185-5193.

(47) Gurusinghe, N. P.; Hewa-Kasakarage, N. N.; Zamkov, M., Composition-Tunable Properties of CdS_xTe_{1-x} Alloy Nanocrystals. *J. Phys. Chem. C* **2008,** *112* (33), 12795-12800.

(48) Wang, R.; Calvignanello, O.; Ratcliffe, C. I.; Wu, X.; Leek, D. M.; Zaman, M. B.; Kingston, D.; Ripmeester, J. A.; Yu, K., Homogeneously-Alloyed CdTeSe Single-Sized Nanocrystals with Bandgap Photoluminescence. *J. Phys. Chem. C* **2009,** *113* (9), 3402-3408.

(49) Bailey, R. E.; Nie, S., Alloyed Semiconductor Quantum Dots: Tuning the Optical Properties Without Changing the Particle Size. *J. Am. Chem. Soc.* **2003,** *125* (23), 7100-7106.

(50) Smith, D. K.; Luther, J. M.; Semonin, O. E.; Nozik, A. J.; Beard, M. C., Tuning the Synthesis of Ternary Lead Chalcogenide Quantum Dots by Balancing Precursor Reactivity. *ACS Nano* **2010,** *5* (1), 183-190.

(51) Bladt, E.; van Dijk-Moes, R. J. A.; Peters, J.; Montanarella, F.; de Mello Donega, C.; Vanmaekelbergh, D.; Bals, S., Atomic Structure of Wurtzite CdSe (Core)/CdS (Giant Shell) Nanobullets Related to Epitaxy and Growth. *J. Am. Chem. Soc.* **2016,** *138* (43), 14288-14293.

(52) Ruberu, T. P. A.; Albright, H. R.; Callis, B.; Ward, B.; Cisneros, J.; Fan, H.; Vela, J., Molecular Control of the Nanoscale: Effect of Phosphine-Chalcogenide Reactivity on CdS-CdSe Nanocrystal Composition and Morphology. *ACS Nano* **2012,** *6* (6), 5348-5359.

(53) Xie, R.; Kolb, U.; Li, J.; Basché, T.; Mews, A., Synthesis and Characterization of Highly Luminescent CdSe−Core $CdS/Zn_{0.5}Cd_{0.5}S$/ZnS Multishell Nanocrystals. *J. Am. Chem. Soc.* **2005,** *127* (20), 7480-7488.

(54) Swafford, L. A.; Weigand, L. A.; Bowers, M. J.; McBride, J. R.; Rapaport, J. L.; Watt, T. L.; Dixit, S. K.; Feldman, L. C.; Rosenthal, S. J., Homogeneously Alloyed CdS_xSe_{1-x} Nanocrystals: Synthesis, Characterization, and Composition/Size-Dependent Band Gap. *J. Am. Chem. Soc.* **2006,** *128* (37), 12299-12306.

(55) Mukherjee, P.; Lim, S. J.; Wrobel, T. P.; Bhargava, R.; Smith, A. M., Measuring and Predicting the Internal Structure of Semiconductor Nanocrystals Through Raman Spectroscopy. *J. Am. Chem. Soc.* **2016,** *138* (34), 10887-10896.

(56) Qian, H.; Qiu, X.; Li, L.; Ren, J., Microwave-Assisted Aqueous Synthesis: A Rapid Approach to Prepare Highly Luminescent ZnSe(S) Alloyed Quantum Dots. *J. Phys. Chem. B* **2006,** *110* (18), 9034-9040.

(57) Jang, E.; Jun, S.; Pu, L., High Quality CdSeS Nanocrystals Synthesized by Facile Single Injection Process and their Electroluminescence. *Chem. Comm.* **2003,** (24), 2694-2695.

(58) Cragg, G. E.; Efros, A. L., Suppression of Auger Processes in Confined Structures. *Nano Lett.* **2010,** *10* (1), 313-317.

(59) Park, Y. S.; Malko, A. V.; Vela, J.; Chen, Y.; Ghosh, Y.; García-Santamaría, F.; Hollingsworth, J. A.; Klimov, V. I.; Htoon, H., Near-unity Quantum Yields of Biexciton Emission from CdSe/CdS Nanocrystals Measured Using Single-Particle Spectroscopy. *Phys. Rev. Lett.* **2011,** *106* (18), 187401.

(60) Morgan, D.; Gong, K.; Kelley, A. M.; Kelley, D. F., Biexciton Dynamics in Alloy Quantum Dots. *J. Phys. Chem. C* **2017,** *121* (33), 18307-18316.

(61) Nelson, D. J.; Nahra, F.; Patrick, S. R.; Cordes, D. B.; Slawin, A. M. Z.; Nolan, S. P., Exploring the Coordination of Cyclic Selenoureas to Gold (I). *Organometallics* **2014,** *33* (13), 3640-3645.

(62) Vummaleti, S. V. C.; Nelson, D. J.; Poater, A.; Gómez-Suárez, A.; Cordes, D. B.; Slawin, A. M. Z.; Nolan, S. P.; Cavallo, L., What Can NMR Spectroscopy of Selenoureas and Phosphinidenes Teach Us About the π-Accepting Abilities of N-Heterocyclic Carbenes? *Chem. Sci.* **2015,** *6* (3), 1895-1904.

(63) Zhou, Y.; Denk, M. K., Synthesis and Reactivity of Subvalent Compounds. Part 13: Reaction of Triethyl Orthoformate with Amines and Selenium-a Convenient One-Step Three-Component Synthesis for Selenoureas. *Tetrahedron Lett.* **2003,** *44* (6), 1295-1299.

(64) Denk, M. K.; Gupta, S.; Brownie, J.; Tajammul, S.; Lough, A. J., C-H Activation with Elemental Sulfur: Synthesis of Cyclic Thioureas from Formaldehyde Aminals and S_8. *Chem. Eur. J.* **2001,** *7* (20), 4477-4486.

(65) Bogatskii, A. V.; Luk'yanenko, N. G.; Kirichenko, T. I., Literature Data on Methods for the Synthesis of Cyclic Thioureas and Their Physicochemical Properties and Transformations are Correlated. *Khimiya Geterotsiklicheskikh Soedinenii* **1982,** *6*, 723-737.

(66) Staab, H. A., New Methods of Preparative Organic Chemistry IV. Syntheses Using Heterocyclic Amides (Azolides) [*]. *Angew. Chem. Int. Ed.* **1962,** *1* (7), 351-367.

(67) Horikawa, M.; Busch-Petersen, J.; Corey, E. J., Enantioselective Synthesis of β-Hydroxy-α-Amino Acid Esters by Aldol Coupling Using a Chiral Quaternary Ammonium Salt as Catalyst. *Tetrahedron Lett.* **1999,** *40* (20), 3843-3846.

(68) Leatherdale, C. A.; Woo, W. K.; Mikulec, F. V.; Bawendi, M. G., On the Absorption Cross Section of CdSe Nanocrystal Quantum Dots. *J. Phys. Chem. B* **2002,** *106* (31), 7619-7622.

(69) Cassidy, C. S.; Reinhardt, L. A.; Cleland, W. W.; Frey, P. A., Hydrogen Bonding in Complexes of Carboxylic Acids with 1-Alkylimidazoles: Steric and Isotopic Effects on Low Barrier Hydrogen Bonding. *J. Chem. Soc., Perkin Trans. 2* **1999,** (3), 635-642.

(70) LaMer, V. K., Nucleation in Phase Transitions. *Ind. Eng. Chem.* **1952,** *44* (6), 1270-1277.
(71) LaMer, V. K.; Dinegar, R. H., Theory, Production and Mechanism of Formation of Monodispersed Hydrosols. *J. Am. Chem. Soc.* **1950,** *72* (11), 4847-4854.
(72) Chu, D. B.; Owen, J. S.; Peters, B., Nucleation and Growth Kinetics from LaMer Burst Data. *J. Phys. Chem. A* **2017,** *121* (40), 7511-7517.
(73) Yu, Z.; Guo, L.; Du, H.; Krauss, T.; Silcox, J., Shell Distribution on Colloidal CdSe/ZnS Quantum Dots. *Nano Lett.* **2005,** *5* (4), 565-570.
(74) Karel Capek, R.; Moreels, I.; Lambert, K.; De Muynck, D.; Zhao, Q.; Van Tomme, A.; Vanhaecke, F.; Hens, Z., Optical Properties of Zincblende Cadmium Selenide Quantum Dots. *J. Phys. Chem. C* **2010,** *114* (14), 6371-6376.
(75) Moreels, I.; Lambert, K.; Smeets, D.; De Muynck, D.; Nollet, T.; Martins, J. C.; Vanhaecke, F.; Vantomme, A.; Delerue, C.; Allan, G., Size-Dependent Optical Properties of Colloidal PbS Quantum Dots. *ACS Nano* **2009,** *3* (10), 3023-3030.
(76) Moreels, I.; Lambert, K.; De Muynck, D.; Vanhaecke, F.; Poelman, D.; Martins, J. C.; Allan, G.; Hens, Z., Composition and size-dependent extinction coefficient of colloidal PbSe quantum dots. *Chem. Mat.* **2007,** *19* (25), 6101-6106.
(77) De Roo, J.; Ibáñez, M.; Geiregat, P.; Nedelcu, G.; Walravens, W.; Maes, J.; Martins, J. C.; Van Driessche, I.; Kovalenko, M. V.; Hens, Z., Highly Dynamic Ligand Binding and Light Absorption Coefficient of Cesium Lead Bromide Perovskite Nanocrystals. *ACS Nano* **2016,** *10* (2), 2071-2081.
(78) Drijvers, E.; De Roo, J.; Geiregat, P.; Fehér, K.; Hens, Z.; Aubert, T., Revisited Wurtzite CdSe Synthesis: A Gateway for the Versatile Flash Synthesis of Multishell Quantum Dots and Rods. *Chem. Mat.* **2016,** *28* (20), 7311-7323.
(79) Nakonechnyi, I.; Sluydts, M.; Justo, Y.; Jasieniak, J.; Hens, Z., Mechanistic Insights in Seeded Growth Synthesis of Colloidal Core/Shell Quantum Dots. *Chem. Mat.* **2017,** *29* (11), 4719-4727.
(80) Angeloni, I.; Raja, W.; Brescia, R.; Polovitsyn, A.; De Donato, F.; Canepa, M.; Bertoni, G.; Proietti Zaccaria, R.; Moreels, I., Disentangling the Role of Shape, Ligands, and Dielectric Constants in the Absorption Properties of Colloidal CdSe/CdS Nanocrystals. *ACS Photonics* **2016,** *3* (1), 58-67.
(81) Anderson, N. C.; Hendricks, M. P.; Choi, J. J.; Owen, J. S., Ligand Exchange and the Stoichiometry of Metal Chalcogenide Nanocrystals: Spectroscopic Observation of Facile Metal-Carboxylate Displacement and Binding. *J. Am. Chem. Soc.* **2013,** *135* (49), 18536-18548.

(82) Hens, Z.; Moreels, I., Light absorption by colloidal semiconductor quantum dots. *J. Mater. Chem.* **2012,** *22* (21), 10406-10415.

(83) Karel Čapek, R.; Moreels, I.; Lambert, K.; De Muynck, D.; Zhao, Q.; Van Tomme, A.; Vanhaecke, F.; Hens, Z., Optical Properties of Zincblende Cadmium Selenide Quantum Dots. *The Journal of Physical Chemistry C* **2010,** *114* (14), 6371-6376.

CHAPTER 4. Structural Characterization of Homogeneous, Graded Alloy, and Core/Crown $CdSe_{1-x}S_x$ Nanoplatelets Synthesized via Kinetic Control

Table of Contents

Some of the experiments described herein were performed by I. Billinge, M. W. Greenberg, N. Saenz, S. Banerjee, and B. H. Savitzky. Their collaboration in this endeavor is gratefully acknowledged.

4.1. Abstract

4.1.1. Technical Abstract

We synthesize 3 monolayer CdSe and CdS nanoplatelets with lateral dimensions varying between 10 nm x 10 nm to 200 nm x 200 nm using substituted thio- and selenoureas possessing 5 orders of magnitude of conversion reactivity with cadmium acetate dihydrate at 195 °C. We simultaneously inject mixtures of sulfur and selenium precursors to generate $CdSe_{1-x}S_x$ nanoplatelet heterostructures of predicted homogeneous alloy, graded alloy, and core/crown compositions. We characterize the relationship between precursor conversion and elemental distributions of sulfur and selenium atoms in the final structures by their absorbance and emission spectra, scanning transmission electron microscopy energy dispersive x-ray spectroscopy (STEM EDX), scanning transmission electron microscopy electron energy-loss spectroscopy (STEM EELS) and pair distribution function analysis (PDF).

4.1.2. Plain English Abstract

Nanoplatelets are distinct from the spherical nanoparticles previously described in this thesis because they are highly anisotropic, possessing one spatial dimension that is several atomic layers thick and two dimensions of substantially larger size. Due to their largely one-dimensional quantum confinement,

nanoplatelets possess extremely narrow emission linewidths that are about half to a third as narrow as those of spherical nanoparticles. The extreme color purity of nanoplatelet emissions could enhance many of the benefits that spherical nanoparticles have as fluorescent emitters. Much like for spherical nanoparticles, compositional control over nanoplatelet structure is very important. We seek to extend the utility of our library of sulfur and selenium containing molecules towards the synthesis of nanoplatelets. Because platelets are two-dimensional structures, we hope to use them as a good model system to elementally map distributions of sulfur and selenium atoms with electron microscopy. Analogous to how tree rings provide information about tree growth over time, we seek to use the elemental distributions of sulfur and selenium atoms in our nanoplatelets to illustrate nanoplatelet growth over time. We were successful in controlling the synthesis of nanoplatelet structures based on molecule reactivity, however, we observe that nanoplatelet crystallization processes are complex and that our structures do not grow as symmetrically as our simplistic kinetic model predicts.

4.2. Context

Two-dimensional colloidal cadmium chalcogenide nanoplatelets possess narrow full-width half max emission linewidths which make them valuable for their color purity.[1] This is due to their uniform confinement in one dimension which is significantly thinner than the material's Bohr radius leading to quantum

confinement effects. They also possess fast fluorescence lifetimes that result from image charges and large exciton binding energies as a consequence of their large surfaces.[2] Their absorption and emission spectra exhibit shifts due to changes in thickness, confinement, and elemental composition. Control over nanoplatelet thickness is achieved through selection of reaction temperature and ligands. Notably, the use of cadmium acetate, a short chain carboxylate (O_2CCH_3), leads to the growth of nanoplatelets as opposed to nanoparticles which form in the presence of a long chain carboxylic acid such as oleic acid ($O_2CC_{17}H_{34}$).[1]

More recently, Moreels et al. has demonstrated control over platelet lateral dimensions and shape via the cadmium acetate/cadmium acetate dihydrate ratio, which points to the role of water in nanoplatelet synthesis. However, this change is non-innocent towards platelet surface chemistry; it is found to alter the presence of bound hydroxide anions.[3] A method for tuning platelet dimensions separate from tuning traditional variables such as temperature or surfactant mixtures is required because during synthesis, these changes have large effects on platelet thickness and surface chemistry. Additionally, small lateral dimensions of platelets are desired to reduce rolling in thin samples[4] as well as attain higher PL efficiencies due to a lower probability of defects.[5]

We recently demonstrated chemical control over chalcogen precursor decomposition rates as an effective way to achieve size control over the synthesis

of spherical nanoparticles.[6-9] We have also demonstrated the synthesis of one-pot core/shells, alloys, and inverse core/shell heterostructures using a single injection of chalcogen precursors that relies solely on reaction kinetics to determine structural control.[9] Extending the utility of this library of chalcogenourea precursors to nanoplatelets will enable new temporal studies on the growth mechanisms of anisotropic particles via electron microscopy techniques that enable elemental mapping.

In this chapter, we add a series of trisubstituted thioureas to our expansive chalcogenourea precursor library which had previously only been used to synthesize spherical nanocrystals or nanorods.[6-8] We demonstrate that precursor conversion rates adjust the lateral dimensions of nanoplatelets and link precursor conversion rates directly to radial distributions of chalcogens in platelet samples.

4.3. Nanoplatelet Synthesis

4.3.1. Precursors for Platelet Synthesis

Trisubstituted thioureas, *N*-monosubstituted cyclic selones, and *N,N'*-disubstituted cyclic selones whose synthesis is described previously,[6, 8-9] possess the appropriate reactivity with cadmium acetate dihydrate for the synthesis of 3 monolayer thick cadmium chalcogenide nanoplatelets. Unlike under nanocrystal forming conditions with long chain carboxylate ligands at 240 °C, trisubstituted

thioureas with differing steric profiles possess noticeably distinct reactivity under the lower temperature nanoplatelet forming conditions (Table 4.3.1). We note that the reactivity trends of trisubstituted compounds is opposite the trend of disubstituted compounds. For example, trialkyl thioureas react the fastest with aryl substituents slowing down precursor reactivity whereas diaryl disubstituted thioureas react faster than dialkyl disubstituted thioureas. This is consistent with our mechanistic hypothesis for the reaction of di- vs. trisubstituted thioureas. Disubstituted thioureas are hypothesized to react via a deprotonation to form a metal thioureate intermediate followed by a second deprotonation to form the carbodiimide. Aryl groups and other electron withdrawing substituents will favor deprotonation. In contrast, trisubstituted thioureas are hypothesized to form a metal thioureate intermediate followed by nucleophilic attack on the thio- or selenocarbonyl by an intermolecular or intramolecular carboxylate. This nucleophilic attack is likely to be heavily affected by sterics.

Platelet kinetics were determined by size independent extinction coefficients at 350 nm for CdSe,[10] and by looking at absorbance at 371 nm, which corresponds to the band edge transition of 3 monolayer thick CdS nanoplatelets. Although the reaction is not expected to be a first order reaction, the production of cadmium chalcogenide material can be fit well to a first order fit. To quantify

differences in reactivity, we extract k_r for the purpose of comparing relative reactivities. Find more details in the experimental (Kinetics Determination).

Table 4.3.1. Reaction scheme to form 3 monolayer thick cadmium chalcogenide nanoplatelets. Compound structures, % Yields of precursor synthesis, and reactivity (k_r) of all precursors under these reaction conditions. [a]Synthesized as previously described.[6] [b]Synthesized as previously described.[8] [c]Synthesized as previously described.[9] [d]Commercially available.

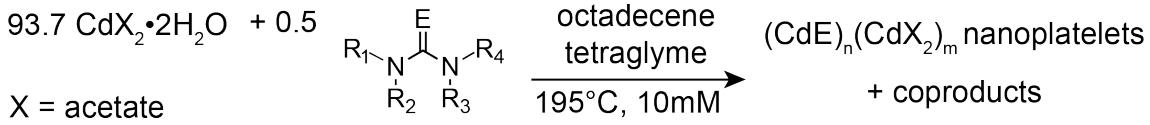

Compound	E	R_1	R_2	R_3	R_4	% Yield Compound	k_r
1	S	H	*n*-C_6H_{13}	H	*n*-$C_{12}H_{25}$	[a]	>1
2	S	H	*n*-C_6H_{13}	*n*-C_8H_{17}	*n*-C_8H_{17}	[a]	6.1 x 10^{-2}
3	S	H	Cy	-CH_2CH_2-		22	5.3 x 10^{-2}
4	S	H	*n*-C_6H_{13}	-CH_2CH_2-		4.7	3.6 x 10^{-2}
5	S	H	Ph	-CH_2CH_2-		31	2.6 x 10^{-2}
6	S	H	Bn	-CH_2CH_2-		30	2.1 x 10^{-2}
7	S	H	Ph	*n*-C_4H_9	*n*-C_4H_9	[a]	1.3 x 10^{-2}
8	S	H	CH_3	Ph	Ph	[b]	3.3 x 10^{-3}
9	S	H	-CH_2CH_2-		H	[d]	2.8 x 10^{-3}
10	S	H	-CH_2CH_2-		Ph	[c]	9.9 x 10^{-4}
11	Se	H	-CH_2CH_2-		Ph	[c]	1.3 x 10^{-1}
12	Se	H	-CH_2CH_2-		*n*-C_2H_5	[c]	6.6 x 10^{-3}
13	Se	Ph	-CH_2CH_2-		Ph	[c]	6.6 x 10^{-3}
14	Se	H	-CH_2CH_2-		iPr	[c]	4.1 x 10^{-3}
15	Se	*t*-Bu	-CH_2CH_2-		*t*-Bu	[c]	2.6 x 10^{-4}

4.3.2. Platelet Synthesis

Analogous to the link between precursor conversion kinetics and final nanoparticle size for II-VI,[6, 8-9, 11-13] IV-VI,[6-7, 14] and III-V[15-17] nanoparticle systems, we demonstrate that decreasing precursor reactivity leads to the formation of larger nanoplatelets (Figure 4.3.1). It is not straightforward to obtain a relationship between k_r and number of platelets nucleated (analogous to the analysis performed in Chapter 3) due to the simultaneous production of unwanted nanocrystal byproducts in our platelet syntheses that must be excluded via centrifugation procedures. However, it has been observed that changing the lateral dimensions of platelets is known to impact nanoplatelet rolling.[4] Thus, it is perhaps not surprising that as the precursor reactivity changes, the platelet lateral dimensions and extent of rolling also change. In order to obtain nanoplatelets that are not rolled, we prefer the use of **11**.

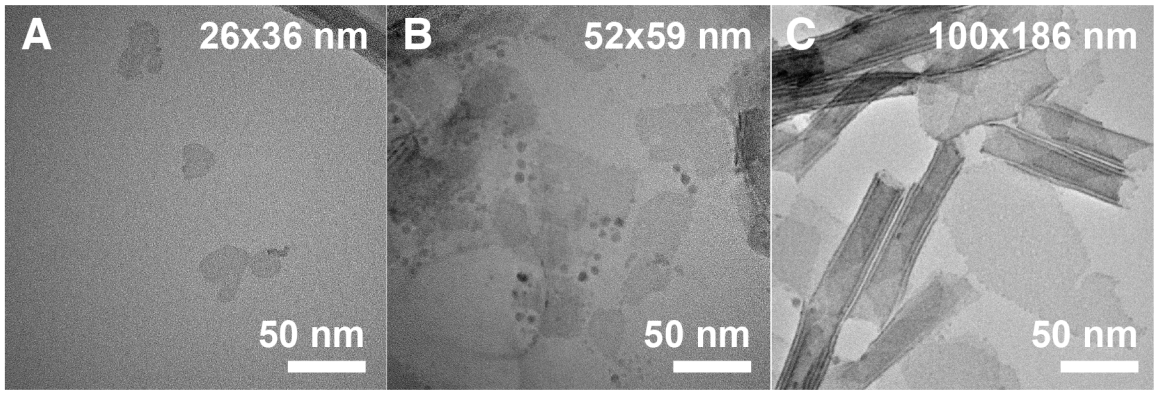

Figure 4.3.1. TEM images of 3 monolayer CdSe platelets synthesized from A) **11**, B) **13**, and C) **15**.

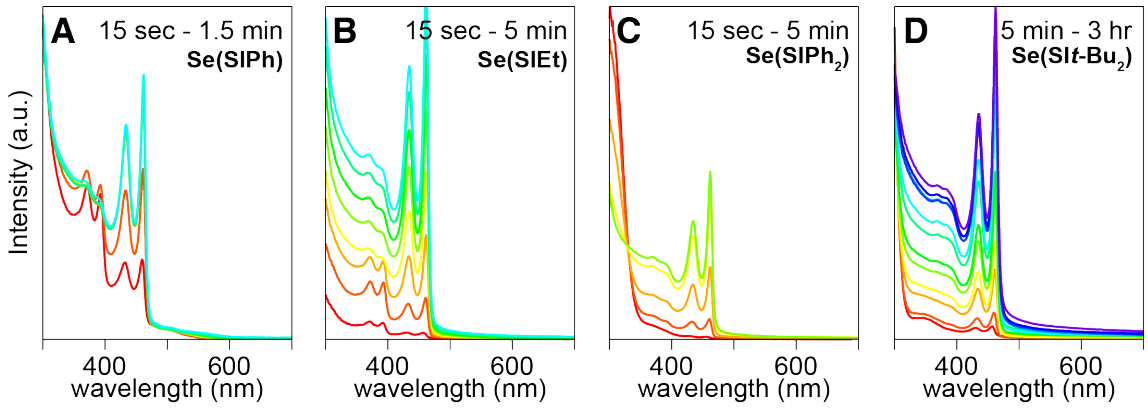

Figure 4.3.2. UV-vis spectra of 3 monolayer CdSe platelets synthesized from A) **11**, B) **12**, C) **13**, and D) **15**.

In the reaction with **11**, despite varying many parameters including temperature, concentration, equivalences of cadmium, **11**, and oleic acid, we are unable to remove a small undesirable population of nanocrystals that nucleates alongside our target nanoplatelet products. In fact, many of our changes increased the intensity of the undesired population as measured by absorbance spectroscopy. We observe that the use of slightly slower precursors such as **12**, **13**, or **15** seem to eliminate this problem (Figure 4.3.2), at least as can be distinguished via absorbance spectroscopy, although there are still small populations of nanoparticles observable via electron microscopy (Figure 4.3.1).

4.3.3. Varying Composition with Precursor Conversion

We simultaneously inject mixtures of sulfur precursor with varying k_r values (**1**, **7**, and **8**) with selenium precursor **11** in order to kinetically grow $CdSe_{1-}$

$_xS_x$ nanoplatelet heterostructures. Based on the conversion kinetics of the single component reaction solutions (Table 4.3.1), we can predict the resulting nanoplatelet structures (Figure 4.3.3 and Structure Simulations).

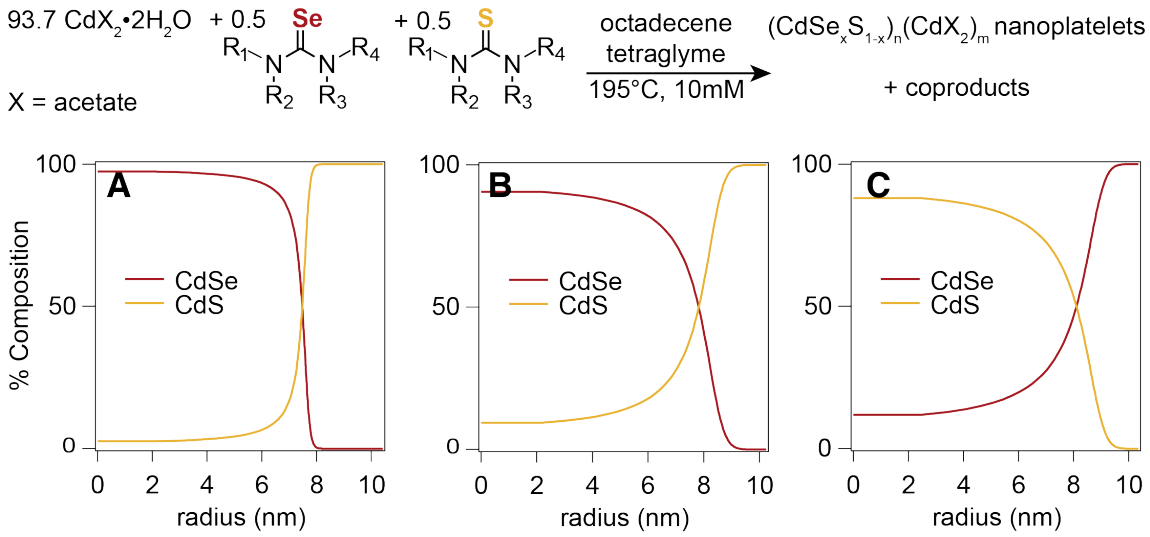

Figure 4.3.3. Synthetic scheme and predicted structure of $CdSe_{1-x}S_x$ nanoplatelets synthesized via a simultaneous injection of **11** and A) **8**, B) **7**, and C) **1**.

UV-vis absorbance spectra of reaction aliquots are shown in Figure 4.3.4. Figure 4.3.4A shows absorbance at early times corresponding with a 3 monolayer CdSe nanoplatelet emitting at 461 nm (fluorescence not shown). As the reaction proceeds and more CdS monomers get supplied to the reaction, a higher energy absorbance peak appears. The reaction spectra taken at early timepoints in Figure 4.3.4B-C are blue shifted compared to the CdSe/CdS core/crown example which

indicates that the platelet cores contain more converted CdS which tracks with what is predicted via our kinetics simulations.

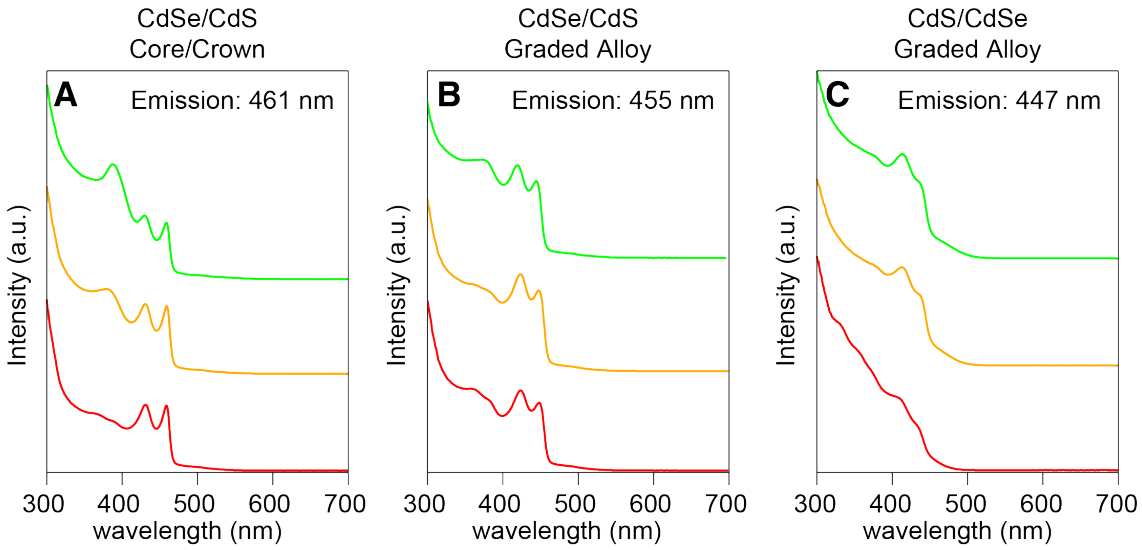

Figure 4.3.4. UV-vis spectra of $CdSe_{1-x}S_x$ nanoplatelets synthesized via a simultaneous injection of **11** and A) **8**, B) **7**, and C) **1**.

4.3.4. Alloy Compositions

To synthesize homogeneous alloys, we simultaneously inject a mixture of precursors **8** and **13** that possess matched reactivity. Based on the conversion kinetics of the single component reaction solutions (Table 4.3.1), the platelets are predicted to be close to homogeneous alloyed platelets (Figure 4.3.5 and Structure Simulations). Further characterization must be done to verify the structure of these platelets.

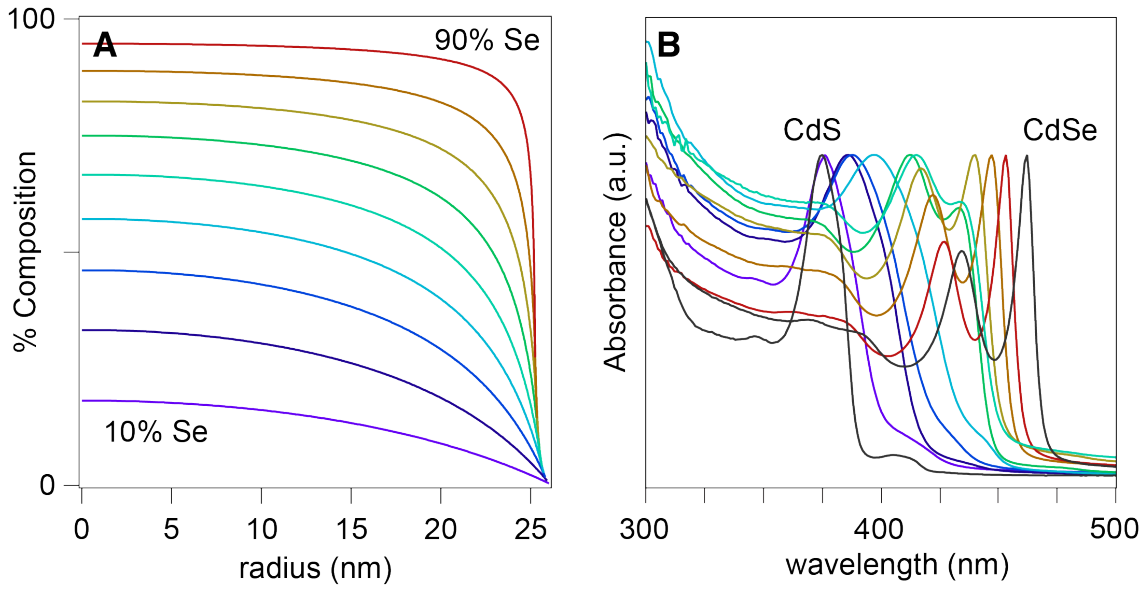

Figure 4.3.5. A) Predicted structure and B) absorbance spectra of $CdSe_{1-x}S_x$ homogeneous alloy nanoplatelets synthesized via a simultaneous injection of **8** and **13**.

4.4. Characterization

4.4.1. Electron Microscopy

Structural and elemental characterization of nanoplatelets is challenging but has been enabled by advances in electron microscopy techniques. Previously, atomic resolution HAADF STEM was used to correct nanoplatelet thicknesses predicted from calculations.[18] Additionally, $CdSe_{1-x}S_x$ alloyed or core/crown platelet compositions have been mapped by STEM EDX on platelets that are 4 or 6 monolayers thick.[19-21] We cannot use 4-6 monolayer thick platelets for our experiments because they are synthesized via a mechanism that is not precursor conversion limited.[22] However, our 3 monolayer platelet synthesis is precursor

conversion limited which directly links precursor reactivity and the final nanoplatelet structure. Due to the increase in sample fragility, elemental mapping via electron microscopy measurements becomes more difficult the thinner a material is. In order to work around sample degradation issues, performing imaging experiments at cryogenic temperatures has previously increased the stability of inorganic nanostructures.[23] We decided to employ this method to enable characterization of chalcogen distributions in our 3 monolayer thick $CdS_{1-x}S_x$ nanoplatelet samples.

4.4.1.1. STEM EDX

Attempts to perform STEM EDX elemental mapping on 3 monolayer platelet samples is limited by sample degradation. Atomic resolution STEM images can be collected at 200kV but at high magnification (>225kx), the sample begins to degrade in seconds. We collected low magnification (40kx) STEM EDX images of hundreds of platelets to quantify elemental compositions present in the samples described in Figure 4.3.3 and Figure 4.3.4 (Table 4.4.1). As expected, the elemental percentages of sulfur and selenium are approximately 50:50 matching the ratio of the original thiourea to selenourea that were injected into the reactions.

Table 4.4.1. Atomic % of sulfur, selenium, and cadmium observed in nanoplatelet samples via STEM EDX whose synthesis is described in Figure 4.3.3 and Figure 4.3.4.

Sample	Atomic % S	Atomic % Se	Atomic % Cd
CdSe/CdS Core/Crown	35%	28%	37%
CdSe/CdS Graded Alloy	31%	29%	39%
CdS/CdSe Graded Alloy	31%	30%	39%

Decreasing the accelerating voltage to 80kV allowed for greater stability on the order of minutes that allows for the collection of EDX maps on single platelets. However, these maps are still limited by poor signal to noise, so we turned to lower accelerating voltages and lower imaging temperatures to try to increase sample stability.

4.4.1.2. STEM EELS

We perform STEM EELS mapping on single nanoplatelets at 60 kV. Elemental mapping was performed at -80 °C in order to reduce beam damage and eliminate contamination while preventing buildup of ice at liquid nitrogen temperatures. We collected data at the cadmium $M_{4,5}$ edge at 404 eV, the selenium L_2 and L_3 edges at 1476 and 1436 eV, and the sulfur $L_{2,3}$ edge at 165 eV. We additionally attempted to find the sulfur K edge at 2472 eV, although this did not

prove fruitful, likely due to issues detecting high energy loss peaks from an already very low energy (60 kV) electron beam.

EELS mapping is consistent with our simulations of the nanoplatelets. The uniform intensity of the ADF images shows that Cd is evenly distributed throughout the whole platelet. Although we were unable to collect cadmium and selenium EELS data on the same map, we observe that the ADF image intensity tracks well with the cadmium content. Thus, for samples without cadmium maps, we can use the ADF image as a proxy for the cadmium content. Selenium is in some cases distributed near the core or crown of the platelet (Figure 4.4.1 and Figure 4.4.3), and in other cases more evenly distributed around the platelet (Figure 4.4.2). Based on the STEM EDX elemental compositions determined in Table 4.4.1, it is reasonable to conclude that if the ADF image looks uniform as a 3 monolayer platelet and there are intensity changes in the selenium map then sulfur is likely localized in the selenium void regions. We are able to confirm this hypothesis albeit not on the same nanoplatelet samples for the CdS/CdSe graded alloy platelet samples synthesized in Figure 4.3.4C (Figure 4.4.4). These images are representative of the ~25 platelets per sample that have been mapped via STEM EELS.

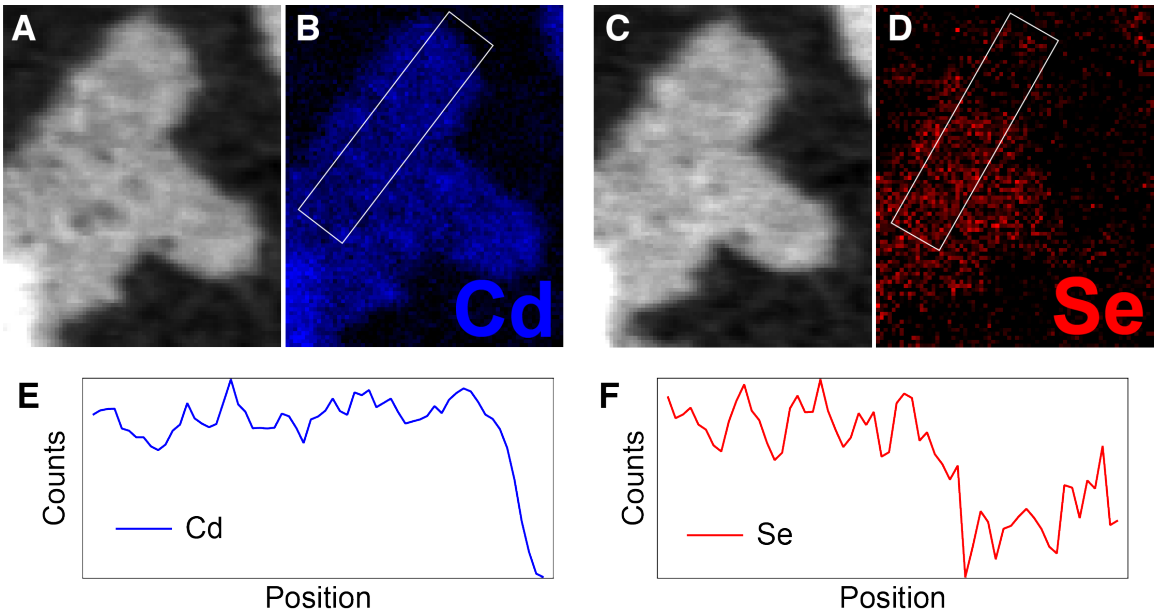

Figure 4.4.1. CdSe/CdS core/crown sample (Figure 4.3.3A and Figure 4.3.4A) A) ADF image, B) Cd $M_{4,5}$ map, C) ADF image, D) Se L_2/L_3 map, E) cadmium map linescan, and F) selenium map linescan.

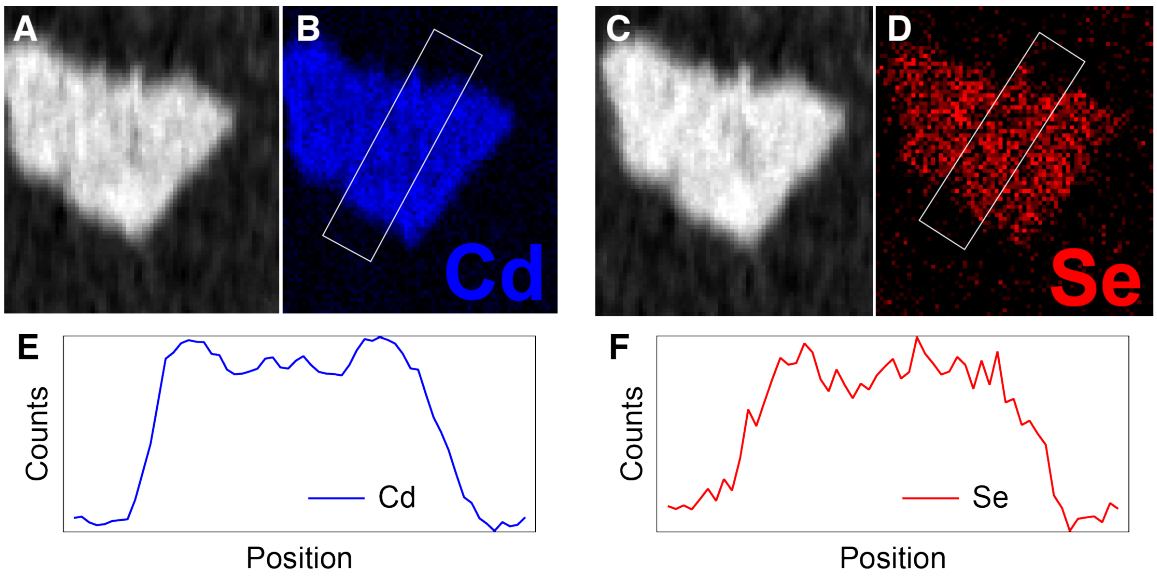

Figure 4.4.2. CdSe/CdS graded alloy sample (Figure 4.3.3B and Figure 4.3.4B) A) ADF image, B) Cd $M_{4,5}$ map, C) ADF image, D) Se L_2/L_3 map, E) cadmium map linescan, and F) selenium map linescan.

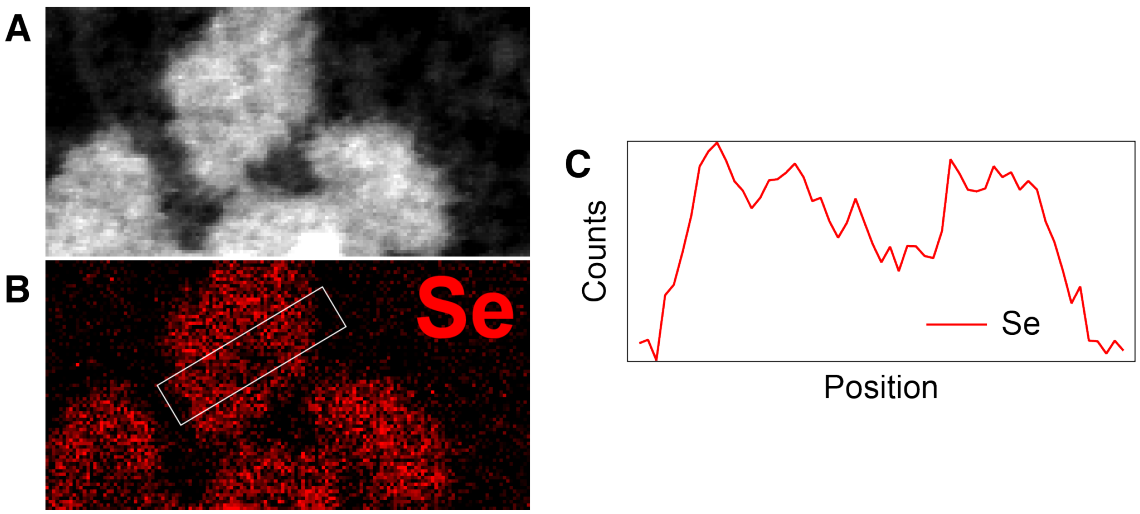

Figure 4.4.3. CdS/CdSe graded alloy sample (Figure 4.3.3C and Figure 4.3.4C) A) ADF image, B) Se L_2/L_3 map, C) selenium map linescan.

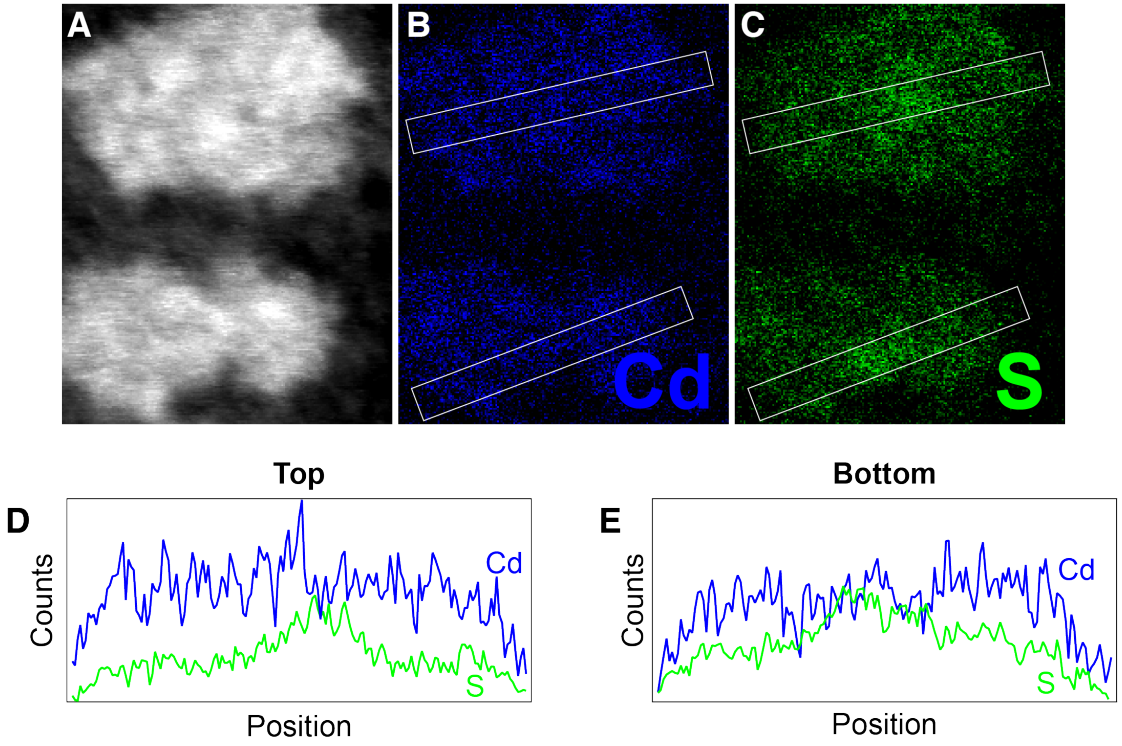

Figure 4.4.4. CdS/CdSe graded alloy sample (Figure 4.3.3C and Figure 4.3.4C) A) ADF image, B) Cd $M_{4,5}$ map, C) S $L_{2,3}$ map, D) cadmium and sulfur linescan (top) and E) cadmium and sulfur linescan (bottom).

4.4.1.3. Extraneous Nucleation of Crown Material

Interestingly, for the core/crown and CdSe/CdS graded alloy samples, we observe some platelets that do not contain selenium as characterized via EELS (Figure 4.4.5). Our interpretation is that these platelets may consist solely of CdS. For the core/crown and CdSe/CdS graded alloy samples in which a slower sulfur precursor deposits CdS onto nucleated CdSe or CdSe-rich cores, it is possible that we see separate nucleation and growth of this shell material, similar to the extraneous nucleation of shell material described in CdSe/CdS one pot core/shell reactions in Chapter 3. This could be occurring due to inherent differences in the growth rates of CdS and CdSe, differences in their critical concentration, or activation barriers to growing CdS on a CdSe platelet.

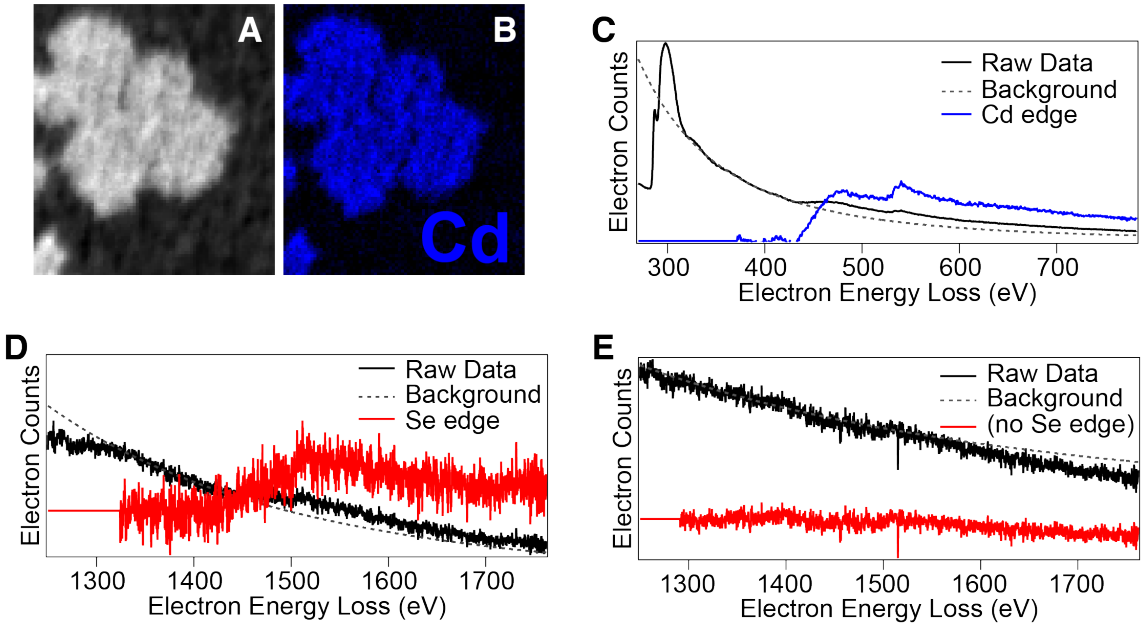

Figure 4.4.5. A) ADF image, B) Cd $M_{4,5}$ map, C) EELS spectrum near the 404 eV onset of the cadmium energy loss peak, D-E) EELS spectra near the 1476 eV onset of the selenium energy loss peak of a platelet in reaction B that does and does not contain a visible Se edge.

4.4.1.4. Studies of chalcogen deposition on platelets

Although we have good control over the chalcogen atom supply rate to the growing nanoplatelets via our chemical control of precursor conversion, it appears that the second material to deposit does not grow isotropically around the nanoplatelet (Figure 4.4.1). Because of their large dimensions, beam stability at cryogenic temperatures, and link between precursor conversion and monomer generation, platelets are a great model system in which to study the deposition of CdS and CdSe monomers onto the growing crystal with temporal resolution.

From reaction A, we observe nonconformal growth of CdS around the CdSe seed platelets. In fact, many of the core/crown nanoplatelets we are able to grow under kinetic control appear T-shaped and the crown is not as conformal as other examples in the literature.[21] It is interesting to note, however, that while the CdS/CdSe graded alloy platelets are also shelled anisotropically, the platelet shape is more isotropic and oval compared with the angular and irregular T-shaped CdSe/CdS core/crown platelets (Figure 4.4.3).

4.4.2. Pair Distribution Function Analysis

We perform pair distribution function (PDF) analysis, which is an X-ray technique aptly suited for the characterization of nanomaterials.[24-25] These nanoplatelets lie in a regime where other X-ray techniques are less useful; single crystal X-ray diffraction must be applied to well-defined, diffraction-quality single crystals which are impossible to produce from distributions of semiconducting nanoparticles, and powder X-ray diffraction produces broad, diffuse X-ray scattering features especially at small sizes.[26] PDF analysis has proved useful for many types of nanomaterial studies including magic-size CdSe[26] or CdS clusters[27] and identifying core/shell vs. alloy heterostructures.[28]

The PDF analysis described herein was performed by M. W. Greenberg and S. Banerjee. We find that the nanoplatelet cores, at low-*r*, are adequately described using a single phase zincblende structure model, with no significant

improvements using a proxy two-phase faulted model consisting of wurtzite and zincblende layers. This suggests that the core structure of the nanoplatelets are predominantly unfaulted (Figure 4.4.6). This is surprising in the context of other cadmium chalcogenide nanomaterials which typically possess stacking fault densities around 30%.[29] However, due to the well-ordered nature of the zincblende nanoplatelets as determined via atomic resolution STEM images and the zincblende directing nature of the short chain carboxylate ligands, perhaps this is not surprising.

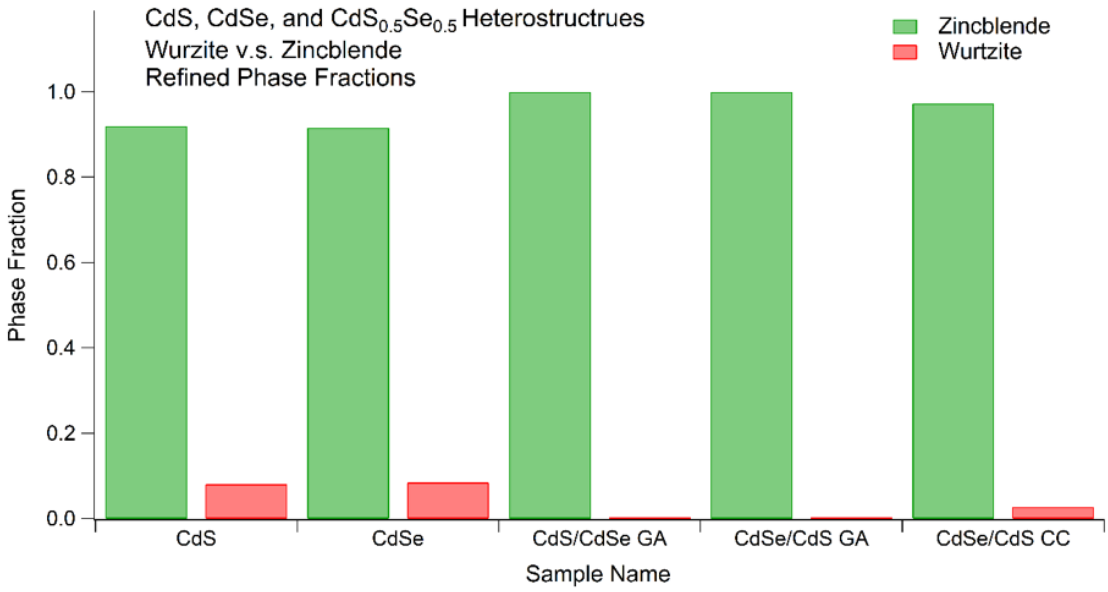

Figure 4.4.6. The PDF analysis of a pure CdS, pure CdSe, and the core/crown and graded alloy samples whose synthesis is described in Figure 4.3.3 show a high zincblende phase purity.

Additional analysis of the PDF patterns (Figure 4.4.7) shows a few important things. First, that the first few atomic correlation peaks are heightened

compared to that of spherical nanoparticles. This is due to the anisotropic structure of the 2-D nanoplatelets. As a result, these nanoplatelets cannot be fully modeled by spherical envelope functions used to fit PDF patterns of nanoparticles. This is perhaps not surprising. Second, we see that the lattice parameter of the $CdSe_{1-x}S_x$ composites lays between that of a 3 monolayer CdS and CdSe nanoplatelet sample with a slight deviation from what might be expected from Vegard's law[30] (Figure 4.4.8). We hope that further analysis of these samples will help us develop a good method to analyze composition of these flat nanoplatelets that can also be extended to the analysis of the rolled nanoplatelet alloys described previously (Figure 4.3.5).

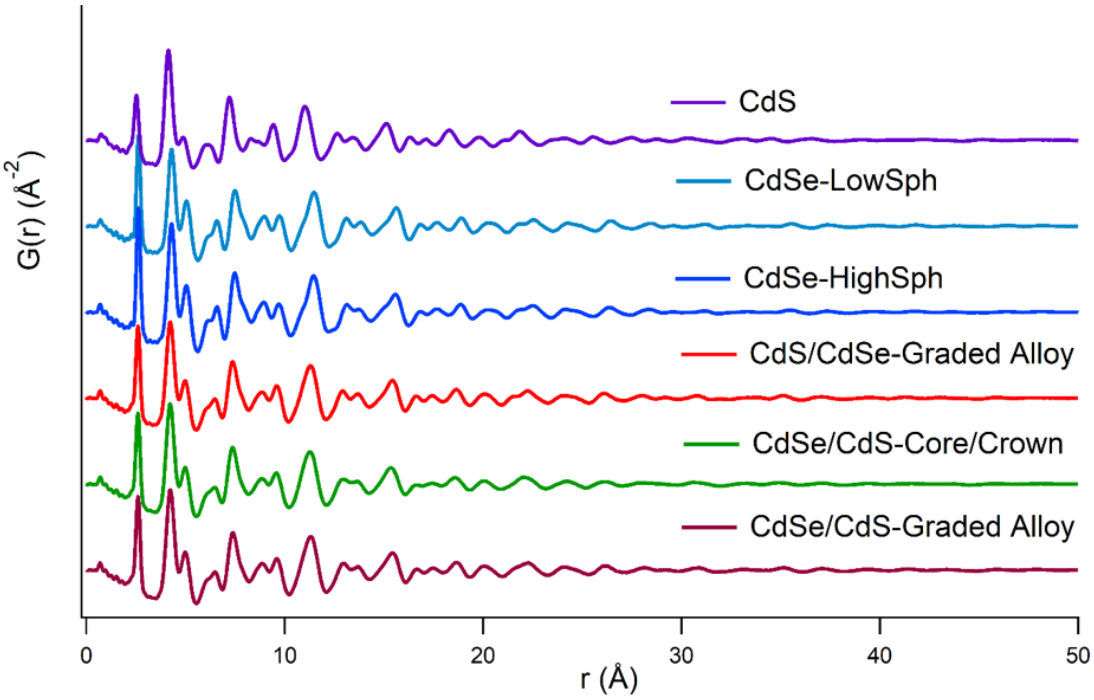

Figure 4.4.7. Experimental PDF data of pure Cd, pure CdSe,* CdS/CdSe graded alloy, CdSe/CdS core/crown, and CdSe/CdS graded alloy nanoplatelets of approximately 10 nm x 10 nm in dimensions. *Our CdSe nanoplatelet samples contain spherical nanoparticle impurities. In order to test how much the presence of this impurity affects the PDF analysis, we measured samples with a different amounts of nanocrystal impurity present.

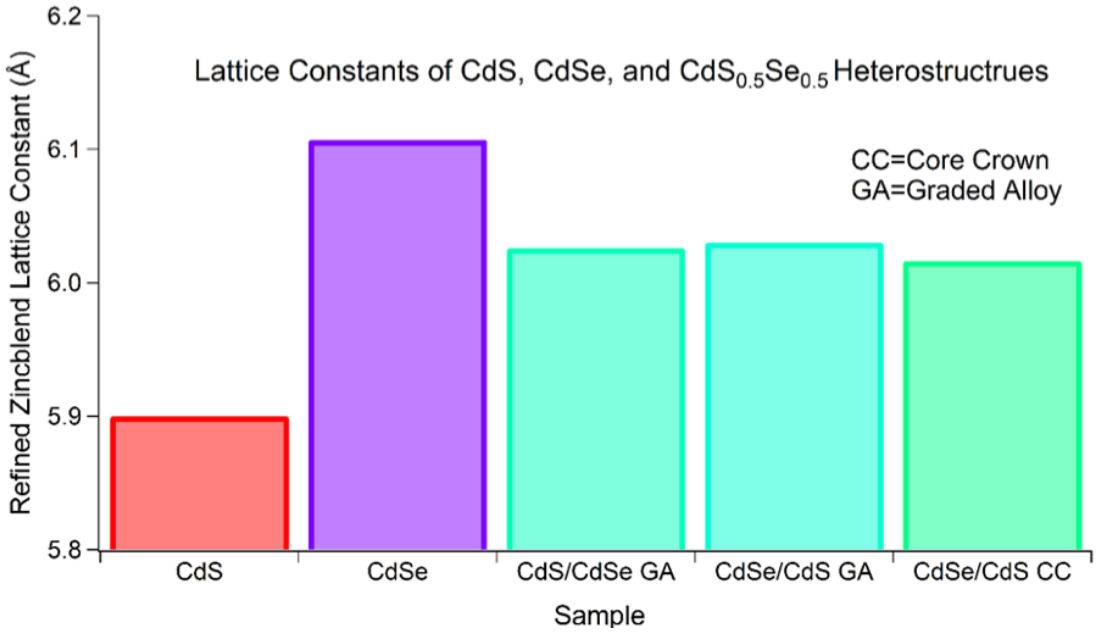

Figure 4.4.8. Extracted lattice constants of the cadmium chalcogenide nanoplatelet structures shows that the $CdS_{0.5}Se_{0.5}$ composites possess intermediate lattice constants.

4.4.3. Raman

As it is a fairly standard technique for the characterization of cadmium chalcogenide heterostructures, with the ability to differentiate between core/shell, graded alloy, and homogeneous alloy structures,[31] N. Saenz and Prof. A. C. Crowther are working on Raman characterization of the nanoplatelets. As of the time of this writing, this experiment is still in progress.

4.5. Summary

We report the reactivity of a library of chalcogenourea compounds whose conversion kinetics to form nanoplatelets can be finely controlled by adjusting the sterics of their substitution pattern. These precursors allow us to control lateral dimensions of the nanoplatelets and adjust nanoplatelet composition ranging from homogeneous and graded alloy structures to core/crown which we characterize by electron microscopy and X-ray scattering techniques. This ideal 2-D system allows us to characterize the link between precursor conversion rates and final nanomaterial compositions.

4.6. Experimental Details

4.6.1. General Methods

All manipulations were performed using standard air-free techniques on a Schlenk line under argon atmosphere or in a nitrogen-filled glovebox unless otherwise indicated.

4.6.2. Chemicals

Reagent alcohol (ACS reagent), hexane (mixture of isomers, ≥98.5%), and toluene (≥99.5%), 1-Octadecene (90%), hexadecane (99%), cadmium acetate dihydrate (98%), cyclohexyl isothiocyanate (98%), hexyl isothiocyanate (95%), phenyl isothiocyanate (98%), benzyl isothiocyanate (98%), and pyrrolidine (99%)

were obtained from Aldrich and used without further purification. Oleic acid (99%) was obtained from Aldrich or Alfa Aesar, stored in a –20 °C freezer, and used without further purification.

4.6.3. Instrumentation

UV-Vis spectra were obtained using a Perkin-Elmer Lambda 950 spectrophotometer equipped with deuterium and halogen lamps. Photoluminescence measurements were performed using a Fluoromax 4 from Horiba Scientific. Powder X-ray diffraction (XRD) was measured on a PANalytical X'Pert Powder X-ray diffractometer. Transmission electron microscopy (TEM) was performed on a FEI Talos F200X. Scanning transmission electron microscopy (STEM and EDX) was performed on a FEI Talos F200X.

STEM EELS experiments were performed on an FEI Titan Thermis CryoS/TEM operating at 60 kV and -80 °C at the Cornell Center for Materials Research (CCMR) under NSF DMR-1719875. The beam convergence angle was 27 mrad. STEM EELS data was processed using the CSI plugin for ImageJ.[32] This experiment was supported by the National Science Foundation (Platform for the Accelerated Realization, Analysis, and Discovery of Interface Materials (PARADIM)) under Cooperative Agreement No. DMR-1539918.

4.6.3.1. Pair Distribution Function Analysis

Total scattering x-ray measurements were performed on the 28-ID-2 (XPD) beamline at the National Synchrotron Light Source II (NSLS-II) at Brookhaven National Laboratory. Six nanoplatelet powder samples, as detailed in Figure 4.3.3 and Figure 4.4.7, were sealed in polyimide capillaries. Diffraction patterns were collected at room temperature in a transmission geometry with an x-ray energy of 66.587 keV (λ=0.1862 Å) and a total exposure time of 4 minutes per sample.[31] A Perkin-Elmer flat-panel 2D detector was used for data collection and mounted with a sample-to-detector distance of 205.342 mm. The experimental geometry, 2θ range, and detector misorientations were calibrated by measuring a crystalline nickel powder directly prior to the nanoplatelets, with the experimental geometry parameters refined using the Fit2D program.[33] Standardized corrections are then made to the data to obtain the total scattering structure function, *F(Q)*, which is then Fourier transformed to obtain the PDF, using PDFgetX3[34] within xPDFsuite.[35] The maximum range of data used in the Fourier transform (Q_{max}, where $Q=4\pi\sin\theta/\lambda$ is the magnitude of the momentum transfer on scattering) was chosen to be 25Å^{-1} for the nanoplatelets studied here, in order to give the best tradeoff between statistical noise and real-space resolution.

The experimental PDF, denoted *G(r)*, is the truncated sine Fourier transform of the total scattering structure function, $F(Q)=Q[S(Q)-1]$:

$$G(r) = \frac{2}{\pi}\int_{Q_{min}}^{Q_{max}} F(Q)\sin(Qr)\,dQ$$

Equation 4.6.1.

where Q is the magnitude of the scattering vector. The structure function, $S(Q)$, is extracted from the Bragg and diffuse components of x-ray, neutron or electron powder diffraction intensity, after normalizing the integrated coherent scattering intensity, $I_c(Q)$, by the total scattering cross-section of the sample, which varies based on the elemental composition, giving

$$S(Q) = \frac{I_c(Q) - \langle f^2 \rangle}{\langle f^2 \rangle} + 1$$

Equation 4.6.2.

where f is the x-ray atomic scattering factor averaged over all elements in the sample.

The PDF gives the scaled probability of finding two atoms in a material a distance r apart and is related to the density of atom pairs in the material.[24] For a macroscopic scatterer, *G(r)* can be calculated from a known structure model according to

$$G(r) = 4\pi r[\rho(r) - \rho_0]$$

Equation 4.6.3.

and

$$\rho(r) = \frac{1}{4\pi r^2 N} \sum_i \sum_{j \neq i} \frac{b_i b_j}{\langle b \rangle^2} \delta(r - r_{ij})$$

Equation 4.6.4.

where ρ_0 is the atomic number density of the material and $\rho(r)$ is the atomic pair density, which is the mean weighted density of neighbor atoms at distance r from an atom at the origin. The sums in $\rho(r)$ run over all atoms in the sample, b_i is the scattering factor of atom i, $\langle b \rangle$ is the average scattering factor and r_{ij} is the distance between atoms i and j.

In practice, we use Equation 4.6.3 and Equation 4.6.4 to fit the PDF generated from a structure model to a PDF determined from experiment. For this purpose, the delta functions in Equation 4.6.4 are Gaussian-broadened and the equation is modified to account for experimental effects. PDF modeling, where it is carried out, is performed by adjusting the parameters of the structure model, such as the lattice constants, atom positions and anisotropic atomic displacement parameters, to maximize the agreement between the theoretical and an experimental PDFs. For nanocrystals, PDF structure modeling can be done using a simple virtual crystal (VC) approximation. VC models are built by applying crystallographic symmetry and periodic boundary conditions to a small unit cell. Nanocrystals are finite

sized, and this is accounted for by attenuating the calculated PDFs with shape functions that encode the morphology. The most widely used software for this kind of analysis is PDFgui,[36] though in the case of highly anisotropic structures such as nanoplatelets, alternative modeling strategies might also be necessary. PDF modeling was performed by M. W. Greenberg and S. Banerjee.

4.6.4. Precursor Synthesis

4.6.4.1. Trisubstituted Thiourea Synthesis

Trisubstituted thioureas are synthesized as described previously with slight modifications.[6, 8] Reactions involving aryl amines were heated to 70°C and heated for 1 hour to drive reactions with these less nucleophilic amines to completion. Following synthesis, a liquid/liquid extraction was performed using 1M HCl, sat. NaCl, and the resulting substance was recrystallized from hot ethanol.

4.6.4.2. Cyclic Selone Synthesis

Cyclic selones are synthesized as described in Chapter 3.

4.6.5. Kinetics Determination

Quantitative aliquots with a volume of 0.1 mL were taken from a CdS or CdSe nanoplatelet reaction and deposited into a previously weighed vial. A mass of toluene equal to 2.5x the weight of the aliquot was added to the vial to

standardize aliquot concentration. UV-vis absorption spectra were taken of each aliquot and the concentration of cadmium chalcogenide in the aliquot was calculated from the size independent absorption coefficient of CdSe at 350 nm.[10] Because there is no such extinction coefficient for CdS, the intensity of the peak at 371 nm was plotted vs. time to extract a proxy for CdS nanoplatelet formation kinetics. The data collected from these methods were fit to a first order fit whose rate constant is reported in Table 4.3.1.

4.6.6. Structure Simulations

Based on extracted k_r values and knowledge of the ratios of sulfur and selenium precursors that we inject into a reaction, we can predict the structure of the resulting nanoplatelet. Based on the rate limiting precursor conversion of chalcogenoureas into solute:

$$CdX_2 \quad + \quad \begin{matrix} Se-precursor \\ S-precursor \end{matrix} \quad \begin{matrix} \overset{k_{Se}}{\longrightarrow} \\ \overset{k_{Se}}{\longrightarrow} \end{matrix} \quad \begin{matrix} [CdSe]_i \\ [CdS]_i \end{matrix} \quad \rightarrow \quad CdS_xSe_{1-x}\ nanoplatelets$$

Equation 4.6.5.

The rate equations are written as:

$$\frac{d[CdSe]}{dt} = -\frac{d[Se]}{dt} = k_{Se} \cdot [Se]$$

Equation 4.6.6.

and

$$\frac{d[CdS]}{dt} = -\frac{d[S]}{dt} = k_{S} \cdot [S]$$

Equation 4.6.7.

where $[CdSe]$, $[CdS]$, $[Se]$ and $[S]$ are the concentrations of crystalized CdSe and CdS, selenium and sulfur precursors, respectively, and k_{Se} and k_S are the first order rate constant of selenium and sulfur precursors.

Although it is hard to empirically determine how many nanoplatelets were nucleated for a given precursor due to reasons previously described, for the purposes of structure modeling, we assume that 1) platelet nucleation happens instantaneously in the beginning of the reaction, 2) the number of platelets stays constant over the course of the reaction, and 3) we numerically set the number of platelets to a value that gives discs with a radius the desired size in nm. Here, we choose to simplify our model of the platelets to that of a circular disc even though they range in geometry between oval shaped discs to T-shaped. We set the height of the circular discs as 1.79 nm which is 3x the average of the CdS and CdSe zincblende lattice parameter.

We use the relative production rates of CdSe and CdS at a given time to model the composition of platelet at time t:

$$CdSe\%(t) = \frac{k_{Se} \cdot [CdSe](t)}{k_{Se} \cdot [CdSe](t) + k_S \cdot [CdS](t)} \cdot 100\%$$

Equation 4.6.8.

and plot these compositional percentages vs. circular disc radius in nm which is calculated by solving the following equation to calculate the volume evolution over time:

$$\frac{dV_{QD}}{dt} = \left(\frac{d[CdSe]}{dt} \cdot V_{m,CdSe} + \frac{d[CdS]}{dt} \cdot V_{m,CdS}\right) \cdot V_{Reaction}/n_\infty$$

Equation 4.6.9.

where $V_{m,CdSe}$ and $V_{m,CdS}$ are the molar volume of CdSe and CdS, respectively, V_{QD} is the volume of each QD, $V_{Reaction}$ is the volume of the reaction solution, and n_∞ is a quantity set empirically. $R_{QD}(t)$ follows, based on modeling the volume as a cylindrical disc with a height of 1.79 nm.

4.6.7. Nanoplatelet Reactions

A three-neck roundbottom flask is loaded with cadmium acetate dihydrate (0.938 mmol, 0.250 g) and 1-octadecene (15 mL) and degassed on a Schlenk line for 15 minutes. In a nitrogen filled glovebox, a 4 mL vial was filled with one or a mixture of chalcogen precursors (0.182 mmol) and tetraglyme (1.1 mL). A separate 4 mL vial is filled with ~1 g oleic acid inside the glovebox. The three-neck

roundbottom flask is put under Ar and heated to 195 °C. Upon reaching the reaction temperature, 60 μL of oleic acid are injected into the reaction flask followed by injection of the chalcogen precursor solution. The reaction is run for the desired amount of time, followed by injection of 0.5 mL of oleic acid. This reaction is sensitive to the amount of time spent degassing.

4.6.8. Precursor Characterization

_N_-cyclohexylpyrrolidine-1-carbothioamide (3)

Yield 0.48 g (22%). ^{1}H NMR (400 MHz, $CDCl_3$): δ = 1.06-1.25 (m, 2H), 1.31-1.48 (m, 2H), 1.56-1.76 (m, 4H), 1.88-2.03 (br, 4H), 2.03-2.14 (m, 2H), 3.29-3.81 (br, 4H), 4.21-4.38 (m, 1H), 4.92-5.07 (br, 1H). ^{13}C{^{1}H} (100 MHz, $CDCl_3$): δ = 24.95, 25.35, 25.62, 33.41, 49.32, 53.55, 177.38. Anal. Calcd for $C_{11}H_{20}N_2S$: C, 62.22; H, 9.49; N, 13.19. Found: C, 62.30; H, 9.50; N, 13.15. MS (ASAP) *m*/*z* calcd for [$C_{11}H_{20}N_2S + H^+$]: 213.14. Found: 213.14.

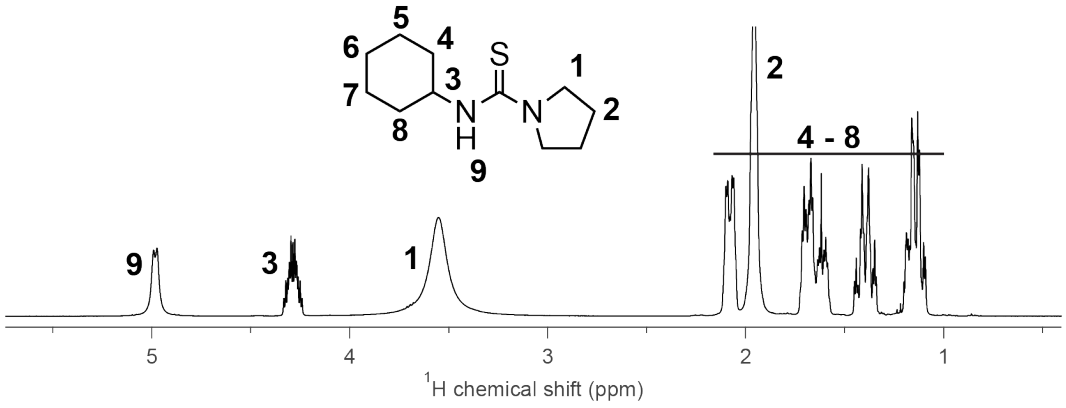

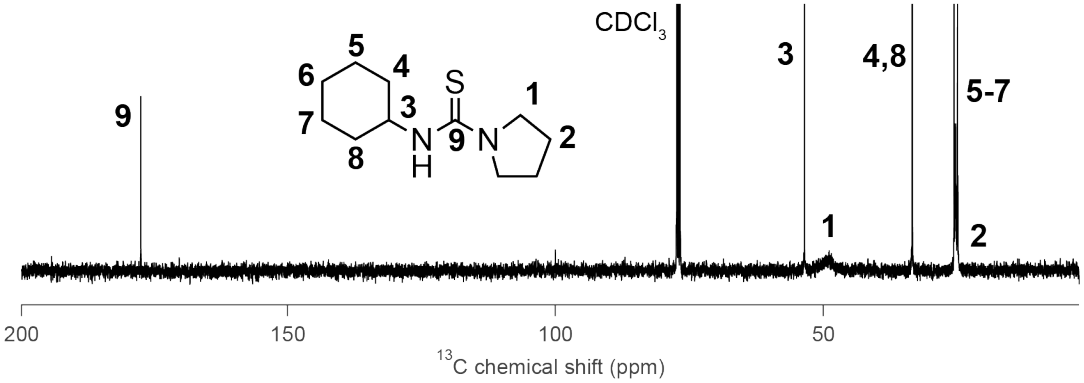

***N*-hexylpyrrolidine-1-carbothioamide (4)**

Yield 0.10 g (4.7%). ^{1}H NMR (400 MHz, $CDCl_3$): δ = 0.86 (t, 3H), 1.3 (m, 6H), 1.58 (m, 2H), 1.96 (br, 4H), 3.56 (br, 4H), 3.60 (m, 2H), 5.16 (br, 1H). $^{13}C\{^{1}H\}$ (100 MHz, $CDCl_3$): δ = 13.99, 22.55, 25.40, 26.61, 29.51, 31.52, 45.63, 49.51, 178.60. Anal. Calcd for $C_{11}H_{22}N_2S$: C, 61.63; H, 10.34; N, 13.07. Found: C, 60.26; H, 10.14; N, 12.71. MS (ASAP) *m*/*z* calcd for [$C_{11}H_{22}N_2S + H^+$]: 215.16. Found: 215.16.

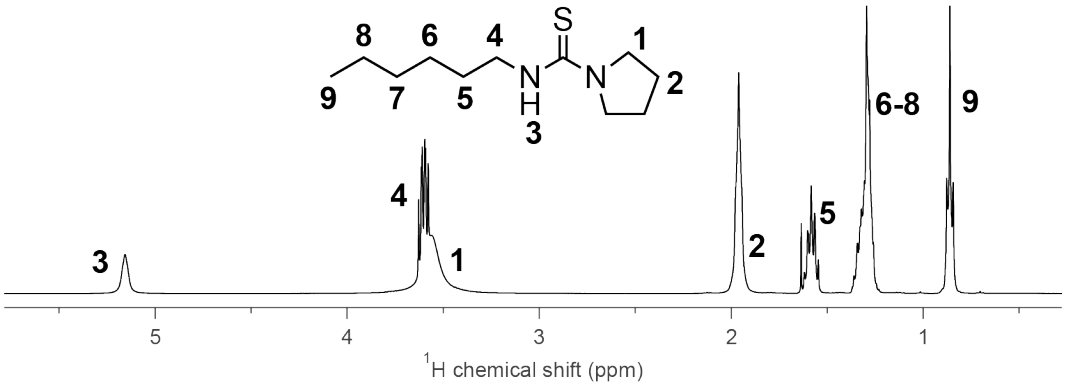

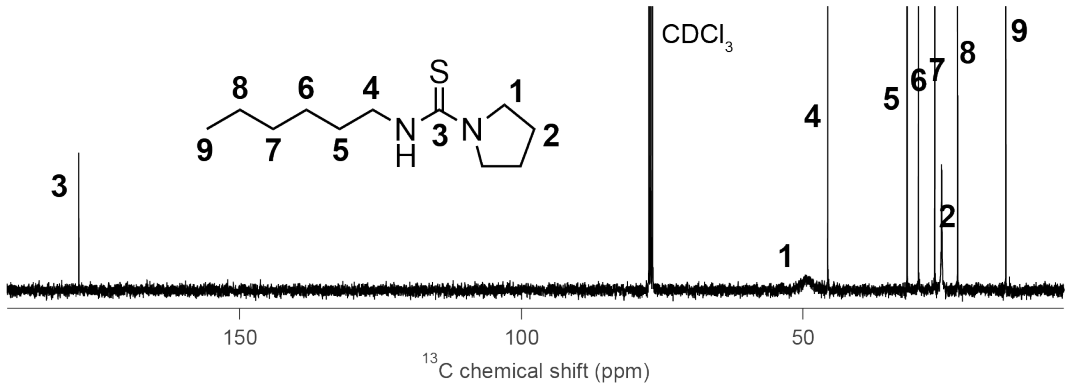

_N_-phenylpyrrolidine-1-carbothioamide (5)

Yield 0.64 g (31%). ^{1}H NMR (400 MHz, $CDCl_3$): δ = 1.91 (br, 4H), 3.57 (br, 4H), (br, 1H), 7.07–7.13 (m, 1H), 7.21–7.29 (m, 3H). $^{13}C\{^{1}H\}$ (100 MHz, $CDCl_3$): δ = 25.56, 49.96, 125.65, 125.77, 128.69, 139.44, 178.38. Anal. Calcd for $C_{11}H_{14}N_2S$: C, 64.04; H, 6.84; N, 13.58. Found: C, 64.24; H, 6.82; N, 13.51. MS (ASAP) *m*/*z* calcd for [$C_{11}H_{14}N_2S + H^+$]: 207.10. Found: 207.10.

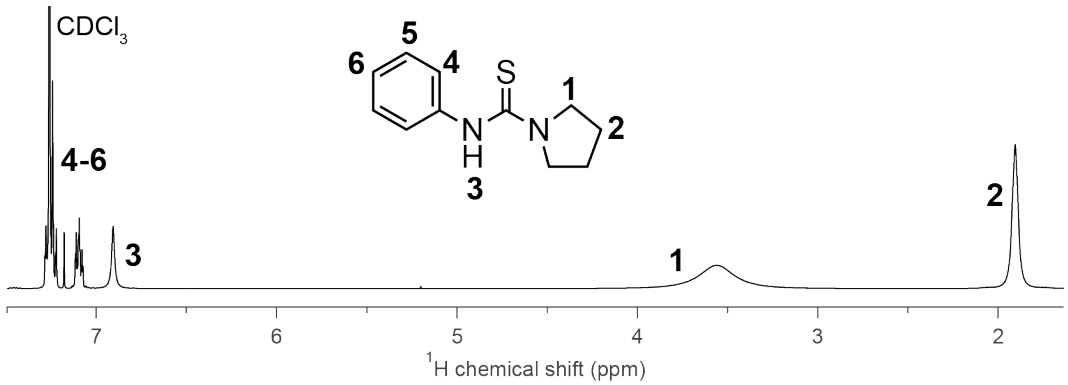

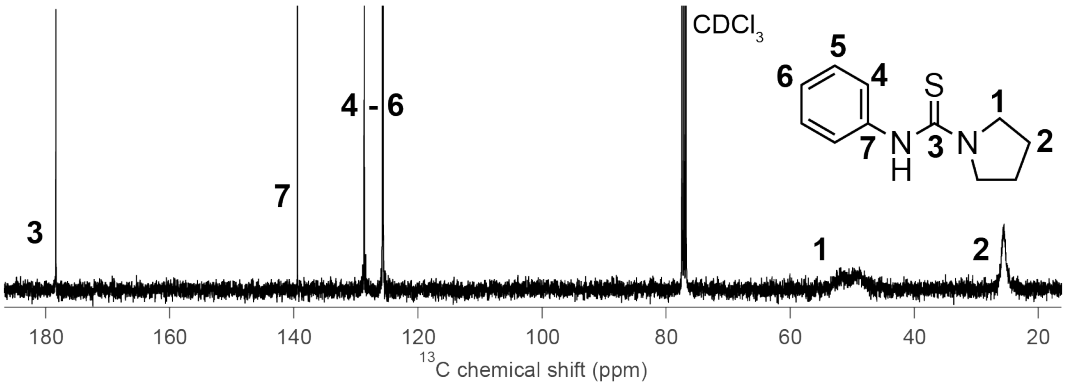

_N_-benzylpyrrolidine-1-carbothioamide (6)

Yield 0.65 g (30%). ^{1}H NMR (400 MHz, $CDCl_3$): δ = 1.89 (br, 4H), 3.50 (br, 4H), 4.77 (d, 2H), 5.43 (br, 1H), 7.16-7.29 (m, 5H). $^{13}C\{^{1}H\}$ (100 MHz, $CDCl_3$): δ = 25.38, 49.50, 127.52, 127.89, 128.67, 138.41, 178.67. Anal. Calcd for $C_{12}H_{16}N_2S$: C, 65.42; H, 7.32; N, 12.71. Found: C, 65.42; H, 7.16; N, 12.71. MS (ASAP) *m*/*z* calcd for [$C_{12}H_{16}N_2S + H^+$]: 221.11. Found: 221.11.

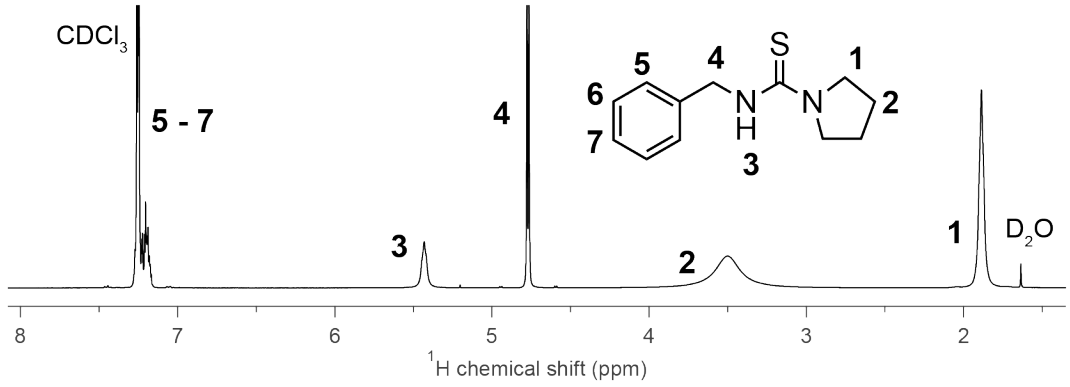

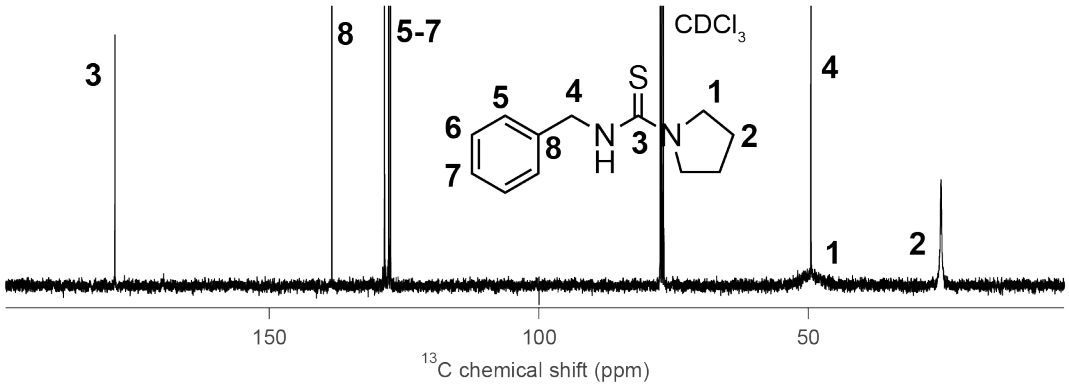

4.7. References

(1) Ithurria, S.; Tessier, M.; Mahler, B.; Lobo, R.; Dubertret, B.; Efros, A. L., Colloidal Nanoplatelets with Two-Dimensional Electronic Structure. *Nat. Mater.* **2011,** *10* (12), 936.

(2) Lhuillier, E.; Pedetti, S.; Ithurria, S.; Nadal, B.; Heuclin, H.; Dubertret, B., Two-Dimensional Colloidal Metal Chalcogenides Semiconductors: Synthesis, Spectroscopy, and Applications. *Acc. Chem. Res.* **2015,** *48* (1), 22-30.

(3) Bertrand, G. H. V.; Polovitsyn, A. P.; Christodoulou, S.; Khan, A. H.; Moreels, I., Shape Control of Zincblende CdSe Nanoplatelets. *Chem. Comm.* **2016,** *52*, 11975-11978.

(4) Bouet, C.; Mahler, B.; Nadal, B.; Abecassis, B.; Tessier, M. D.; Ithurria, S.; Xu, X.; Dubertret, B., Two-Dimensional Growth of CdSe Nanocrystals, From Nanoplatelets to Nanosheets. *Chem. Mater.* **2013,** *25* (4), 639-645.

(5) Nasilowski, M.; Mahler, B.; Lhuillier, E.; Ithurria, S.; Dubertret, B., Two-Dimensional Colloidal Nanocrystals. *Chem. Rev.* **2016,** *116* (18), 10934-10982.

(6) Hendricks, M. P.; Campos, M. P.; Cleveland, G. T.; Jen-La Plante, I.; Owen, J. S., A Tunable Library of Substituted Thiourea Precursors to Metal Sulfide Nanocrystals. *Science* **2015,** *348* (6240), 1226-1230.

(7) Campos, M. P.; Hendricks, M. P.; Beecher, A. N.; Walravens, W.; Swain, R. A.; Cleveland, G. T.; Hens, Z.; Sfeir, M. Y.; Owen, J. S., A Library of Selenourea Precursors to PbSe Nanocrystals with Size Distributions Near the Homogenous Limit. *J. Am. Chem. Soc.* **2017,** *139* (6), 2296-2305.

(8) Hamachi, L. S.; Jen-La Plante, I.; Coryell, A. C.; De Roo, J.; Owen, J. S., Kinetic Control over CdS Nanocrystal Nucleation Using a Library of Thiocarbonates, Thiocarbamates, and Thioureas. *Chem. Mater.* **2017,** *29* (20), 8711-8719.

(9) Hamachi, L. S.; al., e.; Owen, J. S., Precursor Reaction Kinetics Control Compositional Grading in $CdSe_{1-x}S_x$ Nanocrystal Heterostructures. *In preparation.*

(10) Leatherdale, C. A.; Woo, W. K.; Mikulec, F. V.; Bawendi, M. G., On the Absorption Cross Section of CdSe Nanocrystal Quantum Dots. *J. Phys. Chem. B* **2002,** *106* (31), 7619-7622.

(11) Owen, J. S.; Chan, E. M.; Liu, H.; Alivisatos, A. P., Precursor Conversion Kinetics and the Nucleation of Cadmium Selenide Nanocrystals. *J. Am. Chem. Soc.* **2010,** *132* (51), 18206-18213.

(12) Guo, Y.; Alvarado, S. R.; Barclay, J. D.; Vela, J., Shape-Programmed Nanofabrication: Understanding the Reactivity of Dichalcogenide Precursors. *ACS Nano* **2013,** *7* (4), 3616-3625.

(13) Ruberu, T. P. A.; Albright, H. R.; Callis, B.; Ward, B.; Cisneros, J.; Fan, H.; Vela, J., Molecular Control of the Nanoscale: Effect of Phosphine-Chalcogenide Reactivity on CdS-CdSe Nanocrystal Composition and Morphology. *ACS Nano* **2012,** *6* (6), 5348-5359.

(14) Hens, Z., Economical Routes to Colloidal Nanocrystals. *Science* **2015,** *348* (6240), 1211-1212.

(15) Harris, D. K.; Bawendi, M. G., Improved Precursor Chemistry for the Synthesis of III–V Quantum Dots. *J. Am. Chem. Soc.* **2012,** *134* (50), 20211-20213.

(16) Joung, S.; Yoon, S.; Han, C.-S.; Kim, Y.; Jeong, S., Facile Synthesis of Uniform Large-Sized InP Nanocrystal Quantum Dots Using Tris(*tert*-butyldimethylsilyl) Phosphine. *Nanoscale Res. Lett.* **2012,** *7* (1), 93.

(17) Gary, D. C.; Glassy, B. A.; Cossairt, B. M., Investigation of Indium Phosphide Quantum Dot Nucleation and Growth Utilizing Triarylsilylphosphine Precursors. *Chem. Mater.* **2014,** *26* (4), 1734-1744.

(18) Mahler, B.; Nadal, B.; Bouet, C.; Patriarche, G.; Dubertret, B., Core/Shell Colloidal Semiconductor Nanoplatelets. *J. Am. Chem. Soc.* **2012,** *134* (45), 18591-18598.

(19) Fan, F.; Kanjanaboos, P.; Saravanapavanantham, M.; Beauregard, E.; Ingram, G.; Yassitepe, E.; Adachi, M. M.; Voznyy, O.; Johnston, A. K.; Walters, G., Colloidal CdSe1–x Sx Nanoplatelets with Narrow and Continuously-Tunable Electroluminescence. *Nano Lett.* **2015,** *15* (7), 4611-4615.

(20) Delikanli, S.; Guzelturk, B.; Hernández‐Martínez, P. L.; Erdem, T.; Kelestemur, Y.; Olutas, M.; Akgul, M. Z.; Demir, H. V., Continuously Tunable Emission in Inverted Type‐I CdS/CdSe Core/Crown Semiconductor Nanoplatelets. *Adv. Funct. Mater.* **2015,** *25* (27), 4282-4289.

(21) Tessier, M. l. D.; Spinicelli, P.; Dupont, D.; Patriarche, G.; Ithurria, S.; Dubertret, B., Efficient Exciton Concentrators Built From Colloidal Core/Crown CdSe/CdS Semiconductor Nanoplatelets. *Nano Lett.* **2013,** *14* (1), 207-213.

(22) Chen, Y.; Chen, D.; Li, Z.; Peng, X., Symmetry-Breaking for Formation of Rectangular CdSe Two-Dimensional Nanocrystals in Zinc-Blende Structure. *J. Am. Chem. Soc.* **2017,** *139* (29), 10009-10019.

(23) Li, Y.; Li, Y.; Pei, A.; Yan, K.; Sun, Y.; Wu, C.-L.; Joubert, L.-M.; Chin, R.; Koh, A. L.; Yu, Y., Atomic Structure of Sensitive Battery Materials and Interfaces Revealed by Cryo–Electron Microscopy. *Science* **2017,** *358* (6362), 506-510.

(24) Egami, T.; Billinge, S. J. L., *Underneath the Bragg Peaks: Structural Analysis of Complex Materials*. Elsevier Science & Technology Books: 2003.

(25) Billinge, S. J. L.; Levin, I., The Problem With Determining Atomic Structure at the Nanoscale. *Science* **2007,** *316* (5824), 561-565.
(26) Beecher, A. N.; Yang, X.; Palmer, J. H.; LaGrassa, A. L.; Juhas, P.; Billinge, S. J. L.; Owen, J. S., Atomic Structures and Gram Scale Synthesis of Three Tetrahedral Quantum Dots. *J. Am. Chem. Soc.* **2014,** *136* (30), 10645-10653.
(27) Tan, L.; Misquitta, A. J.; Sapelkin, A.; Fang, L.; Wilson, R. M.; Zhang, B.; Zhu, T.; Riehle, F. S.; Han, S.; Yu, K., X-ray Total Scattering Study of Tegular and Magic-Size Nanoclusters of Cadmium Sulphide. *arXiv preprint arXiv:1806.03274* **2018**.
(28) Kumara, L.; Sakata, O.; Kohara, S.; Yang, A.; Song, C.; Kusada, K.; Kobayashi, H.; Kitagawa, H. In *Structural Studies of Metal Nanoparticles Using High-Energy X-ray Diffraction*, AIP Conference Proceedings, AIP Publishing: 2016; p 050016.
(29) Masadeh, A. S.; Božin, E. S.; Farrow, C. L.; Paglia, G.; Juhas, P.; Billinge, S. J. L.; Karkamkar, A.; Kanatzidis, M. G., Quantitative Size-Dependent Structure and Strain Determination of CdSe Nanoparticles Using Atomic Pair Distribution Function Analysis. *Phys. Rev. B* **2007,** *76* (11), 115413.
(30) Denton, A. R.; Ashcroft, N. W., Vegard's Law. *Phys. Rev. A* **1991,** *43* (6), 3161.
(31) Mukherjee, P.; Lim, S. J.; Wrobel, T. P.; Bhargava, R.; Smith, A. M., Measuring and Predicting the Internal Structure of Semiconductor Nanocrystals Through Raman Spectroscopy. *J. Am. Chem. Soc.* **2016,** *138* (34), 10887-10896.
(32) Cueva, P.; Hovden, R.; Mundy, J. A.; Xin, H. L.; Muller, D. A., Data Processing for Atomic Resolution Electron Energy Loss Spectroscopy. *Microsc. Microanal.* **2012,** *18* (4), 667-675.
(33) Hammersley, A. P.; Svensson, S. O.; Hanfland, M.; Fitch, A.; Hausermann, D., Two-Dimensional Detector Software: From Real Detector to Idealised Image or Two-Theta Scan. *Int. J. High Press. Res.* **1996,** *14* (4-6), 235-248.
(34) Juhás, P.; Davis, T.; Farrow, C. L.; Billinge, S. J. L., PDFgetX3: a Rapid and Highly Automatable Program for Processing Powder Diffraction Data Into Total Scattering Pair Distribution Functions. *J. Appl. Crystallogr.* **2013,** *46* (2), 560-566.
(35) Yang, X.; Juhas, P.; Farrow, C. L.; Billinge, S. J. L., xPDFsuite: An End-to-End Software Solution for High Throughput Pair Distribution Function Transformation, Visualization and Analysis. *arXiv preprint arXiv:1402.3163* **2014**.
(36) Farrow, C. L.; Juhas, P.; Liu, J. W.; Bryndin, D.; Božin, E. S.; Bloch, J.; Proffen, T. h.; Billinge, S. J. L., PDFfit2 and PDFgui: Computer Programs for Studying Nanostructure in Crystals. *J. Phys. Condens. Matter.* **2007,** *19* (33), 335219.

Conclusion

There is great opportunity for the synthetic inorganic chemist to make valuable contributions in the field of nanocrystal research. The work of materials scientists, physicists, and engineers motivates the need for development of the next generation of synthetic methods enabling finer control over nanostructures than ever before. The motivation of this thesis was to reinvent the synthesis of a graded alloy core/shell nanocrystal and accomplish fine control over the structure completely via kinetic control.

Based on results of simulations, we find that this goal is near impossible, given reaction time and temperature constraints. Nevertheless, using the new methods described in this thesis, we are able to synthesize high quality materials that can be used in solid state lighting applications, in electroluminescent devices for seizure detection, and in devices and artificial cell membranes as voltage sensitive imaging probes. Although we do not go into great detail on these applications in this thesis, these projects represent a snapshot of ongoing projects which leverage the utility of our compound library.

Another goal of the research in this thesis was to add to the growing libraries of precursor molecules that produce nanocrystals at tunable rates. In this sense, we were successful. In addition to accessing wider ranges of precursor conversion rates and final cadmium chalcogenide nanocrystal sizes, chapters two

and three introduce new sulfur precursors including thiocarbonates and thiocarbamates which have demonstrable effects on particle monodispersity, as well as cyclic thiones and selones whose backbone affects the number of nanocrystals nucleated.

We have also been able to look at fundamental material properties such as the differences in growth rates and critical concentrations between cadmium sulfide and selenide and observe anisotropic structures that arise in both nanoparticle and nanoplatelet systems under regimes of kinetic control. In some sense these fundamental studies raise more questions than they end up answering. Many of these studies are uniquely made possible by the expansion of our precursor library. This also enables studies on the fundamental material properties of the cadmium chalcogenides in relation to the lead chalcogenides.

With the increasingly stringent restrictions placed on the cadmium content present in consumer products in Europe, the direct translation of this research to industrial applications hangs in question. However, lessons that we learn from studying the kinetic control over chalcogen precursor conversion can easily be applied to the synthesis of zinc chalcogenides which are commonly used as shell materials for cadmium-free particle systems. Additionally, the anisotropic particle growth we observe under precursor conversion limited conditions may possess

relevance towards the study of current cadmium-free particles or a currently undiscovered alternative nanocrystal emitter.